

ISSN 1816-112X

Science Citation Index Expanded,  
Materials Science Citation Index  
and ISI Alerting

#### EDITORS-IN-CHIEF

##### Asian Pacific, African and organizing Editor

S.L. Chan  
*The Hong Kong Polyt. Univ.,  
Hong Kong*

##### American Editor

W.F. Chen  
*Univ. of Hawaii at Manoa, USA*

##### European Editor

R. Zandonini  
*Trento Univ., Italy*

#### INTERNATIONAL EDITORIAL BOARD

F.G. Albermani  
*Central Queensland Univ., Australia*

I. Burgess  
*Univ. of Sheffield, UK*

F.S.K. Bijlaard  
*Delft Univ. of Technology, The Netherlands*

R. Bjorhovde  
*The Bjorhovde Group, USA*

M.A. Bradford  
*The Univ. of New South Wales, Australia*

D. Camotim  
*Technical Univ. of Lisbon, Portugal*

C.M. Chan  
*Hong Kong Univ. of Science & Technology, Hong Kong*

T.H.T. Chan  
*Queensland Univ. of Technology, Australia*

T.M. Chan  
*The Hong Kong Polyt. Univ., Hong Kong*

S.P. Chiew  
*Singapore Institute of Technology, Singapore*

W.K. Chow  
*The Hong Kong Polyt. Univ., Hong Kong*

G.G. Deierlein  
*Stanford Univ., California, USA*

L. Dezi  
*Univ. of Ancona, Italy*

D. Dubina  
*The Politehnica Univ. of Timisoara, Romania*

L. Gardner  
*Imperial College of Science, Technology and Medicine, UK*

R. Greiner  
*Technical Univ. of Graz, Austria*

Y. Goto  
*Nagoya Institute of Technology*

L.H. Han  
*Tsinghua Univ. China*

S. Herion  
*University of Karlsruhe, Germany*

G.W.M. Ho  
*Ove Arup & Partners Hong Kong Ltd., Hong Kong*

B.A. Izzuddin  
*Imperial College of Science, Technology and  
Medicine, UK*

J.P. Jaspart  
*Univ. of Liege, Belgium*

S. A. Jayachandran  
*IIT Madras, Chennai, India*

S.E. Kim  
*Sejong Univ., South Korea*

S. Kitipornchai  
*The Univ., of Queensland, Australia*

D. Lam  
*Univ. of Bradford, UK*

G.Q. Li  
*Tongji Univ., China*

J.Y.R. Liew  
*National Univ. of Singapore, Singapore*

Y.P. Liu  
*The Hong Kong Polyt. Univ., Hong Kong*

S.W. Liu  
*NIDA EUROPE Ltd., UK*

E.M. Lui  
*Syracuse Univ., USA*

Y.L. Mo  
*Univ. of Houston, USA*

J.P. Muzeau  
*CUST, Clermont Ferrand, France*

D.A. Nethercot  
*Imperial College of Science, Technology and  
Medicine, UK*

Y.Q. Ni  
*The Hong Kong Polyt. Univ., Hong Kong*

D.J. Oehlers  
*The Univ. of Adelaide, Australia*

J.L. Peng  
*Yunlin Uni. of Science & Technology, Taiwan*

K. Rasmussen  
*The Univ. of Sydney, Australia*

J.M. Rotter  
*The Univ. of Edinburgh, UK*

C. Scawthorn  
*Scawthorn Porter Associates, USA*

P. Schaumann  
*Univ. of Hannover, Germany*

Y.J. Shi  
*Tsinghua Univ., China*

G.P. Shu  
*Southeast Univ. China*

L. Simões da Silva  
*Department of Civil Engineering, University of  
Coimbra, Portugal*

J.G. Teng  
*The Hong Kong Polyt. Univ., Hong Kong*

G.S. Tong  
*Zhejiang Univ., China*

K.C. Tsai  
*National Taiwan Univ., Taiwan*

C.M. Uang  
*Univ. of California, USA*

B. Uy  
*The University of New South Wales, Australia*

M. Veljkovic  
*Univ. of Lulea, Sweden*

F. Wald  
*Czech Technical Univ. in Prague, Czech*

Y.C. Wang  
*The Univ. of Manchester, UK*

Y.L. Xu  
*The Hong Kong Polyt. Univ., Hong Kong*

D. White  
*Georgia Institute of Technology, USA*

E. Yamaguchi  
*Kyushu Institute of Technology, Japan*

Y.B. Yang  
*National Taiwan Univ., Taiwan*

Y.Y. Yang  
*China Academy of Building Research, Beijing, China*

B. Young  
*The Univ. of Hong Kong, Hong Kong*

X.L. Zhao  
*Monash Univ., Australia*

X.H. Zhou  
*Chongqing University, China*

Z.H. Zhou  
*Alpha Consultant Ltd., Hong Kong*

R.D. Ziemian  
*Bucknell University, USA*

Cover: The 139mx73m clear span Spectacle Roof designed by Second-order Direct Analysis without assumption of effective length

e-copy of IJASC is free to download at "www.ascjournal.com" in internet and mobile apps.



## General Information

### *Advanced Steel Construction, an international journal*

#### Aims and scope

The International Journal of Advanced Steel Construction provides a platform for the publication and rapid dissemination of original and up-to-date research and technological developments in steel construction, design and analysis. Scope of research papers published in this journal includes but is not limited to theoretical and experimental research on elements, assemblages, systems, material, design philosophy and codification, standards, fabrication, projects of innovative nature and computer techniques. The journal is specifically tailored to channel the exchange of technological know-how between researchers and practitioners. Contributions from all aspects related to the recent developments of advanced steel construction are welcome.

#### Instructions to authors

**Submission of the manuscript.** Authors may submit on-line at [www.hkisc.org](http://www.hkisc.org)

Asian Pacific, African and organizing editor : Professor S.L. Chan, Email: [ceslchan@polyu.edu.hk](mailto:ceslchan@polyu.edu.hk)  
American editor : Professor W.F. Chen, Email: [waifah@hawaii.edu](mailto:waifah@hawaii.edu)  
European editor : Professor R. Zandonini, Email: [riccardo\\_zandonini@ing.unitn.it](mailto:riccardo_zandonini@ing.unitn.it)

All manuscripts submitted to the journal are recommended to accompany with a list of four potential reviewers suggested by the author(s). This list should include the complete name, address, telephone and fax numbers, email address, and at least five keywords that identify the expertise of each reviewer. This scheme will improve the process of review.

#### Style of manuscript

**General.** Author(s) should provide full postal and email addresses and fax number for correspondence. The manuscript including abstract, keywords, references, figures and tables should be in English with pages numbered and typed with double line spacing on single side of A4 or letter-sized paper. The front page of the article should contain:

- a) a short title (reflecting the content of the paper);
- b) all the name(s) and postal and email addresses of author(s) specifying the author to whom correspondence and proofs should be sent;
- c) an abstract of 100-200 words; and
- d) 5 to 8 keywords.

The paper must contain an introduction and a conclusion. The length of paper should not exceed 25 journal pages (approximately 15,000 words equivalents).

**Tables and figures.** Tables and figures including photographs should be typed, numbered consecutively in Arabic numerals and with short titles. They should be referred in the text as Figure 1, Table 2, etc. Originally drawn figures and photographs should be provided in a form suitable for photographic reproduction and reduction in the journal.

**Mathematical expressions and units.** The Systeme Internationale (SI) should be followed whenever possible. The numbers identifying the displayed mathematical expression should be referred to in the text as Eq. 1, Eq. 2.

**References.** References to published literature should be referred in the text, in the order of citation with Arabic numerals, by the last name(s) of the author(s) (e.g. Zandonini and Zanon [3]) or if more than three authors (e.g. Zandonini et al. [4]). References should be in English with occasional allowance of 1-2 exceptional references in local languages and reflect the current state-of-technology. Journal titles should be abbreviated in the style of the Word List of Scientific Periodicals. References should be cited in the following style [1, 2, 3].

Journal: [1] Chen, W.F. and Kishi, N., "Semi-rigid Steel Beam-to-column Connections, Data Base and Modelling", Journal of Structural Engineering, ASCE, 1989, Vol. 115, No. 1, pp. 105-119.

Book: [2] Chan, S.L. and Chui, P.P.T., "Non-linear Static and Cyclic Analysis of Semi-rigid Steel Frames", Elsevier Science, 2000.

Proceedings: [3] Zandonini, R. and Zanon, P., "Experimental Analysis of Steel Beams with Semi-rigid Joints", Proceedings of International Conference on Advances in Steel Structures, Hong Kong, 1996, Vol. 1, pp. 356-364.

**Proofs.** Proof will be sent to the corresponding author to correct any typesetting errors. Alternations to the original manuscript at this stage will not be accepted. Proofs should be returned within 48 hours of receipt on-line.

**Copyright.** Submission of an article to "Advanced Steel Construction" implies that it presents the original and unpublished work, and not under consideration for publication nor published elsewhere. On acceptance of a manuscript submitted, the copyright thereof is transferred to the publisher by the Transfer of Copyright Agreement and upon the acceptance of publication for the papers, the corresponding author must sign the form for Transfer of Copyright.

**Permission.** Quoting from this journal is granted provided that the customary acknowledgement is given to the source.

**Page charge and Reprints.** There will be no page charges if the length of paper is within the limit of 25 journal pages. A total of 30 free offprints will be supplied free of charge to the corresponding author. Purchasing orders for additional offprints can be made on order forms which will be sent to the authors. These instructions can be obtained at the Hong Kong Institute of Steel Construction, Journal website: <http://www.hkisc.org>

The International Journal of Advanced Steel Construction is published quarterly by learnt society, The Hong Kong Institute of Steel Construction, c/o Department of Civil & Environmental Engineering, The Hong Kong Polytechnic University, Hung Hom, Kowloon, Hong Kong.

**Disclaimer.** No responsibility is assumed for any injury and / or damage to persons or property as a matter of products liability, negligence or otherwise, or from any use or operation of any methods, products, instructions or ideas contained in the material herein.

**Subscription inquiries and change of address.** Address all subscription inquiries and correspondence to Member Records, IJASC. Notify an address change as soon as possible. All communications should include both old and new addresses with zip codes and be accompanied by a mailing label from a recent issue. Allow six weeks for all changes to become effective.

#### The Hong Kong Institute of Steel Construction

HKISC  
c/o Department of Civil and Environmental Engineering,  
The Hong Kong Polytechnic University,  
Hung Hom, Kowloon, Hong Kong, China.  
Tel: 852- 2766 6047 Fax: 852- 2334 6389  
Email: [ceslchan@polyu.edu.hk](mailto:ceslchan@polyu.edu.hk) Website: <http://www.hkisc.org/>  
ISSN 1816-112X

Science Citation Index Expanded, Materials Science Citation Index and ISI Alerting

Copyright © 2017 by:

The Hong Kong Institute of Steel Construction.







ISSN 1816-112X

Science Citation Index Expanded,  
Materials Science Citation Index and  
ISI Alerting

## EDITORS-IN-CHIEF

### Asian Pacific, African and organizing Editor

S.L. Chan

*The Hong Kong Polyt. Univ.,  
Hong Kong*

Email: ceslchan@polyu.edu.hk

### American Editor

W.F. Chen

*Univ. of Hawaii at Manoa, USA*

Email: waifah@hawaii.edu

### European Editor

R. Zandonini

*Trento Univ., Italy*

Email: riccardo.zandonini@ing.unitn.it

# Advanced Steel Construction

*an international journal*

VOLUME 13 NUMBER 3

SEPTEMBER 2017

## Technical Papers

Field Monitoring and Numerical Analysis of Thermal Behavior of Large Span Steel Structures under Solar Radiation 190

*Zhongwei Zhao, Hongbo Liu and Zhihua Chen*

A 3-Node Co-Rotational Triangular Elasto-Plastic Shell Element Using Vectorial Rotational Variables 206

*Zhongxue Li, Bassam A. Izzuddin, Loc Vu-Quoc, Zihan Rong and Xin Zhuo*

Seismic Performance Analysis of a Resilient Prestressed Steel Frame with Intermediate Column Containing Friction Dampers 241

*Yanxia Zhang, Anran Liu, Ailin Zhang and Xuechun Liu*

Concurrent Multi-Scale Modeling of a Transmission Tower Structure and its Experimental Verification 258

*F.Y. Wang, Y.L. Xu and S. Zhan*

Seismic Collapse Analysis of Concentrically-Braced Frames by the IDA Method 273

*Gang Li, Zhi-Qian Dong, Hong-Nan Li and Y. B. Yang*

Experiment and Stability Analysis on Heavy-Duty Scaffold Systems with Top Shores 293

*Jui-Lin Peng, Chung-Sheng Wang, Chung-Wei Wu and Wai-Fah Chen*

## Announcements by IJASC :

Announcement for ICASS 2018



# FIELD MONITORING AND NUMERICAL ANALYSIS OF THERMAL BEHAVIOR OF LARGE SPAN STEEL STRUCTURES UNDER SOLAR RADIATION

Zhongwei Zhao<sup>2</sup>, Hongbo Liu<sup>1,2\*</sup> and Zhihua Chen<sup>1,2</sup>

<sup>1</sup> State Key Laboratory of Hydraulic Engineering Simulation and Safety, Tianjin University, Tianjin 300072, China

<sup>2</sup> School of Civil Engineering, Tianjin University, China

\*(Corresponding author: E-mail: hbliu@tju.edu.cn)

Received: 15 March 2016; Revised: 9 June 2016; Accepted: 13 August 2016

---

**ABSTRACT:** The erection process of large span structures is complex and requires long time to complete, even a few years for some major engineering projects. The structure will expose to solar radiation which will result in larger temperature change in service phase. In order to obtain the temperature distribution and thermal behaviour of large span steel structures under solar radiation, a numerical simulation method based on the ASHRAE model is presented in this paper. In order to provide insights into temperature distribution and data to verify the presented numerical simulation method, field monitoring system was designed for an actual project. The temperature distribution mechanical response of the entire structure was derived by fielding monitoring. Using the temperature numerical simulation method, the temperature distribution and thermal behaviour of a typical steel structure, the lattice shell structures, were studied. The study showed that: 1) the daily temperature variation caused by solar radiation has little effect on the components which located at upper part of spatial latticed shell structures, the internal force can be released by deformation. 2) The components connected to supports were sensitive to thermal load. They were in shadow of the upper structures in general, so the temperature caused by solar radiation has smaller effect than effect of seasonal temperature difference. 3) The shell-shaped latticed shell structures behave like arch, and the internal force can be released by deformation.

**Keywords:** Large span steel structures, thermal behavior, solar radiation, field monitoring, numerical analysis

**DOI:** 10.18057/IJASC.2017.13.3.1

---

## 1. INTRODUCTION

Steel structures have been popular in recent years. They have many engineering advantages, such as light weight, fast assembly, large span capability and ease to form various attractive geometrical surfaces. Therefore, steel structures are used widely in sport stadiums and gymnasiums, exhibition centers, airport, factory buildings.

The erection process of large span structures is complex and needs long time to complete, even a few years for some major engineering projects. So the structures under-construction will also experience daily and seasonal temperature changes. If the main structure of one building is completed without accessory structures, for example the roof board, the whole structure will be exposed to solar radiation and the maximum temperature of the steel structure surface may exceed 60°C in summer. In most cases, the thermal load during this erection process is not considered in design process of the structure. And so far few researchers have investigated the effect of this kind of thermal load on mechanical behavior of structures.

In the past decades, most researches have devoted to design approaches and investigation on the structural behavior of steel structures [1-8]. In the design process of steel structures, the structural behavior under the gravity load, dead load, live load, wind load, thermal load, snow load and earthquake action are analyzed. For long span steel structures, the thermal load has a significant effect on its structural behavior. For structures without roof board, more attentions should be paid to the thermal load induced by solar radiation.

The thermal load of structures without roof board under construction induced by ambient is more non-uniform and higher than the corresponding ambient air temperature due to the solar radiation. Liu [9] divided the structures influenced by solar radiation into three categories. The first type is the steel structures exposed to solar radiation, such as the steel arches and the steel structures under construction is also included. The second type is the steel structures which use glass or ETFE as its roof materials. The third type is the steel structures which use light steel as its roof materials. For the first type steel structures, the solar radiation can radiate on the steel surface directly.

For large-span steel spatial structures, thermal load caused by solar radiation may lead some members to reach ultimate state [10-15]. However, few researches have conducted studies on thermal behavior of spatial structures under construction. This limitation motivates this study on the thermal behavior of steel structures under construction considering solar radiation. Liu [9] put forward a precise numerical simulation method for the temperature distribution induced by solar radiation of large-span steel spatial structures. The method was adopted in this paper to calculate temperature field under solar radiation of an actual project.

## 2. ENGINEERING SITUATION

YUJIAPU Railway Station Building is located in Tianjin, China with a building area of 86200m<sup>2</sup>. The three-story building with complex roof shapes has two stories underground. The station hall, including waiting and entrance halls, machine rooms, and an office, are on the first story. The platform that has three island platforms and six arrival-departure tracks are on the second story. Above ground is a shell-shaped single-layer lattice lighting roof. The main members of the whole structure are 72 curved steel box girders that intersect each other, as shown in Figure 1. Figure 2 shows the main steel structures after unloading process, which is 142 m in length, 80 m in width, and the vector height is 24 m. A ring beam was set on the top and bottom of the shell to connect and constrain the steel box girders.

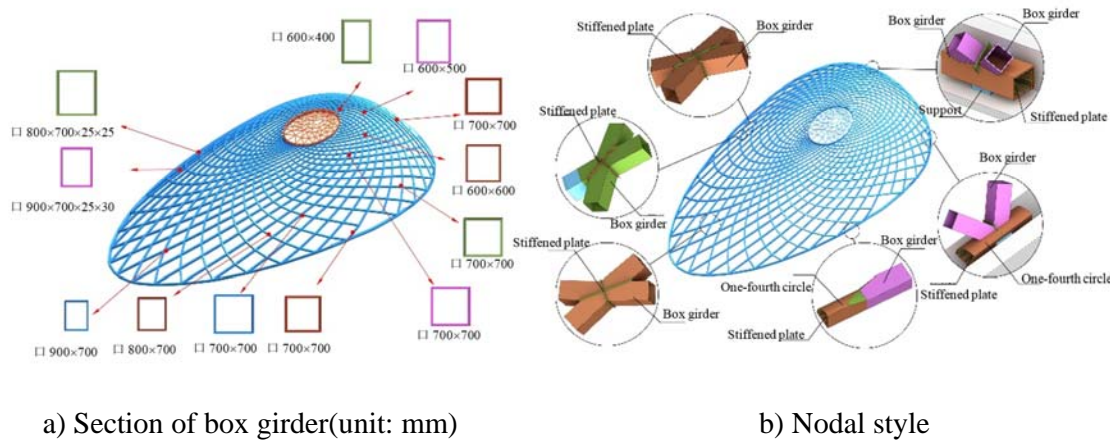


Figure 1. Section and Node of YUJIAPU Railway Station



a) Vertical view

b) Upward view

Figure 2. YUJIAPU Railway Station after Unloading Process

The somatotype of the structure is similar to a shell. The structure is under complex stress, and 10 kinds of nodes, each different from one another, were used. Every component torsion has different angles to keep the configuration smooth. Performing construction simulation on this project is necessary to overcome several construction difficulties.

### 3. NUMERICAL SIMULATIONS METHOD

In 1950s, many researchers had already begun to evaluate the temperature distribution of pavements [16-17], bridges [18-20] and dams [21] considering the solar radiation. In these studies, the one-dimensional or two-dimensional heat conductivity model was adopted in the numerical simulation. However, the temperature distribution of the spatial steel structures cannot be predicted using these numerical methods under solar radiation because of its three-dimension spatial property. Then Liu [9] developed the method for calculating temperature distribution of spatial structures. In this paper, the same method was adopted for calculating temperature field of YUJIAPU railway station building which is during construction phase.

The decisive factors in Liu's [9] method mainly include convection heat, solar radiation and long wave radiation. So the boundary condition of the steel surface can be expressed as Eq. 1 correspondingly. The first term indicates the contribution of convection heat. The second and third term refer the solar radiation and long wave radiation respectively. The thermal properties of steels were acquired from the corresponding codes as listed in Table 1.

$$\lambda \frac{\partial T}{\partial n} \Big|_{\Gamma} = h[T_a(t) - T] + q_s(t) + q_L(t) \quad (1)$$

Where  $h$  is heat convection coefficient ( $W/m^2 \cdot ^\circ C$ ) and it can be calculated by the method presented by Yazdanian and Klems<sup>[22]</sup>;  $T_a$  is ambient air temperature.

Table 1. Thermal Properties of Steel

properties	density $kg/m^3$	Heat conduction coefficient $J/(m \cdot s \cdot ^\circ C)$	Specific heat $J/(kg \cdot ^\circ C)$
value	7850	56	480

The ASHRAE clear-sky model was adopted for calculation of solar radiation. In this model, the total global solar radiation is assumed to be the sum of direct radiation, diffuse radiation, and the solar radiation reflected from the surrounding surface<sup>[21]</sup>, as shown in Eq. 2.

$$q_s = \varepsilon (G_D + G_d + G_R) \quad (2)$$

Where  $\varepsilon$  is the solar absorption coefficient,  $G_D$  is the direct radiation,  $G_d$  is the diffuse radiation and  $G_R$  is the solar radiation reflected from the surrounding surface. The detailed computational method of each item can be found in [9].

The Stefan-Boltzmann equation was used for calculation of long wave radiation, shown as Eq.3.

$$q_l = \varepsilon_f \sigma (F_{wg} (T_g^4 - T^4) + F_{ws} (T_{sky}^4 - T^4)) \quad (3)$$

Where  $\varepsilon_f$  is the ratio of the radiation emitted by a surface;  $\sigma$  is Stefan-Boltzmann constant  $= 5.67 \times 10^{-8} \text{ W}/(\text{m}^2 \cdot \text{K}^4)$ ;  $T_{sky}$  is the effective temperature of sky, usually calculated by  $T_a - 6$ ;  $T_g$  is the ground temperature.

In addition, the ambient temperature and wind speed are critical parameters affecting the steel temperature, because the convection heat transfer between steel surface and air is determined by the ambient temperature and the long wave radiation irradiating on steel surface. In this paper, the air temperature data for the monitoring site were used as shown in Figure 3.

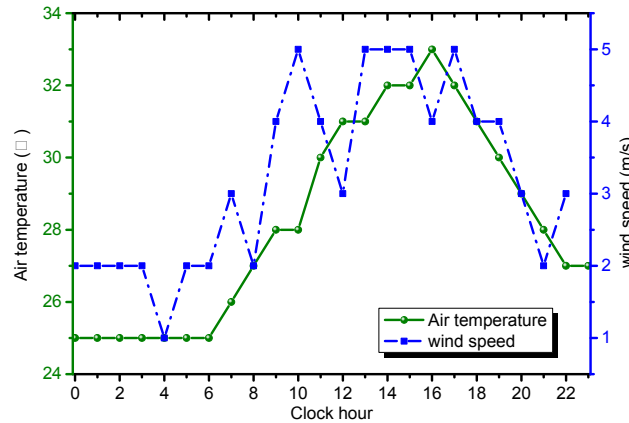


Figure 3 Monitored air temperature and wind speed on August 1, 2014

#### 4. FIELD MONITORING SYSTEM

A temperature and stress monitoring system devised for the Yujiapu railway station building was installed in July, 2014 and has been operated since then. There were 44 temperature sensors and 22 strain gages were used, and 4 temperature sensors and 2 strain gages for each components. Distribution of monitoring components was shown as in Figure 4.

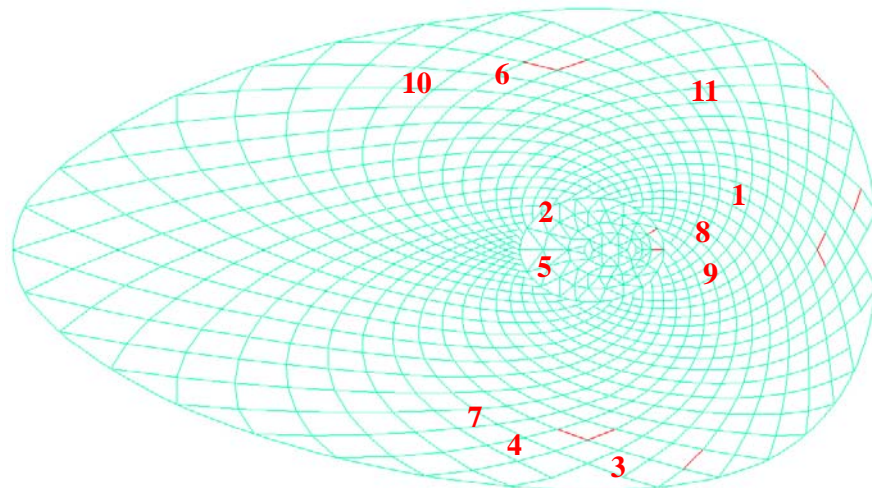


Figure 4. Distribution of Monitoring Components

Figure 5. showed installation form of monitoring sensors on each component in detail. Four temperature sensors and two stress sensors were installed on middle part of each component. Temperature sensors were installed on each side of the component and stress sensors were installed on top and bottom of the components. The section of component located at skylight is circle and the others are rectangular section. Figure 6 shows actual structure under solar radiation and monitoring sensors on each component.

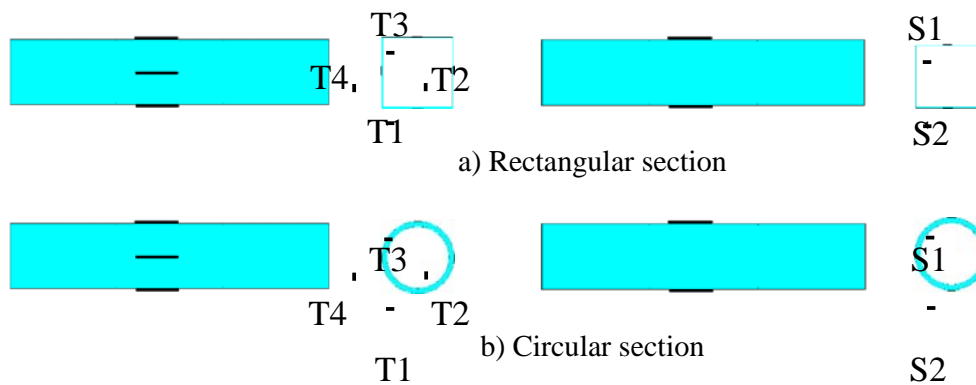
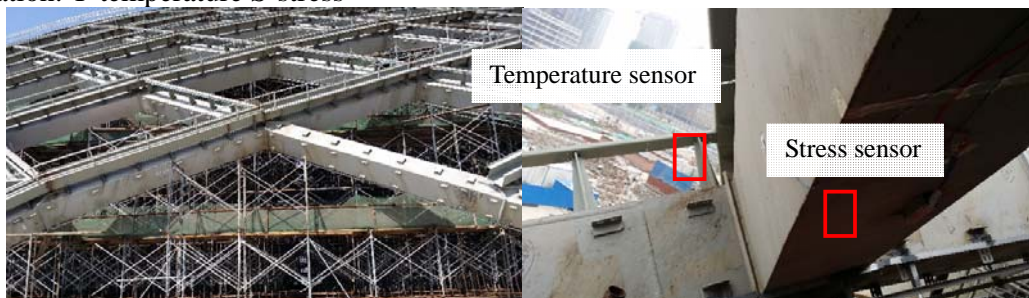


Figure 5. Positions of Temperature Sensors and Strain Gauges

Notation: T-temperature S-stress



a) Solar radiation

b) Monitoring component





c) Temperature sensor



d) Stress sensor

Figure 6. Installation of Temperature Sensor and Stress Sensor

## 5. RESULTS AND DISCUSSIONS

### 5.1 Uniform Temperature Field under Solar Radiation

The field temperature was collected per 15 minutes. The temperature-time curves of each monitoring component on 1<sup>st</sup> August are shown in Figure 7~Figure 17. The results derived by field monitoring and numerical analysis were compared with each other. In numerical analysis, the maximum and minimum temperature of monitoring components was extracted and the field air temperature and wind speed were taken in account.

It can be seen from the curves of monitoring temperature that some monitoring point present a sawtooth shape, that is caused by shadow effect among components. The monitoring component will be in shadow caused by other components from time to time. The maximum temperature happened at component 2 which is located at skylight of the structure.

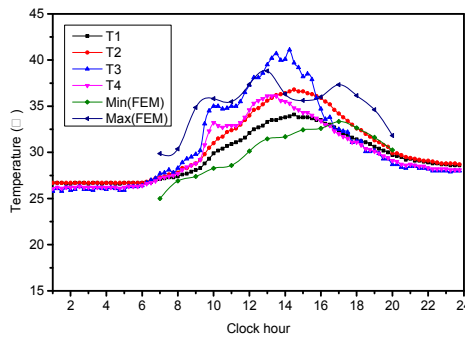


Figure 7. The Temperature-time Curve for Component 1

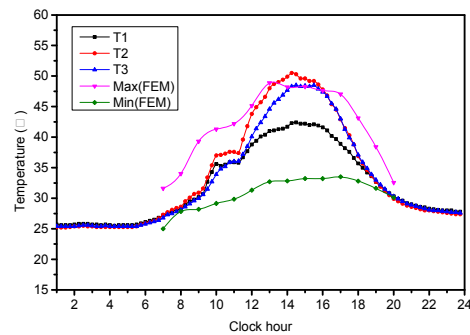


Figure 8. The Temperature-time Curve for Component 2



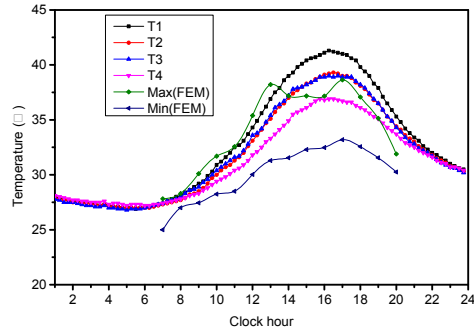


Figure 9. The Temperature-time Curve for Component 3

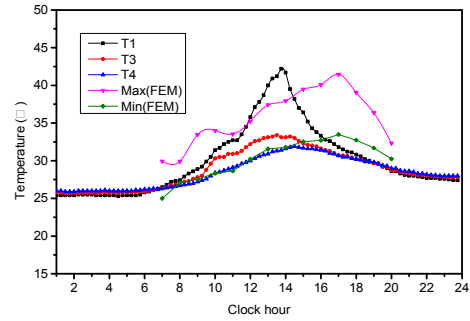


Figure 10. The Temperature-time Curve for Component 4

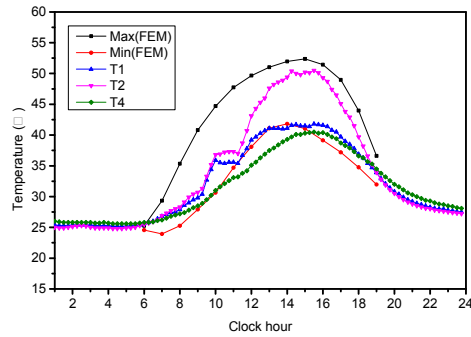


Figure 11. The Temperature-time Curve for Component 5

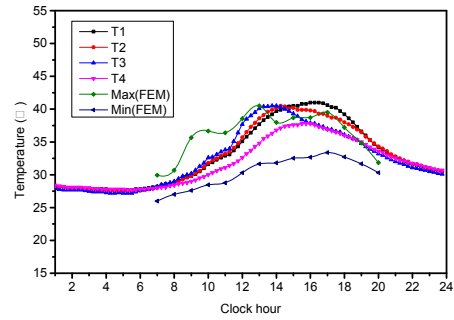


Figure 12. The Temperature-time Curve for Component 6

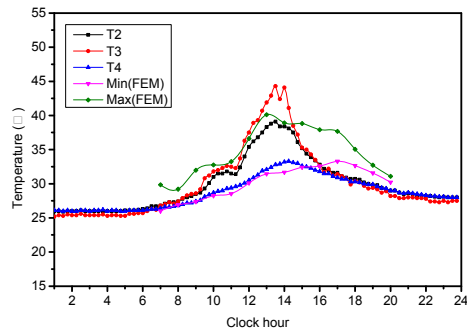


Figure 13. The Temperature-time Curve for Component 7

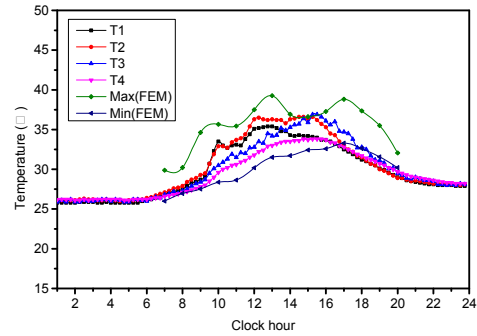


Figure 14. The Temperature-time Curve for Component 8

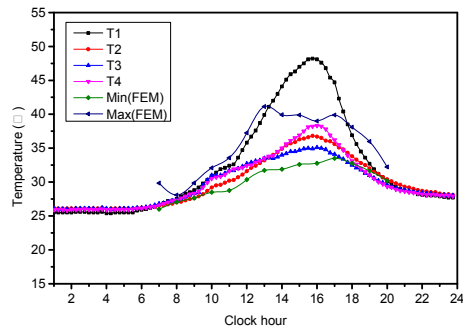


Figure 15. The Temperature-time Curve for Component 9

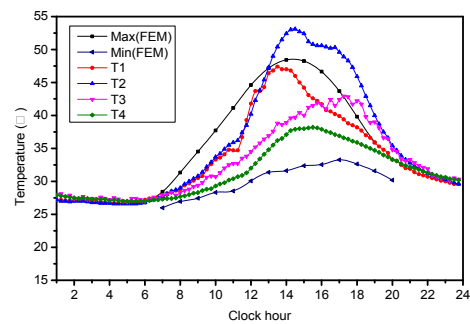


Figure 16. The Temperature-time Curve for Component 10

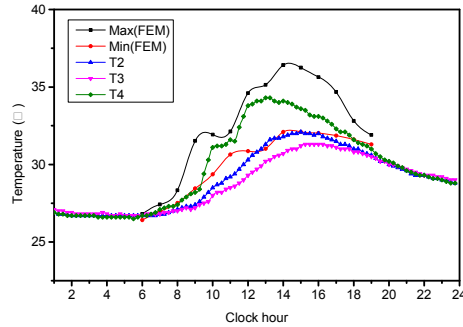


Figure 17. The Temperature–time Curve for Component 11

Table 2. Temperature of 11 Components

NUM	CM1	CM2	CM3	CM4	CM5	CM6
Temperature from monitoring	40.7	50.5	41.3	42.2	50.5	41
Temperature from FEM analysis	38.8	48.8	38.2	41.45	52.3	40.51
Error1	0.046	0.033	0.075	0.017	0.035	0.011
NUM	CM7	CM8	CM9	CM10	CM11	
Temperature from monitoring	44.1	36.5	48.2	53.1	32	
Temperature from FEM analysis	40.12	39.2	41.1	48.4	36.4	
Error	0.090	0.073	0.147	0.088	0.13	

It is clear that the temperature value obtained by numerical analysis was generally consistent with the monitoring results, with a maximum difference of 14.7%.

Reasons attributing to the discrepancies might be due to variance in the solar radiation model, variance in solar radiation absorption and ground reflectance, wind speed at each component, etc. As the complexity of the algorithm, the shadow effect among components was not taken into account which is the main cause of difference between temperature derived by FEM method and field monitoring.

## 5.2 Stress Caused by Non-uniform Temperature

The finite element model of the structure constitutes of beam element and Beam 188 in ANSYS was adopted, support at the bottom of the structure was constraint in radial and vertical direction. The temperature field of the whole structure was obtained in above section, it was applied as beam thermal load, shown as in Figure 18.

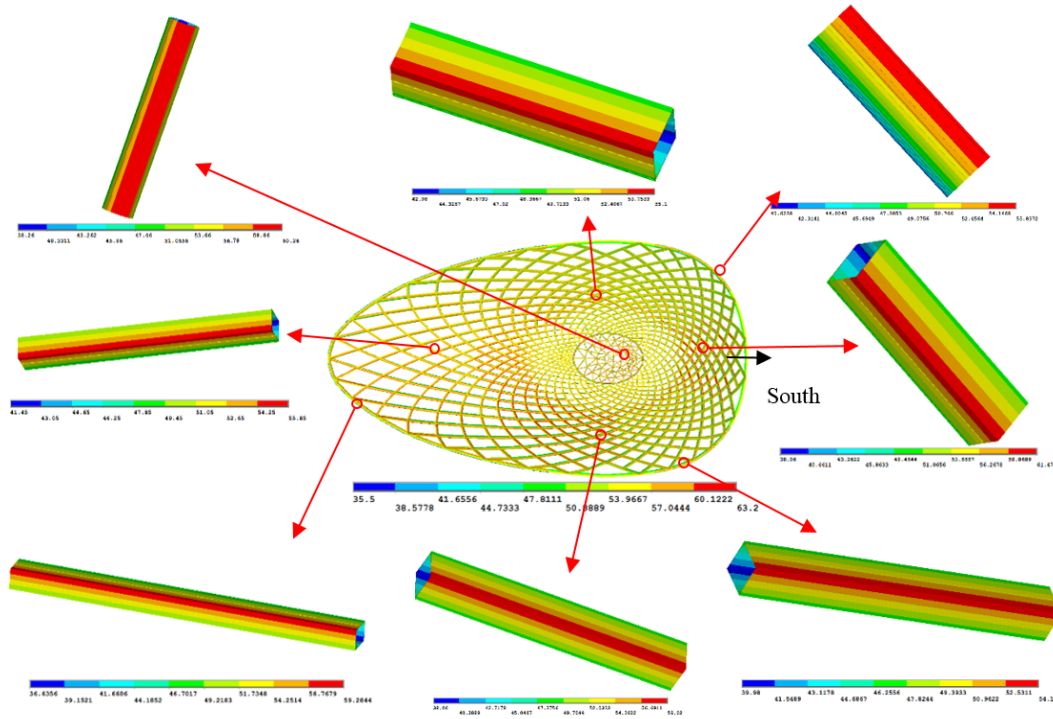


Figure 18. Contour of Temperature Field under Solar Radiation at 12 o'clock

Temperature at different clock hour was input as thermal load to get the stress variation along with temperature. The stress-time curves of components were shown in Figure 19~Figure 29. It can be concluded that the results obtained by FEM method agree well with that obtained by field monitoring.

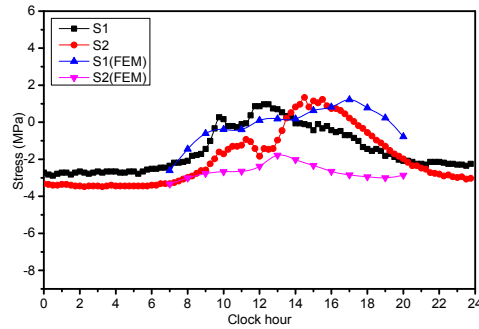


Figure 19. The Stress-time Curve for Component 1

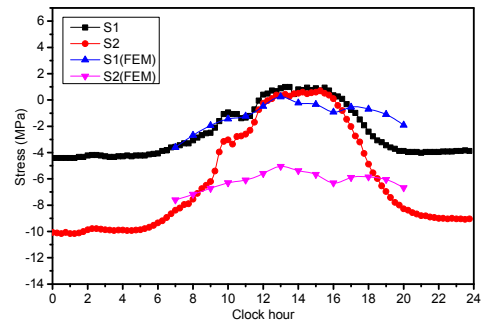


Figure 20. The Stress-time Curve for Component 2

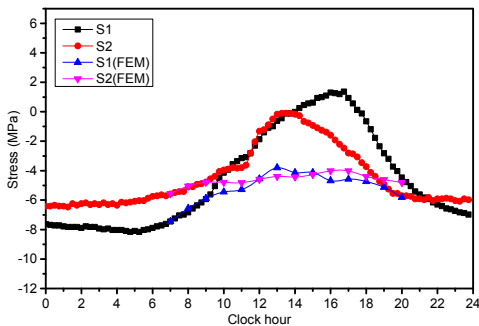


Figure 21. The Stress-time Curve for Component 3

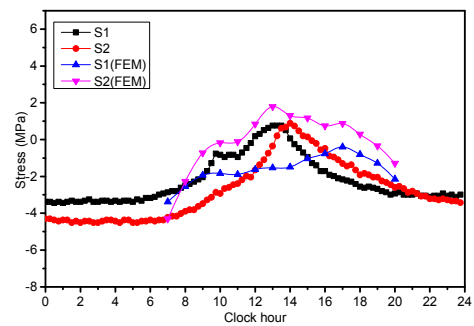


Figure 22. The Stress-time Curve for Component 4

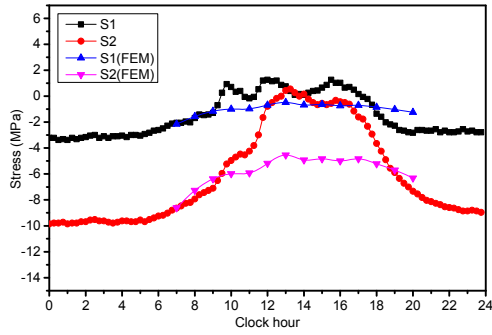


Figure 23. The Stress-time Curve for Component 5

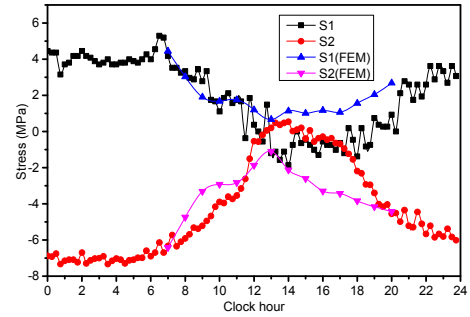


Figure 24. The Stress-time Curve for Component 6

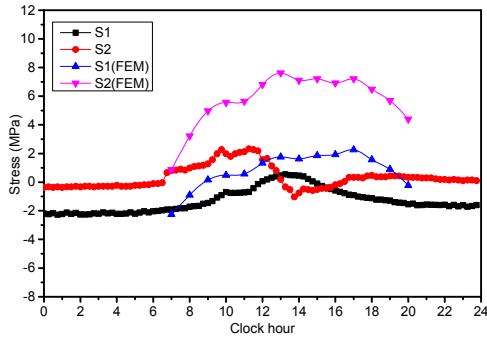


Figure 25. The Stress-time Curve for Component 7

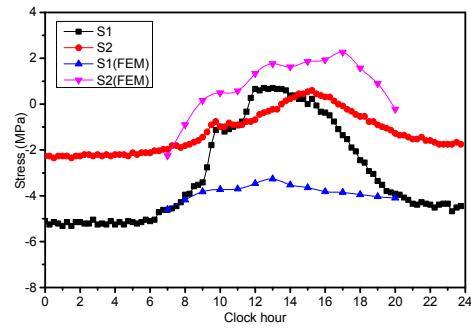


Figure 26. The Stress-time Curve for Component 8

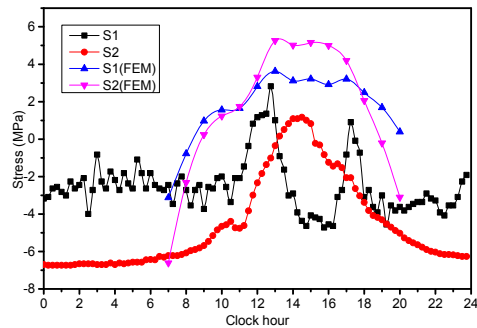


Figure 27. The Stress-time Curve for Component 9

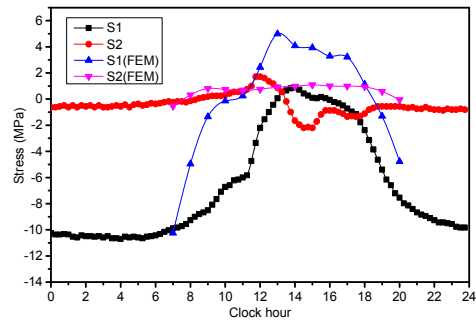


Figure 28. The Stress-time Curve for Component 10

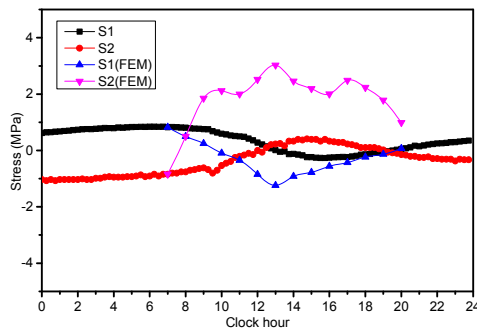


Figure 29. The Stress-time Curve for Component 11

Although correlated well with changing trends of stress obtained from field monitoring, FE simulations again predict smaller values of stress changing. However, as the stress changing is very small in value, it is difficult to accurately quantify monitoring value. It can be seen from comparison that there is larger errors existing at individual monitoring points. The difference between calculated temperature field and actual condition is the main cause of difference between stress computed and monitored. Due to exact temperature field of each component cannot be obtained by field monitoring method, the temperature field derived by FEM method was adopted. Beam element whose temperature field can only change linearly along axis was adopted in numerical model, this determined there must be errors between simulated temperature field and actual condition. At the same time, the construction error, the construction load, etc., are all responsible for the computed errors. The results derived by numerical analysis relatively precise due to influence of error in solar radiation, wind speed and shadow effect, etc.. After all, the maximum deviation for stress is less than 10 MPa.

To investigate the influence of the thermal load on deformation of the structure, nodal displacement at typical location, shown as in Figure 30, was extracted. Curves of displacement-time were shown as in Figure 31. It can be concluded that nodal displacement at node 2 and node 4 is large than that at node 5. Similarly, nodal displacement at node 1 and node 3 is large than that at node 5. This present a mechanical behaviour like arch, which is shown in Figure 32, wether in length or short direction.

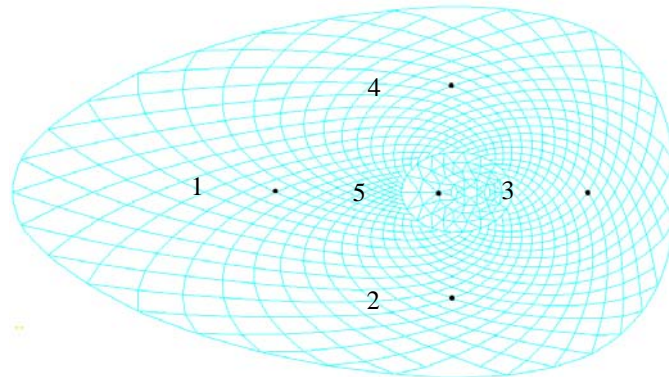


Figure 30. Distribution of Typical Nodes

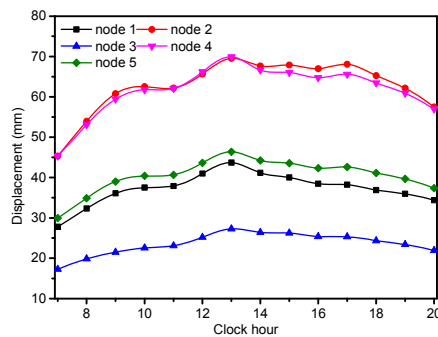


Figure 31. Displacement Curve at Typical Nodes

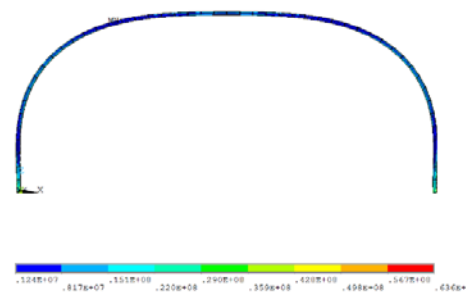


Figure 32. Deformation of Arch in Positive Temperature Difference Conditions

To investigate mechanical behaviour of arch to thermal load, an arch with different vector height and 80 m in span direction was studied. Arches with rigid connected arch foot and pinned connected arch foot were investigated in this subsection. Figure 33 shows the curves of maximum stress versus vector height at different thermal load. Figure 34 shows that of the pinned arch.

It can be concluded through comparison of maximum stress in different conditions that the arch with rigid connected foot is more sensitive to thermal load. Thermal load will not influence thermal stress of pinned arch when vector height is larger than 20 m. Similarly, vector height will have a slight influence on thermal stress of rigid arch. The maximum stress happens at arch foot in all cases. The arch with small vector height is more sensitive to thermal load and the rigid arch is more sensitive to thermal load than pinned arch, almost two times.

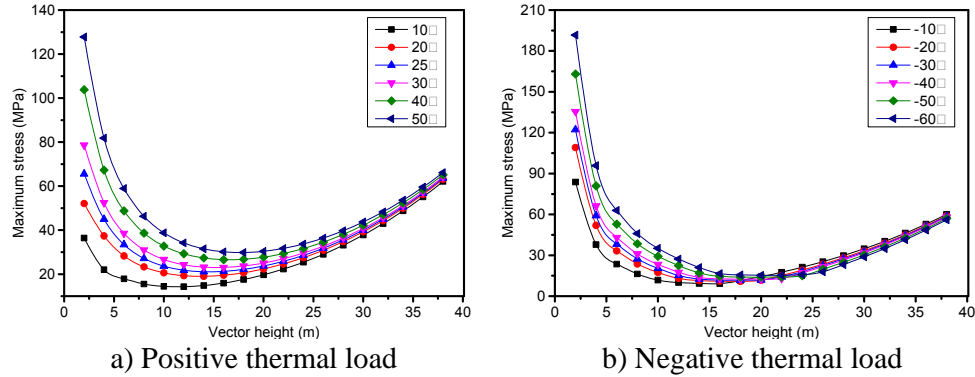


Figure 33 Rigid arch

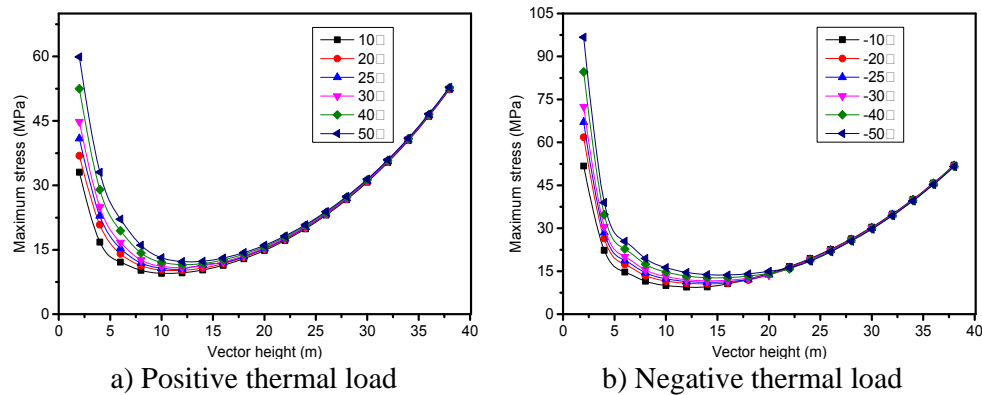


Figure 34. Pinned Arch

### 5.3 Monitoring Results of Stress in Different Months

To investigate the role seasonal temperature difference playing in the changing of stress. The monitoring results of stress in different months were compared. Due to limited space, monitoring results of component 1 were listed as below, shown as in Figure 35.

It can be concluded that change value of stress caused by seasonal temperature variation is commensurate to that caused by daily temperature variation. Similar to that daily temperature caused by solar radiation, seasonal temperature difference will also not cause big changes in stress for components of upper lattice shell. The change magnitude of stress in summer is large than that in winter for the solar radiation in summer is intensive than that in winter. The change value of stress caused by solar radiation may even larger than that caused by seasonal temperature difference. Figure 36 shows the changing history of stress of component 11. It can be concluded that as the influence of shadow effect, solar radiation will also not induce big change in stress of components which located at bottom of the entire structure. At the same time, installation of the bottom girder was done in summer, the enclosed structure is not sensitive to negative temperature difference.

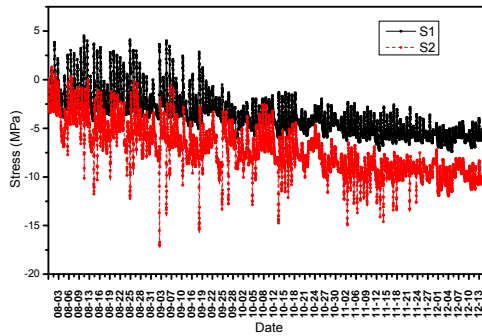


Figure 35. Time History of Monitoring Results for Component 1

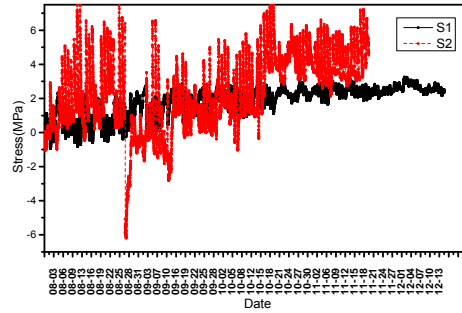


Figure 36. Time History of Monitoring Results for Component 11

#### 5.4 Thermal Behavior of the Entire Structure

To investigate the influence of temperature difference on different parts of the structure, the entire structure was divided into three parts according to characteristic of the entire structure. That is the bottom girder (BG), the upper lattice shell (ULS) and the upper girder (UG), shown as in Figure 37.

The healing temperature was  $14 \pm 5^\circ\text{C}$  according in actual construction process. The temperature field under solar radiation on 22<sup>th</sup> July, 2014, and 22<sup>th</sup> December, 2014, was obtained by conducting numerical analysis. The changing curves of maximum stress of different parts of the whole structure was obtained by applying thermal load.

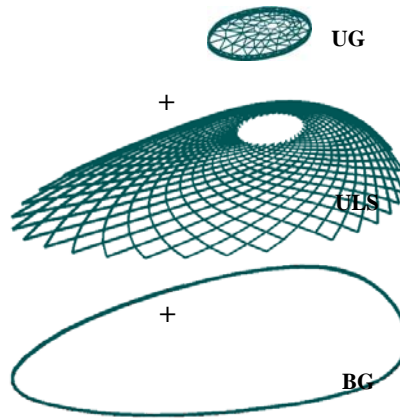


Figure 37. Constitution of the Whole Structure

The changing curves of maximum stress (only under the influence of thermal load) of different parts were shown as in Figure 38. It can be concluded from Figure 38 a) that the changing value of ULS, BG and UG are 11.9MPa, 13.1MPa and 22.15MPa, respectively, in summer. The maximum stress of BG is 86.5MPa and is much larger than the other two parts which is 48.7MPa and 60.2MPa, respectively. This indicates the UG is much sensitive to positive thermal load and the ULS is the least sensitive compared to other two parts.

The temperature field on 22<sup>th</sup> December was also applied and the reference temperature in ANSYS software package was changed to simulate ambient temperature. The changing curves of maximum stress is shown as in Figure 38 b). It can also be concluded that the changing value of ULS, BG and UG are 4.6MPa, 11.4MPa and 3.4MPa, respectively. The maximum stress of BG is 114.2MPa and is much larger than the other two parts which is 37.8MPa and 28 MPa, respectively. It is similar to that



mentioned before, the UG is much sensitive to negative thermal load and the ULS is the least sensitive compared to other two parts.

The maximum stress of lattice shell, bottom girder and upper girder under gravity are 85.2MPa, 48.4MPa and 94.6MPa, respectively. So the thermal stress takes significant proportion compared to stress cause by gravity, about 57%, 237% and 63.4% for ULS, BG and UG, respectively.

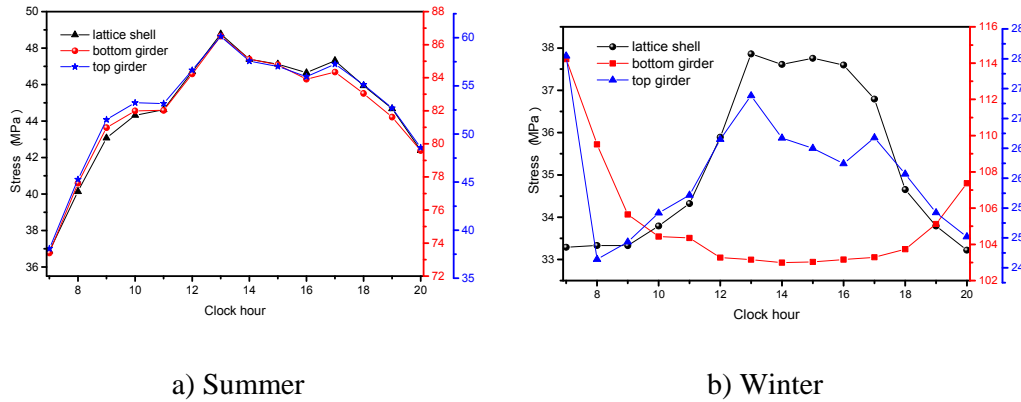


Figure 38. Changing Curves of Maximum Stress of Each Part

From what has been discussed above, it can be concluded that the ULS is not sensitive to daily temperature variation caused by solar radiation, and the planar closed structure, for example the BG and UG is sensitive to temperature variation caused by solar radiation in summer. But the BG is always in the shadow of the upper structures, so the daily temperature variation would have no significant effect on it.

## 6. CONCLUSIONS

- 1) A numerical model, based on a transient thermal FE analysis, was presented. The temperature field of the whole structure was obtained and accuracy of the result was verified by the monitoring data. The results derived by numerical analysis are relatively precise due to influence of error in solar radiation, wind speed and shadow effect, etc.. After all, the maximum deviation for stress is less than 10 MPa.
- 2) Stress of monitoring point was derived by applying thermal load obtained by method presented in this paper. Results were compared with that field monitoring data. It was concluded that the influence of daily variation of temperature caused by solar radiation on component of steel latticed shell is not significant.
- 3) Shadow effect among components will cause difference between results obtained by FEM method, but the results is conservative for structural design process.
- 4) Different parts of the structure has different sensitivity to thermal load. The bottom girder (BG) is most sensitive to seasonal thermal load. The thermal load caused by solar radiation has little influence on it due to shadow effect of the upper structure.



## ACKNOWLEDGEMENTS

This work was supported by the National Science Foundation of Tianjin (No. 16JCQNJC07100).

## REFERENCES

- [1] Alinia, M.M. and Kashizadeh, S., "Effect of Flexibility of Substructures upon Thermal Behaviour of Spherical Double Layer Space Truss Domes, Part I: Uniform Thermal Loading", *Journal of Constructional Steel Research*, 2006, Vol. 62, No. 4, pp. 359-368.
- [2] Alinia, M.M. and Kashizadeh, S., "Effect of Flexibility of Substructures upon Thermal Behaviour of Spherical Double Layer Space Truss Domes, Part II: Gradient & Partial Loading", *Journal of Constructional Steel Research*, 2006, Vol. 62, No. 7, pp. 675-681.
- [3] Alinia, M.M. and Kashizadeh, S., "Effects of Support Positioning on the Thermal Behaviour of Double Layer Space Truss Domes", *Journal of Constructional Steel Research*, 2007, Vol. 63, No. 3, pp. 375-382.
- [4] Yong, D., "A Practical Approach for Fire Resistance Design of Large Space Building Grid Structures [D]", Shanghai, Tongji University, 2007.
- [5] Liu, H.B., Chen, Z.H. and Zhou, T., "Research on the Process of Pre-Stressing Construction of Suspended-Dome Considering Temperature Effect", *J. Advances in Structural Engineering*, 2012, Vol. 15, No. 3, pp. 489-493.
- [6] Liu, H.B., Chen, Z.H. and Zhou, T., "Numerical and Experimental Investigation on the Temperature Distribution of Steel Tubes under Solar Radiation", *J. Structural Engineering and Mechanics*, 2012, Vol. 43, No. 6, pp. 725-737.
- [7] Liu, H.B., Chen, Z.H. and Zhou, T., "Theoretical and Experimental Study on the Temperature Distribution of H-shaped Steel Members under Solar Radiation", *J. Applied Thermal Engineering*, 2012, Vol. 37, pp. 329-335.
- [8] Liu, H.B. and Chen, Z.H., "Non-Uniform Thermal Behaviour of Suspended-Dome with Stacked Arch Structures", *J. Advances in Structural Engineering*, 2013, Vol. 16, No. 6, pp. 1001-1009.
- [9] Liu, H.B., Chen, Z.H. and Zhou, T., "Investigation on Temperature Distribution and Thermal Behavior of Large Span Steel Structures Considering Solar Radiation", *J. Advanced Steel Construction*, 2013, Vol. 9, No. 1, pp. 41-58.
- [10] Li, G.Q. and Zhang, C., "Thermal Response to Fire of Uniformly Insulated Steel Members: Background and Verification of the Formulation Recommended by Chinese Code CECS200", *Advanced Steel Construction*, 2010, Vol. 6, No. 2, pp. 788-802.
- [11] Fan, Z., Wang, Z. and Tian, J., "Analysis on Temperature Field and Determination of Temperature upon Heating of Large-span Steel Structure of the National Stadium", *Journal of Building Structures*, 2007, Vol. 28, No. 2, pp. 32-40. (in Chinese)
- [12] Pei, Y.Z., Bai, Y., Shi, Y.J., Zhu, D. and Wang, Y.Q., "Temperature Distribution in a Long-span Aircraft Hanger [J]", *Tsinghua Science and Technology*, 2008, Vol. 13, No. 2, pp. 184-190.
- [13] Xiao, J.C., Xu, H., Liu, J.K. and Ma, K.J., "The Influence of Intense Solar Radiation on Long-span Spatial Steel Structures [J]", *Chinese Journal of Solid Mechanics*, 2010, Vol. 31, pp. 275-280.
- [14] Wang, Y.Q., Lin, C.C. and Shi, Y.J., "Experimental Study on the Temperature of Steel Members in Sunshine [J]", *Journal of Building Structures*, 2010, Supplementary Issue Vol. 1, pp. 140-147.

- [15] Jin, X.F., Fan, F. and Shen, S.Z., "Effect of Non-uniform Temperature Field under Sunshine on the Structure Supporting the Reflector of a Large Radio Telescope-FAST [J]", *China Civil Engineering Journal*, 2008, Vol. 41, No. 11, pp. 71-77.
- [16] Briss, K., Diefenderfer, Imad L. and Al-Qadi Stacey, D. Diefenderfer., "Model to Predict Pavement Temperature Profile: Development and Validation", *Journal of Transportation Engineering*, 2006, Vol. 132, No. 2, pp. 162-167.
- [17] Andrew, D. Chiasson, Cenk, Yavuzturk and Khaled, Ksaibati, "Linearized Approach for Predicting Thermal Stresses in Asphalt Pavements due to Environmental Conditions", *Journal of Materials in Civil Engineering*, 2008, Vol. 20, No. 2, pp. 118-127.
- [18] Tong, M., Tham, L.G. and Au, F.T.K., "Numerical Modeling for Temperature Distribution in Steel Bridges", *Computers and Structures*, 2001, Vol. 79, No. 6, pp. 583-593.
- [19] Kim, S.-H., Cho, K.-I., Won, J.-H. and Kim, J.-H., "A Study on Thermal Behavior of Curved Steel Box Girder Bridges Considering Solar Radiation", *Archives of Civil and Mechanical Engineering*, 2009, Vol. 9, No. 3, pp: 59-76.
- [20] Xu, Y.L., Chen, B., Ng, C.L., Wong, K.Y. and Chan, W.Y., "Monitoring Temperature Effect on a Long Suspension Bridge", *Structural Control and Health Monitoring*, 2010, Vol. 17, No. 6, pp. 632-653.
- [21] Jin, F., Chen, Z., Wang, J.T., Yang, J., "Practical Procedure for Predicting Non-uniform Temperature on the Exposed Face of Arch Dams", *Applied Thermal Engineering*, 2010, Vol. 30, No. 14-15, pp. 2146-2156.
- [22] Faye, C. McQuiston, Jerald, D. Parker and Jeffrey, D. Spitler, "Heating, Ventilating, and Air Conditioning Analysis and Design, USA, John Wiley and Sons, 2005.

# A 3-NODE CO-ROTATIONAL TRIANGULAR ELASTO-PLASTIC SHELL ELEMENT USING VECTORIAL ROTATIONAL VARIABLES

Zhongxue Li <sup>1,\*</sup>, Bassam A. Izzuddin <sup>2</sup>, Loc Vu-Quoc <sup>3</sup>, Zihan Rong <sup>4</sup> and Xin Zhuo <sup>4</sup>

<sup>1, \*</sup> *Department of Civil Engineering, Zhejiang University, China*

<sup>2</sup> *Department of Civil and Environmental Engineering, Imperial College London, United Kingdom*

<sup>3</sup> *Department of Mechanical and Aerospace Engineering, University of Florida, USA*

<sup>4</sup> *Department of Civil Engineering, Zhejiang University, PR China*

*\*(Corresponding author: E-mail: lizx19993@zju.edu.cn)*

*Received: 21 March 2016; Revised: 31 July 2016; Accepted: 3 August 2016*

---

**ABSTRACT:** A 3-node co-rotational triangular elasto-plastic shell element is developed. The local coordinate system of the element employs a zero-‘macro spin’ framework at the macro element level, thus reducing the material spin over the element domain, and resulting in an invariance of the element tangent stiffness matrix to the order of the node numbering. The two smallest components of each nodal orientation vector are defined as rotational variables, achieving the desired additive property for all nodal variables in a nonlinear incremental solution procedure. Different from other existing co-rotational finite-element formulations, both element tangent stiffness matrices in the local and global coordinate systems are symmetric owing to the commutativity of the nodal variables in calculating the second derivatives of strain energy with respect to the local nodal variables and, through chain differentiation with respect to the global nodal variables. For elasto-plastic analysis, the Maxwell-Huber-Hencky-von Mises yield criterion is employed together with the backward-Euler return-mapping method for the evaluation of the elasto-plastic stress state, where a consistent tangent modulus matrix is used. Assumed membrane strains and assumed shear strains---calculated respectively from the edge-member membrane strains and the edge-member transverse shear strains---are employed to overcome locking problems, and the residual bending flexibility is added to the transverse shear flexibility to improve further the accuracy of the element. The reliability and convergence of the proposed 3-node triangular shell element formulation are verified through two elastic plate patch tests as well as three elastic and three elasto-plastic plate/shell problems undergoing large displacements and large rotations.

**Keywords:** Co-rotational approach, elasto-plasticity, triangular shell element, assumed strain, vectorial rotational variable, zero-‘macro spin’

**DOI:** 10.18057/IJASC.2017.13.3.2

---

## 1. INTRODUCTION

Shell structures with different geometry, thickness, loading and boundary conditions are widely applied in engineering practice. Shell finite elements play an important role in analyzing, designing and optimizing shell structures. An optimal shell element should (1) be applicable to arbitrary shell geometries for both thick and thin structures, (2) provide accurate displacements and stresses with low computational cost, and (3) be robust with low sensitivity to element distortion [1-7]. Formulations for flat 3-node triangular shell elements are simpler, and computationally more efficient, than for curved triangular elements with more than 3 nodes. Furthermore, 3-node triangular mesh is the most robust and efficient option of mesh generation. As a result, reliable and computationally efficient 3-node triangular shell elements have important applications in modeling shell structures with arbitrary and complex geometries [8].

A 3-node triangular shell element can be formulated by combining a membrane element and a bending element [9-12], or by relying on three-dimensional continuum mechanics with the Reissner–Mindlin kinematic hypothesis and the plane-stress assumption [8,13]. Existing 3-node triangular shell elements can be categorized into 4 types: Type 1 with only 3 displacement

degrees-of-freedom (dofs) per node [14-22]; Type 2 with 3 displacement dofs and 2 rotational dofs per node [23-25]; Type 3 with 3 displacement dofs at the vertices and the rotational dofs at side nodes [26-27]; Type 4 with 3 displacement dofs and 3 rotational dofs per node [28-33]. Most existing 3-node rotation-free triangular shell elements are based on the Kirchhoff assumption, ignoring shear deformation, can therefore only be employed in modeling thin plate and shell problems [21]. To extend rotation-free flat 3-node triangular shell elements with transverse shear deformation effects, Zárate and Oñate [21] added two transverse shear angles to the element curvatures which are calculated over the domain formed by the element itself and the three adjacent triangular elements. These two transverse shear angles are considered as rotational degrees of freedom for thick shell problems, and they vanish for thin shell problems. A flat shell element with 5 degrees-of-freedom per corner node can be obtained by combining a conventional triangular membrane element with a standard 9-dof triangular bending element. On the other hand, if several elements of this type sharing the same node are coplanar, it is difficult to achieve inter-element compatibility between membrane and transverse displacements, and the assembled global stiffness matrix is singular in shell analysis due to the absence of in-plane rotation degrees-of-freedom [9-12,34]. In addition, flat shell elements with 5 degrees-of-freedom per node lack proper nodal degrees of freedom to model folded plate/shell structures, making the assembly of elements troublesome [35]. To avoid the singularity of the assembled global stiffness matrix, some researchers defined the displacement degrees-of-freedom at the vertices and the rotational degrees-of-freedom at side nodes of flat shell elements [26-27]. This type of elements cannot, however, be easily matched with other types of elements in modeling of complex structures. Alternatively, some researchers [9-12] added a sixth degree of freedom (the drilling rotation) at each node of flat triangular shell elements by combining a bending element and a membrane element with drilling rotational degrees-of-freedom. Such shell elements are very convenient for engineering applications since no special connection scheme is necessary at the shell edges and intersections, and no particular care needs to be taken when coupling shell and rod elements [36]. Such approach renders, however, the numerical method inconsistent, possibly leading to a poor element convergence [37]. Then, Reissner [38], Hughes and Brezzi [39], and Hughes et al. [40-41] endeavored to develop variational formulations employing independent rotation fields so as to obtain a theoretically sound and practically useful formulation for engineering application.

A major difficulty in developing flat 3-node triangular shell elements is to overcome locking phenomena arising in bending dominated situations without destroying the ability of the procedure to accurately capture membrane dominated and mixed behaviors [7]. In general, flat 3-node triangular shell element cannot well approximate the pure bending displacement field; thus, locking problems are serious and inevitable. As the shell thickness decreases, the convergence of the finite element solution rapidly deteriorates [8]. Researchers developed methods to overcome locking phenomena in flat triangular shell elements, such as the Mixed Interpolation of Tensorial Components method used in the MITC3 element [8], the line integration method used in TRIA3 element [42], the mixed or hybrid formulation [43-45], incompatible displacement methods [46-47], stabilization methods [29,48-54], assumed strain methods [19,28,55], etc.

In the present 3-node elasto-plastic triangular shell element formulation, 3 displacement dofs and 2 vectorial rotational dofs are employed at per node, the Reissner-Mindlin theory is used, in which both the thickness deformation and the normal stress in the direction of the shell thickness are ignored, and an assumed strain method is employed to alleviate the membrane and shear locking phenomena. Here, the assumed membrane strains are calculated from 3 edge-member membrane strains of the 3-node triangular shell element, while the assumed transverse shear strains are evaluated from the 3 edge-member transverse shear strains [42]. In addition, the residual bending flexibility is added to the transverse shear flexibility to improve the accuracy of the element further. For elasto-plastic modeling, the fibre approach which can describe the plastic zone spreading

process in shell structures undergoing large elastoplastic deformation [56-59] is adopted, the Maxwell-Huber-Hencky-von Mises yield criterion for isotropic hardening case [60-64] is introduced, and the material is assumed to be linear hardening. A backward-Euler return-mapping integration algorithm [60-61] is used to trace the yield surface, and a consistent elasto-plastic tangent modulus matrix is employed. To exclude the influence of element rigid-body rotations from the local displacement field, a zero-‘macro spin’ co-rotational framework, which can significantly reduce the rigid-body rotations of infinitesimal segments at different material points within the element domain in an aggregate sense [65], is employed for the present element to simplify the stress-strain constitutive relation. Compared to other existing co-rotational element formulations [61-66], the present 3-node triangular elasto-plastic shell element formulation has several features: i) All nodal variables are additive in a nonlinear incremental solution procedure, and as a result, updating the element matrices is simple and efficient; ii) Symmetric element tangent stiffness matrices are obtained in both the local and global coordinate systems, leading to computational efficiency and significant computer storage saving; and iii) The element tangent stiffness matrix is updated using the total values of the nodal variables in an incremental solution procedure, making it advantageous for solving dynamic problems [67-70]. The present 3-node triangular shell element demonstrates satisfying convergence and reliability in solving elastic and elasto-plastic plate/shell problems undergoing large displacements [36, 71-81].

The outline of the paper is as follows. Section 2 presents the kinematics of the 3-node triangular shell element in the local co-rotational system. Section 3 describes the local element response, the assumed-strain procedure used to alleviate locking problems, the calculation of the shear strain correction coefficients corresponding to the residual bending flexibility, and the consideration of elasto-plasticity within the element formulation. Section 4 presents the transformation matrix between the local and global systems, and the element formulation in the global coordinate system. In Section 5, several elastic patch tests and elastic/elasto-plastic plate/shell problems are solved to demonstrate the reliability and convergence of the proposed element formulation. Concluding remarks are given in Section 6.

## 2. ELEMENT KINEMATICS IN THE LOCAL CO-ROTATIONAL SYSTEM

The optimal orientation of the local reference system provides a rotated undeformed configuration such that the relative spin of the material in the current deformed configuration to that in the rotated undeformed configuration is zero. In developing the current triangular shell element formulation, the local co-rotational system is based on zero-spin at the macro element level [65], which reduces the material spin in an aggregate sense over the element domain, and maintains the benefits of invariance to nodal ordering and symmetry of the tangent stiffness matrix. The local and the global Cartesian coordinate systems, and the natural coordinate system, are defined respectively as in Figure 1. The local coordinate system always rotates with the element rigid-body rotation in the deformed configuration, but doesn’t deform with the element.

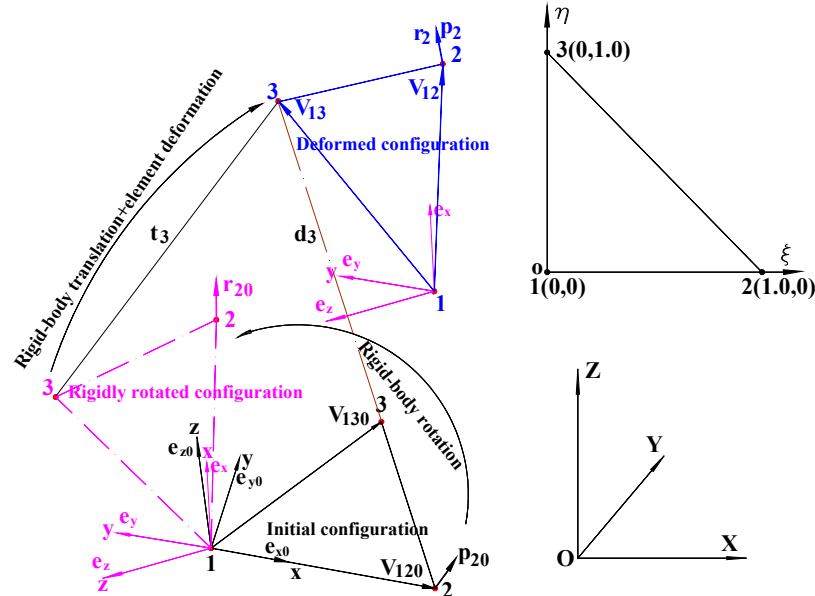


Figure 1. Description of the Co-rotational Framework and the Natural Coordinate System

(Note: The vectors  $\mathbf{t}_3$  and  $\mathbf{r}_2$  are associated with the local coordinate system o-x-y-z, whereas the vectors  $\mathbf{d}_3$ ,  $\mathbf{p}_{20}$ ,  $\mathbf{p}_2$ ,  $\mathbf{v}_{120}$ ,  $\mathbf{v}_{12}$ ,  $\mathbf{v}_{130}$ ,  $\mathbf{v}_{13}$ ,  $\mathbf{e}_{x0}$ ,  $\mathbf{e}_{y0}$ ,  $\mathbf{e}_{z0}$ ,  $\mathbf{e}_x$ ,  $\mathbf{e}_y$  and  $\mathbf{e}_z$  are associated with the global coordinate system O-X-Y-Z.)

In Figure 1,  $\mathbf{v}_{ij0}$  and  $\mathbf{v}_{ij}$  are the vectors connecting Node  $i$  to Node  $j$  in the initial configuration and the current deformed configuration, respectively.

$$\mathbf{v}_{ij0} = \mathbf{X}_{j0} - \mathbf{X}_{i0}, \quad i, j = 1, 2, 3 \quad \text{and} \quad i \neq j \quad (1a)$$

$$\mathbf{v}_{ij} = \mathbf{X}_{j0} - \mathbf{X}_{i0} + \mathbf{d}_j - \mathbf{d}_i, \quad i, j = 1, 2, 3 \quad \text{and} \quad i \neq j \quad (1b)$$

where, the vector  $\mathbf{X}_{i0}$  ( $i = 1, 2, 3$ ) contains the coordinates of Node  $i$  in the global coordinate system; the vector  $\mathbf{d}_i$  ( $i = 1, 2, 3$ ) represents the displacement of Node  $i$  in the global coordinate system. The orientation vector  $\mathbf{e}_{x0}$  of the local  $x$ -axis as being aligned with edge 1-2 of the element in the initial configuration,

$$\mathbf{e}_{x0} = \frac{\mathbf{v}_{120}}{|\mathbf{v}_{120}|} \quad (2)$$

and the orientation vector  $\mathbf{e}_z$  of the local  $z$ -axis in the current deformed configuration is defined as

$$\mathbf{e}_z = \frac{\mathbf{v}_{12} \times \mathbf{v}_{13}}{|\mathbf{v}_{12} \times \mathbf{v}_{13}|} \quad (3)$$

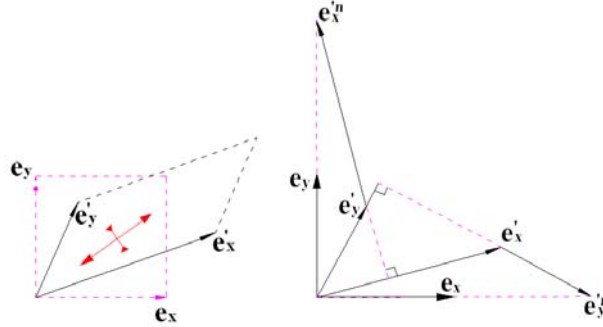


Figure 2. Definition of the Zero-‘macro spin’ Local Coordinate System

The zero-‘macro spin’ local coordinate system is generated as follows: A unit square area defined by the two orthogonal unit vectors  $\mathbf{e}_x$  and  $\mathbf{e}_y$  (the orientation vectors of the  $x$ - and  $y$ -axes in the deformed configuration, respectively) is subjected to a uniform planar ‘stretch’ operation in any two orthogonal directions (see Figure 2). Under this planar stretch operation, the vectors  $\mathbf{e}_x$  and  $\mathbf{e}_y$  will be transformed into vectors  $\mathbf{e}'_x$  and  $\mathbf{e}'_y$ , respectively. The vector  $\mathbf{e}_x$  is always obtained as the normalized sum of  $\mathbf{e}'_x$  and  $\mathbf{e}''_y$ , where  $\mathbf{e}''_y$  is a planar rotation of  $\mathbf{e}'_y$  by  $-\pi/2$ ; likewise, the vector  $\mathbf{e}_y$  is always obtained as the normalized sum of  $\mathbf{e}'_y$  and  $\mathbf{e}''_x$ , where  $\mathbf{e}''_x$  is a planar rotation of  $\mathbf{e}'_x$  by  $\pi/2$ . Then, the orientation vectors  $\mathbf{e}_x$  and  $\mathbf{e}_y$  of the local coordinate system in the current deformed configuration can be obtained from the stretched vectors as:

$$\mathbf{e}_x = \frac{\mathbf{e}'_x + \mathbf{e}''_y}{|\mathbf{e}'_x + \mathbf{e}''_y|}, \quad \mathbf{e}''_y = \mathbf{e}'_y \times \mathbf{e}_z, \quad \mathbf{e}_y = \mathbf{e}_z \times \mathbf{e}_x \quad (4a,b,c)$$

and the stretched vectors  $\mathbf{e}'_x$  and  $\mathbf{e}'_y$  in the current deformed configuration are calculated as

$$\mathbf{e}'_x = a_{x1}\mathbf{v}_{12} + a_{x2}\mathbf{v}_{23} \quad (5a)$$

$$\mathbf{e}'_y = a_{y1}\mathbf{v}_{12} + a_{y2}\mathbf{v}_{23} \quad (5b)$$

Considering that the orientation vectors  $\mathbf{e}_{x0}$ ,  $\mathbf{e}_{y0}$  and  $\mathbf{e}_{z0}$  of the local coordinate system in the initial configuration can also be obtained by the same procedure as  $\mathbf{e}_x$ ,  $\mathbf{e}_y$  and  $\mathbf{e}_z$ :

$$\mathbf{e}'_{x0} = \mathbf{e}_{x0} = \frac{\mathbf{v}_{120}}{|\mathbf{v}_{120}|} = a_{x1}\mathbf{v}_{120} + a_{x2}\mathbf{v}_{230} \quad (6a)$$

$$\mathbf{e}'_{y0} = \mathbf{e}_{y0} = \mathbf{e}_{z0} \times \mathbf{e}_{x0} = \frac{\mathbf{v}_{120} \times \mathbf{v}_{230} \times \mathbf{v}_{120}}{|\mathbf{v}_{120} \times \mathbf{v}_{230}| |\mathbf{v}_{120}|} = a_{y1}\mathbf{v}_{120} + a_{y2}\mathbf{v}_{230} \quad (6b)$$

then, the constants used in Eqs. 5a,b can be determined from Eqs. 6a,b as

$$a_{x1} = \frac{1}{|\mathbf{v}_{120}|}, \quad a_{x2} = 0 \quad (7a,b)$$

$$a_{y1} = -\frac{\mathbf{e}_{120}^T \mathbf{e}_{230}}{|\mathbf{v}_{120}| \sqrt{1 - (\mathbf{e}_{120}^T \mathbf{e}_{230})^2}}, \quad a_{y2} = \frac{1}{|\mathbf{v}_{230}| \sqrt{1 - (\mathbf{e}_{120}^T \mathbf{e}_{230})^2}} \quad (7c,d)$$

There are 15 degrees of freedom for each element in the local coordinate system. In addition to the three translational displacements, two components of the mid-surface normal vector at each node are defined as vectorial rotational variables. The vector of the local nodal variables is given below

$$\mathbf{u}_L = [u_1 \ u_1 \ w_1 \ r_{1,x} \ r_{1,y} \ u_2 \ v_2 \ w_2 \ r_{2,x} \ r_{2,y} \ u_3 \ v_3 \ w_3 \ r_{3,x} \ r_{3,y}]^T \quad (8)$$

where  $u_i, v_i, w_i$  are the three displacement dofs of Node  $i$ , while  $r_{i,x}, r_{i,y}$  are the two vectorial rotational dofs of Node  $i$ , and are the two components of the mid-surface normal vector  $\mathbf{r}_i$  in the local coordinate system.

There are 15 degrees of freedom in the global coordinate system. The nodal variable vector is given by

$$\mathbf{u}_G = [U_1 \ V_1 \ W_1 \ p_{1,n_1} \ p_{1,m_1} \ U_2 \ V_2 \ W_2 \ p_{2,n_2} \ p_{2,m_2} \ U_3 \ V_3 \ W_3 \ p_{3,n_3} \ p_{3,m_3}]^T \quad (9)$$

where  $U_i, V_i, W_i$  are the three displacement dofs of Node  $i$ , and  $p_{i,n_i}, p_{i,m_i}$  the vectorial rotational dofs, and are the two smallest components of the mid-surface normal vector  $\mathbf{p}_i$  at Node  $i$  in the X, Y, Z directions of the global coordinate system. This definition avoids ill-conditioning in the resulting equations [82].

The local nodal coordinates are calculated from those in the global coordinate system as follows

$$\mathbf{x}_{i0} = \mathbf{R}_0 \mathbf{v}_{i0} \quad (10)$$

where  $\mathbf{x}_{i0}^T = [x_{i0} \ y_{i0} \ z_{i0}]$ ,  $\mathbf{R}_0^T = [\mathbf{e}_{x0} \ \mathbf{e}_{y0} \ \mathbf{e}_{z0}]$  and  $\mathbf{v}_{i0} = \mathbf{X}_{i0} - \mathbf{X}_{10}$ .

The relationships between the local nodal dofs and the global nodal dofs are given by

$$\mathbf{t}_i = \mathbf{R}(\mathbf{d}_i + \mathbf{v}_{i0}) - \mathbf{R}_0 \mathbf{v}_{i0} \quad (11a)$$

$$\boldsymbol{\theta}_{i0} = \mathbf{R}_{h0} \mathbf{p}_{i0} \quad (11b)$$

$$\boldsymbol{\theta}_i = \mathbf{R}_h \mathbf{p}_i, \quad i=1,2,\dots,3 \quad (11c)$$

where the components of the vector  $\mathbf{t}_i^T = [u_i \ v_i \ w_i]$  are the three displacement dofs of Node  $i$  in the local coordinate system; the following matrices contain the unit basis vectors  $\mathbf{R}_{h0}^T = [\mathbf{e}_{x0} \ \mathbf{e}_{y0}]$ ;  $\mathbf{R}^T = [\mathbf{e}_x \ \mathbf{e}_y \ \mathbf{e}_z]$ ;  $\mathbf{R}_h^T = [\mathbf{e}_x \ \mathbf{e}_y]$ ; the components of the vector  $\mathbf{d}_i^T = [U_i \ V_i \ W_i]$  are the three displacement dofs of Node  $i$  in the global coordinate system;  $\mathbf{e}_x$ ,  $\mathbf{e}_y$  and  $\mathbf{e}_z$  are updated



by using  $\mathbf{d}_i$  obtained at each iteration of every incremental loading step (referred to Eqs.(1b),(3),(4a-c) and (5a,b) ); the vectors  $\boldsymbol{\theta}_i$  and  $\boldsymbol{\theta}_{i0}$  are respectively the sub-vectors of the deformed and the initial mid-surface normal vectors  $\mathbf{r}_i$  and  $\mathbf{r}_{i0}$  at Node  $i$  in the local coordinate system;  $\boldsymbol{\theta}_i^T = [r_{i,x} \ r_{i,y}]$ ;  $\boldsymbol{\theta}_{i0}^T = [r_{i0,x} \ r_{i0,y}]$ ; the vectors  $\mathbf{p}_i$  and  $\mathbf{p}_{i0}$  are respectively the deformed and the initial mid-surface normal vectors at Node  $i$  in the global coordinate system. In Eq. (11a), the vectors  $\mathbf{R}_0 \mathbf{v}_{i0}$  and  $\mathbf{R}(\mathbf{d}_i + \mathbf{v}_{i0})$  are respectively the local coordinates of Node  $i$  in the initial and deformed configurations.

For the description of the geometry and of the displacement field in the 3-node triangular shell element, the interpolation functions used are:

$$N_1 = 1 - \xi - \eta, \quad N_2 = \xi, \quad N_3 = \eta \quad (12a,b,c)$$

In the initial configuration, the local coordinates  $\mathbf{x}^T = [x \ y \ z]$  at any point on the element mid-surface are obtained as:

$$\mathbf{x} = \sum_{i=1}^3 N_i(\xi, \eta) \mathbf{x}_{i0} \quad (13)$$

The same shape functions are used to interpolate the displacement and rotation fields, leading to an isoparametric formulation:

$$\mathbf{t} = \sum_{i=1}^3 N_i(\xi, \eta) \mathbf{t}_i \quad (14a)$$

$$\bar{\mathbf{r}}_h = \sum_{i=1}^3 N_i(\xi, \eta) \boldsymbol{\theta}_i \quad (14b)$$

where the components in the vector  $\mathbf{t}^T = [u \ v \ w]$  are the local displacement fields, and the components in the vector  $\bar{\mathbf{r}}_h^T = [r_x \ r_y]$  are the local rotation fields.

The initial mid-surface normal vector at each node of the triangular shell element is obtained by calculating the cross-product of the tangent lines along two natural coordinate axes, i.e.,

$$\bar{\mathbf{p}}_{i0} = \frac{\partial \mathbf{X}_0}{\partial \xi} \times \frac{\partial \mathbf{X}_0}{\partial \eta} \bigg|_{(\xi_i, \eta_i)}, \quad i = 1, 2, 3 \quad (15)$$

where  $\mathbf{X}_0 = \sum_{j=1}^3 N_j(\xi, \eta) \mathbf{X}_{j0}$  represents the global coordinates of a point on the mid-surface of the element;  $(\xi_i, \eta_i)$  takes the natural coordinates of Node  $i$  (referred to Figure 2).

To minimize the discontinuity between the slopes of adjacent elements at Node  $i$ , the mean value of the normal vectors from the surrounding elements is adopted:

$$\mathbf{p}_{i0} = \frac{\sum \bar{\mathbf{p}}_{i0} / \|\bar{\mathbf{p}}_{i0}\|}{\left\| \sum \bar{\mathbf{p}}_{i0} / \|\bar{\mathbf{p}}_{i0}\| \right\|}, \quad i = 1, 2, 3 \quad (16)$$

the symbol  $\sum$  in Eq. (16) is the summation on the number of elements having the same common Node  $i$ .

On the other hand, if the true mid-surface of the curved shell is not smooth along the inter-element edges, the normal vector of each shell element must be obtained independently, and three global rotation degrees of freedom would then be required for each node along the edges of slope discontinuity. In general, the two smallest components of one orientation vector and one smaller component of another orientation vector at a node can be selected as global rotational variables, and these vectors can be oriented to three global coordinate axes in the initial configuration or defined as those of the beam element presented in [83-85].

### 3. LOCAL ELASTO-PLASTIC ELEMENT FORMULATIONS

#### 3.1 Local Response

The general virtual work statement can be expressed as:

$$\delta W = \int_V \boldsymbol{\sigma}^T \delta \boldsymbol{\varepsilon} dV - \mathbf{f}_{ext}^T \delta \mathbf{u}_L \quad (17)$$

where  $V$  is the volume of the element,  $\boldsymbol{\sigma}$  the stress vector,  $\mathbf{f}_{ext}$  the external force vector, and  $\boldsymbol{\varepsilon}$  the material strain vector; in the case of our shell element, the Reissner-Mindlin theory is adopted,  $\boldsymbol{\varepsilon}$  is the Green-Lagrange strain specialized for a shallow curved shell [61,71-72]. For the convenience of calculating the assumed strains below, the material strain vector  $\boldsymbol{\varepsilon}$  is split into three parts,  $\boldsymbol{\varepsilon}_m$ ,  $z_l \boldsymbol{\chi}$  and  $\boldsymbol{\gamma}$ , representing the membrane strains, bending strains and out-of-plane shear strains, respectively. It follows that Eq. (17) can be rewritten as:

$$\delta W = \int_V \boldsymbol{\sigma}^T \delta \begin{Bmatrix} \boldsymbol{\varepsilon}_m + z_l \boldsymbol{\chi} \\ \boldsymbol{\gamma} \end{Bmatrix} dV - \mathbf{f}_{ext}^T \delta \mathbf{u}_L \quad (18)$$

The internal force vector in the local coordinate system is therefore obtained as:

$$\mathbf{f} = \mathbf{f}_{ext} = \int_V \begin{bmatrix} \mathbf{B}_m + z_l \mathbf{B}_b \\ \mathbf{B}_s \end{bmatrix}^T \boldsymbol{\sigma} dV \quad (19)$$

where  $\mathbf{B}_m$ ,  $z_l \mathbf{B}_b$ , and  $\mathbf{B}_s$  are respectively the first derivatives of the membrane strain vector  $\boldsymbol{\varepsilon}_m$ , the bending strain vector  $z_l \boldsymbol{\chi}$ , and the out-of-plane shear strain vector  $\boldsymbol{\gamma}$  with respect to the local nodal variable vector  $\mathbf{u}_L$ ; the details of these matrices are given in Appendix A.

By differentiating the internal force vector with respect to the local nodal variables, the local tangent stiffness matrix of the 3-node triangular shell element is determined as:

$$\mathbf{k}_T = \int_V \begin{bmatrix} \mathbf{B}_m + z_l \mathbf{B}_b \\ \mathbf{B}_s \end{bmatrix}^T \mathbf{D}_T \begin{bmatrix} \mathbf{B}_m + z_l \mathbf{B}_b \\ \mathbf{B}_s \end{bmatrix} dV + \int_V \begin{bmatrix} \frac{\partial \mathbf{B}_m}{\partial \mathbf{u}_L^T} \\ \mathbf{0} \end{bmatrix}^T \boldsymbol{\sigma} dV \quad (20)$$

where  $\mathbf{D}_T$  is a symmetric consistent tangent modulus matrix [61,71-72],  $\frac{\partial \mathbf{B}_m}{\partial \mathbf{u}_L^T}$  is the second derivative of the membrane strain vector  $\boldsymbol{\varepsilon}_m$  with respect to the local nodal variable vector; the details are given in Appendix A. The first term on the right-hand side of Eq. (20) is symmetric; the second term is also symmetric due to the commutativity in calculating the second derivative of the membrane strain vector  $\boldsymbol{\varepsilon}_m$  with respect to the local nodal variable vector. Thus the element tangent stiffness matrix  $\mathbf{k}_T$  is symmetric.

In the present elasto-plastic shell element, we adopt a condensed elastic constitutive relationship in combination with a yield surface based on the five stress components excluding the normal out-of-plane stress [66,71-72]. This adoption avoids the need for elasto-plastic condensation of the normal out-of-plane stress and achieves the same results with a relatively simple formulation based only on five stress and corresponding strain components. We adopt the Maxwell-Huber-Hencky-von Mises yield criterion together with an isotropic strain hardening. The Maxwell-Huber-Hencky-von Mises yield function is expressed as

$$f = \sigma_e - \sigma_y \quad (21)$$

where  $\sigma_e$  is the equivalent uniaxial stress at the current stress state:

$$\sigma_e = \sqrt{\sigma_{xx}^2 + \sigma_{yy}^2 - \sigma_{xx}\sigma_{yy} + 3(\tau_{xy}^2 + \tau_{yz}^2 + \tau_{zx}^2)} \quad (22)$$

$\boldsymbol{\sigma}^T = [\sigma_{xx} \quad \sigma_{yy} \quad \tau_{xy} \quad \tau_{xz} \quad \tau_{yz}]$  represents the current stress state,  $\sigma_y$  is the current value of uniaxial yield stress, dependent on the accumulated equivalent plastic strain:

$$\sigma_y = f_y + H \lambda \quad (23)$$

in which  $f_y$  is the initial value of uniaxial yield stress,  $H$  is the hardening parameter, and  $\lambda$  is the plastic strain multiplier.

In a nonlinear incremental solution procedure, the incremental material strains  $\Delta \boldsymbol{\varepsilon}_j^T = [\Delta \varepsilon_{xxj}^i \quad \Delta \varepsilon_{yyj}^i \quad \Delta \gamma_{xyj}^i \quad \Delta \gamma_{xzj}^i \quad \Delta \gamma_{yzj}^i]$ , which, under elastic deformation, leads to a stress increment  $\Delta \boldsymbol{\sigma}_j^i$  and an elastic stress state  $\boldsymbol{\sigma}_j^i$ . If  $f > 0$ , the stress state  $\boldsymbol{\sigma}_j^i$  falls outside the yield surface, then a plastic material strain increment  $\Delta \boldsymbol{\varepsilon}_{pj}^i$  must be introduced so that the solution satisfies the flow rule and stays on the yield surface. The backward-Euler return-mapping procedure is then used due to its efficiency and the fact that it results in a symmetric consistent tangent modulus matrix [61]. The details of developing the consistent tangent modulus matrix and the elasto-plastic formulation can be found in [71-72].

### 3.2 Strategies for Overcoming Locking Problems

Eqs. 19 and 20 represent the conforming element formulation for the 3-node triangular shell element in the local coordinate system. In solving thin shell problems, membrane and shear locking phenomena could lead to deterioration in the computational efficiency and accuracy of the

conforming element. Therefore, to improve the performance of the triangular shell element, the membrane strains and out-of-plane shear strains are replaced with the corresponding assumed strains [42]; accordingly, the modified element formulations are given as follows:

$$\mathbf{f} = \int_V \begin{bmatrix} \tilde{\mathbf{B}}_m + z_l \mathbf{B}_b \\ \tilde{\mathbf{B}}_s \end{bmatrix}^T \tilde{\boldsymbol{\sigma}} dV \quad (24)$$

$$\mathbf{k}_T = \int_V \left\{ \begin{bmatrix} \tilde{\mathbf{B}}_m + z_l \mathbf{B}_b \\ \tilde{\mathbf{B}}_s \end{bmatrix}^T \mathbf{D}_T \begin{bmatrix} \tilde{\mathbf{B}}_m + z_l \mathbf{B}_b \\ \tilde{\mathbf{B}}_s \end{bmatrix} + \begin{bmatrix} \frac{\partial \tilde{\mathbf{B}}_m}{\partial \mathbf{u}_L^T} \\ \frac{\partial \tilde{\mathbf{B}}_s}{\partial \mathbf{u}_L^T} \end{bmatrix}^T \tilde{\boldsymbol{\sigma}} \right\} dV \quad (25)$$

where the matrices  $\tilde{\mathbf{B}}_m$  and  $\tilde{\mathbf{B}}_s$  are respectively the first derivatives of the assumed membrane strain vector  $\tilde{\boldsymbol{\epsilon}}_m$  and the assumed out-of-plane shear strain vector  $\tilde{\boldsymbol{\gamma}}$  with respect to the local nodal variable vector  $\mathbf{u}_L$ ; the matrices  $\frac{\partial \tilde{\mathbf{B}}_m}{\partial \mathbf{u}_L^T}$  and  $\frac{\partial \tilde{\mathbf{B}}_s}{\partial \mathbf{u}_L^T}$  are respectively the second derivative of the assumed membrane strain vector  $\tilde{\boldsymbol{\epsilon}}_m$  and the second derivative of the assumed out-of-plane shear strain vector  $\tilde{\boldsymbol{\gamma}}$  with respect to the local nodal variable vector  $\mathbf{u}_L$ ; the details of these matrices are given in Appendix A. The stress vector  $\tilde{\boldsymbol{\sigma}}$  is obtained by replacing the incremental material strains  $\Delta \boldsymbol{\epsilon}_j^i$  with the incremental assumed material strains  $\Delta \tilde{\boldsymbol{\epsilon}}_j^i$  [61,71-72], and the incremental assumed material strains  $\Delta \tilde{\boldsymbol{\epsilon}}_j^i$  is accumulated from the initial iteration to the  $j^{th}$  iteration of the  $i^{th}$  incremental loading step to avoid the occurrence of “spurious unloading” during the iterations.

The first term in the right-hand side of Eq. (25) is symmetric, and the second term is also symmetric due to the commutativity in calculating the second derivative of the assumed membrane strain vector  $\tilde{\boldsymbol{\epsilon}}_m$  with respect to the local nodal variable vector. Thus the modified element tangent stiffness matrix  $\mathbf{k}_T$  is still symmetric.

The assumed material strains are calculated as:

$$\tilde{\boldsymbol{\epsilon}} = \begin{Bmatrix} \tilde{\boldsymbol{\epsilon}}_m + z_l \boldsymbol{\chi} \\ \tilde{\boldsymbol{\gamma}} \end{Bmatrix} \quad (26)$$

where the distribution of membrane strains are assumed to be:

$$\tilde{\boldsymbol{\epsilon}}_m = \mathbf{P} \boldsymbol{\alpha} \quad (27)$$

$$\mathbf{P} = \begin{bmatrix} 1 & 0 & 0 \\ 0 & 1 & 0 \\ 0 & 0 & 1 \end{bmatrix} \quad (28)$$

$$\boldsymbol{\alpha}^T = [\alpha_1 \quad \alpha_2 \quad \alpha_3] \quad (29)$$

and the distribution of the transverse shear strains and the torsion of the top face of the element

relative to the bottom face (Figure 3) are assumed to be:

$$\begin{Bmatrix} \tilde{\gamma} \\ \tilde{\gamma}_t \end{Bmatrix} = \mathbf{P}\boldsymbol{\beta} \quad (30)$$

$$\boldsymbol{\beta}^T = [\beta_1 \ \beta_2 \ \beta_3] \quad (31)$$

with  $\alpha_i$  and  $\beta_j$  ( $i,j=1,2,3$ ) being undetermined assumed strain coefficients.

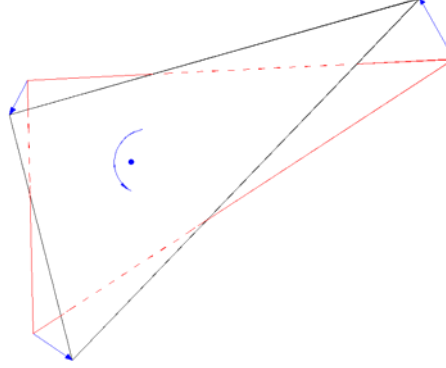


Figure 3. Torsion of the Top Face of the Element Relative to the Bottom Face

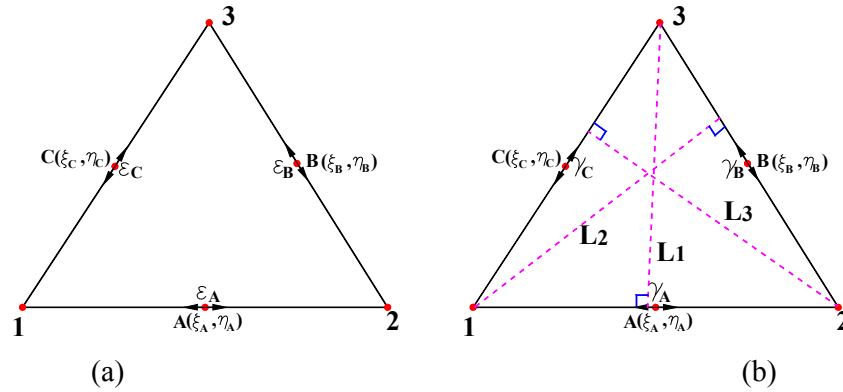


Figure 4. Member Strains and Edge-member Transverse Shear Strains for Present Shell Element

Inspired by the line integration approach proposed by MacNeal [42], the member strains (namely, the edge-member membrane strains in the direction of each side of the element) corresponding to the membrane strains of the present 3-node triangular shell element are related to the displacements at two neighboring nodes, and are evaluated by

$$\varepsilon_k = \frac{(\mathbf{t}_j - \mathbf{t}_i)^T \mathbf{a}_{ij0}}{|\mathbf{a}_{ij0}|^2} + \frac{1}{2} \left( \frac{w_j - w_i}{|\mathbf{a}_{ij0}|} \right)^2 \quad (32)$$

where the ordered triplets  $(k,i,j)$  are given by (A,1,2), (B,2,3) and (C,3,1) (see Figure 4a), and

$$\mathbf{a}_{ij0} = \mathbf{x}_{j0} - \mathbf{x}_{i0} \quad (33)$$

The relationships of the edge-member strains  $\varepsilon_k$  and the membrane strains  $\boldsymbol{\varepsilon} = [\varepsilon_{xx} \ \varepsilon_{yy} \ \gamma_{xy}]^T$  at Point  $k$  ( $k=A,B,C$ ) are approximately expressed as

$$\varepsilon_k = c_k^2 \varepsilon_{xx} + s_k^2 \varepsilon_{yy} + c_k s_k \gamma_{xy} \quad (34)$$

where  $c_k = \cos \psi_k$ ,  $s_k = \sin \psi_k$ , and  $\psi_k$  ( $k = A, B, C$ ) is the angle from the  $x$ -axis to the  $i$ - $j$  edge of the element. The natural coordinates  $(\xi_k, \eta_k)$  of Points  $k=A, B, C$  take the values shown in Table 1:

Table 1. The Natural Coordinates of Points A, B and C

k	A	B	C
$\xi_k$	0.5	0.5	0.0
$\eta_k$	0.0	0.5	0.5

Considering Eq. 27, the edge-member strains  $\varepsilon_k$  ( $k=A, B, C$ ) (see Figure. 4a) can be evaluated in terms of the assumed membrane strain coefficients:

$$\{\varepsilon_k\} = \mathbf{\Gamma} \mathbf{a}, \quad k=A, B, C \quad (35a)$$

$$\mathbf{\Gamma} = \begin{bmatrix} c_A^2 & s_A^2 & c_A s_A \\ c_B^2 & s_B^2 & c_B s_B \\ c_C^2 & s_C^2 & c_C s_C \end{bmatrix} \quad (35b)$$

From Eqs. 27 and 35a,b, the assumed membrane strains can be expressed in terms of the edge-member strains  $\varepsilon_k$  ( $k=A, B, C$ ) as

$$\tilde{\mathbf{\varepsilon}}_m = \mathbf{P} \mathbf{\Gamma}^{-1} \{\varepsilon_k\}, \quad k=A, B, C \quad (36)$$

Similarly, the edge-member transverse shear strains  $\gamma_k$  ( $k=A, B, C$ ) along the 3 edges of the 3-node triangular shell element (see Figure. 4b) are related to the displacements at two neighboring nodes. Considering that the components of the mid-surface normal vectors  $\mathbf{r}$  and  $\mathbf{r}_0$  along these line segments are linear functions of distance, the edge-member transverse shear strain  $\gamma_k$  of the edge  $i$ - $j$  can be evaluated by

$$\gamma_k = \frac{w_j - w_i}{|\mathbf{a}_{ij0}|} + \frac{(\mathbf{r}_j - \mathbf{r}_{j0} + \mathbf{r}_i - \mathbf{r}_{i0})^T \mathbf{a}_{ij0}}{2|\mathbf{a}_{ij0}|} \quad (37)$$

where the ordered triplets  $(k, i, j)$  are given by (A, 1, 2), (B, 2, 3) and (C, 3, 1); the first term of Eq. 37 gives the ratio of the incremental out-of-plane displacement from Node  $i$  to Node  $j$  with respect to the length of Edge  $ij$ ; the second term is the average of the two projections of the incremental mid-surface normal vectors, at Node  $i$  and at Node  $j$ , on the Edge  $ij$ .

The edge-member transverse shear strain at Point  $k$  ( $k=A, B, C$ ) is calculated from the transverse shear strains and the torsion of the top face of the element relative to the bottom face [42]:

$$\gamma_k = c_k \gamma_{xz} + s_k \gamma_{yz} + \gamma_t \quad (38)$$

Considering Eqs. 30 and 38, the edge-member transverse shear strain  $\gamma_k$  can be expressed as:

$$\{\gamma_k\} = \mathbf{\Omega} \mathbf{\beta}, \quad k=A,B,C \quad (39a)$$

$$\mathbf{\Omega} = \begin{bmatrix} c_A & s_A & 1 \\ c_B & s_B & 1 \\ c_C & s_C & 1 \end{bmatrix} \quad (39b)$$

According to Eqs. 30 and 39a,b, the assumed shear strains can be given as

$$\begin{Bmatrix} \tilde{\gamma} \\ \tilde{\gamma}_t \end{Bmatrix} = \mathbf{P} \mathbf{\Omega}^{-1} \{\gamma_k\}, \quad k=A,B,C \quad (40)$$

To improve further the accuracy of the present 3-node triangular shell element, the residual bending flexibility is added to the shear flexibility matrix coupling  $\tilde{\gamma}_{xz}$  and  $\tilde{\gamma}_{yz}$  by dividing the three edge-member transverse shear strains by a correction coefficient, respectively. These coefficients are selected to give correct results for cubic bending in directions perpendicular to the three sides of the triangle [86-87], and are calculated as

$$\rho_k = \sqrt{1 + \frac{5L_k^2}{24(1+\mu)h^2}} \quad (41)$$

where  $L_k$  is the height of the triangle corresponding to the edge-member transverse shear strain  $\gamma_k$  (see Figure 4b), and  $h$  the thickness of the element.

In MacNeal [42], the flexibility assigned to  $\gamma_t$  was treated as a free parameter to be selected to improve particular test results; the value of this flexibility is unimportant, and is ignored in the presented 3-node triangular shell element.

The incremental form of the assumed material strains is given by

$$\Delta \tilde{\mathbf{\epsilon}} = \begin{Bmatrix} \Delta \tilde{\mathbf{\epsilon}}_m + z_t \Delta \chi \\ \Delta \tilde{\gamma} \end{Bmatrix} \quad (42)$$

in which the vectors  $\Delta \tilde{\mathbf{\epsilon}}_m$  and  $\Delta \tilde{\gamma}$  are respectively the incremental form of  $\tilde{\mathbf{\epsilon}}_m$  and  $\tilde{\gamma}$ ; these increments can be obtained by the first-order Taylor expansion of Eqs. 36 and 40 with  $\Delta \mathbf{t}_i, \Delta \mathbf{r}_i, \Delta w_i$  accumulated from the initial iteration to the current iteration of the present incremental loading step in a nonlinear incremental solution procedure.

#### 4. TRANSFORMATION OF LOCAL TO GLOBAL RESPONSE

The global nodal force vector  $\mathbf{f}_g$  of the triangular shell element can be obtained as a transformation of the local nodal force vector  $\mathbf{f}$  according to:

$$\mathbf{f}_g = \mathbf{T}^T \mathbf{f} \quad (43)$$

where  $\mathbf{T}$  is a  $15 \times 15$  transformation matrix consisting of the first derivatives of the local dofs with respect to the global nodal dofs, and can be readily determined from Eqs. 11a,c.

For convenience, the local nodal dofs and the global nodal dofs are rewritten below

$$\mathbf{u}_L^T = [\mathbf{t}_1^T \quad \boldsymbol{\theta}_1^T \quad \mathbf{t}_2^T \quad \boldsymbol{\theta}_2^T \quad \mathbf{t}_3^T \quad \boldsymbol{\theta}_3^T] \quad (44)$$

$$\mathbf{u}_G^T = [\mathbf{d}_1^T \quad \mathbf{n}_{g1}^T \quad \mathbf{d}_2^T \quad \mathbf{n}_{g2}^T \quad \mathbf{d}_3^T \quad \mathbf{n}_{g3}^T] \quad (45)$$

where  $\boldsymbol{\theta}_k^T = [r_{k,x} \quad r_{k,y}]$  represents the two local vectorial rotational dofs at Node  $k$  in the local coordinate system, and  $\mathbf{n}_{gk}^T = [p_{k,n_k} \quad p_{k,m_k}]$  denotes the two global vectorial rotational dofs. Accordingly, the transformation matrix is given as follows:

$$\mathbf{T} = \frac{\partial \mathbf{u}_L}{\partial \mathbf{u}_G^T} = \begin{bmatrix} \frac{\partial \mathbf{t}_1}{\partial \mathbf{d}_1^T} & \mathbf{0} & \frac{\partial \mathbf{t}_1}{\partial \mathbf{d}_2^T} & \mathbf{0} & \frac{\partial \mathbf{t}_1}{\partial \mathbf{d}_3^T} & \mathbf{0} \\ \frac{\partial \boldsymbol{\theta}_1}{\partial \mathbf{d}_1^T} & \frac{\partial \boldsymbol{\theta}_1}{\partial \mathbf{n}_{g1}^T} & \frac{\partial \boldsymbol{\theta}_1}{\partial \mathbf{d}_2^T} & \frac{\partial \boldsymbol{\theta}_1}{\partial \mathbf{n}_{g2}^T} & \frac{\partial \boldsymbol{\theta}_1}{\partial \mathbf{d}_3^T} & \frac{\partial \boldsymbol{\theta}_1}{\partial \mathbf{n}_{g3}^T} \\ \frac{\partial \mathbf{t}_2}{\partial \mathbf{d}_1^T} & \mathbf{0} & \frac{\partial \mathbf{t}_2}{\partial \mathbf{d}_2^T} & \mathbf{0} & \frac{\partial \mathbf{t}_2}{\partial \mathbf{d}_3^T} & \mathbf{0} \\ \frac{\partial \boldsymbol{\theta}_2}{\partial \mathbf{d}_1^T} & \frac{\partial \boldsymbol{\theta}_2}{\partial \mathbf{n}_{g1}^T} & \frac{\partial \boldsymbol{\theta}_2}{\partial \mathbf{d}_2^T} & \frac{\partial \boldsymbol{\theta}_2}{\partial \mathbf{n}_{g2}^T} & \frac{\partial \boldsymbol{\theta}_2}{\partial \mathbf{d}_3^T} & \frac{\partial \boldsymbol{\theta}_2}{\partial \mathbf{n}_{g3}^T} \\ \frac{\partial \mathbf{t}_3}{\partial \mathbf{d}_1^T} & \mathbf{0} & \frac{\partial \mathbf{t}_3}{\partial \mathbf{d}_2^T} & \mathbf{0} & \frac{\partial \mathbf{t}_3}{\partial \mathbf{d}_3^T} & \mathbf{0} \\ \frac{\partial \boldsymbol{\theta}_3}{\partial \mathbf{d}_1^T} & \frac{\partial \boldsymbol{\theta}_3}{\partial \mathbf{n}_{g1}^T} & \frac{\partial \boldsymbol{\theta}_3}{\partial \mathbf{d}_2^T} & \frac{\partial \boldsymbol{\theta}_3}{\partial \mathbf{n}_{g2}^T} & \frac{\partial \boldsymbol{\theta}_3}{\partial \mathbf{d}_3^T} & \frac{\partial \boldsymbol{\theta}_3}{\partial \mathbf{n}_{g3}^T} \end{bmatrix} \quad (46)$$

with the details of the sub-matrices of  $\mathbf{T}$  presented in Appendix B.

The element tangent stiffness matrix  $\mathbf{k}_{TG}$  in the global coordinate system can now be obtained as follows:

$$\begin{aligned} \mathbf{k}_{TG} &= \frac{\partial \mathbf{f}_g}{\partial \mathbf{u}_G^T} = \mathbf{T}^T \frac{\partial \mathbf{f}}{\partial \mathbf{u}_L^T} + \frac{\partial \mathbf{T}^T}{\partial \mathbf{u}_G^T} \mathbf{f} = \mathbf{T}^T \frac{\partial \mathbf{f}}{\partial \mathbf{u}_L^T} \mathbf{T} + \frac{\partial \mathbf{T}^T}{\partial \mathbf{u}_G^T} \mathbf{f} \Rightarrow \\ \mathbf{k}_{TG} &= \mathbf{T}^T \mathbf{k}_T \mathbf{T} + \frac{\partial \mathbf{T}^T}{\partial \mathbf{u}_G^T} \mathbf{f} \end{aligned} \quad (47)$$

with:



$$\frac{\partial \mathbf{T}}{\partial \mathbf{u}_G^T} = \begin{bmatrix} \frac{\partial^2 \mathbf{t}_1}{\partial \mathbf{d}_1^T \partial \mathbf{u}_G^T} & \mathbf{0} & \cdots & \frac{\partial^2 \mathbf{t}_1}{\partial \mathbf{d}_3^T \partial \mathbf{u}_G^T} & \mathbf{0} \\ \frac{\partial^2 \boldsymbol{\theta}_1}{\partial \mathbf{d}_1^T \partial \mathbf{u}_G^T} & \frac{\partial^2 \boldsymbol{\theta}_1}{\partial \mathbf{n}_{g1}^T \partial \mathbf{u}_G^T} & \cdots & \frac{\partial^2 \boldsymbol{\theta}_1}{\partial \mathbf{d}_3^T \partial \mathbf{u}_G^T} & \frac{\partial^2 \boldsymbol{\theta}_1}{\partial \mathbf{n}_{g3}^T \partial \mathbf{u}_G^T} \\ \vdots & \vdots & \vdots & \vdots & \vdots \\ \frac{\partial^2 \mathbf{t}_3}{\partial \mathbf{d}_1^T \partial \mathbf{u}_G^T} & \mathbf{0} & \cdots & \frac{\partial^2 \mathbf{t}_3}{\partial \mathbf{d}_3^T \partial \mathbf{u}_G^T} & \mathbf{0} \\ \frac{\partial^2 \boldsymbol{\theta}_3}{\partial \mathbf{d}_1^T \partial \mathbf{u}_G^T} & \frac{\partial^2 \boldsymbol{\theta}_3}{\partial \mathbf{n}_{g1}^T \partial \mathbf{u}_G^T} & \cdots & \frac{\partial^2 \boldsymbol{\theta}_3}{\partial \mathbf{d}_3^T \partial \mathbf{u}_G^T} & \frac{\partial^2 \boldsymbol{\theta}_3}{\partial \mathbf{n}_{g3}^T \partial \mathbf{u}_G^T} \end{bmatrix} \quad (48)$$

where the various second derivatives in Eq. 48 are given in Appendix B. In the right side of Eq. 47, the first term is symmetric. Considering the commutativity of the global nodal variables in the differentiation of Eq. 48, the second term (its component at  $j^{\text{th}}$  row and  $k^{\text{th}}$  column is

$\sum_{i=1}^{15} \frac{\partial u_{Li}}{\partial u_{Gj} \partial u_{Gk}} f_i$ ,  $j, k=1,2,\dots,15$ ;  $u_{Li}$  and  $f_i$  are respectively the  $i^{\text{th}}$  components of  $\mathbf{u}_L$  and  $\mathbf{f}$ ;  $u_{Gj}$  and  $u_{Gk}$  are respectively the  $j^{\text{th}}$  and  $k^{\text{th}}$  components of  $\mathbf{u}_G$  in the right side of Eq. 47 is also symmetric, so the element tangent stiffness matrix in the global coordinate system is symmetric.

## 5. NUMERICAL EXAMPLES

In the present newly developed 3-node co-rotational triangular shell element (abbreviated to “TRIS3” element in the following examples), assumed membrane strains and shear strains are employed to alleviate membrane and shear locking problems. To demonstrate the reliability and convergence of the TRIS3 element in solving elastic and elasto-plastic plate/shell problems with large displacements, (1) two plate patch tests, (2) three elastic plate/shell problems, and (3) three elasto-plastic plate/shell problems are analyzed using this element. With regard to numerical integration over the thickness, 2 Gauss points are adopted for the two patch tests (Example 5.1) and the three elastic plate/shell problems (Examples 5.2-5.4), and 6 Gauss points are adopted for the three elasto-plastic plate/shell problems (Examples 5.5-5.7) in accordance with the corresponding references considering these examples. Meanwhile, one Gauss point is adopted in numerical integration over the element domain for all examples. The results are also compared to those from other researchers [36, 73-81].

### 5.1 Patch Tests

Two patch tests for the membrane behavior and the transverse out-of-plane bending behavior of plate and shell elements were suggested by MacNeal and Harder [73]. The linear results from the TRIS3 element agree exactly with the theoretical results [73].

### 5.2 Clamped Annular Plate Strip subject to Transverse Uniformly-Distributed End Load

An annular plate strip has a geometry of the internal radius  $r=6\text{m}$ , the external radius  $R=10\text{m}$ , and the thickness  $h=0.03\text{m}$ . Its elastic modulus and Poisson's ratio are  $E=2.1 \times 10^8 \text{KN/m}^2$  and  $\mu=0.0$ , respectively. The plate is laid horizontally, and clamped at one end and uniformly loaded on the other end. The load is in downward direction along the free edge (see Figure 5),  $q=6\text{KN/m}$ .

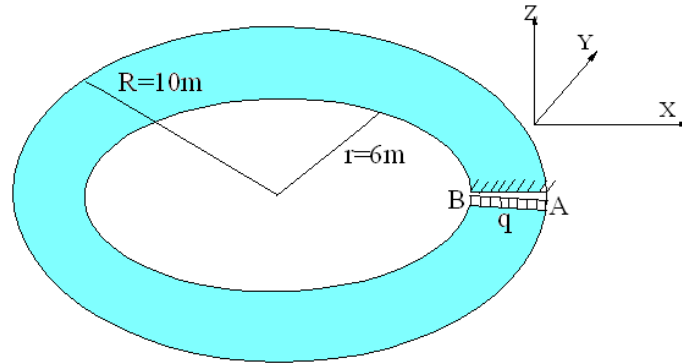


Figure 5. Clamped Annular Plate under Uniformly Distributed Line Load

The load-deflection curves at Points A and B of the plate calculated respectively by using a  $4 \times 32 \times 2$  TRIS3-element mesh (the 1<sup>st</sup> two numbers ' $4 \times 32$ ' represents a mesh of quadrilateral elements, with the 3<sup>rd</sup> number ' $\times 2$ ' indicating that each quadrilateral element is further subdivided into 2 triangular elements), a  $8 \times 64 \times 2$  TRIS3-element mesh, and a  $16 \times 128 \times 2$  TRIS3-element mesh are presented in Figure 6, where it can be observed that the results obtained with the  $4 \times 32 \times 2$  TRIS3-element mesh are already accurate compared with the even more accurate results using the  $8 \times 64 \times 2$  TRIS3-element mesh or the  $16 \times 128 \times 2$  TRIS3-element mesh. For comparison purpose, the results from Campello et al.[36] and Buechter & Ramm [74] are also depicted in this figure. The solutions obtained from using  $4 \times 32 \times 2$ ,  $8 \times 64 \times 2$  and  $16 \times 128 \times 2$  lower order TRIS3 elements compare favourably with those from Campello et al.[36], employing  $8 \times 64$  higher order six-node triangular shell elements, and Buechter & Ramm [74], employing  $2 \times 16$  higher order bi-cubic quadrilateral shell elements.

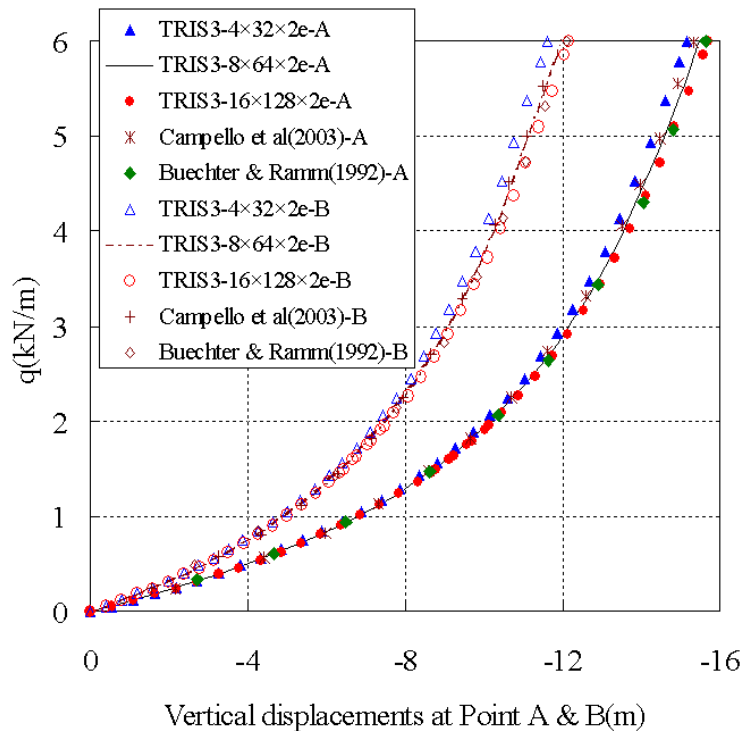


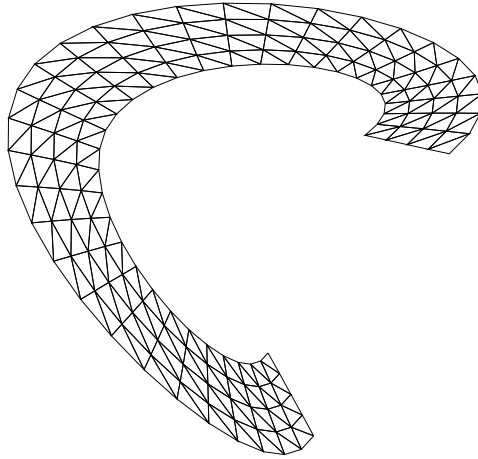
Figure 6. Load-deflection Curves at Points A and B of the Clamped Annular Plate

Table 2. Deflections at Points A and B of the Clamped Annular Plate under End Load  $q=6\text{KN/m}$ 

Element mesh	Deflection at Point A		Deflection at Point B	
TRIS3-4×32×2	-15.1581m	-3.48%	-11.6028m	-4.67%
TRIS3-8×64×2	-15.4847m	-1.40%	-11.9445m	-1.86%
TRIS3-16×128×2	-15.7051m	--	-12.1711m	--

To evaluate the convergence of the solutions obtained with the TRIS3 element using respectively the  $4\times 32\times 2$ ,  $8\times 64\times 2$  and  $16\times 128\times 2$  meshes, the deflections at Points A and B of the clamped annular plate under end loading  $q=6\text{KN/m}$  and their relative errors based on the results from the highest-density  $16\times 128\times 2$  TRIS3-element mesh are presented in Table 2.

The deformed shape of the clamped annular plate under end load  $q=6\text{KN/m}$  obtained using  $4\times 32\times 2$  TRIS3 elements is presented in Figure 7, where large displacements and rotations are evident.

Figure 7. Deformed Shape of the Clamped Annular Plate under End Load  $q=6\text{KN/m}$ 

### 5.3 Lateral Buckling of L-shaped Plate Strip

A flat L-shaped plate strip is fully clamped on one edge and subjected to an in-plane point load at the free end (Figure 8), having Young's modulus  $E=71,240\text{N/mm}^2$ , and Poisson's ratio  $\mu=0.31$ . The plate has a geometry of  $L=240\text{mm}$ ,  $b=30\text{mm}$ , and  $h=0.6\text{mm}$ .

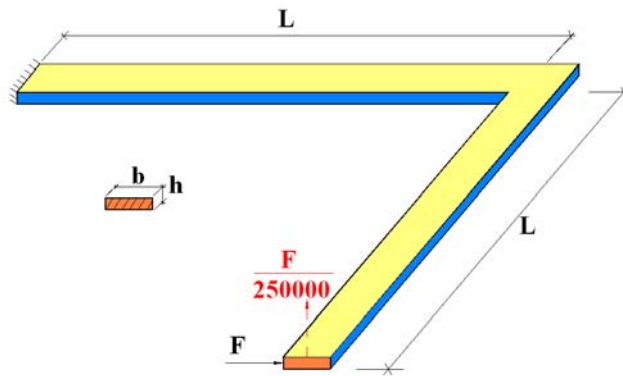


Figure 8. Fully Clamped L-shaped Plate Strip subject to in-plane Point Load at Free End

To investigate the lateral stability of the L-shaped plate, a very small perturbation load ( $F/250,000$ )

is imposed on the free edge in the out-of-plane direction to trigger the post-critical lateral deflection (see Figure 8). The meshes used for this analysis are a  $64 \times 2$  TRIS3-element mesh (where, '64' represents quadrilateral elements, ' $\times 2$ ' means that each quadrilateral element is further subdivided into 2 triangular elements), a  $256 \times 2$  TRIS3-element mesh, and a  $1024 \times 2$  TRIS3-element mesh; the results are presented in Figure 9. To verify the reliability of the present TRIS3 element, the results from a mesh with 136 six-node triangular shell elements [36] and a mesh with 68 four-node EAS elements [75] are also represented in Figure 9.

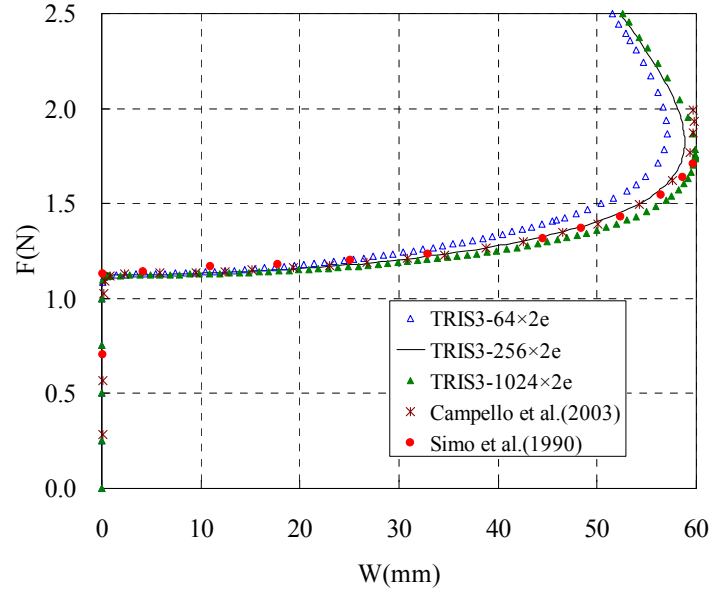


Figure 9. Out-of-plane Lateral Deflection at Free End of L-shaped Plate

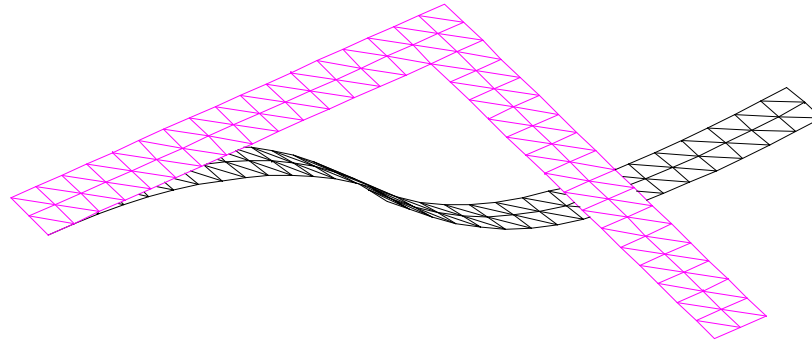


Figure 10. L-shaped Plate: Initial and Deformed Shape

The deformed shape of the L-shape plate (with the  $64 \times 2$  TRIS3-element mesh) at the load level of  $F=2.5\text{N}$  is presented in Figure 10, where large displacement and large rotation can be observed in the post-buckling stage of the L-shape plate.

#### 5.4 Pull-out of Open Cylindrical Shell

An open cylindrical shell has a geometry of  $L=10.35$ ,  $R=4.953$ , and  $h=0.094$ . Its material properties are  $E=10.5 \times 10^6$  and  $\mu=0.3125$ , respectively. The cylindrical shell is pulled by two diametrically opposite point forces  $F$  (Figure 11). For symmetry reasons, only one-eighth of the cylindrical shell (i.e. the colored part) is analyzed.

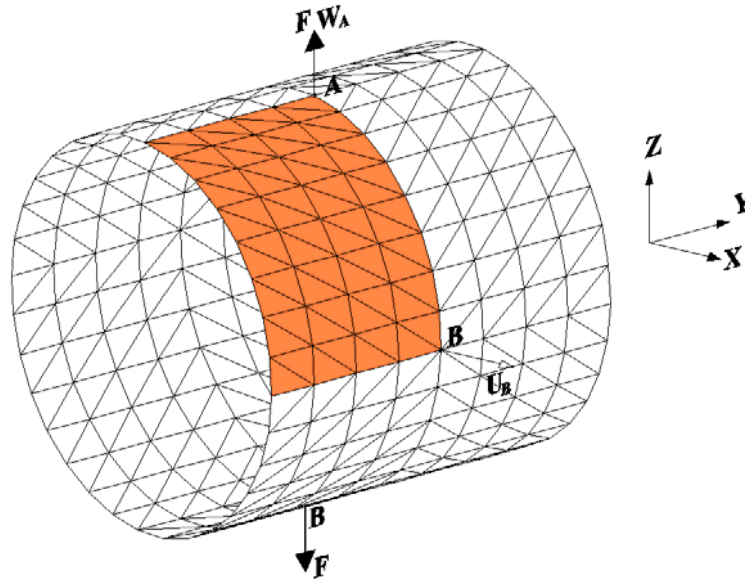


Figure 11. Open Cylindrical Shell subject to Two Diametrically Opposite Point Forces

Three meshes with  $4 \times 8 \times 2$ ,  $8 \times 16 \times 2$  and  $16 \times 32 \times 2$  TRIS3 elements are employed respectively to calculate the deflection at the loading point A of the cylindrical shell. For comparison, we also represent in Figure 12 the results from Campello *et al.* [36] using a  $8 \times 16 \times 2$  mesh of six-node triangular elements, the results from Jiang & Chernuka [76] using a  $8 \times 12$  mesh of four-node ANS degenerated-shell elements, and the results from Sze *et al.* [77] using a  $8 \times 12$  mesh of eight-node hybrid-stress solid-shell element based on the total Lagrangian framework.

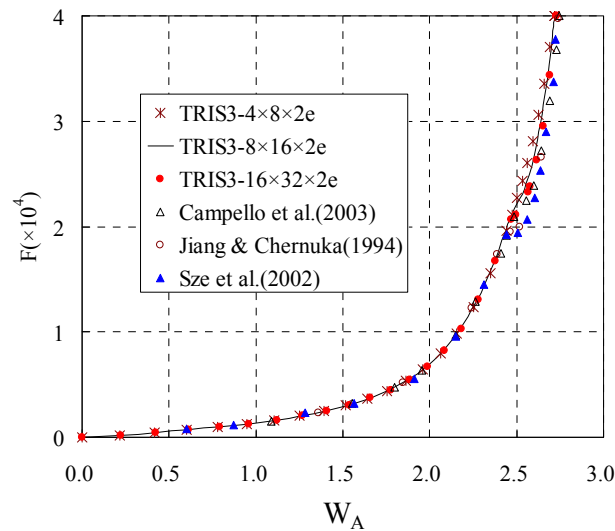


Figure 12. Load-deflection Curve at Point A of Open Cylindrical Shell

To demonstrate the convergence of the present element, the solution calculated respectively from using the meshes with  $4 \times 8 \times 2$ ,  $8 \times 18 \times 2$ ,  $16 \times 32 \times 2$  and  $32 \times 64 \times 2$  TRIS3 elements are presented in Table 3, with the relative errors based on the results from the highest-density  $32 \times 64 \times 2$  mesh.

Table 3. Displacements at Points A and B of the Pulled Cylinder under End Load  $F=4 \times 10^4$ 

Element meshes	$W_A$ (Displacement at Point A)		$U_B$ (Displacement at Point B)	
TRIS3-4×8×2	2.7169	0.90%	-4.5083	-0.94%
TRIS3-8×16×2	2.7207	0.76%	-4.5606	-0.20%
TRIS3-16×32×2	2.7295	0.44%	-4.5553	-0.08%
TRIS3-32×64×2	2.7416	--	-4.5515	--

The deformed shape of the pulled cylindrical shell at the load level of  $F=40,000$  is presented in Figure 13.

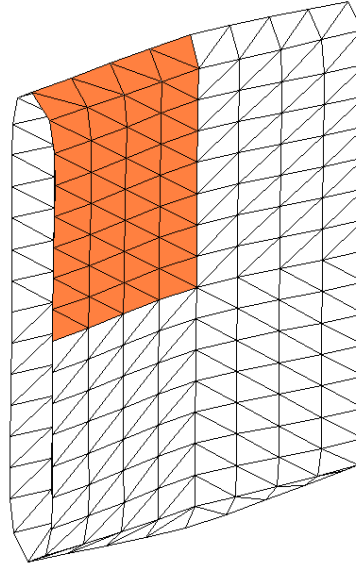


Figure 13. Deformed Shape of the Open Cylindrical Shell

### 5.5 Square Plate subjected to Constant Pressure Load

A square plate is simply supported along the edges (the out-of-plane displacements along its four edges are restrained), and subjected to a deformation dependent pressure load  $q=f \times p_0$  on one side (Figure 14), where  $p_0=10^{-2} \text{ N/mm}^2$ . The plate has side length of  $2L=508 \text{ mm}$  and thickness  $h=2.54 \text{ mm}$ , with material properties: Young's modulus  $E=6.9 \times 10^4 \text{ N/mm}^2$ , Poisson's ratio  $\mu=0.3$ , initial yield stress  $f_y=248 \text{ N/mm}^2$ , and hardening parameter  $H=0.0$ .

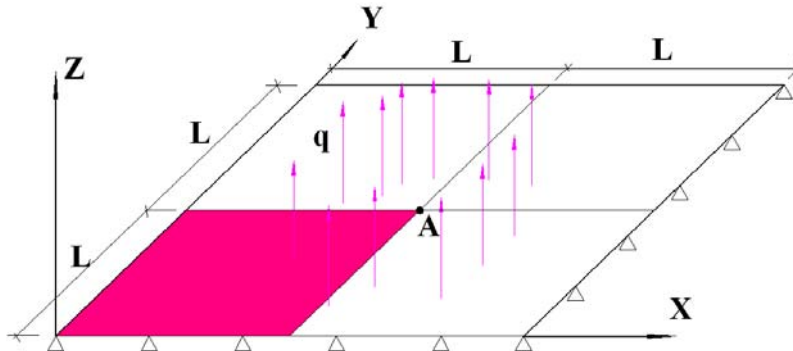


Figure 14. A Simply-supported Square Plate

Due to symmetry, only a quarter of the plate (the colored zone in Figure 14) is analyzed using respectively a mesh of  $12 \times 12 \times 2$ , a mesh of  $24 \times 24 \times 2$ , and a mesh of  $48 \times 48 \times 2$  TRIS3 elements. The load-deflection curves at the central point of the plate, from our present element, are presented in Figure 15. For comparison, the following results are also presented in this figure: (1) Eberlein & Wriggers [78] using  $15 \times 15$  five- or six-parameter quadrilateral 4-node elements with refined mesh toward the outer corner, (2) Betsch & Stein [79] using  $24 \times 24$  quadrilateral 4-node shell elements with regular mesh, (3) Valente *et al.*[80] using more refined mesh of 1375 S4E6P5 elements and  $24 \times 24$  S4E6P5 elements with regular mesh. The results from the three meshes with  $12 \times 12 \times 2$ ,  $24 \times 24 \times 2$ , and  $48 \times 48 \times 2$  of the present TRIS3 elements agree well with those from Betsch & Stein [79] and Valente *et al.*[80].

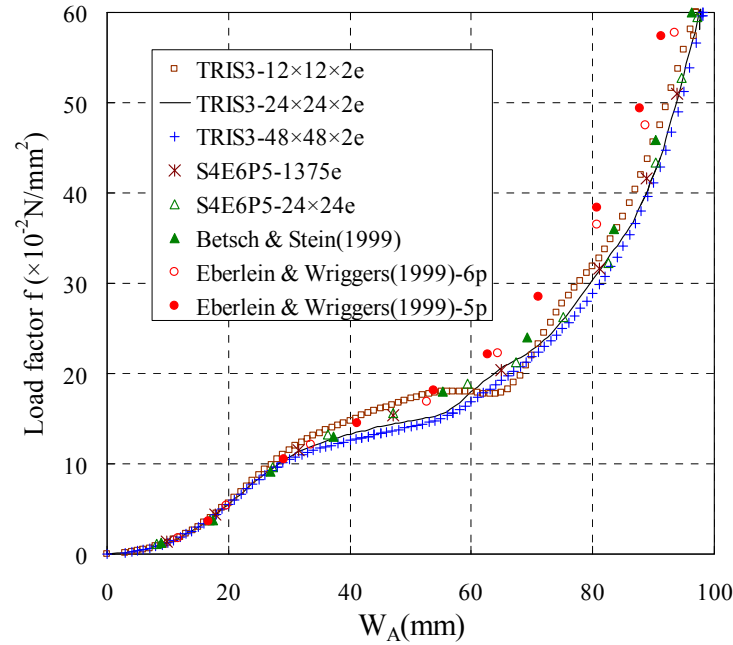


Figure 15. Load-deflection Curves at the Central Point of the Plate

Table 4. Deflection at the Central Point of the Plate under  $q=0.6\text{N/mm}^2$

Element meshes	Deflection at Point A	
TRIS3- $12 \times 12 \times 2$	96.9707mm	-1.19%
TRIS3- $24 \times 24 \times 2$	97.6775mm	-0.47%
TRIS3- $48 \times 48 \times 2$	98.1339mm	--

To evaluate the convergence of the TRIS3 element, the deflections at the central point of the plate under the pressure of  $0.6\text{ N/mm}^2$  calculated from using the meshes with  $12 \times 12 \times 2$ ,  $24 \times 24 \times 2$  and  $48 \times 48 \times 2$  TRIS3 elements are presented in Table 4.

In our analysis, the deformation-dependent pressure load is first decomposed in the directions of the three global coordinate axes by multiplying the value of the pressure with the mid-surface normal vector at each integration point on the mid-surface of the plate, the loads at the integration points are then transformed into equivalent nodal loads. The mid-surface normal vectors at integration points are updated at each iteration of every incremental step. We omit the geometric stiffness matrix corresponding to a pressure load to avoid the occurrence of an asymmetric element tangent stiffness matrix within the co-rotational framework. We note, however, that the convergence of the iterative solution procedure in the present problem is not compromised by such omission.

The deformed shape of the plate at the load level of  $q=0.6 \text{ N/mm}^2$  is presented in Figure 16, showing large displacement and large rotation; plastic zone occurred in the plate.

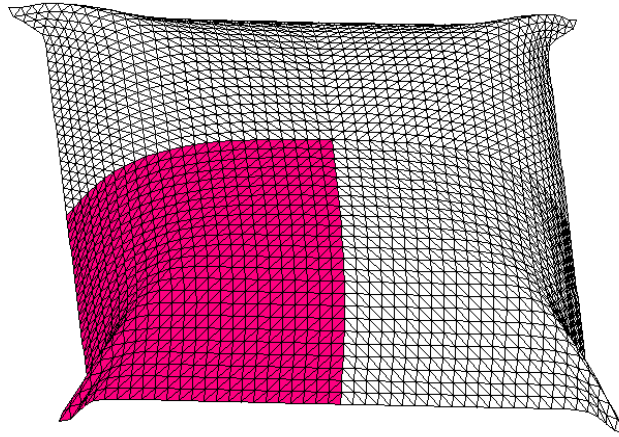


Figure 16. Deformed Shape of Plate under Constant Pressure of  $0.60 \text{ N/mm}^2$

### 5.6 Pinched Hemispherical Shell

A hemispherical shell is loaded by two inward and two outward forces at the quarter points of its open edge (Figure 17); the shell has a radius of 10 and a thickness of 0.5. The material parameters are  $E=10.0$ ,  $\mu=0.2$ ,  $f_y=0.2$  and  $H=9.0$ , respectively.

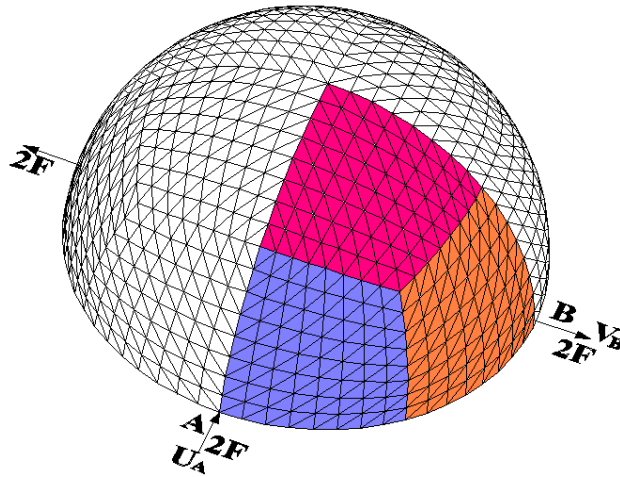


Figure 17. Hemispherical Shell subject to Pinched Forces

Due to symmetry, only a quarter of this hemispherical shell is analyzed (see the colored zone of Figure 17), using a mesh composed of three subdomains, with each subdomain discretized with either (a)  $4 \times 4 \times 2$ , or (b)  $8 \times 8 \times 2$ , or (c)  $16 \times 16 \times 2$  TRIS3 elements. The load-displacement curves at the pinching points A and B are depicted in Figure 18, where it can be observed that the results obtained with three subdomains of  $8 \times 8 \times 2$  TRIS3 elements are already accurate compared with the even more accurate results using three subdomains of  $16 \times 16 \times 2$  TRIS3 elements. These results also agree well with those from Bestch & Stein [79] using three subdomains of  $16 \times 16$  bi-linear quadrilateral shell elements, and Eberlein & Wriggers [78] using three subdomains of  $12 \times 12$  quadrilateral 4-node elements.



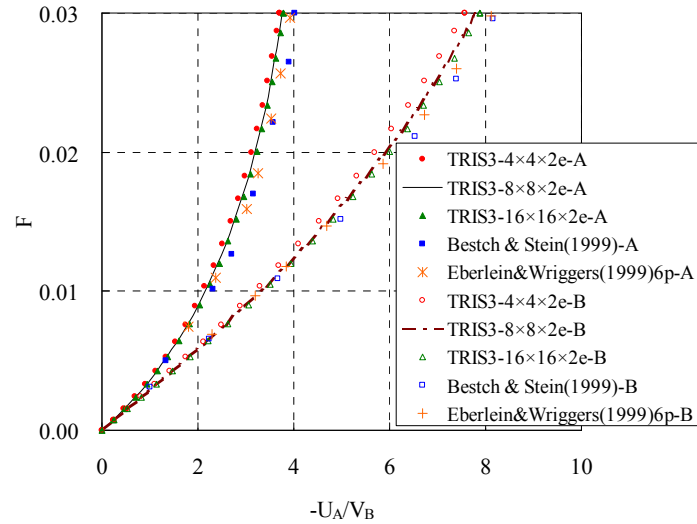


Figure 18. Load-deflection Curves at Pinching Points A and B of hemispherical shell

To illustrate the convergence characteristics of the TRIS3 element, the deflections at the pinched points A and B of the hemispherical shell under  $F=0.03$  are presented in Table 5, with the relative errors based on the results from the highest-density  $24 \times 24 \times 2$  mesh.

Table 5. Deflection at the Pinched Point A and B under  $F=0.03$

Element Meshes	Displacement at Point A ( $U_A$ )		Displacement at Point B ( $V_B$ )	
TRIS3-4x4x2	-3.7003	-2.42%	7.5705	-4.15%
TRIS3-8x8x2	-3.7526	-1.04%	7.7905	-1.36%
TRIS3-16x16x2	-3.7812	-0.29%	7.8764	-0.27%
TRIS3-24x24x2	-3.7922	--	7.8979	--

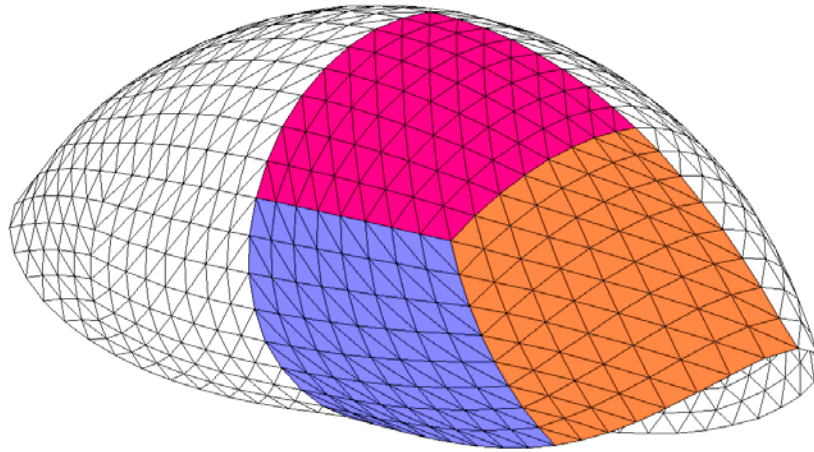


Figure 19. Deformed Shape of a Pinched Hemispherical Shell

The deformed shape of the complete hemispherical shell at the load level of  $F=0.03$  is presented in Figure 19. Plastic zone occurred in the pinched hemispherical shell at this load level.

## 5.7 Pinched Cylinder

Consider a cylinder supported by two rigid diaphragms at its two ends, where only the displacement along the longitudinal axis is allowed (see Figure 20), with length  $2L=600$ , radius  $R=300$ , and thickness  $h=3$ . The material properties are  $E=3000$ ,  $\mu=0.3$ ,  $f_y=24.3$  and  $H=300$ . The cylinder is subjected to a pair of pinching concentrated loads (Figure 20).

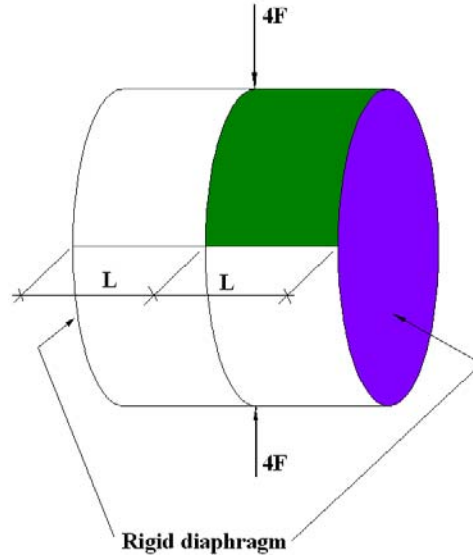


Figure 20. A Pinched Cylinder with Two End Diaphragms

Again, owing to symmetry, only one-eighth of the cylinder (the colored zone of Figure 20) is analyzed with three different uniform meshes: (a)  $24 \times 24 \times 2$ , (b)  $32 \times 32 \times 2$  and (c)  $48 \times 48 \times 2$  TRIS3 elements. The load-displacement curves at one pinched point are presented in Figure 21, where it can be seen that the results agree well with those from Eberlein & Wriggers [78] using  $32 \times 32$  four-node quadrilateral shell elements, Valente *et al.* [80] using  $32 \times 32$  S4E6P5 shell elements, and Miehe [81] using  $32 \times 32$  mixed brick-type shell elements.

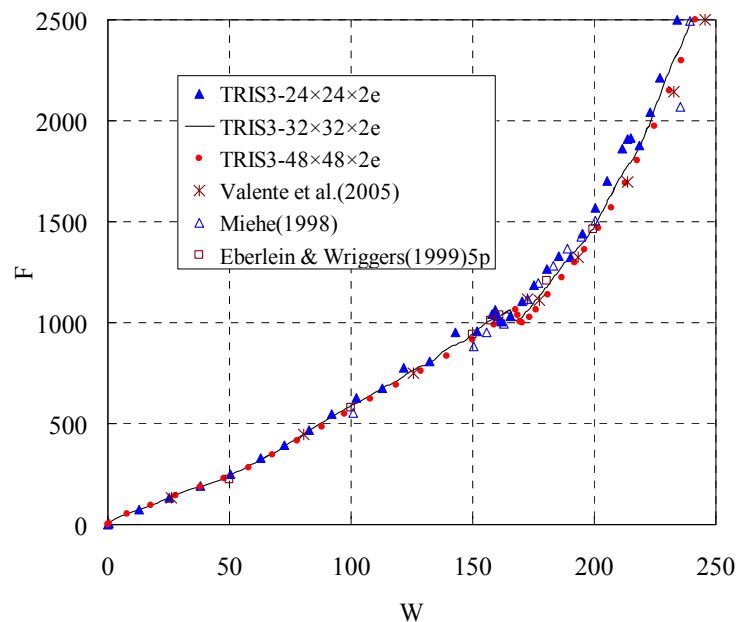


Figure 21. Load-displacement Curves at One Pinched Point of the Cylinder

To evaluate the convergence of the TRIS3 element, the deflections at the pinched point of the cylinder under  $F=2500$  are presented in Table 6, with the relative errors based on the results of the highest-density  $48 \times 48 \times 2$  mesh.

Table 6. Deflection at the Pinched Point of the Cylinder

Element meshes	Deflection at the loading point	
TRIS3- $24 \times 24 \times 2$	234.1663	-3.11%
TRIS3- $32 \times 32 \times 2$	239.6611	-0.83%
TRIS3- $48 \times 48 \times 2$	241.6718	--

The deformed shape of the overall cylinder obtained using  $24 \times 24 \times 2$  TRIS3 elements at a load level  $F=2500$  is depicted in Figure 22, showing clear large displacements and large nodal rotations; plastic deformation occurs even at a very low loading level.

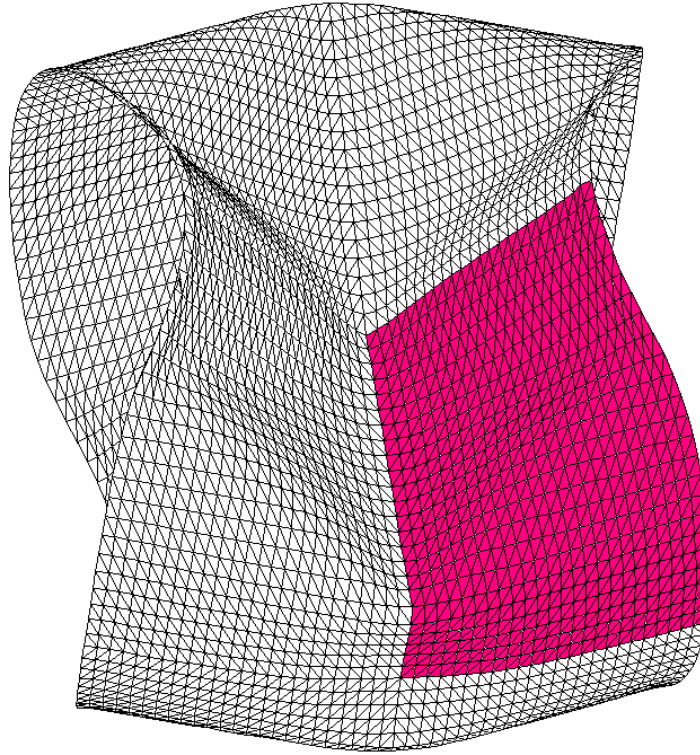


Figure 22. Deformed Shape of the Pinched Cylinder

## 6. CONCLUSIONS

A 3-node co-rotational triangular shell element formulation has been proposed for elasto-plastic plate/shell analysis involving large displacement and large rotation. To overcome the locking problems, assumed membrane strains and assumed shear strains calculated respectively from the edge-member membrane strains and the edge-member transverse shear strains by using the line integration methods are employed in the present element formulation. The residual bending flexibility is added to the transverse shear flexibility to improve further the accuracy of the element. The reliability and convergence of the present shell formulation are demonstrated in a number of problems that include linear elastic patch tests together with six elastic/elasto-plastic plate and shell problems involving large displacement and large rotation.

## APPENDIX A: Various derivatives of strains with respect to local nodal variables

The first derivatives of membrane strains with respect to local nodal variables:

$$\mathbf{B}_m = [\mathbf{B}_{m1} \quad \mathbf{0} \quad \mathbf{B}_{m2} \quad \mathbf{0} \quad \mathbf{B}_{m3} \quad \mathbf{0}] \quad (\text{A-1a})$$

$$\mathbf{B}_{mi} = \begin{bmatrix} N_{i,x} & 0 & \frac{\partial(w+z)}{\partial x} N_{i,x} \\ 0 & N_{i,y} & \frac{\partial(w+z)}{\partial y} N_{i,y} \\ N_{i,y} & N_{i,x} & \frac{\partial(w+z)}{\partial y} N_{i,x} + \frac{\partial(w+z)}{\partial x} N_{i,y} \end{bmatrix} \quad i=1,2,\dots,3 \quad (\text{A-1b})$$

where,

$$N_{i,x} = J_{11}^{-1} N_{i,\xi} + J_{12}^{-1} N_{i,\eta} \quad (\text{A-2a})$$

$$N_{i,y} = J_{21}^{-1} N_{i,\xi} + J_{22}^{-1} N_{i,\eta} \quad (\text{A-2b})$$

$J_{jk}^{-1} (j,k=1,2)$  is the component of inverse Jacobian matrix at  $j$ th row and  $k$ th column;  $N_{i,\xi}$  and  $N_{i,\eta}$  are respectively the first derivative of the shape function  $N_i$  with respect to  $\xi$  and  $\eta$ .

The first derivatives of assumed membrane strains with respect to local nodal variables:

$$\tilde{\mathbf{B}}_m = \mathbf{P} \mathbf{\Gamma}^{-1} [\mathbf{B}_k] \quad (\text{A-3a})$$

$$\mathbf{B}_{k,5i-4:5i-3} = -\frac{\mathbf{a}_{ij0}^T(1:2)}{|\mathbf{a}_{ij0}|^2} \quad (\text{A-3b})$$

$$\mathbf{B}_{k,5i-2} = -\frac{w_j - w_i}{|\mathbf{a}_{ij0}|^2} \quad (\text{A-3c})$$

$$\mathbf{B}_{k,5j-4:5j-3} = \frac{\mathbf{a}_{ij0}^T(1:2)}{|\mathbf{a}_{ij0}|^2} \quad (\text{A-3d})$$

$$\mathbf{B}_{k,5j-2} = \frac{w_j - w_i}{|\mathbf{a}_{ij0}|^2} \quad (\text{A-3e})$$

where, the ordered triplets  $(k,i,j)$  are given by (A,1,2), (B,2,3) and (C,3,1);  $\mathbf{a}_{ij0}(1:2)$  represents the sub-vector of the vector  $\mathbf{a}_{ij0}$  consisting of its first two components.

The first derivatives of shear strains with respect to local nodal variables:

$$\mathbf{B}_s = [\mathbf{B}_{s1} \mathbf{B}_{s2} \mathbf{B}_{s3} \mathbf{B}_{s4} \mathbf{B}_{s5} \mathbf{B}_{s6}] \quad (\text{A-4a})$$

$$\mathbf{B}_{s(2i-1)} = \begin{bmatrix} 0 & 0 & N_{i,x} \\ 0 & 0 & N_{i,y} \end{bmatrix} \quad i=1,2,3 \quad (\text{A-4b})$$

$$\mathbf{B}_{s(2i)} = \begin{bmatrix} N_i & 0 \\ 0 & N_i \end{bmatrix} \quad i=1,2,3 \quad (\text{A-4c})$$

The first derivatives of assumed shear strains with respect to local nodal variables:

$$\tilde{\mathbf{B}}_s = \mathbf{P}\mathbf{\Omega}^{-1} \begin{bmatrix} \mathbf{B}_{sk} \\ \rho_k \end{bmatrix} \quad (\text{A-5a})$$

$$\mathbf{B}_{sk,5i-2} = -\frac{1}{|\mathbf{a}_{ij0}|} \quad (\text{A-5b})$$

$$\mathbf{B}_{sk,5j-2} = \frac{1}{|\mathbf{a}_{ij0}|} \quad (\text{A-5c})$$

$$\mathbf{B}_{sk,5i-1:5i} = \frac{\mathbf{a}_{ij0}^T (1:2)}{2|\mathbf{a}_{ij0}|} \quad (\text{A-5d})$$

$$\mathbf{B}_{sk,5j-1:5j} = \frac{\mathbf{a}_{ij0}^T (1:2)}{2|\mathbf{a}_{ij0}|} \quad (\text{A-5e})$$

where,  $\mathbf{B}_{sk}$  represents the first derivative of the edge-member transverse shear strain at Point  $k$  ( $k=A,B,C$ ) with respect to local nodal variables; the ordered triplets  $(k,i,j)$  in Eqs. (A-5a~e) are given by (A,1,2), (B,2,3) and (C,3,1).

The first derivatives of bending strains with respect to local nodal variables:

$$\mathbf{B}_b = [\mathbf{0} \mathbf{B}_{b1} \mathbf{0} \mathbf{B}_{b2} \mathbf{0} \mathbf{B}_{b3}] \quad (\text{A-6a})$$

$$\mathbf{B}_{bi} = \begin{bmatrix} N_{i,x} & 0 \\ 0 & N_{i,y} \\ N_{i,y} & N_{i,x} \end{bmatrix} \quad i=1,2,3 \quad (\text{A-6b})$$

The second derivatives of membrane strains with respect to local nodal variables:

$$\begin{aligned} \left( \frac{\partial \mathbf{B}_m}{\partial \mathbf{u}_L^T} \right)_{1,5i-2,5j-2} &= N_{i,x} N_{j,x} \\ \left( \frac{\partial \mathbf{B}_m}{\partial \mathbf{u}_L^T} \right)_{2,5i-2,5j-2} &= N_{i,y} N_{j,y} \quad i,j=1,2,3 \\ \left( \frac{\partial \mathbf{B}_m}{\partial \mathbf{u}_L^T} \right)_{3,5i-2,5j-2} &= N_{i,x} N_{j,y} + N_{i,y} N_{j,x} \end{aligned} \quad (\text{A-7})$$

where, three subscripts outside the parentheses in the left side of (A-7) represent the position of the component at the three dimensional matrix. The values of other unmentioned components of the three dimensional matrix are equal to zero.

The second derivatives of assumed membrane strains with respect to local nodal variables:

$$\frac{\partial \tilde{\mathbf{B}}_m}{\partial \mathbf{u}_L^T} = \mathbf{P}\mathbf{\Gamma}^{-1} \begin{bmatrix} \partial \mathbf{B}_k \\ \partial \mathbf{u}_L^T \end{bmatrix}, \quad k=A,B,C \quad (\text{A-8a})$$

$$\left( \frac{\partial \mathbf{B}_k}{\partial \mathbf{u}_L^T} \right)_{5i-2, 5i-2} = \left( \frac{\partial \mathbf{B}_k}{\partial \mathbf{u}_L^T} \right)_{5j-2, 5j-2} = \frac{1}{|\mathbf{a}_{ij0}|^2} \quad (\text{A-8b})$$

$$\left( \frac{\partial \mathbf{B}_k}{\partial \mathbf{u}_L^T} \right)_{5i-2, 5j-2} = \left( \frac{\partial \mathbf{B}_k}{\partial \mathbf{u}_L^T} \right)_{5j-2, 5i-2} = -\frac{1}{|\mathbf{a}_{ij0}|^2} \quad (\text{A-8c})$$

## APPENDIX B: Sub-matrices of transformation matrix $\mathbf{T}$ and its first derivatives with respect to global nodal variables

Sub-matrices of transformation matrix  $\mathbf{T}$ :

$$\frac{\partial \mathbf{t}_k}{\partial \mathbf{d}_l^T} = \frac{\partial \mathbf{R}}{\partial \mathbf{d}_l^T} (\mathbf{d}_k + \mathbf{v}_{k0}) + \mathbf{R} \delta_{kl} \mathbf{I} = \left( \frac{\partial}{\partial \mathbf{d}_l^T} \begin{bmatrix} \mathbf{e}_x^T \\ \mathbf{e}_y^T \\ \mathbf{e}_z^T \end{bmatrix} \right) (\mathbf{d}_k + \mathbf{v}_{k0}) + \mathbf{R} \delta_{kl} \mathbf{I} \quad (\text{B1})$$

$$\frac{\partial \boldsymbol{\theta}_k}{\partial \mathbf{d}_l^T} = \frac{\partial \mathbf{R}_h}{\partial \mathbf{d}_l^T} \mathbf{p}_k = \left( \frac{\partial}{\partial \mathbf{d}_l^T} \begin{bmatrix} \mathbf{e}_x^T \\ \mathbf{e}_y^T \end{bmatrix} \right) \mathbf{p}_k \quad (\text{B2})$$

$$\frac{\partial \boldsymbol{\theta}_k}{\partial \mathbf{n}_{gl}^T} = \mathbf{R}_h \delta_{kl} \frac{\partial \mathbf{p}_k}{\partial \mathbf{n}_{gl}^T} = \begin{bmatrix} \mathbf{e}_x^T \\ \mathbf{e}_y^T \end{bmatrix} \delta_{kl} \frac{\partial \mathbf{p}_k}{\partial \mathbf{n}_{gl}^T} \quad (\text{B3})$$

$$\frac{\partial \mathbf{e}_x}{\partial \mathbf{d}_l^T} = \left[ \frac{\mathbf{I}}{|\mathbf{e}'_x + \mathbf{e}'_y|} - \frac{(\mathbf{e}'_x + \mathbf{e}'_y) \otimes (\mathbf{e}'_x + \mathbf{e}'_y)}{|\mathbf{e}'_x + \mathbf{e}'_y|^3} \right] \left( \frac{\partial \mathbf{e}'_x}{\partial \mathbf{d}_l^T} + \frac{\partial \mathbf{e}'_y}{\partial \mathbf{d}_l^T} \right) \quad (\text{B4})$$

$$\frac{\partial \mathbf{e}'_y}{\partial \mathbf{d}_l^T} = \frac{\partial \mathbf{e}'_y}{\partial \mathbf{d}_l^T} \times \mathbf{e}_z + \mathbf{e}'_y \times \frac{\partial \mathbf{e}_z}{\partial \mathbf{d}_l^T} \quad (\text{B5})$$

$$\frac{\partial \mathbf{e}'_x}{\partial \mathbf{d}_l^T} = a_{x1} \frac{\partial \mathbf{v}_{12}}{\partial \mathbf{d}_l^T} \quad (\text{B6})$$

$$\frac{\partial \mathbf{e}'_y}{\partial \mathbf{d}_l^T} = a_{y1} \frac{\partial \mathbf{v}_{12}}{\partial \mathbf{d}_l^T} + a_{y2} \frac{\partial \mathbf{v}_{23}}{\partial \mathbf{d}_l^T} \quad (\text{B7})$$

$$\frac{\partial \mathbf{e}_z}{\partial \mathbf{d}_l^T} = \left[ \frac{\mathbf{I}}{|\mathbf{v}_{12} \times \mathbf{v}_{13}|} - \frac{(\mathbf{v}_{12} \times \mathbf{v}_{13}) \otimes (\mathbf{v}_{12} \times \mathbf{v}_{13})}{|\mathbf{v}_{12} \times \mathbf{v}_{13}|^3} \right] \left( \frac{\partial \mathbf{v}_{12}}{\partial \mathbf{d}_l^T} \times \mathbf{v}_{13} + \mathbf{v}_{12} \times \frac{\partial \mathbf{v}_{13}}{\partial \mathbf{d}_l^T} \right) \quad (\text{B8})$$

$$\frac{\partial \mathbf{e}_y}{\partial \mathbf{d}_l^T} = \frac{\partial \mathbf{e}_z}{\partial \mathbf{d}_l^T} \times \mathbf{e}_x + \mathbf{e}_z \times \frac{\partial \mathbf{e}_x}{\partial \mathbf{d}_l^T} \quad (\text{B9})$$

In Eqs. B6-B8,  $\frac{\partial \mathbf{v}_{12}}{\partial \mathbf{d}_l^T} = -\mathbf{I}$ ,  $l=1$ ;  $\frac{\partial \mathbf{v}_{12}}{\partial \mathbf{d}_l^T} = \mathbf{I}$ ,  $l=2$ ;  $\frac{\partial \mathbf{v}_{12}}{\partial \mathbf{d}_l^T} = 0$ ,  $l=3$ ;  $\frac{\partial \mathbf{v}_{13}}{\partial \mathbf{d}_l^T} = -\mathbf{I}$ ,  $l=1$ ;  $\frac{\partial \mathbf{v}_{13}}{\partial \mathbf{d}_l^T} = \mathbf{I}$ ,

$l=3$ ;  $\frac{\partial \mathbf{v}_{13}}{\partial \mathbf{d}_l^T} = 0$ ,  $l=2$ .

$$\frac{\partial \mathbf{p}_k}{\partial \mathbf{n}_{gk}^T} = \begin{bmatrix} \frac{\partial p_{k,X}}{\partial p_{k,n_k}} & \frac{\partial p_{k,X}}{\partial p_{k,m_k}} \\ \frac{\partial p_{k,n_k}}{\partial p_{k,Y}} & \frac{\partial p_{k,m_k}}{\partial p_{k,Y}} \\ \frac{\partial p_{k,n_k}}{\partial p_{k,Z}} & \frac{\partial p_{k,m_k}}{\partial p_{k,Z}} \\ \frac{\partial p_{k,n_k}}{\partial p_{k,n_k}} & \frac{\partial p_{k,m_k}}{\partial p_{k,m_k}} \end{bmatrix} \quad (\text{B10})$$

where,  $p_{k,X}, p_{k,Y}, p_{k,Z}$  are three components of the mid-surface normal vector  $\mathbf{p}_i$  in the global coordinate axes  $X, Y, Z$  directions;  $p_{k,n_k}, p_{k,m_k}$  are two vectorial rotational variables of Node  $i$ ,

they are the two smallest components among  $p_{k,X}, p_{k,Y}, p_{k,Z}$ ;  $\frac{\partial p_{k,n_k}}{\partial p_{k,n_k}} = \frac{\partial p_{k,m_k}}{\partial p_{k,m_k}} = 1$ ;

$$\frac{\partial p_{k,n_k}}{\partial p_{k,m_k}} = \frac{\partial p_{k,m_k}}{\partial p_{k,n_k}} = 0; \quad \frac{\partial p_{k,l_k}}{\partial p_{k,n_k}} = -\frac{p_{k,n_k}}{p_{k,l_k}} \quad \text{and} \quad \frac{\partial p_{k,l_k}}{\partial p_{k,m_k}} = -\frac{p_{k,m_k}}{p_{k,l_k}}, \quad l_k \neq n_k \neq m_k, \quad l_k, n_k, m_k \in \{X, Y, Z\}.$$

$$\frac{\partial^2 \mathbf{t}_i}{\partial \mathbf{d}_j^T \partial \mathbf{u}_G^T} = \begin{bmatrix} \frac{\partial^2 \mathbf{t}_i}{\partial \mathbf{d}_j^T \partial \mathbf{d}_1^T} & \mathbf{0} & \frac{\partial^2 \mathbf{t}_i}{\partial \mathbf{d}_j^T \partial \mathbf{d}_2^T} & \mathbf{0} & \frac{\partial^2 \mathbf{t}_i}{\partial \mathbf{d}_j^T \partial \mathbf{d}_3^T} & \mathbf{0} \end{bmatrix} \quad (\text{B11})$$

$$\frac{\partial^2 \boldsymbol{\theta}_i}{\partial \mathbf{d}_j^T \partial \mathbf{u}_G^T} = \begin{bmatrix} \frac{\partial^2 \boldsymbol{\theta}_i}{\partial \mathbf{d}_j^T \partial \mathbf{d}_1^T} & \frac{\partial^2 \boldsymbol{\theta}_i}{\partial \mathbf{d}_j^T \partial \mathbf{n}_{g1}^T} & \frac{\partial^2 \boldsymbol{\theta}_i}{\partial \mathbf{d}_j^T \partial \mathbf{d}_2^T} & \frac{\partial^2 \boldsymbol{\theta}_i}{\partial \mathbf{d}_j^T \partial \mathbf{n}_{g2}^T} & \frac{\partial^2 \boldsymbol{\theta}_i}{\partial \mathbf{d}_j^T \partial \mathbf{d}_3^T} & \frac{\partial^2 \boldsymbol{\theta}_i}{\partial \mathbf{d}_j^T \partial \mathbf{n}_{g3}^T} \end{bmatrix} \quad (\text{B12})$$

$$\frac{\partial^2 \boldsymbol{\theta}_i}{\partial \mathbf{n}_{gj}^T \partial \mathbf{u}_G^T} = \begin{bmatrix} \frac{\partial^2 \boldsymbol{\theta}_i}{\partial \mathbf{n}_{gj}^T \partial \mathbf{d}_1^T} & \frac{\partial^2 \boldsymbol{\theta}_i}{\partial \mathbf{n}_{gj}^T \partial \mathbf{n}_{g1}^T} & \frac{\partial^2 \boldsymbol{\theta}_i}{\partial \mathbf{n}_{gj}^T \partial \mathbf{d}_2^T} & \frac{\partial^2 \boldsymbol{\theta}_i}{\partial \mathbf{n}_{gj}^T \partial \mathbf{n}_{g2}^T} & \frac{\partial^2 \boldsymbol{\theta}_i}{\partial \mathbf{n}_{gj}^T \partial \mathbf{d}_3^T} & \frac{\partial^2 \boldsymbol{\theta}_i}{\partial \mathbf{n}_{gj}^T \partial \mathbf{n}_{g3}^T} \end{bmatrix} \quad (\text{B13})$$

$$\begin{aligned} \frac{\partial^2 \mathbf{t}_i}{\partial \mathbf{d}_j^T \partial \mathbf{d}_k^T} &= \frac{\partial^2 \mathbf{R}}{\partial \mathbf{d}_j^T \partial \mathbf{d}_k^T} (\mathbf{d}_i + \mathbf{v}_{i0}) + \frac{\partial \mathbf{R}}{\partial \mathbf{d}_j^T} \delta_{ik} \mathbf{I} + \frac{\partial \mathbf{R}}{\partial \mathbf{d}_k^T} \delta_{ij} \mathbf{I} \\ &= \begin{bmatrix} \frac{\partial^2 \mathbf{e}_x^T}{\partial \mathbf{d}_j^T \partial \mathbf{d}_k^T} \\ \frac{\partial^2 \mathbf{e}_y^T}{\partial \mathbf{d}_j^T \partial \mathbf{d}_k^T} \\ \frac{\partial^2 \mathbf{e}_z^T}{\partial \mathbf{d}_j^T \partial \mathbf{d}_k^T} \end{bmatrix} (\mathbf{d}_i + \mathbf{v}_{i0}) + \begin{bmatrix} \frac{\partial \mathbf{e}_x^T}{\partial \mathbf{d}_j^T} \\ \frac{\partial \mathbf{e}_y^T}{\partial \mathbf{d}_j^T} \\ \frac{\partial \mathbf{e}_z^T}{\partial \mathbf{d}_j^T} \end{bmatrix} \delta_{ik} \mathbf{I} + \begin{bmatrix} \frac{\partial \mathbf{e}_x^T}{\partial \mathbf{d}_k^T} \\ \frac{\partial \mathbf{e}_y^T}{\partial \mathbf{d}_k^T} \\ \frac{\partial \mathbf{e}_z^T}{\partial \mathbf{d}_k^T} \end{bmatrix} \delta_{ij} \mathbf{I} \end{aligned} \quad (\text{B14})$$

$$\frac{\partial^2 \boldsymbol{\theta}_i}{\partial \mathbf{d}_j^T \partial \mathbf{d}_k^T} = \frac{\partial^2 \mathbf{R}_h}{\partial \mathbf{d}_j^T \partial \mathbf{d}_k^T} \mathbf{p}_i = \begin{bmatrix} \frac{\partial^2 \mathbf{e}_x^T}{\partial \mathbf{d}_j^T \partial \mathbf{d}_k^T} \\ \frac{\partial^2 \mathbf{e}_y^T}{\partial \mathbf{d}_j^T \partial \mathbf{d}_k^T} \\ \frac{\partial^2 \mathbf{e}_z^T}{\partial \mathbf{d}_j^T \partial \mathbf{d}_k^T} \end{bmatrix} \mathbf{p}_i \quad (\text{B15})$$

$$\frac{\partial^2 \boldsymbol{\theta}_i}{\partial \mathbf{d}_j^T \partial \mathbf{n}_{gk}^T} = \frac{\partial \mathbf{R}_h}{\partial \mathbf{d}_j^T} \delta_{ik} \frac{\partial \mathbf{p}_i}{\partial \mathbf{n}_{gk}^T} = \begin{bmatrix} \frac{\partial \mathbf{e}_x^T}{\partial \mathbf{d}_j^T} \\ \frac{\partial \mathbf{e}_y^T}{\partial \mathbf{d}_j^T} \\ \frac{\partial \mathbf{e}_z^T}{\partial \mathbf{d}_j^T} \end{bmatrix} \delta_{ik} \frac{\partial \mathbf{p}_i}{\partial \mathbf{n}_{gk}^T} \quad (\text{B16})$$

$$\frac{\partial^2 \boldsymbol{\theta}_i}{\partial \mathbf{n}_{gj}^T \partial \mathbf{n}_{gk}^T} = \mathbf{R}_h \delta_{ij} \delta_{ik} \frac{\partial^2 \mathbf{p}_i}{\partial \mathbf{n}_{gj}^T \partial \mathbf{n}_{gk}^T} \quad (\text{B17})$$

$$\begin{aligned} \frac{\partial^2 \mathbf{e}_x}{\partial \mathbf{d}_j^T \partial \mathbf{d}_k^T} &= -\frac{(\mathbf{e}'_x + \mathbf{e}'_y)^T}{|\mathbf{e}'_x + \mathbf{e}'_y|^3} \left( \frac{\partial \mathbf{e}'_x}{\partial \mathbf{d}_k^T} + \frac{\partial \mathbf{e}'_y}{\partial \mathbf{d}_k^T} \right) \otimes \left( \frac{\partial \mathbf{e}'_x}{\partial \mathbf{d}_j^T} + \frac{\partial \mathbf{e}'_y}{\partial \mathbf{d}_j^T} \right) + \frac{1}{|\mathbf{e}'_x + \mathbf{e}'_y|} \frac{\partial^2 \mathbf{e}'_y}{\partial \mathbf{d}_j^T \partial \mathbf{d}_k^T} \\ &\quad - \frac{1}{|\mathbf{e}'_x + \mathbf{e}'_y|^3} \left[ \left( \frac{\partial \mathbf{e}'_x}{\partial \mathbf{d}_k^T} + \frac{\partial \mathbf{e}'_y}{\partial \mathbf{d}_k^T} \right) \otimes (\mathbf{e}'_x + \mathbf{e}'_y) + (\mathbf{e}'_x + \mathbf{e}'_y) \otimes \left( \frac{\partial \mathbf{e}'_x}{\partial \mathbf{d}_k^T} + \frac{\partial \mathbf{e}'_y}{\partial \mathbf{d}_k^T} \right) \right] \left( \frac{\partial \mathbf{e}'_x}{\partial \mathbf{d}_j^T} + \frac{\partial \mathbf{e}'_y}{\partial \mathbf{d}_j^T} \right) \\ &\quad + \frac{3}{|\mathbf{e}'_x + \mathbf{e}'_y|^5} \left[ (\mathbf{e}'_x + \mathbf{e}'_y)^T \left( \frac{\partial \mathbf{e}'_x}{\partial \mathbf{d}_k^T} + \frac{\partial \mathbf{e}'_y}{\partial \mathbf{d}_k^T} \right) \otimes (\mathbf{e}'_x + \mathbf{e}'_y) \otimes (\mathbf{e}'_x + \mathbf{e}'_y) \right] \left( \frac{\partial \mathbf{e}'_x}{\partial \mathbf{d}_j^T} + \frac{\partial \mathbf{e}'_y}{\partial \mathbf{d}_j^T} \right) \end{aligned} \quad (\text{B18})$$

$$\frac{\partial^2 \mathbf{e}_y'}{\partial \mathbf{d}_j^T \partial \mathbf{d}_k^T} = \frac{\partial \mathbf{e}_y'}{\partial \mathbf{d}_j^T} \times \frac{\partial \mathbf{e}_z}{\partial \mathbf{d}_k^T} + \frac{\partial \mathbf{e}_y'}{\partial \mathbf{d}_k^T} \times \frac{\partial \mathbf{e}_z}{\partial \mathbf{d}_j^T} + \mathbf{e}_y' \times \frac{\partial^2 \mathbf{e}_z}{\partial \mathbf{d}_j^T \partial \mathbf{d}_k^T} \quad (\text{B19})$$

$$\begin{aligned} \frac{\partial^2 \mathbf{e}_z}{\partial \mathbf{d}_j^T \partial \mathbf{d}_k^T} = & \left[ \frac{\mathbf{I}}{|\mathbf{v}_{12} \times \mathbf{v}_{13}|} - \frac{(\mathbf{v}_{12} \times \mathbf{v}_{13}) \otimes (\mathbf{v}_{12} \times \mathbf{v}_{13})}{|\mathbf{v}_{12} \times \mathbf{v}_{13}|^3} \right] \left( \frac{\partial \mathbf{v}_{12}}{\partial \mathbf{d}_j^T} \times \frac{\partial \mathbf{v}_{13}}{\partial \mathbf{d}_k^T} + \frac{\partial \mathbf{v}_{12}}{\partial \mathbf{d}_k^T} \times \frac{\partial \mathbf{v}_{13}}{\partial \mathbf{d}_j^T} \right) \\ & - \left( \frac{\partial \mathbf{v}_{12}}{\partial \mathbf{d}_j^T} \times \mathbf{v}_{13} + \mathbf{v}_{12} \times \frac{\partial \mathbf{v}_{13}}{\partial \mathbf{d}_j^T} \right) \otimes \left[ \frac{(\mathbf{v}_{12} \times \mathbf{v}_{13})^T}{|\mathbf{v}_{12} \times \mathbf{v}_{13}|^3} \left( \frac{\partial \mathbf{v}_{12}}{\partial \mathbf{d}_k^T} \times \mathbf{v}_{13} + \mathbf{v}_{12} \times \frac{\partial \mathbf{v}_{13}}{\partial \mathbf{d}_k^T} \right) \right] \\ & - \frac{(\mathbf{v}_{12} \times \mathbf{v}_{13})}{|\mathbf{v}_{12} \times \mathbf{v}_{13}|^3} \otimes \left[ \left( \frac{\partial \mathbf{v}_{12}}{\partial \mathbf{d}_j^T} \times \mathbf{v}_{13} + \mathbf{v}_{12} \times \frac{\partial \mathbf{v}_{13}}{\partial \mathbf{d}_j^T} \right)^T \left( \frac{\partial \mathbf{v}_{12}}{\partial \mathbf{d}_k^T} \times \mathbf{v}_{13} + \mathbf{v}_{12} \times \frac{\partial \mathbf{v}_{13}}{\partial \mathbf{d}_k^T} \right) \right] \\ & - \left( \frac{\partial \mathbf{v}_{12}}{\partial \mathbf{d}_k^T} \times \mathbf{v}_{13} + \mathbf{v}_{12} \times \frac{\partial \mathbf{v}_{13}}{\partial \mathbf{d}_k^T} \right) \otimes \left[ \frac{(\mathbf{v}_{12} \times \mathbf{v}_{13})^T}{|\mathbf{v}_{12} \times \mathbf{v}_{13}|^3} \left( \frac{\partial \mathbf{v}_{12}}{\partial \mathbf{d}_j^T} \times \mathbf{v}_{13} + \mathbf{v}_{12} \times \frac{\partial \mathbf{v}_{13}}{\partial \mathbf{d}_j^T} \right) \right] \\ & + \frac{3(\mathbf{v}_{12} \times \mathbf{v}_{13})}{|\mathbf{v}_{12} \times \mathbf{v}_{13}|^5} \otimes \left[ (\mathbf{v}_{12} \times \mathbf{v}_{13})^T \left( \frac{\partial \mathbf{v}_{12}}{\partial \mathbf{d}_j^T} \times \mathbf{v}_{13} + \mathbf{v}_{12} \times \frac{\partial \mathbf{v}_{13}}{\partial \mathbf{d}_j^T} \right) \right] \otimes \left[ (\mathbf{v}_{12} \times \mathbf{v}_{13})^T \left( \frac{\partial \mathbf{v}_{12}}{\partial \mathbf{d}_k^T} \times \mathbf{v}_{13} + \mathbf{v}_{12} \times \frac{\partial \mathbf{v}_{13}}{\partial \mathbf{d}_k^T} \right) \right] \end{aligned}$$

(B20)

$$\frac{\partial^2 \mathbf{e}_y}{\partial \mathbf{d}_j^T \partial \mathbf{d}_k^T} = \frac{\partial^2 \mathbf{e}_z}{\partial \mathbf{d}_j^T \partial \mathbf{d}_k^T} \times \mathbf{e}_x + \mathbf{e}_z \times \frac{\partial^2 \mathbf{e}_x}{\partial \mathbf{d}_j^T \partial \mathbf{d}_k^T} + \frac{\partial \mathbf{e}_z}{\partial \mathbf{d}_j^T} \times \frac{\partial \mathbf{e}_x}{\partial \mathbf{d}_k^T} + \frac{\partial \mathbf{e}_z}{\partial \mathbf{d}_k^T} \times \frac{\partial \mathbf{e}_x}{\partial \mathbf{d}_j^T} \quad (\text{B21})$$

$$\frac{\partial^2 \mathbf{p}_i}{\partial \mathbf{n}_{gi}^T} = \begin{bmatrix} \frac{\partial^2 \mathbf{p}_i}{\partial p_{i,n_i}^2} & \frac{\partial^2 \mathbf{p}_i}{\partial p_{i,n_i} \partial p_{i,m_i}} \\ \frac{\partial^2 \mathbf{p}_i}{\partial p_{i,m_i} \partial p_{i,n_i}} & \frac{\partial^2 \mathbf{p}_i}{\partial p_{i,m_i}^2} \end{bmatrix} \quad (\text{B22})$$

$$\frac{\partial^2 \mathbf{p}_i}{\partial p_{i,n_i}^2} = \begin{Bmatrix} \frac{\partial^2 p_{i,X}}{\partial p_{i,n_i}^2} \\ \frac{\partial^2 p_{i,Y}}{\partial p_{i,n_i}^2} \\ \frac{\partial^2 p_{i,Z}}{\partial p_{i,n_i}^2} \end{Bmatrix}, \quad \frac{\partial^2 \mathbf{p}_i}{\partial p_{i,m_i}^2} = \begin{Bmatrix} \frac{\partial^2 p_{i,X}}{\partial p_{i,m_i}^2} \\ \frac{\partial^2 p_{i,Y}}{\partial p_{i,m_i}^2} \\ \frac{\partial^2 p_{i,Z}}{\partial p_{i,m_i}^2} \end{Bmatrix}, \quad \frac{\partial^2 \mathbf{p}_i}{\partial p_{i,n_i} \partial p_{i,m_i}} = \begin{Bmatrix} \frac{\partial^2 p_{i,X}}{\partial p_{i,n_i} \partial p_{i,m_i}} \\ \frac{\partial^2 p_{i,Y}}{\partial p_{i,n_i} \partial p_{i,m_i}} \\ \frac{\partial^2 p_{i,Z}}{\partial p_{i,n_i} \partial p_{i,m_i}} \end{Bmatrix} \quad (\text{B23a,b,c})$$

$$\frac{\partial^2 p_{i,l_i}}{\partial p_{i,n_i}^2} = -\frac{1}{p_{i,l_i}} - \frac{p_{i,n_i}^2}{p_{i,l_i}^3}, \quad \frac{\partial^2 p_{i,l_i}}{\partial p_{i,m_i}^2} = -\frac{1}{p_{i,l_i}} - \frac{p_{i,m_i}^2}{p_{i,l_i}^3}, \quad \frac{\partial^2 p_{i,l_i}}{\partial p_{i,n_i} \partial p_{i,m_i}} = -\frac{p_{i,n_i} p_{i,m_i}}{p_{i,l_i}^3} \quad (\text{B24a,b,c})$$

where,  $p_{i,l_i}$  is the biggest component of Vector  $\mathbf{p}_i$  in the global coordinate axes X,Y,Z directions; the second derivatives of other two components with respect to the vectorial rotational variables are equal to zero.

$$p_{i,l_i} = s_1 \sqrt{1 - p_{i,n_i}^2 - p_{i,m_i}^2} \quad i = 1, 2, 3 \quad (\text{B25})$$

$s_1$  is equal to 1 or -1. In an incremental solution procedure, it has the same sign as  $p_{i,l_i}$  of the last incremental step, and its value will be updated after each incremental loading step.



## ACKNOWLEDGMENTS

This work is financed by the support program of the National Twelfth Five-Year-Plan for Science & Technology (2012BAJ13B04).

## REFERENCES

- [1] Jeon, H.M., Lee, Y.Y., Lee, P.S. and Bathe, K.J., "The MITC3+ Shell Element in Geometric Nonlinear Analysis", *Computers and Structures*, 2015, Vol. 146, pp. 91-104.
- [2] Lee, Y.Y., Lee, P.S., and Bathe, K.J., "The MITC3+ Shell Element and its Performance", *Computers and Structures*, 2014, Vol. 138, pp. 12-23.
- [3] Jeon, H.M., Lee, P.S. and Bathe, K.J., "The MITC3 Shell Finite Element Enriched by Interpolation Covers", *Computers and Structures*, 2014, Vol. 134, pp. 128-142.
- [4] Lee, P. S. and Bathe, K. J., "Development of MITC Isotropic Triangular Shell Finite Elements", *Computers and Structures*, 2004, Vol. 82, No. 11-12, pp. 945-962.
- [5] Lee, P.S. and Bathe, K. J., "The Quadratic MITC Plate and MITC Shell Elements in Plate Bending", *Advances in Engineering Software*, 2010, Vol. 41, No. 5, pp. 712-728.
- [6] Laulusa, A., Bauchau, O.A., Choi, J.Y., Tan, V.B.C., and Li, L., "Evaluation of Some Shear Deformable Shell Elements", *International Journal of Solids and Structures*, 2006, Vol. 43, No. 17, pp. 5033-5054.
- [7] Chapelle, D. and Suarez, I.P., "Detailed Reliability Assessment of Triangular MITC Elements for Thin Shells", *Computers and Structures*, 2008, Vol. 86,, No. 23-24, pp. 2192-2202.
- [8] Lee, P.S., Noh, H.C. and Bathe, K.J., "Insight into 3-node Triangular Shell Finite Elements: The Effects of Element Isotropy and Mesh Patterns", *Computers and Structures*, 2007, Vol. 85, No. 7-8, pp. 404-418.
- [9] Mohan, P. and Kapania, R.K., "Updated Lagrangian Formulation of a Flat Triangular Element for Thin Laminated Shells", *AIAA Journal*, 1998, Vol. 36, No. 2, pp. 273-281.
- [10] Providasa, E. and Kattis, M.A., "An Assessment of Two Fundamental Flat Triangular Shell Elements with drilling Rotations", *Computers and Structures*, 2000, Vol. 77, No. 2, pp. 129-139.
- [11] Khosravi, P., Ganesan, R. and Sedaghati, R., "Corotational Non-linear Analysis of Thin Plates and Shells using a New Shell Element", *International Journal for Numerical Methods in Engineering*, 2007, Vol. 69, No. 4, pp. 859-885.
- [12] Khosravi, P., Ganesan, R. and Sedaghati, R., "An Efficient Facet Shell Element for Corotational Nonlinear Analysis of Thin and Moderately Thick Laminated Composite Structures", *Computers and Structures*, 2008, Vol. 86, No. 9, pp. 50-858.
- [13] Carpenter, N., Stolarski, H. and Belytschko, T., "Improvements in 3-Node Triangular Shell Elements", *International Journal for Numerical Methods in Engineering*, 1986, Vol. 23, No. 9, pp. 1643-1667.
- [14] Sabourin, F. and Brunet, M., "Analysis of Plates and Shells with a Simplified 3-node Triangular Element", *Thin-Walled Structures*, 1995, Vol. 21, No. 3, pp. 209-223.
- [15] Sabourin, F., and Brunet, M., "Detailed Formulation of the Rotation-free Triangular Element "S3" for General Purpose Shell Analysis", *Engineering Computations*, 2006, Vol. 23, No. 5-6, pp. 469-502.
- [16] Oñate, E. and Zárte, F., "Rotation-free Triangular Plate and Shell Elements", *International Journal for Numerical Methods in Engineering*, 2000, Vol. 47, No. 1-3, pp. 557-603.
- [17] Flores, F.G. and Oñate, E., "A Basic Thin Shell Triangle with Only Translational DOFs Large Strain Plasticity", *International Journal for Numerical Methods in Engineering*, 2001, Vol. 51, No. 1, pp. 57-83.

- [18] Oñate, E. and Flores, F.G., “Advances in the Formulation of the Rotation-free Basic Shell Triangle”, *Computer Methods in Applied Mechanics and Engineering*, 2005, Vol. 194, No. 21-24, pp. 2406–2443.
- [19] Flores, F.G. and Oñate, E., “Improvements in the Membrane Behaviour of the Three Node Rotation-free BST Shell Triangle using an Assumed Strain Approach”, *Computer Methods in Applied Mechanics and Engineering*, 2005, Vol. 194, No. 6-8, pp. 907–932.
- [20] Oñate, E. and Zárte, F., “Extended Rotation-free Plate and Beam Elements with Shear Deformation Effects”, *International Journal for Numerical Methods in Engineering*, 2010, Vol. 83, No. 2, pp. 196-227.
- [21] Zárte, F. and Oñate, E., “Extended Rotation-free Shell Triangles with Transverse Shear Deformation Effects”, *Computational Mechanics*, 2012, Vol. 49, No. 4, pp. 487-503.
- [22] Stolarski, H., Gilmanov, A. and Sotiropoulos, F., “Nonlinear Rotation-free Three-node Shell Finite Element Formulation”, *International Journal for Numerical Methods in Engineering* 2013, Vol. 95, No. 9, pp. 740-770.
- [23] Kabir, H. R. H., “A Shear-locking Free Robust Isoparametric 3-node Triangular Element for General Shells”, *Computers and Structures*, 1994, Vol. 51, No. 4, pp. 425-436.
- [24] Wu, S., Li, G.Y. and Belytschko, T., “A DKT Shell Element for Dynamic Large Deformation Analysis”, *Communications in Numerical Methods in Engineering*, 2005, Vol. 21, No. 11, pp. 651-674.
- [25] Kuznetsov, V.V. and Levyakov, S.V., “Geometrically Nonlinear Shell Finite Element based on the Geometry of a Planar Curve”, *Finite Elements in Analysis and Design*, 2008, Vol. 44, No. 8, pp. 450-461.
- [26] Kolahi, A.S. and Crisfield, M.A., “A Large-strain Elasto–plastic Shell Formulation using the Morley Triangle”, *International Journal for Numerical Methods in Engineering*, 2001, Vol. 52, No. 8, pp. 829–849.
- [27] Providas, E. and Kattis, M.A., “A Simple Finite Element Model for the Geometrically Nonlinear Analysis of Thin Shells”, *Computational Mechanics*, 1999, Vol. 24, No. 2, pp. 127-137.
- [28] Carpenter, N. and Stolarski, H. and Belytschko, T., “A Flat Triangular Shell Element with Improved Membrane Interpolation”, *Communications in Applied Numerical Methods*, 1985, Vol. 1, No. 4, pp. 161-168.
- [29] Fish, J. and Belytschko, T., “Stabilized Rapidly Convergent 18-degrees-of-freedom Flat Shell Triangular Element”, *International Journal for Numerical Methods in Engineering*, 1992, Vol. 33, No. 1, pp. 149-162.
- [30] Allman, D.J., “On the assumed displacement-fields of a shallow curved shell finite-element”, *Communications in Numerical Methods in Engineering*, 1995, Vol. 11, No. 2, pp. 159-166.
- [31] To, C. W. S. and Wang, B., “Hybrid Strain-based Three-node Flat Triangular Laminated Composite Shell Elements”, *Finite Elements in Analysis and Design*, 1998, Vol. 28, No. 3, pp. 177-207.
- [32] Fajman, P., “New Triangular Plane Element with Drilling Degrees of Freedom”, *Journal of Engineering Mechanics-ASCE*, 2002, Vol. 128, No. 4, pp. 413-418.
- [33] Cai, Y.C. and Atluri, S.N., “Large Rotation Analyses of Plate/Shell Structures based on the Primal Variational Principle and a Fully Nonlinear Theory in the Updated Lagrangian Co-rotational Reference Frame”, *CMES-Computer Modeling in Engineering & Sciences*, 2012, Vol. 83, No. 3, pp. 249-273.
- [34] Zhang, Y.X. and Cheung, Y.K., “A Refined Non-linear Non-conforming Triangular Plate/Shell Element”, *International Journal for Numerical Methods in Engineering*, 2003, Vol. 56, No. 15, pp. 2387–2408.
- [35] Poulsen, P. and Damkilde, L., “A Flat Triangular Shell Element with Loof Nodes”, *International Journal for Numerical Methods in Engineering*, 1996, Vol. 39, No. 22, pp.

- 3867-3887.
- [36] Campello, E. M. B., Pimenta, P. M. and Wriggers, P., "A Triangular Finite Shell Element based on a Fully Nonlinear Shell Formulation", *Computational Mechanics*, 2003, Vol. 31, No. 6, pp. 505-518.
  - [37] Yang, H. T. Y., Saigal, S., Masud, A. and Kapania, R. K., "Survey of Recent Shell Finite Elements", *International Journal for Numerical Methods in Engineering*, 2000, Vol. 47, No. 1-3, pp. 101-127.
  - [38] Reissner, E., "A Note on Variational Theorems in Elasticity", *International Journal of Solids and Structures*, 1965, Vol. 1, No. 1, pp. 93-95.
  - [39] Hughes, T. J. R. and Brezzi, F., "On Drilling Degrees of Freedom", *Computer Methods in Applied Mechanics and Engineering*, 1989, Vol. 72, No. 1, pp. 105-121.
  - [40] Hughes, T. J. R., Masud, A. and Harari, I., "Numerical Assessment of Some Membrane Elements with Drilling Degrees of Freedom", *Computers and Structures*, 1995, Vol. 55, No. 2, pp. 297-314.
  - [41] Hughes, T. J. R., Masud, A. and Harari, I., "Dynamic Analysis with Drilling Degrees of Freedom", *International Journal for Numerical Methods in Engineering*, 1995, Vol. 38, No. 19, pp. 3193-3210.
  - [42] MacNeal, R.H., "Derivation of Element Stiffness Matrices by Assumed Strain Distribution", *Nuclear Engineering and Design*, 1982, Vol. 70, No. 1, pp. 3-12.
  - [43] Liu, M. L. and To, C. W. S., "Hybrid Strain-based 3-node Flat Triangular Shell Elements", 1. Nonlinear-theory and Incremental Formulation", *Computers and Structures*, 1995, Vol. 54, No. 6, pp. 1031-1056.
  - [44] Liu, M. L. and To, C. W. S., "A Further Study of Hybrid Strain-based Three-node Flat Triangular Shell Elements", *Finite Elements in Analysis and Design*, 1998, Vol. 31, No. 2, pp. 135-152.
  - [45] To, C. W. S. and Wang, B., "Hybrid Strain-based Three-node Flat Triangular Laminated Composite Shell Elements", *Finite Elements in Analysis and Design*, 1998, Vol. 28, No. 3, pp. 177-207.
  - [46] Ibrahimbegovic, A. and Wilson, E.L., "A Modified Method of Incompatible Modes", *Communications in Applied Numerical Methods*, 1991, Vol. 7, No. 3, pp. 187-194.
  - [47] Bischoff, M. and Romero, I., "A Generalization of the Method of Incompatible Modes", *International Journal for Numerical Methods in Engineering*, 2007, Vol. 69, No. 9, pp. 1851-1868.
  - [48] Liu, W.K., Belytschko, T., Ong, J. S. J. and Law, S. E., "Use of Stabilization Matrices in Non-linear Analysis", *Engineering Computations*, 1985, Vol. 2, No. 1, pp. 47-55.
  - [49] Belytschko, T., Wong, B.L. and Stolarski, H., "Assumed Strain Stabilization Procedure for the 9-node Lagrange Shell Element", *International Journal for Numerical Methods in Engineering*, 1989, Vol. 28, No. 2, pp. 385-414.
  - [50] Liu, W. K., Ong, J. S. J. and Uras, R. A., "Finite-element Stabilization Matrices - A Unification Approach", *Computer Methods in Applied Mechanics and Engineering*, 1985, Vol. 53, No. 1, pp. 13-46.
  - [51] Belytschko, T., Tsay, C.S. and Liu, W.K., "A Stabilization Matrix for the Bilinear Mindlin Plate Element", *Computer Methods in Applied Mechanics and Engineering*, 1981, Vol. 29, No. 3, pp. 313-327.
  - [52] Masud, A., Tham, C.L., and Liu, W.K., "A Stabilized 3-D Co-rotational Formulation for Geometrically Nonlinear Analysis of Multi-layered Composite Shells", *Computational Mechanics* 2000, Vol. 26, No. 1, pp. 1-12.
  - [53] Belytschko, T. and Leviathan, I., "Physical Stabilization of the 4-node Shell Element with One-point Quadrature", *Computer Methods in Applied Mechanics and Engineering*, 1994, Vol. 113, No. 3-4, pp. 321-350.

- [54] Nguyen-Xuan, H., Liu, G. R. and Thai-Hoang, C. and Nguyen-Thoi, T., "An Edge-based Smoothed Finite Element Method (ES-FEM) with Stabilized Discrete Shear Gap Technique for Analysis of Reissner-Mindlin Plates", *Computer Methods in Applied Mechanics and Engineering*, 2010, Vol. 199, No. 9-12, pp. 471-489.
- [55] Argyris, J. H., Papadrakakis, M., Apostolopoulou, C. and Koutsourelakis, S., "The TRIC Shell Element: Theoretical and Numerical Investigation", *Computer Methods in Applied Mechanics and Engineering* 2000, Vol. 182, No. 1-2, pp. 217-245.
- [56] Ibrahimbegovic, A., "Finite Elastoplastic Deformations of Space-Curved Membranes", *Computer Methods in Applied Mechanics and Engineering*, 1994, Vol. 119, No. 3-4, pp. 371-394.
- [57] El-Metwally, S. E., El-Shahhat, A. M. and Chen, W. F., "3-D Nonlinear-analysis of R/C Slender Columns", *Computers and Structures*, 1990, Vol. 37, No. 5, pp. 863-872.
- [58] Izzuddin, B. A. and Elnashai, A.S., "Adaptive Space Frame Analysis .2. AD Distributed Plasticity Approach", *Proceedings of the Institution of Civil Engineers-Structures and Buildings*, 1993, Vol. 99, No. 3, pp. 317-326.
- [59] Spacone, E., Filippou, F.C. and Taucer, F.F., "Fibre Beam-column Model for Non-linear Analysis of R/C Frames", 1. Formulation, *Earthquake Engineering & Structural Dynamics*, 1996, Vol. 25, No. 7, pp. 711-725.
- [60] Izzuddin, B.A. and Lloyd Smith, D., "Large-displacement Analysis of Elastoplastic Thin-walled Frames" 1. Formulation and Implementation, *Journal of Structural Engineering-ASCE*, 1996, Vol. 122, No. 8, pp. 905-914.
- [61] Crisfield, M. A., "Nonlinear Finite Element Analysis of Solid and Structures", Vol 1: Essentials. Wiley: Chichester, 1991.
- [62] Becker, M. and Hackenberg, H. P., "A Constitutive Model for Rate Dependent and Rate Independent inelasticity, Application to IN718, *International Journal of Plasticity*, 2011, Vol. 27, No. 4, pp. 596-619.
- [63] Simo, J. C. and Hughes, T. J. R., "Computational Inelasticity. Springer: New York, 1998.
- [64] Khan, A. S. and Huang, S. J., "Continuum Theory of Plasticity. John Wiley & Sons, Inc: New York. 1995; P94.
- [65] Izzuddin, B.A. and Liang, Y., "Bisector and Zero-macrospin Co-rotational Systems for Shell Elements", *International Journal for Numerical Methods in Engineering*, 2015, Vol. 105, No. 4, pp. 286-320.
- [66] Nour-Omid, B. and Rankin, C.C., "Finite Rotation Analysis and Consistent Linearization using Projectors", *Computer Methods in Applied Mechanics and Engineering*, 1991, Vol. 93, No. 3, pp. 353-384.
- [67] Simo, J. C. and Tarnow, N. "A New Energy and Momentum Conserving Algorithm for the Non-linear Dynamics of Shells", *International Journal for Numerical Methods in Engineering*, 1994, Vol. 37, No. 15, pp. 2527-2549.
- [68] Simo, J.C., Rifai, M.S. and Fox, D.D., "On a Stress Resultant Geometrically Exact Shell-model .6. Conserving Algorithms for Nonlinear Dynamics", *International Journal for Numerical Methods in Engineering*, 1992, Vol. 34, No. 1, pp. 117-164.
- [69] Tan, X. G. and Vu-Quoc, L., "Efficient and Accurate Multilayer Solid-shell Element: Nonlinear Materials at Finite Strain", *International Journal for Numerical Methods in Engineering* 2005, Vol. 63, No. 15, pp. 2124-2170.
- [70] Vu-Quoc, L. and Tan, X. G., "Optimal Solid Shells for Nonlinear Analyses of Multilayer Composites", Part II: Dynamics, *Computer Methods in Applied Mechanics and Engineering*, 2003, Vol. 192, No. 9-10, pp. 1017-1059.
- [71] Li, Z. X., Zhuo, X., Vu-Quoc, L., Izzuddin, B.A. and Wei, H.Y., "A 4-node Co-rotational Quadrilateral Elasto-plastic Shell Element using Vectorial Rotational Variables", *International Journal for Numerical Methods in Engineering*, 2013, Vol. 95, No. 3, pp. 181-211.

- [72] Li, Z. X., Xiang, Y., Izzuddin, B. A., Vu-Quoc, L., Zhuo, X. and Zhang, C.J., "A 6-node Co-rotational Triangular Elasto-plastic Shell Element", *Computational Mechanics*, 2015, Vol. 55, No. 5, pp. 837-859.
- [73] MacNeal, R. H. and Harder, R. L., "Proposed Standard Set of Problems to Test Finite Element Accuracy", *Finite Elements in Analysis and Design*, 1985, Vol. 1, No. 1, pp. 3-20.
- [74] Buechter, N. and Ramm, E., "Shell Theory Versus Degeneration - A Comparison in Large Rotation Finite-element Analysis", *International Journal for Numerical Methods in Engineering*, 1992, Vol. 34, No. 1, pp. 39-59.
- [75] Simo, J. C., Fox, D.D. and Rifai, M. S., "On a Stress Resultant Geometrically Exact Shell Model", Part III: Computational Aspects of the Nonlinear Theory", *Computer Methods in Applied Mechanics and Engineering*, 1990, Vol. 79, No. 1, pp. 21-70.
- [76] Jiang, L. and Chernuka, M.W., "A Simple 4-noded Corotational Shell Element for Arbitrarily Large Rotations", *Computers and Structures*, 1994, Vol. 53, No. 5, pp. 1123-1132.
- [77] Sze, K.Y., Chan, W.K. and Pian, T. H. H., "An 8-node Hybrid-stress Solid-shell Element for Geometric Nonlinear Analysis of Elastic Shells", *International Journal for Numerical Methods in Engineering*, 2000, Vol. 55, No. 7, pp. 853-878.
- [78] Eberlein, R. and Wriggers, P., "Finite Element Concepts for Finite Elastoplastic Strains and Isotropic Stress Response in Shells: Theoretical and Computational Analysis", *Computer Methods in Applied Mechanics and Engineering*, 1999, Vol. 171, No. 3-4, pp. 243-279.
- [79] Betsch, P. and Stein, E., "Numerical Implementation of Multiplicative Elasto-plasticity into Assumed Strain Elements with Application to Shells at Large Strains", *Computer Methods in Applied Mechanics and Engineering*, 1999, Vol. 179, No. 3-4, pp. 215-245.
- [80] Valente, R. A. F., Parente, M. P. L., Jorge, R. M. N., de Sa, J. M. A. C. and Gracio, J. J., "Enhanced Transverse Shear Strain Shell Formulation Applied to Large Elasto-plastic Deformation Problems", *International Journal for Numerical Methods in Engineering*, 2005, Vol. 62, No. 10, pp.1360-1398.
- [81] Miehe, C., "A Theoretical and Computational Model for Isotropic Elastoplastic Stress Analysis in Shells at Large Strains", *Computer Methods in Applied Mechanics and Engineering*, 1998, Vol. 155, No. 3-4, pp. 193-233.
- [82] Izzuddin, B. A., "An Enhanced Co-rotational Approach for Large Displacement Analysis of Plates", *International Journal for Numerical Methods in Engineering*, 2005, Vol. 64, No. 10, pp. 1350-1374.
- [83] Li, Z. X., "A Co-rotational Formulation for 3D Beam Element using Vectorial Rotational Variables", *Computational Mechanics*, 2007, Vol. 39, No. 3, pp. 309-322.
- [84] Li, Z. X., and Vu-Quoc, L., "A Mixed Co-rotational 3D Beam Element Formulation for Arbitrarily Large Rotations", *Advanced Steel Construction*, 2010, Vol. 6, No. 2, pp. 767-787.
- [85] Li, Z. X., "Bionics and Computational Theory using Advanced Finite Element Methods", Science Press: Beijing, 2009.
- [86] Tessler, A., and Hughes, T. J. R., "A 3-node Mindlin Plate Element with Improved Transverse-shear", *Computer Methods in Applied Mechanics and Engineering*, 1985, Vol. 50, No. 1, pp. 71-101.
- [87] MacNeal, R. H., "Finite Elements: Their Design and Performance", Marcel Dekker Inc. New York, 1993, pp. 369-417.



# SEISMIC PERFORMANCE ANALYSIS OF A RESILIENT PRESTRESSED STEEL FRAME WITH INTERMEDIATE COLUMN CONTAINING FRICTION DAMPERS

Yanxia Zhang<sup>1\*</sup>, Anran Liu<sup>2</sup>, Ailin Zhang<sup>3</sup> and Xuechun Liu<sup>4</sup>

<sup>1</sup> Professor, Beijing Advanced Innovation Center for Future Urban Design, Beijing University of Civil Engineering and Architecture, Beijing 100044, China

<sup>2</sup> Postgraduate, School of Civil and Transportation Engineering, Beijing University of Civil Engineering and Architecture, Beijing 100044, China

<sup>3</sup> Professor, School of Civil and Transportation Engineering, Beijing University of Civil Engineering and Architecture, Beijing 100044, Beijing Engineering Research Center of High-Rise and Large-Span Prestressed Steel Structure, Beijing University of Technology, Beijing 100124, China

<sup>4</sup> Associate Professor, Beijing Engineering Research Center of High-Rise and Large-Span Prestressed Steel Structure, Beijing University of Technology, Beijing 100124, China

\*(Corresponding author: E-mail: zhangyanxia@bucea.edu.cn)

Received: 18 August 2015; Revised: 13 June 2016; Accepted: 3 August 2016

---

**ABSTRACT:** A resilient prestressed steel frame system with intermediate columns containing friction dampers (ICRPSF) has been proposed for the use in a large span, seismically active regions and a high-value building. Seismic performance analysis of overall structure of a resilient prestressed steel frame with intermediate column friction damper are analyzed, compared with the resilient performance of a resilient prestressed steel frame (RPSF) with beam web friction damper. The results show that an ICRPSF effectively controls the story drift, dissipates more energy through the intermediate column friction damper (ICFD) and curbs the plastic development of the component. This system has a small post-seismic residual story drift and its structure demonstrates excellent self-centering capability.

**Keywords:** Intermediate column, friction dampers, resilient prestressed steel frame, seismic performance analysis, energy dissipation

**DOI:** 10.18057/IJASC.2017.13.3.3

---

## 1. INTRODUCTION

Resilient prestressed steel frame structures (hereafter known as RPSF) can reduce structural damage, reduce or eliminate residual deformations, and is easy to repair after a strong earthquake. Therefore, it has caused researchers' widespread attention, and has been extensively studied. The connection for RPSF used post-tensioned steel strands being with bolted top and seat angles was proposed by Ricles et al. [1]. Garlock et al. [2,3] investigated the connection behavior through experiments and the design procedures of post-tensioned frame systems has been put forward. Christopoulos et al. [4] invented a post-tensioned energy dissipating connection with post-tensioned high-strength bars, and investigated connection performance analytically and experimentally. Rojas et al. [5] developed a connection which adopted friction devices on the top and bottom flanges of the beam and post-tensioned high strength strands running parallel to the beam. In order to avoid interference with the floor slab, Wolski et al. [6] developed another the flange friction device which only attached to the bottom flange of the beam. Tsai et al [7] presented experimental and analytical studies on the connection with bolted web friction devices (WFD). Lin et al. [8,9] carried out an experimental study of self-centering moment-resisting steel frame (SC-MRF) with WFD connections under the action of design basis earthquake and maximum considered earthquake ground motions. Zhang et al. performed the experiments, finite element analysis and theory analysis of the self-centering connections with the WFDs [10], as well as investigated the dynamic behavior through the time-history analysis of integral SC-MRFs with finite element software

ABAQUS [11]. Thereafter, Zhang et al. [12] proposed a prefabricated post-tensioned self-centering beam-column connection using a bolted web friction device, conducted the low-cycle loading experiments, carried out relevant theoretical analyses and investigated the seismic performance of the connection. Therefore, the pseudo-dynamic test towards the resilient prefabricated prestressed steel frame has been performed by Zhang et al.[13]. In the research of the large-span resilient steel frame, the resilient prestressed frame with intermediate columns containing friction damper (hereafter known as ICRPSF) has been proposed by Zhang et al., which both the static pushover test and the finite element analysis toward the first 2 floor plane frame have been carried out to investigate the working behavior of intermediate columns and the hysteretic performance of ICRPSF [14]. In this thesis, the finite element model of an eight-floor ICRPSF structure is built up, and the comparative analysis with the RPSF used beam web friction dampers is performed in the consideration of the seismic performance. The properties of the ICRPSF, such as the base shear, the story drift, the residual story drift, the energy dissipation capability and the post-seismic structure recovery performance, are investigated.

## 2. SYSTEM STRUCTURE OF THE ICRPSF

A plane steel frame system is used to illustrate the detailed structure of the system, as shown in Figure 1 and Figure 2. ICRPSF is composed of RPSF with web friction damper and the intermediate column containing friction damper (ICFD). ICFD can be divided into three parts: the upper column, the lower column, and the damper [15]. The upper and lower columns are welded to the floor beams or column base, and the haunches are set up at the connecting ends to increase the strength of the joints. The upper and lower columns are connected through the damper. The damper includes a T-shaped steel plate that used to connect with the upper column and two L-shaped steel plates that used to connect the lower column. In addition, there are brass plates sandwiched between the L-shaped and T-shaped plates through high-strength bolts. An elongated hole in the T-shaped plate allows the ends of the upper and lower columns to move relatively under an earthquake. And therefore, the high-strength bolts can dissipate energy by friction. To enable easy replacement of the damper following an earthquake, the T-shaped and L-shaped steel plates are connected to the upper and lower columns with high-strength bolts, respectively.



Figure 1. Photograph of ICRPSF



Figure 2. Details of the ICFD

## 3. IMPLEMENTATION OF THE ICFD HYSTERESIS PERFORMANCE IN THE STRUCTURAL ANALYSIS

A group of friction-sliding tests are designed to analyze the friction damper under repeated loads, as shown in Figure 3. The force-slippage hysteresis curve of the friction damper is obtained, which shape is approaching an ideal rectangle, as shown in Figure 4.



In the overall structural model of the ICRPSF, a connector is defined to simulate the force- slippage relation of the intermediate column, which the rectangular hysteresis curve of the ICFD is implemented. The connector spring unit is created in the interaction module of the software ABAQUS, and the translator connector is used to constrain all rotational degrees of freedom (DOFs), as shown in Figure 5. The translational DOF in the U1 direction is defined as the direction that the slip of the friction damper occurs. Simultaneously, translational DOFs in the other 2 directions are constrained, and the input is the friction  $F_f$ . The connector slippage and the connector force in the corresponding direction are monitored to obtain the force- slippage hysteresis curve of the friction damper, as shown in Figure 6. The data in Figure 4 and Figure 6 show that the force-slippage hysteresis curve obtained from the finite element analysis (FEA) is consistent with the curve obtained from the test.



Figure 3. Friction-sliding Test

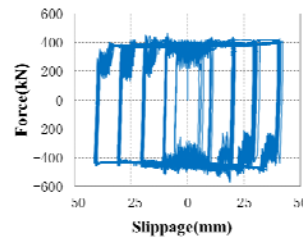


Figure 4. Hysteresis Curve of Friction Damper Test

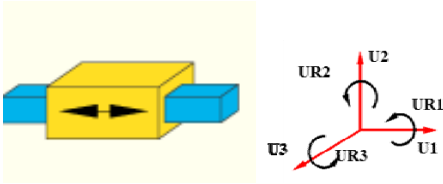


Figure 5. Schematic of Translator Connector

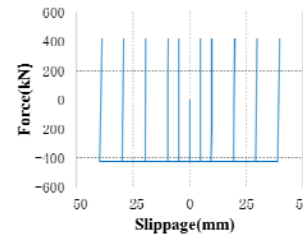


Figure 6. Force- Slippage Hysteresis Curve from FEA

#### 4. SAMPLE STRUCTURE AND MODAL ANALYSIS RESULTS OF 2 TYPES OF STRUCTURES

##### 4.1. Sample Structure

Sample frame structure has 8 floors. The height of the first floor is 3.9m, and the height is 3.6m for 2-8 floors. There are 3 spans widthwise and 5 spans lengthwise, and each span measures 12m. The plane diagram of the structure is shown in Figure 7. The red sections shown Figure 7 used ICRPSF for floors 1-6, and the RPSF for floors 7-8. Meanwhile, the frame adopted the hinge system except the red sections. Three-dimension finite element model of ICRPSF is shown in Figure 8. The fortification strength was 8 degree. The floor constant load was  $7.0\text{kN/m}^2$ , the floor variable load was  $2.0\text{kN/m}^2$ , and the roof variable load was  $0.5\text{kN/m}^2$ . The main parameters of the structure are defined as follows. For the dimensions of the frame, the box column is  $650\text{mm} \times 650\text{mm} \times 32\text{mm} \times 32\text{mm}$ , the H-shaped rigid beam is  $750\text{mm} \times 350\text{mm} \times 24\text{mm} \times 30\text{mm}$ , the box hinge column is  $500\text{mm} \times 500\text{mm} \times 24\text{mm} \times 24\text{mm}$ , the H-shaped hinge beam is  $650\text{mm} \times 300\text{mm} \times 12\text{mm} \times 20\text{mm}$ , and the H-shaped intermediate column is  $500\text{mm} \times 350\text{mm} \times 14\text{mm} \times 20\text{mm}$ , as well as six 10.9-degree grade M20 bolts are used in the ICFD. The prestressed beam-column connection uses web friction energy dissipation device. Twelve 10.9-degree M24 high-strength bolts are used in an even distribution, with 4 rows and 3 columns. Each beam-column connection adopted twelve  $1 \times 19$  low relaxation high strength steel strands with

the nominal tensile strength grade valued 1860MPa. The initial prestressed value of each steel strand is set to  $0.4T_u$ . RPSF model is established after removing all intermediate columns from the model introduced above, which is used to analyze the seismic performance of ICRPSF in comparison.

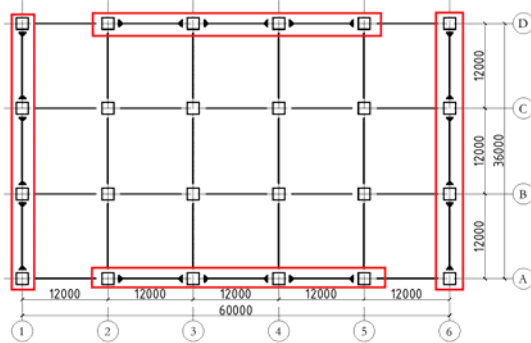


Figure 7. Plane Schematic of Structure

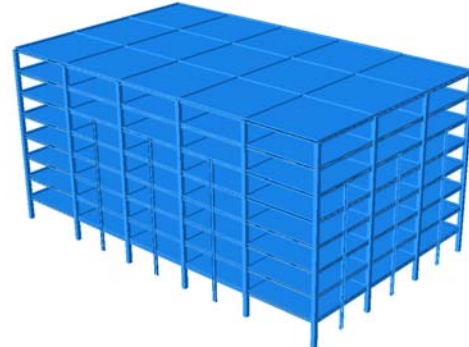


Figure 8. Three-dimensional FEA Model of ICRPSF

## 4.2 Modal Analysis Results of 2 Types of the Structure

Using the ABAQUS software, a linear perturbation analysis is set up to perform the modal analysis and obtain the natural frequencies of the structure. The eigenvalue solver uses the Lanczos method to calculate the first 18 frequencies and periods for both types of frames (ICRPSF and RPSF). Each vibration mode of 2 types of the frame is investigated and compared. The comparison of the first three vibration modes shows that the first three vibration modes of ICRPSF are consistent with those of RPSF. Each natural period calculated from the frequency is shown in Table 1. The data show that, compared with the RPSF, the period of the ICRPSF is significantly reduced, i.e., the reduction amplitudes of first three natural periods can reach 26% at the least. The result indicates that, ICFD, which is used in the design of the ICRPSF, provides higher lateral rigidity and torsional rigidity than those of RPSF significantly. Therefore, the utilization of ICFD in the ICRPSF contributes significantly to the overall rigidity of the structure.

Table 1. Comparison of the First Three Natural Vibration Periods of Two Frames (s)			
Frame	1	2	3
RPSF	2.697	2.665	1.644
ICRPSF	1.993	1.915	1.203
Deviation ratio	26.08%	28.16%	26.81%

## 5. GROUND MOTION SELECTION FOR THE TIME HISTORY ANALYSIS

The 3-dimension ground motion data of 22 far-field earthquakes recommended in report ATC-63 [16] and the EL-Centro, the Taft wave and the Wenchuan earthquake's 4 waves are used to perform the time history analysis. The natural period of the ICRPSF is around 2 seconds. The percentages of the difference (delta) of earthquake influence coefficient between every ground motion response spectrum and the standard spectrum at the natural period of 2 seconds is calculated. As the space is limited, 8 selected typical ground motions are selected according to the calculated difference of influence coefficients. The typical acceleration Fourier spectrum transformed by software SeismoSignal is shown in Figure 9. Differences of the earthquake influence coefficients, in descending order, are GM1 to GM8, as shown in Table 2.

During the finite element calculation, the bi-directional horizontal component of each ground motion is used, and its amplitude is modulated to 8-degree frequent, design, rare, and 8.5-degree rare earthquake conditions according to Chinese Code for Seismic Design of Buildings [17], i.e., the peak ground acceleration (PGA) are 0.07g, 0.2g, 0.4g and 0.51g, respectively. In the model, the primary direction is Z, the secondary direction is X which the amplitude is scaled to 0.85.

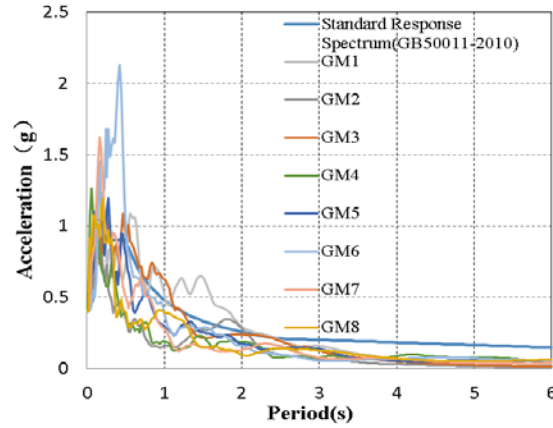


Figure 9. Acceleration Response Spectrum

Table 2. 8 Ground Motions for Time-history Analysis

Ground motions	Magnitude	Year	Description	Influence coefficient delta
GM1	6.9	1995	Kobe, Japan	13.11%
GM2	6.7	1994	Northridge	8.66%
GM3	7	1940	Imperial Valley	-7.04%
GM4	6.5	1979	Imperial Valley	-27.12%
GM5	7.1	1999	Hector Mine	-32.53%
GM6	8	2008	Shifang Bajiao	-55.32%
GM7	7.4	1990	Manjil, Iran	-48.99%
GM8	7.1	1999	Duzce, Turkey	-62.43%

## 6. TIME HISTORY DYNAMIC ANALYSIS RESULTS

The dynamic responses of the ICRPSF and RPSF under 8-degree frequent, design, rare earthquakes and 8.5-degree rare earthquake are analyzed in detail to investigate the seismic performance of the ICRPSF. Because the two frames have no connection gap opening and ICFD slippage under the 8-degree frequent earthquakes, and due to the space is limited, only the analytical results under 8-degree design (0.2g) and 8.5-degree rare earthquake (0.51g) are listed here.

### 6.1 The 8-degree Design Ground Motion (PGA=0.2g)

#### (1) Slippages of the friction damper and connection gap opening

Table 3 shows the maximum slippages of the friction damper of ICRPSF in both directions under 8-degree design earthquake conditions. The maximum slippage response of the ICFD is higher under the ground motions with larger influence coefficients. The maximum slippage is 20.2 mm in X-direction under the GM3 ground motion. Table 4 shows the maximum connection gap opening under 8-degree design earthquake, indicating that the difference of connection gap opening is not much.

Table 3. Maximum ICFD Slippage under 8-degree Design Earthquake (mm)

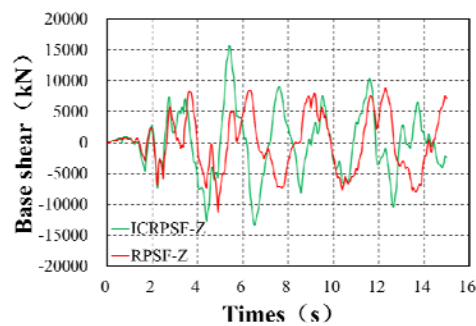
Ground motions		GM 1	GM 2	GM 3	GM 4	GM 5	GM 6	GM 7	GM 8
ICRPSF	Z direction	14.9	0.5	15.4	0	3.4	2.1	3.6	0
	X direction	10.9	7.8	20.2	0.1	0.1	0.1	0.1	0.1

Table 4. Maximum Connection Gap Opening under 8-degree Design Earthquake (mm)

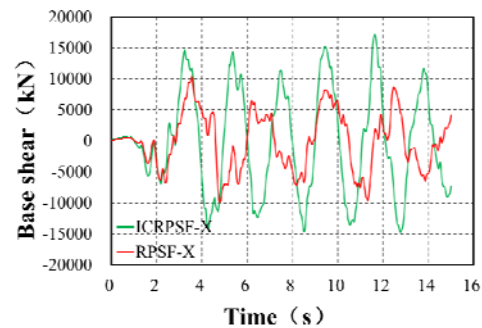
Ground motions		GM 1	GM 2	GM 3	GM 4	GM 5	GM 6	GM 7	GM 8
ICRPSF	Z direction	1.925	0.365	1.624	0.168	0.563	0.42	0.577	0.266
	X direction	0.999	1.398	1.753	0.24	0.176	0.109	0.116	0.258
RPSF	Z direction	1.343	0.274	1.996	0.141	1.76	0.243	1.036	0.266
	X direction	2.821	1.217	2.981	0.197	0.11	0.151	0.263	0.198

## (2) Comparison of the base shear

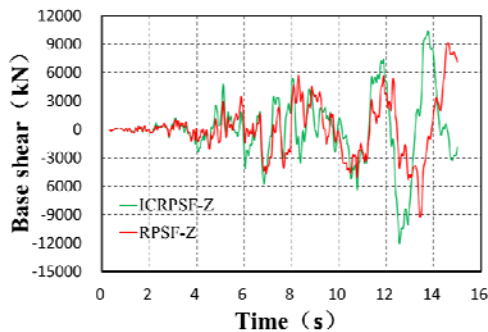
Figure 10 shows the base shear time history comparisons of both frames under 3 ground motions of 8-degree design earthquake. Table 5 shows the maximum base shears of the ICRPSF and the RPSF in the primary and secondary directions under 8 typical ground motions of 8-degree design earthquake. The data in Figure 10 and Table 5 show that, in both directions, the base shears of ICRPSF are greater than those of RPSF except under the action of ground motion GM6, and the maximum value of ICRPSF is 134% higher than that of RPSF. Because ICRPSF has higher lateral rigidity and a shorter structure period, which would result in a corresponding increase of the base shear.



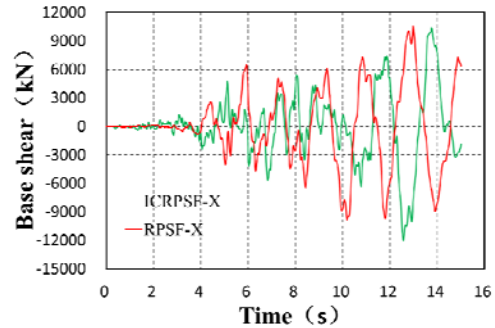
a) GM3 primary direction



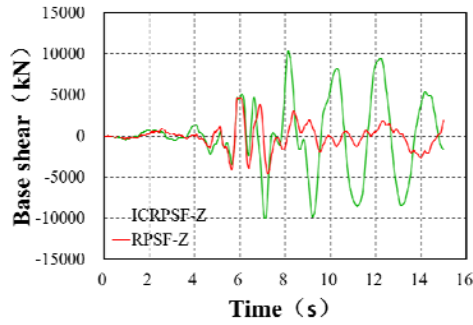
b) GM3 secondary direction



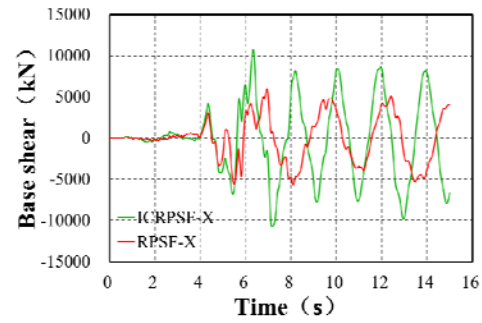
c) GM5 primary direction



d) GM5 secondary direction



e) GM8 primary direction



f) GM8 secondary direction

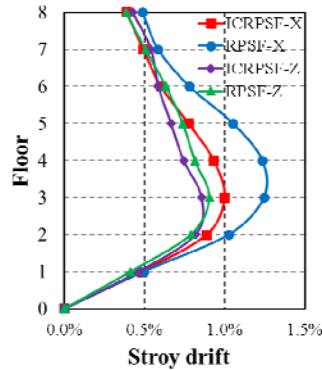
Figure 10. Base-shear time-histories of Two Frames under 8-degree Design Earthquake

Table 5. Maximum Base-shear of Two Frames under 8-degree Design Earthquake

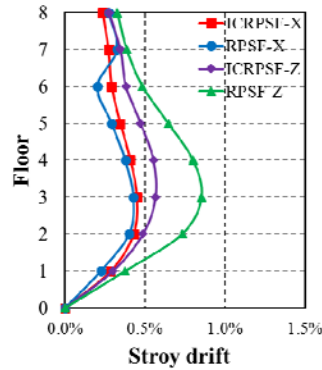
Ground motions	Primary direction (Z)			Secondary direction (X)		
	RPSF kN	ICRPSF kN	Delta %	RPSF kN	ICRPSF kN	Delta %
GM1	9595	18303	91	10940	16253	49
GM2	6426	10055	56	7311	15752	115
GM3	11199	15697	40	10350	17190	66
GM4	5148	8242	60	8572	10797	26
GM5	9285	12056	30	5396	10508	95
GM6	9157	5914	-35	11494	8700	-24
GM7	8299	13034	57	7772	10324	33
GM8	4649	10405	124	5995	10770	80

### (3) Comparison of the story drift

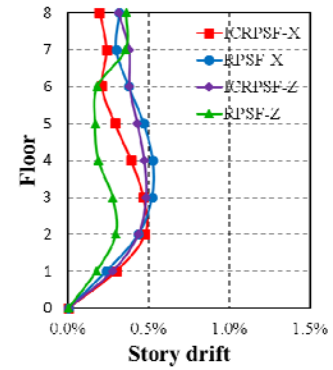
Figure 11 shows the envelope values of the story drifts of ICRPSF and RPSF in the primary and the secondary directions under different 8-degree design ground motions. The maximum story drifts of each floor are shown in Table 6. The data in Figure 11 and Table 6 show that the most of maximum story drifts of the ICRPSF are close to or less than those of the RPSF under most of ground motions. The largest values of RPSF and ICRPSF occur in the secondary direction at 3rd floor of the structure under the action of GM3. The maximum story drift of RPSF is 1.244%, and the maximum story drift of ICRPSF is 0.998%.



a) GM3



b) GM5



c) GM8

Figure 11. Comparison of Maximum Story Drifts under 8-degree Design Earthquake

Table 6. Maximum Story Drifts of Two Frames under 8-degree Design Earthquake (%rad)

Ground motions	Primary direction (Z)		Secondary direction (X)	
	RPSF	ICRPSF	RPSF	ICRPSF
GM1	0.757	0.871	1.117	0.654
GM2	0.531	0.536	0.776	0.842
GM3	0.916	0.865	1.244	1.0
GM4	0.368	0.382	0.491	0.469
GM5	0.856	0.567	0.427	0.450
GM6	0.448	0.540	0.426	0.404
GM7	0.707	0.566	0.607	0.369
GM8	0.359	0.483	0.525	0.477

## (4) Comparison of the residual story drift

Figure 12 shows the comparison of the maximum residual story drifts between ICRPSF and RPSF of each floor under the actions of different 8-degree design ground motions. Large residual story drifts occur primarily in floors with large story drifts. Residual story drifts of ICRPSF are generally greater than those of RPSF. However, the maximum post-seismic residual story drifts of the ICRPSF and RPSF are 0.0646% and 0.0059% respectively, which are small enough to be ignored.

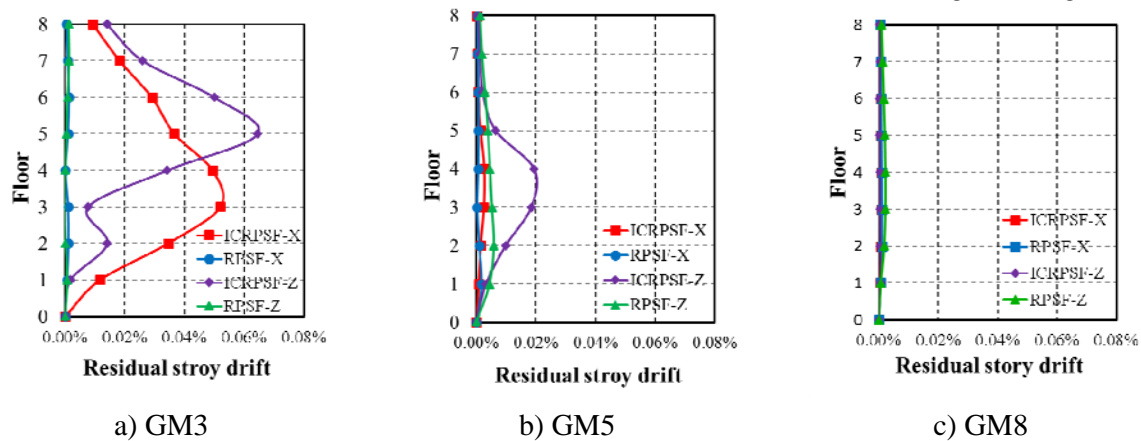


Figure 12. Maximum Residual Story Drift of Two Frames under 8-degree Design Earthquake

Table 7 shows the maximum residual slippage of the friction damper in both directions under the 8-degree design ground motions. The corresponding residual slippage of ICRPSF, the maximum residual slippage of the friction damper is 8.8mm, is relatively larger after a larger slippage generated by the friction damper. After all, the prestressed strand on the beam provide ICFD limited recovery capability. This will have a few influences on the overall performance of the structure. However, after an earthquake, the high strength bolt can be relaxed to restore the ICFD to its original position.

Table 7. Maximum ICFD Residual Slippage under 8-degree Design Earthquake (mm)

Ground motions		GM 1	GM 2	GM 3	GM 4	GM 5	GM 6	GM 7	GM 8
ICRPSF	Z direction	7.9	0.4	8.8	0	2.9	2.1	1.4	0
	X direction	1.7	7.1	3.6	0	0	0	0	0



## (5) Comparison of the energy dissipation

Figure 13 shows the energy dissipation comparison of both frames under the action of 8-degree design ground motions. Each symbol represents the following meanings: ■ EKE—kinetic energy, ■ EFD—friction energy dissipation, ■ EV—damping energy dissipation, ■ EP—plasticity energy dissipation, ■ ESE —elastic strain energy. Table 8 shows the energy dissipation values in detail. Under different ground motions, the total energy absorption of the ICRPSF structure is 35%, which is greater than that of the RPSF on average, as well as the maximum energy absorption is 60% higher than that of the RPSF. The kinetic energy and the elastic strain energy of the structure are only part of the energy transformation, which would not dissipate any energy. Under design earthquake conditions, except the friction energy dissipation of the structure is relatively high under a few of intensive ground motions, the friction energy dissipation of the structure is small under most ground motions with lower influence coefficients. Both frames are primarily in the state of damping energy dissipation where non-elastic strain energy dissipation is relatively small, which indicates that the structure is basically in an elastic state at this moment.

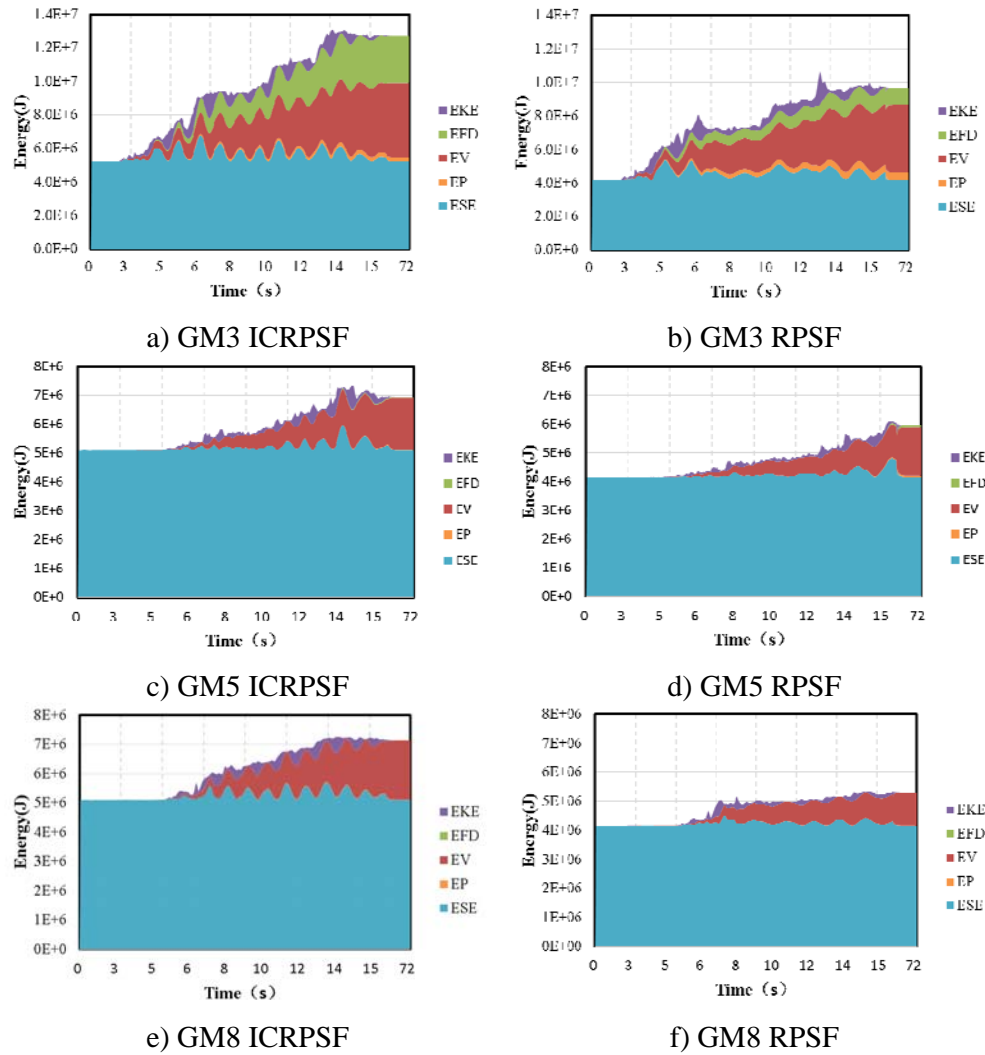


Figure 13. Comparison of Energy Dissipation of Two Frames under 8-degree Design Earthquake

Table 8. Energy Dissipation of Two Frames under 8-degree Design Earthquake

Ground motions		WK (J)	ESE (J)	EKE (J)	EWK (J)	EP (J)	EP/EWK (%)	EV/EWK (%)	EFD/EWK (%)
GM1	RPSF	7627810	4428420	191085	3008305	158786	5.28	76.73	16.92
	ICRPSF	9491640	5194160	125857	4171623	132659	3.18	74.56	18.82
GM2	RPSF	5787700	4223510	19350	1544840	22134	1.43	93.04	3.40
	ICRPSF	9406120	5203900	215156	3987064	89918	2.26	76.76	17.33
GM3	RPSF	9771210	4624010	17251	5129949	446161	8.70	70.52	20.04
	ICRPSF	12899800	5473830	40417	7385553	256293	3.47	56.16	38.27
GM4	RPSF	5395010	4211120	260586	923304	5322	0.58	95.55	0.02
	ICRPSF	6927530	5491450	115991	1320089	2913	0.22	88.76	0.26
GM5	RPSF	6084410	4748510	62998	1272902	37949	2.98	90.40	3.72
	ICRPSF	7089060	5274910	46209	1767941	14080	0.80	89.50	1.61
GM6	RPSF	6963080	4412530	44769	2505781	6002	0.24	97.99	0.00
	ICRPSF	8994810	5251080	15423	3728307	6031	0.16	95.32	0.28
GM7	RPSF	6030410	4505720	140299	1384391	63450	4.58	90.85	1.65
	ICRPSF	6868140	5271590	25392	1571158	30204	1.92	86.11	2.43
GM8	RPSF	5344160	4302850	70480	970830	3452	0.36	96.40	0.05
	ICRPSF	7302010	5296490	63183	1942337	14930	0.77	92.03	0.03

\*: total energy absorption : WK= ESE+ EKE+ EWK; total energy dissipation: EWK= EP+ EV+EFD

## 6.2 The 8.5-degree Rare Earthquake (PGA=0.51g)

### (1) Slippages of the friction damper and connection gap opening

Table 9 shows the maximum slippages of the friction damper of ICRPSF in both directions under 8.5-degree rare earthquake conditions. The ICFD maximum slippage response occurs under the ground motion with the largest influence coefficient. The maximum slippage is 67.3 mm in X-direction under the action of GM1 ground motion. Therefore, during the seismic design of the structure under the condition of 8.5-degree rare earthquake, the redundancy of the intermediate column damper chute should be taken into account. Table 10 shows the maximum connection gap opening under the action of 8-degree rare earthquake. The data from the Table 10 show that the difference of connection gap opening is not much under most of the ground motions.

Table 9. Maximum ICFD Slippage under 8.5-degree Rare Earthquake (mm)

Ground motions		GM 1	GM 2	GM 3	GM 4	GM 5	GM 6	GM 7	GM 8
ICRPSF	Z direction	59.2	19.9	49.5	17.9	26.3	4.0	40.9	31.5
	X direction	67.3	48.1	67.0	26.6	23.0	3.9	23.9	4.2

Table 10. Maximum Connection Gap opening under 8.5-degree Rare Earthquake (mm)

Ground motions		GM 1	GM 2	GM 3	GM 4	GM 5	GM 6	GM 7	GM 8
ICRPSF	Z direction	10.906	3.538	5.078	2.353	3.339	0.688	4.018	3.206
	X direction	14.124	4.271	6.072	2.694	2.179	0.501	2.202	2.050
RPSF	Z direction	4.608	3.559	6.179	2.466	5.166	2.864	4.813	4.028
	X direction	7.784	4.085	9.713	9.307	2.235	3.074	3.519	2.725



## (2) Comparison of the base shear

Figure.14 shows comparison towards the base shear time history responses between both frames in both directions under 8.5-degree rare earthquake conditions. The base shear time history responses of both frame structures under different ground motions show that both the trends of responses are in the same under rare earthquake conditions, where the response magnitude of ICRPSF is approximately 10% higher than that of the RPSF.

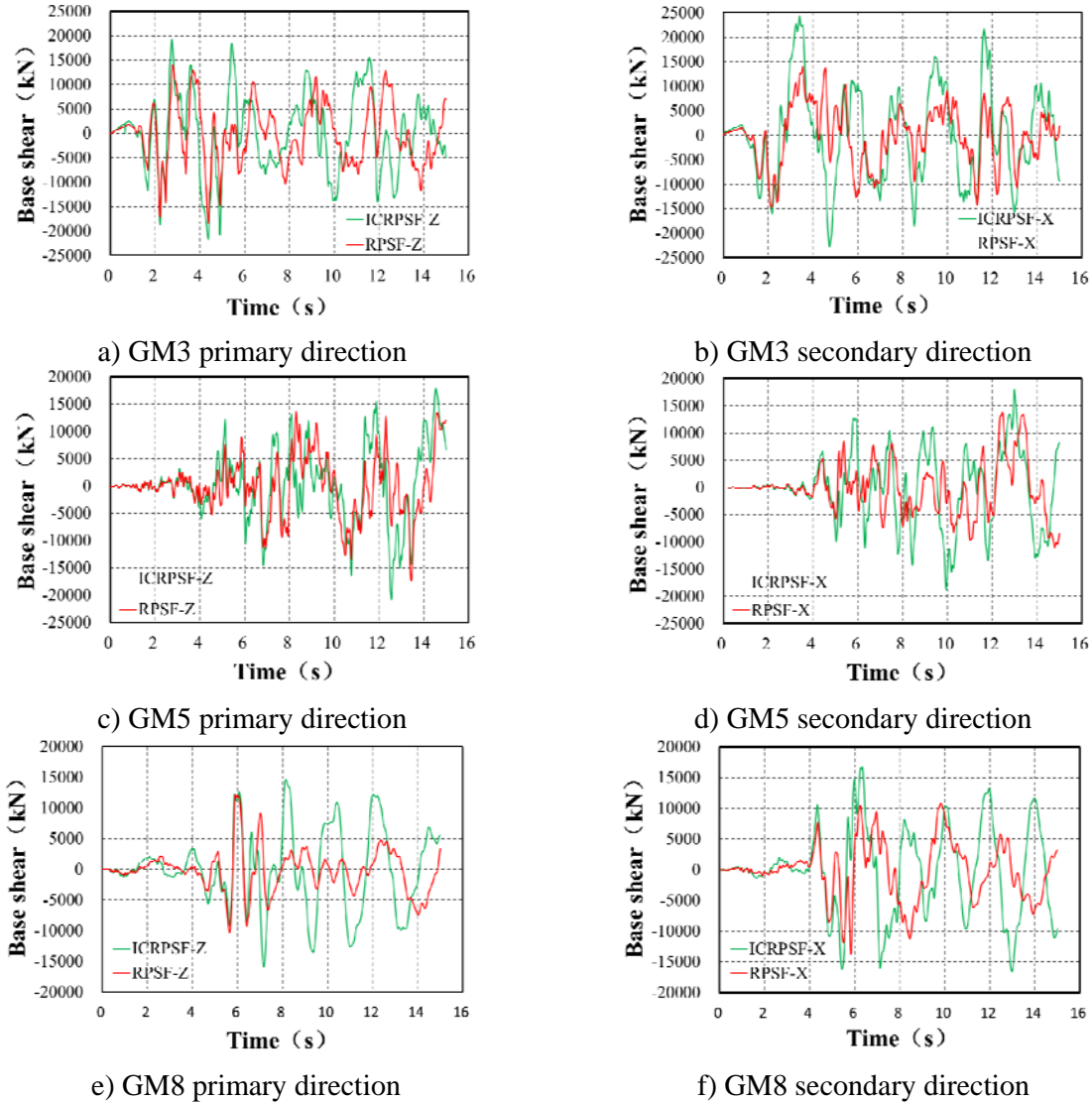


Figure 14. Base-shear Time-histories of Two Frames under 8.5-degree Rare Earthquake

The maximum base shears of both frames under 8.5-degree rare earthquake conditions both in primary and secondary directions are shown in Table 11. The data show that the ground motion with higher influence coefficient would exert a larger base shear on the structure. However, when compared with the response under rare earthquake ground motion, the corresponding increase is less significant. This indicates that, with the further increase of the earthquake magnitude and horizontal slippage of intermediate column, the contribution of ICFD to the overall rigidity of the structure decreases.

Table 11. Maximum Base-shears of Two Frames under 8.5-degree Rare Earthquake

Ground motions	Primary direction (Z)			Secondary direction (X)		
	RPSF kN	ICRPSF kN	Delta %	RPSF kN	ICRPSF kN	Delta %
GM1	20206	26591	32	16377	26677	63
GM2	16474	17587	7	12414	20530	65
GM3	18560	21651	17	14630	24384	67
GM4	12451	16609	33	19327	21454	11
GM5	17340	20824	20	13807	18827	36
GM6	17884	12954	-28	14090	16216	15
GM7	14683	19502	33	13898	20648	49
GM8	12126	15913	31	13725	16747	22

## (3) Comparison of the story drift

Figure 15 shows the envelope curves of the story drifts of each floor for both frames in the primary and secondary directions under different ground motions. The maximum story drifts are shown in Table 12. The data in Figure 15 and Table 12 show that, in the primary and the secondary directions, the maximum story drifts of the ICRPSF are smaller than those of the RPSF under most ground motions. The maximum story drift of RPSF is 3.223% under GM3 ground motion, which is greater than the maximum story drift of 2.190% of ICRPSF under the same ground motion. The ICRPSF is superior to the RPSF on the control of the story drift.

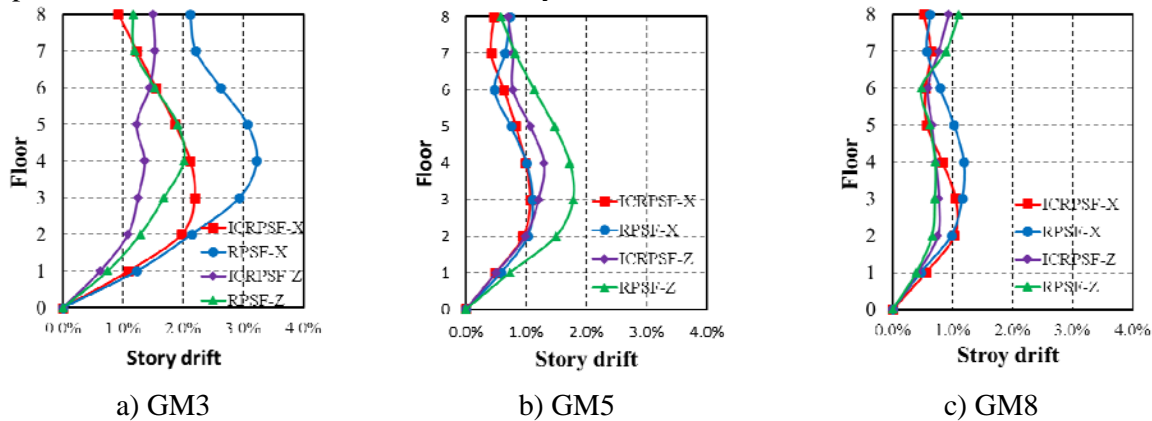


Figure 15. Comparison of Maximum Story Drift of Two Frames under 8.5-degree Rare Earthquake

Table 12. Maximum Story Drift of Two Frames under 8.5-degree Rare Earthquake (%rad)

Ground motions	Primary direction (Z)		Secondary direction (X)	
	RPSF	ICRPSF	RPSF	ICRPSF
GM1	1.625	2.014	2.206	2.197
GM2	1.176	1.523	1.630	1.693
GM3	2.012	1.527	3.223	2.190
GM4	0.749	0.731	1.318	0.919
GM5	1.779	1.298	1.108	1.071
GM6	0.389	0.569	0.446	0.586
GM7	1.651	1.568	1.452	1.090
GM8	1.102	0.930	1.186	1.048

#### (4) Comparison of the residual story drift

Figure 16 shows a comparison of the maximum residual story drifts between both frames of each floor under different 8.5-degree rare ground motions. The maximum residual story drift of the ICRPSF is smaller than that of the RPSF, i.e., they are 0.121% and 0.287%, respectively. The former has superior post-seismic recovering capability.

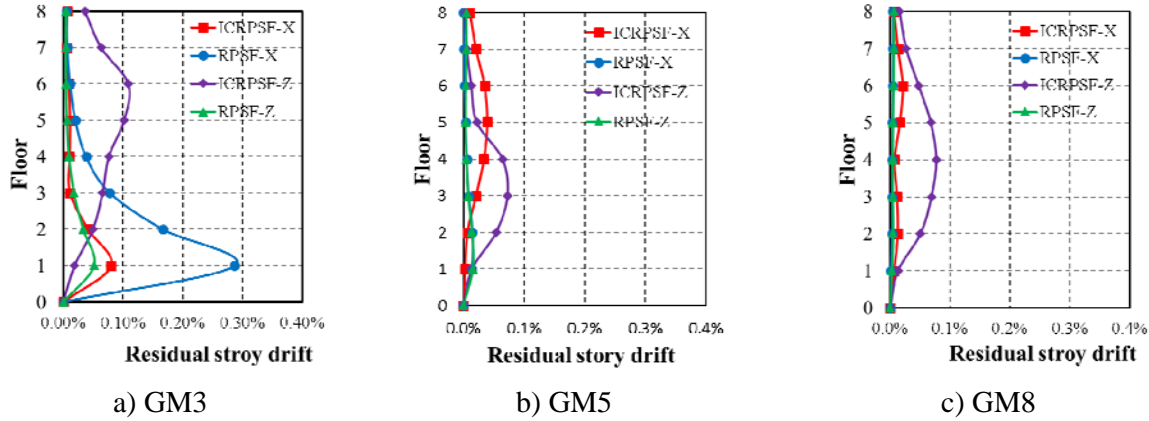


Figure 16. Maximum residual story drift of two frames under 8.5-degree rare earthquake

Table 13 shows the maximum residual slippages of the friction dampers of both frames under 8.5-degree rare earthquake conditions. After the friction damper experiences a larger slip, the corresponding residual slippage also increases. However, this will have significant influence on the overall performance of the structure. Additionally, after an earthquake, the high-strength bolt can be relaxed to restore the ICFD to its original position.

Table 13. Maximum ICFD Residual Slippage under 8.5-degree Rare Earthquake (mm)

Ground motions		GM 1	GM 2	GM 3	GM 4	GM 5	GM 6	GM 7	GM 8
ICRPSF	Z direction	14.4	3.1	0.4	15.2	2.2	4.0	4.0	9.8
	X direction	13.1	3.0	7.3	4.9	4.4	3.8	2.9	2.7

#### (5) Comparison of frame plasticity and energy dissipation

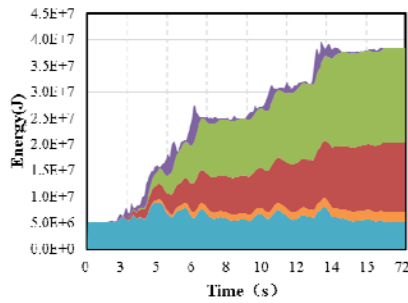
Under 8.5-degree rare earthquake conditions, the PEEQ for the column bases and beams of both frames is shown in Table 14. The data in Table 14 show that the PEEQ in the column base of both frames increases slightly than that under 8-degree rare earthquake conditions. The frame beam still remains in an elastic state, and the column bottoms of both frames have the similar plastic developing conditions.

Table 14. PEEQ of Two Frames under 8.5-degree Rare Earthquake

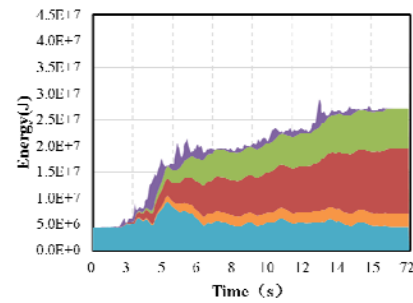
Ground motions	RPSF		ICRPSF		
	column base	beam	column base	intermediate column base	beam
GM1	$1.79 \times 10^{-3}$	—	$2.73 \times 10^{-3}$	$1.24 \times 10^{-3}$	—
GM2	$2.39 \times 10^{-4}$	—	$5.52 \times 10^{-4}$	$3.22 \times 10^{-4}$	—
GM3	$4.71 \times 10^{-3}$	—	$4.95 \times 10^{-3}$	$7.29 \times 10^{-4}$	—
GM4	—	—	—	—	—
GM5	$3.81 \times 10^{-6}$	—	—	$2.30 \times 10^{-7}$	—
GM6	$5.82 \times 10^{-5}$	—	$1.56 \times 10^{-5}$	—	—
GM7	—	—	—	$9.59 \times 10^{-4}$	—
GM8	—	—	$2.26 \times 10^{-4}$	$2.17 \times 10^{-4}$	—

\*: —represent elastic

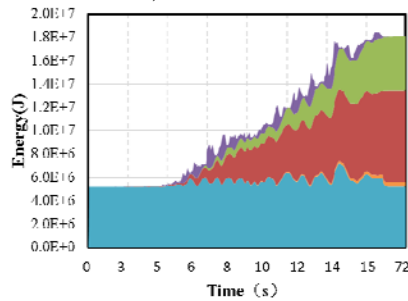
Figure 17 shows a comparison of the energy dissipation between the two frames. Table 15 shows the detailed energy dissipation values. Under different ground motions, the total energy absorbed by the ICRPSF structure is 44.4% greater than that by the RPSF on average, the maximum energy absorbed by the ICRPSF under GM2 is twice as that by the RPSF, indicating that the intermediate column contributes to the overall rigidity of the structure significantly. Under 8.5-degree rare earthquake conditions, the friction energy dissipation increases and the damping energy dissipation decreases. Under the three ground motions with larger influence coefficients, the friction energy dissipation takes up more than half of the total energy dissipation, which the maximum value reaches 55.12%. The friction energy dissipation performance of the ICRPSF is superior to the RPSF significantly. The non-elastic energy dissipation of ICRPSF and RPSF has the relatively small proportion of the total energy dissipation under 8.5-degree rare earthquakes, which the average value of RPSF is 7.37% and to ICRPSF, is only 3.91%. Therefore, the plastic development of the ICRPSF is less than that of the RPSF, which improves post-seismic recovery performance.



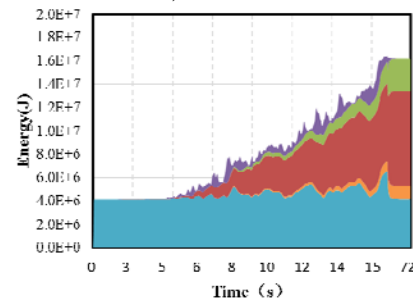
a) GM3 ICRPSF



b) GM3 RPSF



c) GM5 ICRPSF



d) GM5 RPSF

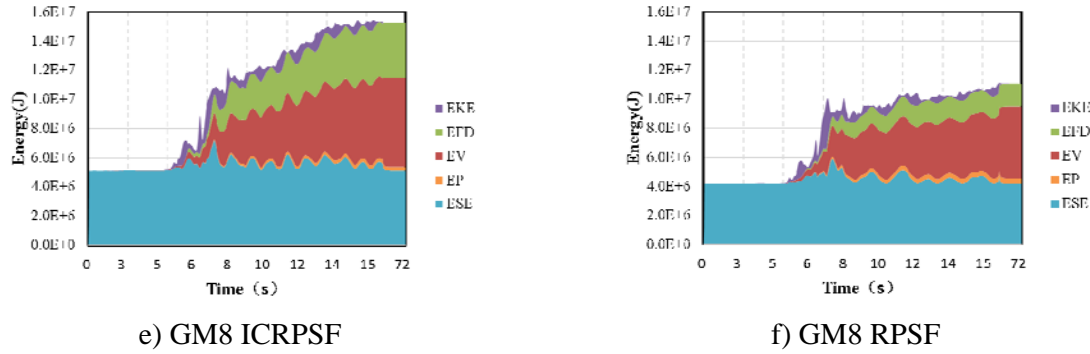


Figure 17 Comparison of energy dissipation of two frames under 8.5-degree rare earthquake

Table 15. Energy Dissipation of Two Frames under 8.5-degree Rare Earthquake

Ground motions		WK(J)	ESE(J)	EKE(J)	EWK(J)	EP(J)	EP/EWK (%)	EV/EWK (%)	EFD/EWK (%)
GM1	RPSF	21276800	4275280	151868	16849652	1433040	8.50	54.40	36.78
	ICRPSF	31000800	5698340	111802	25190658	1618030	6.42	39.34	53.65
GM2	RPSF	12875000	4182780	8610	8683610	437003	5.03	70.42	24.02
	ICRPSF	24426800	5256710	253515	18916575	686605	3.63	50.29	45.27
GM3	RPSF	27270300	4679850	447171	22143279	2498360	11.28	53.81	34.58
	ICRPSF	38641100	5580590	502779	32557731	1839880	5.65	38.74	55.12
GM4	RPSF	12176800	4453980	1422920	6299900	397867	6.32	78.40	14.62
	ICRPSF	15180200	5694810	1243090	8242300	233834	2.84	63.37	31.95
GM5	RPSF	16454200	6536690	537917	9379593	846174	9.02	70.52	19.69
	ICRPSF	18341800	5957690	218524	12165586	297370	2.44	58.47	37.70
GM6	RPSF	23329100	4589540	367320	18372240	916400	4.99	83.56	10.81
	ICRPSF	13866200	5287400	676589	7902211	60007	0.76	95.99	1.42
GM7	RPSF	13012300	4251090	637004	8124206	654308	8.05	66.80	24.20
	ICRPSF	19606900	5485520	602023	13519357	832700	6.16	46.65	46.00
GM8	RPSF	11028900	4298690	673499	6056711	350814	5.79	69.02	24.54
	ICRPSF	15450000	5646320	74586	9729094	274582	2.82	57.32	38.36

\*: total energy absorption: WK= ESE+ EKE+ EWK; total energy dissipation: EWK= EP+ EV+EFD

## 7. CONCLUSIONS

- (1) Compared with the RPSF frame, the ICRPSF has a shorter period. The difference between the two frames is 26% approximately. The existence of the ICFD results in a significant increase of the lateral rigidity and torsional rigidity of ICRPSF compared with the RPSF. The intermediate column contributes to the overall translational and rotational rigidity of the structure significantly.
- (2) Additional rigidity provided by the ICFD causes the greater maximum base shear of the ICRPSF than that of the RPSF under most conditions. Slip occurs at the ICFD with the increase of earthquake magnitude, decreasing the difference between the lateral rigidities of the two frames, and resulting in approximate base shears of the two frames.
- (3) The lateral rigidity of ICRPSF is higher than that of RPSF. Under various earthquake conditions, the maximum story drifts of ICRPSF are all smaller than those of RPSF. Under the action of 8.5-degree rare earthquakes, the maximum story drift of RPSF is 3.22%, which is far

beyond the elasto-plastic story drift limit of 2% in current code. The corresponding story drift of ICRPSF is only 2.19% (1/46), which just exceeds the code limit. These results show that ICRPSF has a significantly superior performance on the control of the story drift than RPSF.

- (4) Both frames have very small post-seismic residual story drift under design earthquakes, which can be ignored. The maximum residual story drifts of ICRPSF under 8.5-degree rare earthquake conditions are all smaller than those of the RPSF, and the maximum residual deformation of the structure is 0.121%. However, the larger ICFD slip results in the larger residual slippage correspondingly. This will have a few influences on the overall performance of the structure. However, after an earthquake, the high strength bolt can be relaxed to restore the ICFD to its original position.
- (5) When the earthquake magnitude is relatively small, the energy absorbed by the frames is elastic strain energy primarily. With the increase of the earthquake magnitude, the damping energy dissipation and friction energy dissipation increasing gradually, while the increase in the non-elastic energy dissipation is relatively small in either of the frame. The total absorbed energy and friction energy dissipation in the ICRPSF are always greater than those of the RPSF, while its non-elastic energy dissipation is always less than that of the RPSF. Under the earthquake conditions of high earthquake magnitudes, the friction energy dissipation of the ICRPSF represents almost half of the total energy dissipation, and ICFD contributes to the overall seismic energy dissipation of the structure significantly.
- (6) In conclusion, the resilient prestressed steel frame with intermediate column containing friction dampers can effectively control the story drift and dissipate more energy, slow down the plastic development of the components even further, and achieve small post-seismic structure residual story drift. Such superior performance will be more evident with the increase of the earthquake magnitudes. Therefore, this system is very suitable for the resilient prestressed steel frame structure with a large span, the structure which locates in the frequent earthquake zone and a high-value building.

## ACKNOWLEDGEMENT

This work was supported by the National Key Basic Research and Development Program of China under Grant No.2016YFC0701504 and the Key Project of Beijing Natural Science Foundation under Grant No.8131002.

## REFERENCES

- [1] Ricles, J.M., Sause, R., Garlock, M. and Zhao, C., "Post-tensioned Seismic-resistant Connections for Steel Frames," *Journal of Structure Engineering*, 2001, Vol. 127, No. 2, pp.113-121.
- [2] Garlock, M., Ricles, J. M. and Sause, R. "Cyclic Load Tests and Analysis of Bolted Top-and-seat Angle Connections," *Journal of Structure Engineering*, 2003, Vol. 129, No. 12, pp.1615-1625.
- [3] Garlock, M., Sause, R. and Ricles, J. "Behavior and Design of Posttensioned Steel Frame Systems," *Struct. Eng.*, 2007, Vol. 133, No. 3, pp.389 - 399.
- [4] Christopoulos, C., Filiatrault, A., Uang, C. M., and Folz, B. "Post-tensioned Energy Dissipating Connections for Moment-resisting Steel Frames," *Journal of Structural Engineering*, 2002, Vol. 128, No. 9, pp. 1111-1120.

- [5] Rojas, P., Ricles, J. M. and Sause, R. "Seismic Performance of Post-tensioned Steel Moment Resisting Frames with Friction Devices," *Journal of Structural Engineering*, 2005, Vol. 131, No. 4, pp. 529 – 540.
- [6] Wolski, M., Ricles, J. M. and Sause, R., "Experimental Study of a Self-centering Beam–column Connection with Bottom Flange Friction Device," *Journal of Structure Engineering*, 2009, Vol. 135, No. 5, pp. 479-488.
- [7] Tsai, K. C., Chou, C. C., Lin, C. L., Chen, P. C. and Jhang, S. J., "Seismic Self-centering Steel Beam-to- column Moment Connections using Bolted Friction Devices, " *Earthquake Engineering and Structural Dynamics*, 2008, Vol. 37, pp. 627–645.
- [8] Lin, Y.C., Sause, R. and Ricles, J.M., "Seismic Performance of Steel Self-centering, Moment-resisting Frame: Hybrid Simulations under Design Basis Earthquake", *Journal of Structural Engineering*, 2013, Vol. 139, No. 5, pp. 1823-1832.
- [9] Lin, Y. C., Sause, R. and Ricles, J. M., "Seismic Performance of a Large-scale Steel Self-centering Moment-resisting Frame : MCE Hybrid Simulations and Quasi-static Pushover Tests", *Journal of Structural Engineering*, 2013, Vol. 139, No. 7, pp.1227–1236.
- [10] Zhang, Y. X., Zhang, A. L. and Sun, W.L., "Behavior Study of Self-centering Beam-column Connections in Resilient Steel Frames after Earthquake", *Industrial Construction*, 2014, Vol. 44, No. 502, pp. 160-167. (in Chinese)
- [11] Zhang, Y. X., Ye, J. J., Yang, F. and Chen, Y. Y., "Dynamic Behavior and Time-history Analysis of Integral Self-centering Moment Resisting Frames", *China Civil Engineering Journal*, 2015, Vol. 48, No. 7, pp. 30-40 (in Chinese)
- [12] Zhang, A. L., Zhang, Y. X., Li, R. and Wang, Z. Y., "Cyclic Behavior of a Prefabricated Self-centering Beam–column Connection with a Bolted Web Friction Device", *Engineering Structures*, 2016, Vol. 111, pp. 185-198
- [13] Zhang, A. L., Zhang, Y. X., Zhao, W. and F, C. C., "Pseudo Dynamic Test Study of Resilient Prefabricated Prestressed Steel Frame", *Journal of Vibration and Shock*, 2016, Vol. 35, No. 05, pp. 207-215 (in Chinese)
- [14] Zhang, A. L., Zhang, Y. X., Cheng, Y. Y. and Wang, Z.Y., "Static Pushover Test on Resilient Prestressed Steel Frame with Intermediate Column Containing Friction Dampers", *Journal of Building Structures*, 2016, Vol. 03, pp. 125-133 (in Chinese)
- [15] Japan Association of Vibration Isolation Structure, "Passive Suspension Structure Design and Construction Manuals," *Architecture & Building Press*, Beijing, China, 2008. (in Chinese)
- [16] ATC-63. "Quantification of Building Seismic Performance Factors," *Applied Technology Council*, 2008.
- [17] GB 50011-2010, "Code for Seismic Design of Buildings," *Architecture & Building Press*, Beijing, China, 2010. (in Chinese)





# CONCURRENT MULTI-SCALE MODELING OF A TRANSMISSION TOWER STRUCTURE AND ITS EXPERIMENTAL VERIFICATION

F.Y. Wang\*, Y.L. Xu and S. Zhan

*Department of Civil and Environmental Engineering, The Hong Kong Polytechnic University, Kowloon, Hong Kong*

*\*(Corresponding author: E-mail fy11423@sina.com)*

*Received: 16 February 2016; Revised: 21 June 2016; Accepted: 3 September 2016*

---

**ABSTRACT:** The interruption of electrical service due to failure of transmission tower structures can have devastating economic and social consequences. The current method for analyzing transmission tower structures is often to treat the angle members of the tower as either pin-ended truss elements or fix-ended beam elements. This approach ignores the effects of joint flexibility, local geometric and material nonlinearity, bolt slippage and deformation, making the structural analysis and design of the tower inadequate. In an effort to improve the structural analysis of transmission tower structures, this study aims at developing a multi-scale modeling method for transmission tower structures, in which critical joints of the tower are modeled using solid elements in a great detail while other members are modeled with common beam elements. The critical joint model includes gusset plates, angle members and bolts. The effects of local geometric and material nonlinearity and the contact problem between the bolts, plates and angles are all taken into consideration. New multi-point constraints for beam-to-solid connections at interface developed by the authors are used to couple the critical local joint model with the beam elements to form a multi-scale model of the tower. To verify the multi-scale modeling method, a physical model of a transmission tower structure was constructed and tested. The displacement and strain response of the tower model measured from the static tests are compared with the numerical results. The dynamic characteristics of the tower model identified from the dynamic tests are also compared with the numerical results. The comparative results show that the multi-scale modeling method is feasible and accurate for simultaneously predicting both global and local responses as well as estimating dynamic characteristics of the transmission tower structure.

**Keywords:** Multi-scale modeling, transmission tower, bolted connection, new multi-point constraints, experiment, comparison

**DOI:** 10.18057/IJASC.2017.13.3.4

---

## 1. INTRODUCTION

Transmission towers are vital components of transmission lines. Most of transmission tower structures are constructed by thin-walled angle members that are eccentrically connected to each other by bolts directly or through gusset plates. In the global analysis of a transmission tower, its angle members are often modeled using either pin-ended truss elements or fix-ended beam elements to form a global finite element (FE) model for the tower [1-5]. Nevertheless, this kind of global model ignores the effects of joint flexibility, local geometric and material nonlinearity, bolt slippage and deformation on the global behavior of the tower, which make the structural analysis and design of the tower inadequate. To overcome this problem, the joints in the global FE model are sometime modified as semi-rigid linear or nonlinear joints to consider joint effects on the global behavior of the tower [6-9]. In this regard, Rao and Kalyanaraman [5] presented a non-linear analysis method for lattice towers in consideration of member eccentricity, material non-linearity and rotational rigidity of joints. Ungkurapinan et al. [10] developed some formulas to describe joint slips based on the relevant test data. However, the use of semi-rigid joints cannot guarantee the accuracy of the analysis because there are a variety of joints, in terms of the number of bolts and the shape of gusset plates, making it difficult to determine the structural parameters for semi-rigid joints. For the analysis and design of local joints of the tower, the local joints are then modeled

using solid or shell elements [11-14]. The boundary conditions of a local joint model are often assigned by using the information extracted from the global analysis of the global FE model of the tower. This approach for the analysis and design of the global structure and local joints may be called the information-passing multi-scale method [15]. However, it is difficult to determine dynamic boundary conditions for the local joint model, and inaccurate boundary conditions will lead to large error in the calculated structural responses. Furthermore, if the solid and shell elements are used to model all the members and joints of the tower, the computational size for the global structure analysis will be too large to be implemented.

Recently, the concurrent multi-scale method is proposed to model large civil structures [15-17], in which the local joints are simulated with shell or plate elements in much detail while other components in the structure are simulated with beam or truss elements. Different scales of elements are then coupled to form a multi-scale FE model. Such a concurrent multi-scale simulation can simultaneously capture not only the global structural behavior but also the local joint behavior without a huge computation cost. The key issue of concurrent multi-scale modeling is the coupling of mixed-dimensional elements (beam, shell and solid) at their interfaces. Broadly speaking, there are two major coupling methods currently available: volume coupling and surface coupling [18]. Volume coupling refers to a region in which different models co-exist and it is usually realized using the Arlequin method [19, 20]. The Arlequin method is best suited for coupling different physical models such as continuum particles [21, 22] among others. In surface coupling, there is no overlapping of different models and different models can be coupled using one of the following methods: (a) transition element method; and (b) multipoint constraint (MPC) method. Transition elements can be used for shell-solid transition [23], beam-solid transition [24, 25], and beam-shell transition [26]. Unfortunately, the transition elements have not been widely adopted because of its limitations. Transition elements can only be used to a one-to-one coupling of elements and different element transitions require different formulations, which make it difficult and impractical for a commercial FE code. The MPC method is attractive for mixed-dimensional coupling by imposing constraint equations for nodal displacements at the interface. The MPC method can be used for static and dynamic analysis of linear or nonlinear structures [27-29]. In commercial FE software, MPC can be easily used for coupling different types of elements. Nevertheless, although there are several types of MPC in existing FE software, inaccurate constraint equations due to inappropriate assumptions may result in stress disturbance at the interface. The authors recently developed a reliable method for constructing appropriate MPC to guarantee the displacement compatibility and stress equilibrium at the multi-scale interface [30].

With all the aforementioned, this study aims at developing a concurrent multi-scale modeling method for transmission tower structures, in which critical joints of the tower are modeled using solid elements in much detail while other angle members are modeled with common beam elements. The detailed model for a critical joint includes gusset plates, angle members and bolts. The effects of local geometric and material nonlinearity and the contact problem between the bolts, plates and angles are all taken into consideration. The new multi-point constraints for beam-to-solid interface connections developed by the authors are used to ensure the computational accuracy and efficiency at interfaces so that the critical local joint models can be coupled with the common tower model to form a multi-scale model of the tower. To verify the proposed multi-scale modeling method, a physical model of a transmission tower structure at a length scale of 1:10 was constructed and tested. The displacements and strains of the tower model measured from the static tests are compared with the numerical results obtained by the multi-scale modeling method. The dynamic characteristics of the tower identified from the dynamic tests are also compared with the numerical results.

## 2. A PHYSICAL MODEL OF A TRANSMISSION TOWER STRUCTURE

In order to verify the accuracy of multi-scale modeling and analysis of a transmission tower structure, a physical model of a transmission tower structure was built. The prototype of the tower is a cup-type and straight-line tower, having a 50.50m height and a 22.02m width. It is used in 500kv networks of the state grid of China, suitable for the areas with heavy icing or high lightning incidence. The tower is assembled from 23 types of angle members, which are connected to each other at joint plates with bolts. In consideration of the physical modeling of bolts and joint plates as well as the availability of laboratory space, the length ratio of the reduced-scale model to the prototype was selected as 1:10. The stainless steel was chosen as the material to make angle members and joint plates. The scaled model was designed and fabricated following the geometric similarity laws as close as possible. In order to guarantee the precision of local joints of the transmission tower, the components of local joints, such as bolts and gusset plate, were also fabricated according to the length ratio. The angle members and gusset plates were tailor-made in the factory by using the stainless steel plates. The completed tower model had 930 angle members, 402 gusset plates, and 3649 bolts. The completed physical model of the tower and a local joint are shown in Figure 1(a) and Figure 1(b) respectively. The tower model was finally connected to the four steel bases by bolts at its four legs and the four steel bases were in turn firmly fixed on a large concrete block ( see Figure 1(c) ) while the concrete block was connected to the strong floor of the laboratory. Both static and dynamic tests were performed to provide test data for verifying the numerical results from multi-scale analysis.

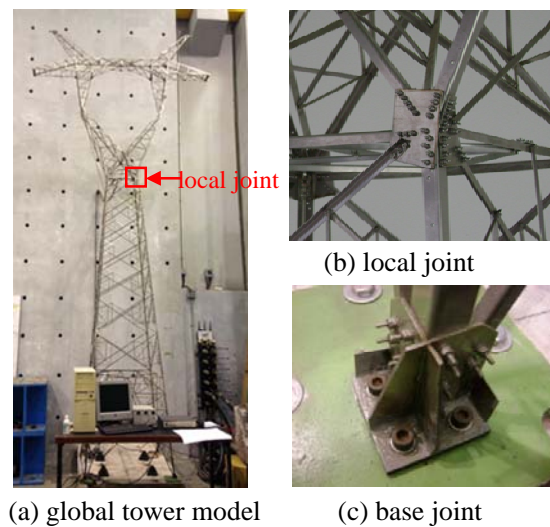


Figure 1. Physical Model of a Transmission Tower

## 3. MULTI-SCALE MODELING OF THE TRANSMISSION TOWER

For a transmission tower, there are many complex problems to deal with in the process of multi-scale modeling, such as the interface coupling of mix-dimensional elements and the contact problem between bolts and plates. Most of the commercial FE software has the features of dealing with these problems. It is therefore more convenient to build the multi-scale model of the test transmission tower using commercial FE software. The FE software ANSYS is used in this study together with the self-written supplemental programs for multi-scale modeling and analysis of the transmission tower structure.

The main purpose of the multi-scale modeling and analysis of the transmission tower is to obtain its global and local responses simultaneously. For the sake of a clear demonstration of the proposed method, only one typical and most important joint between the crank arm and the tower body is selected to construct a detailed local FE joint model. The selected joint consists of 9 angle members of a shortened length, 3 gusset plates and 40 bolts. In order to accurately simulate the bolt connection, all the components of the joint are modeled using solid elements. Consequently, the 20-node SOLID95 elements of higher order, which can simulate irregular shapes with no loss in accuracy, are used to model angle members, gusset plate and bolts of the selected joint. Apart from this joint, all other joints (including the base joints) are modeled as rigid joints and all other angle members of the tower are modeled using beam elements, which are actually the BEAM188 elements in the FE software ANSYS. Like the conventional modeling, the joint eccentricity is neglected when the beam elements and rigid joints are used. The completed multi-scale model of the transmission tower is shown in Figure 2 together with the local joint model. It is noted that there is an interface for each of 9 angle members used in the joint between the global tower model and the local joint model.

One of the most complex problems in the local modeling of the joint is the interaction between different components for bolt connection, such as the contact between the bolt and the angle member, the contact between the bolt and the gusset plate, and the contact between the angle member and the gusset plate. These interactions are achieved by using the contact elements TARGE170 and CONTA174 of surface-to-surface type, which avoid one element to penetrate into another. Furthermore, these contact elements can simulate friction forces between the two surfaces according to the Mohr–Coulomb law. The friction forces depend on the smoothness of the surfaces and the pretension forces of the bolts. The value of the coefficient of friction is taken as 0.3 in this study. The pretension force elements PRETS179 are used to simulate the pre-tightening of the bolts. In terms of stiffness, the interaction between the angle member and gusset plate is defined as the flexible-to-flexible contact problem because both of them are of equal stiffness. The interaction between the bolt and the gusset plate or angle member is defined as the rigid-to-flexible contact problem because the bolt is considered stiffer than the plate or the angle member. In the contact problem concerned, the first part refers to the target and the second part to the contact surface. For a rigid-to-flexible contact, the target surface is always more stiff and the contact surface is always less stiff. The contact elements are applied to the joint components by the Augmented Lagrange formulation, and the contact stiffness is updated during equilibrium iteration. Figure 3 shows the contact interaction between angle member, gusset plate and bolt of the local joint. Finally, the interface of the angle member between the solid and beam elements is coupled by using the constraint method recently developed by the authors [30]. The new constraint method is briefly described in the following section for the sake of completion and easy understanding.

#### 4. INTERFACE COUPLING OF MIXED-DIMENSIONAL ELEMENTS

Taking the interface coupling of beam-to-solid elements as an example, the displacement constraint can be established in the sense that the displacement of beam at the interface equals to the generalized displacement of solid at the interface, which can be expressed as

$$c(\mathbf{u}_B, \mathbf{u}_S) = \mathbf{u}_B - \mathbf{C}\mathbf{u}_S = 0 \quad (1)$$

where  $\mathbf{u}_B$  and  $\mathbf{u}_S$  are the nodal displacement vector of beam and solid, respectively, at the interface;  $\mathbf{C}$  is the weighting coefficient matrix of the displacement constraint equation.

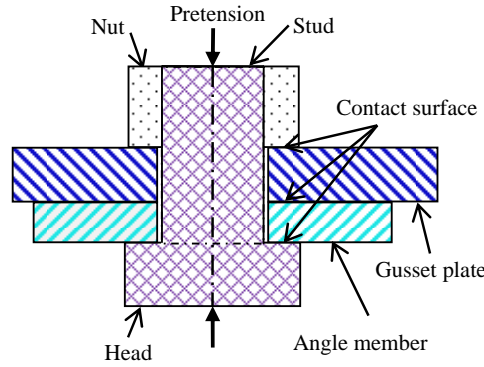
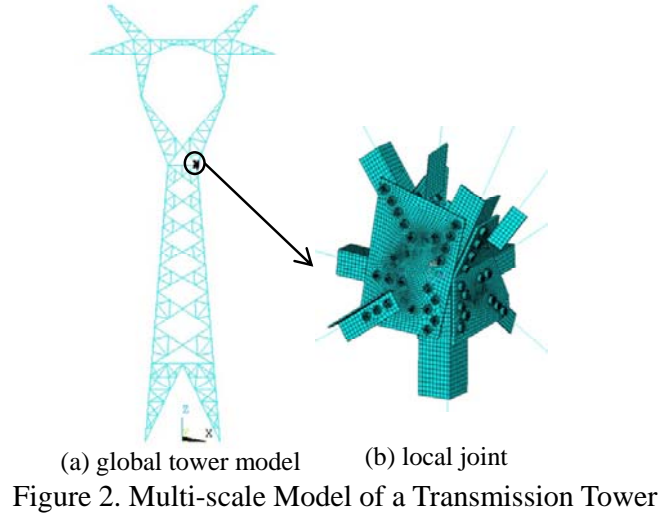


Figure 3. Contact between Angle Member, Gusset Plate and Bolt of the Local Joint

The variation of Eq. 1 can be expressed as

$$\delta c(\mathbf{u}_B, \mathbf{u}_S) = \delta \mathbf{u}_B^T \mathbf{C} \delta \mathbf{u}_S = 0 \quad (2)$$

in which  $\delta \mathbf{u}_B$  and  $\delta \mathbf{u}_S$  are the virtual displacement vectors at the interface of beam and solid, respectively.

The sum of virtual work done by the corresponding forces at the interface of the two types of elements shall be zero.

$$\delta W_B + \delta W_S = 0 \quad (3)$$

where  $\delta W_B$  and  $\delta W_S$  are the virtual works done by the nodal forces at the interface of beam and solid, respectively.

The virtual works done by the nodal forces at the interface of solid and beam are respectively

$$\begin{aligned} \delta W_S &= \delta \mathbf{u}_S^T \mathbf{F}_S \\ \delta W_B &= \delta \mathbf{u}_B^T \mathbf{F}_B \end{aligned} \quad (4)$$

where  $\mathbf{F}_S$  and  $\mathbf{F}_B$  are the nodal forces at the interface of solid and beam, respectively.

By substituting Eq. (4) into Eq. (3), we have the following equation

$$\delta \mathbf{u}_S^T \mathbf{F}_S + \delta \mathbf{u}_B^T \mathbf{F}_B = 0 \quad (5)$$

From Eq. 2, we have  $\delta \mathbf{u}_B = \mathbf{C} \delta \mathbf{u}_S$ . Eq. 5 then becomes

$$\delta \mathbf{u}_S^T \mathbf{F}_S + \delta \mathbf{u}_S^T \mathbf{C}^T \mathbf{F}_B = 0 \quad (6)$$

Eq. 6 shall hold for any arbitrary virtual displacements, and thus the nodal forces shall be related by

$$\mathbf{F}_S = -\mathbf{C}^T \mathbf{F}_B \quad (7)$$

Eq. 7 gives the constraint equation of nodal forces of beam and solid at the interface. The matrix  $\mathbf{C}^T$  can be regarded as a distribution matrix to distribute the forces or moment at the beam node to the solid nodes at the interface, and one column of the distribution matrix  $\mathbf{C}^T$  actually corresponds to the nodal forces of the solid at the interface under unit force or moment. Therefore, a numerical method has been developed to calculate the nodal forces of the solid by applying unit force or moment and finally to construct the distribution matrix  $\mathbf{C}^T$  [30]. Once distribution matrix is obtained, the displacement constraint equation can be easily found by the transpose of the distribution matrix.

In this study, the interface coupling of mixed-dimensional elements is achieved by imposing the constraint equations in the commercial software ANSYS [31] using the CE command. The FE model of local joint and the interface coupling between the beam and solid elements are shown in Figure 4.

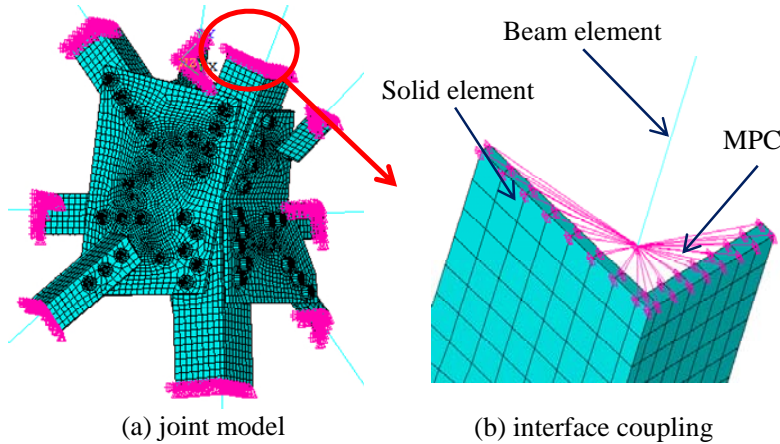


Figure 4. Finite Element Model of Local Joint and Interface Coupling

## 5. VERIFICATION OF MULTI-SCALE MODELING METHOD

### 5.1 Test Cases

A static test was first carried out on the physical model of the transmission tower fixed on the ground of the laboratory. A horizontal concentrated load was applied at the middle of cross arm of the transmission tower in the longitudinal direction (transmission line direction) as shown in Figure 5.

The concentrated load was increased step by step up to 60N at an incremental load of 10 N. A total of 3 displacement transducers (D1-D3) and 26 strain gauges (S1-S26) were used to measure the static responses of the tower due to the concentrated load. The measurement results of static displacements and stains are listed in Table 1-Table 3.

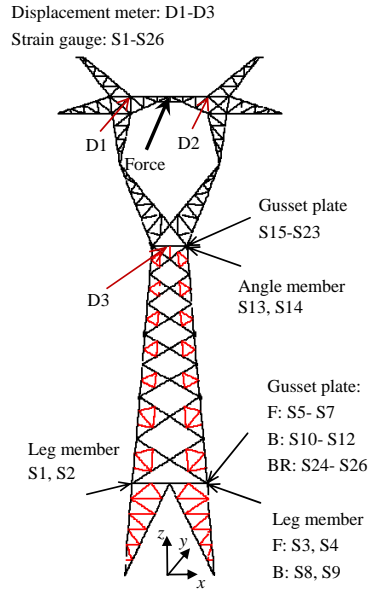


Figure 5. Locations of Loading Point and Measurement Points in Static Test

Table 1. Comparison of Static Displacement Responses (mm)

Measurement point	Load (N)	Measured displacement	Beam model	Error (%)	Multi-scale model	Error (%)
D1	10	0.224	0.228	1.8	0.228	1.8
	20	0.468	0.457	-2.4	0.457	-2.4
	30	0.701	0.685	-2.3	0.686	-2.1
	40	0.915	0.913	-0.2	0.915	0.0
	50	1.132	1.142	0.9	1.144	1.1
	60	1.378	1.370	-0.6	1.373	-0.4
D2	10	0.223	0.228	2.2	0.228	2.2
	20	0.462	0.456	-1.3	0.458	-0.9
	30	0.689	0.684	-0.7	0.688	-0.1
	40	0.907	0.911	0.4	0.917	1.1
	50	1.130	1.139	0.8	1.147	1.5
	60	1.377	1.367	-0.7	1.377	0.0
D3	10	0.059	0.063	6.8	0.061	3.4
	20	0.120	0.126	5.0	0.123	2.5
	30	0.181	0.189	4.4	0.184	1.7
	40	0.247	0.252	2.0	0.245	-0.8
	50	0.305	0.315	3.3	0.307	0.7
	60	0.367	0.378	3.0	0.368	0.3

Table 2. Comparison of Static Strain on the Main Member of the Tower Leg ( $10^{-6}$ )

Gauge number	Measured strain	Beam model	Error (%)	Multi-scale model	Error (%)
S1	21.59	22.33	3.43	22.34	3.47
S2	26.55	25.73	3.09	25.73	3.09
S3	26.93	25.69	4.60	25.68	4.64
S4	22.52	22.33	0.84	22.33	0.84
S8	-21.09	-22.30	5.74	-22.31	5.76
S9	-25.41	-25.71	1.18	-25.71	1.18

Table 3. Comparison of Static Strain on the Local Joint ( $10^{-6}$ )

Gauge number	Measured strain	Beam model	Error (%)	Multi-scale model	Error (%)
S13	34.10	28.83	15.45	34.62	1.52
S14	12.27	24.48	99.51	11.70	4.65
S15, S16, S17	21.90	-	-	23.63	7.90
S18, S19, S20	8.20	-	-	8.82	7.56

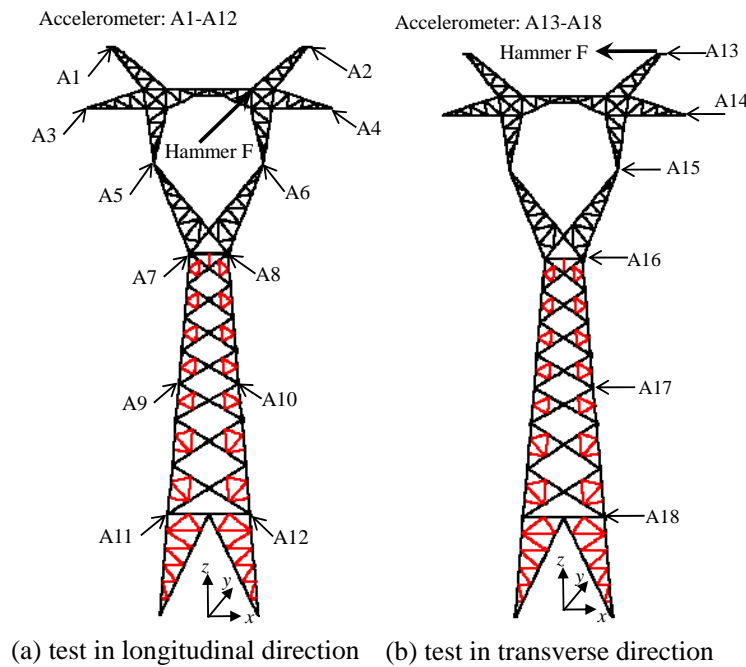


Figure 6. Locations of Accelerometers in Hammer Test

After the static tests were completed, the hammer tests were then carried out on the physical model of the transmission tower to identify the natural frequencies and modal shapes of the tower. Accelerometers were accordingly arranged in both longitudinal and transverse directions and their locations are shown in Figure 6. The measured first 9 natural frequencies are listed in Table 4.

## 5.2 Comparison of Static Displacements and Strains

In addition to the multi-scale model of the tower, the beam model of the tower is also built in a conventional way, in which the BEAM188 elements and the rigid joints are used without considering joint eccentricity. Both the beam model and multi-scale model of the transmission tower are used to calculate the strain and displacement responses of the tower under the concentrated load, and the results from the multi-scale model and the beam model are then compared with those from the static tests. Table 1 lists the displacement values against concentrated load for the multi-scale model, the beam model, and the physical model. The force-displacement relationships of the measurement points D1, D2 and D3 are shown in Figure 7. It can be seen that the force-displacement relationship is almost linear within the applied load range. For D1 and D2, the results from the beam model and the multi-scale model are almost the same. The results obtained from the multi-scale model are also very close to the test results. For D3, the displacements obtained from the multi-scale model are closer to the test results than the results from the beam model. In consideration of the locations of D1, D2 and D3 as shown in Figure 5, D1 and D2 locate on the cross arm of the tower and they are far away from the local joint modeled by



the solid elements. Therefore, the displacement results of D1 and D2 from the multi-scale model and the beam model are very close. On the other hand, D3 locates on the angle member that is connected to the local joint modeled by the solid elements. The multi-scale model can therefore improve the accuracy of the displacement of the angle member at D3.

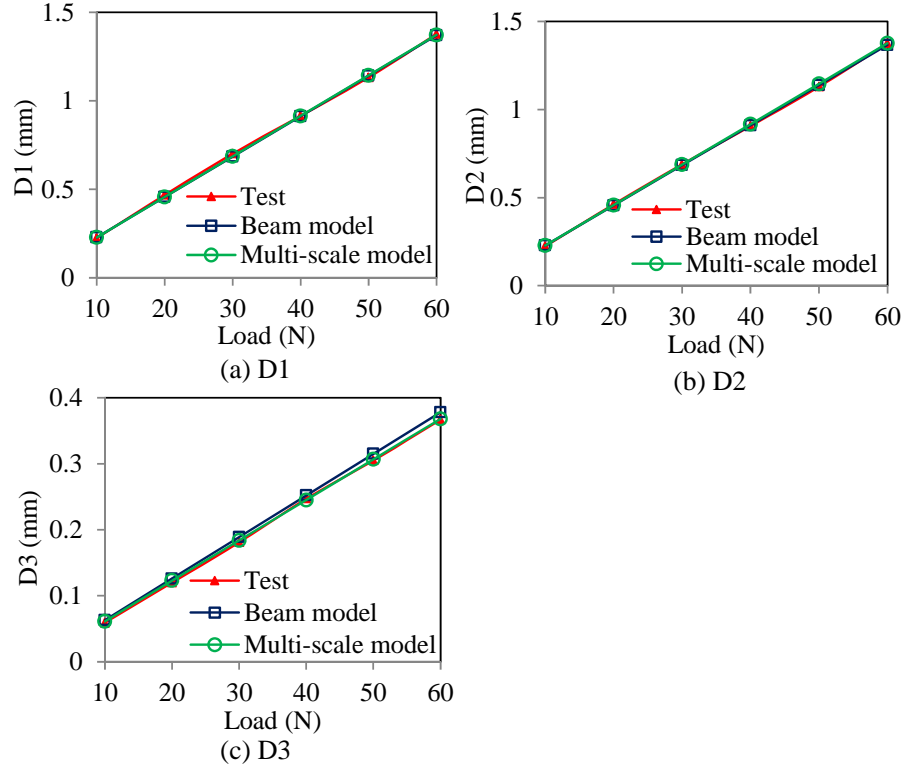


Figure 7. Force-displacement Relationship

The comparison results of the strain responses to the horizontal concentrated load of 60N are listed in Table 2 for the main member of the tower leg. The strain results obtained from the multi-scale model are very close to the test results. For the strain responses of the main member of the tower leg, the multi-scale model and the beam model provide almost the same accuracy. The reason is that the measurement points on the tower leg are far away from the local joint modeled by the solid elements.

Figure 8 shows the locations of strain gauges on the gusset plate and the main member of the local joint, which are modeled in much detail using the solid elements in the multi-scale model of the tower. The equivalent strain used for the comparison of strain responses on the gusset plate is computed by

$$\varepsilon_e = \frac{1}{1+\nu} \left[ \frac{(\varepsilon_1 - \varepsilon_2)^2 + (\varepsilon_2 - \varepsilon_3)^2 + (\varepsilon_3 - \varepsilon_1)^2}{2} \right]^{\frac{1}{2}} \quad (8)$$

where  $\varepsilon_1$ ,  $\varepsilon_2$  and  $\varepsilon_3$  are the principal strains; and  $\nu$  is the effective Poisson's ratio. In the static test, the strain rosettes were used to measure the strain state of the gusset plate, and two principal strains are calculated from the measured strain state. Eq. (8) is then used to calculate the equivalent strain by combining the two principal strains obtained from the measured results of the strain rosette and a zero principal strain.

The comparison results of strains of the local joint are listed in Table 3. It can be seen that the strain responses of the main member near the local joint (measurement points S13 and S14) calculated from the multi-scale model are more accurate than those from the beam model if the test results are referred. The maximum error by using the beam model and the multi-scale model are 99.51% and 4.65%, respectively, with respect to the test results. From the test results of S13 and S14, it can be seen that the main member is under large bending moment caused by the bolt connection. However, the beam model built by rigid joints cannot simulate this bending moment caused by the bolt connection. Therefore, the errors in the strain responses of the main members connected to the local joint are very large if the beam model is used. The multi-scale model uses solid elements for modeling the local joint, which can effectively simulate the force transmission from the bolt connection. Therefore, the multi-scale model can obtain good accuracy for the strain responses of the main members connected to the local joint. Furthermore, the multi-scale model can obtain the strain responses of the gusset plate with good accuracy of the maximum error less than 7.90%. From the comparison of the static responses of displacement and strain, it can be concluded that the multi-scale model can obtain more accurate strain and displacement responses at the region near the local joint modeled by the solid elements.

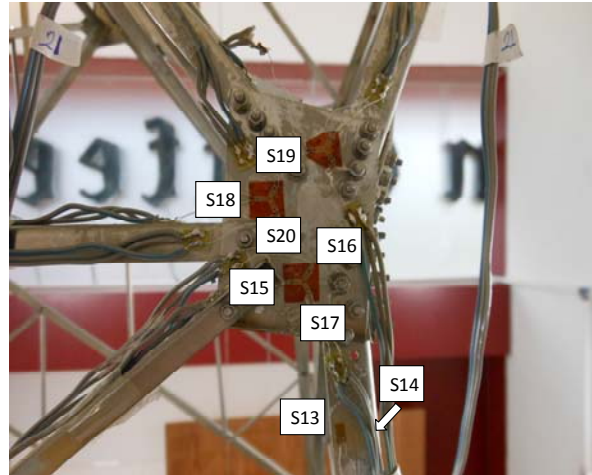


Figure 8. Locations of Strain Gauges on Local Joint

### 5.3 Comparison of Dynamic Characteristics

The modal analysis is carried out using the beam model and multi-scale model of the transmission tower. The natural frequencies are obtained and compared with the test results, as listed in Table 4. It can be seen that the maximum error using the multi-scale model occurs at the sixth natural frequency with a relative error of 5.41%. The first, second and third mode shapes of the tower obtained from the multi-scale model are shown in Figure 9. It can be seen that the first mode of vibration is the translational mode mainly in the longitudinal direction. The second mode of vibration is also the translational mode but mainly in the transverse direction. The third mode of vibration is the torsional mode. The comparison of the first nine mode shapes from the multi-scale analysis (MSA) and the test are shown in Figure 10, in which the mode shapes are shown in different directions. The first, third, fourth, fifth and sixth order mode shapes are shown in the longitudinal direction, whereas the second, seventh, eighth and ninth order mode shapes are shown in the transverse direction. The first three mode shapes from the multi-scale analysis agree well with the test results. For other higher order mode shapes, some differences exist between the multi-scale analysis and the test.

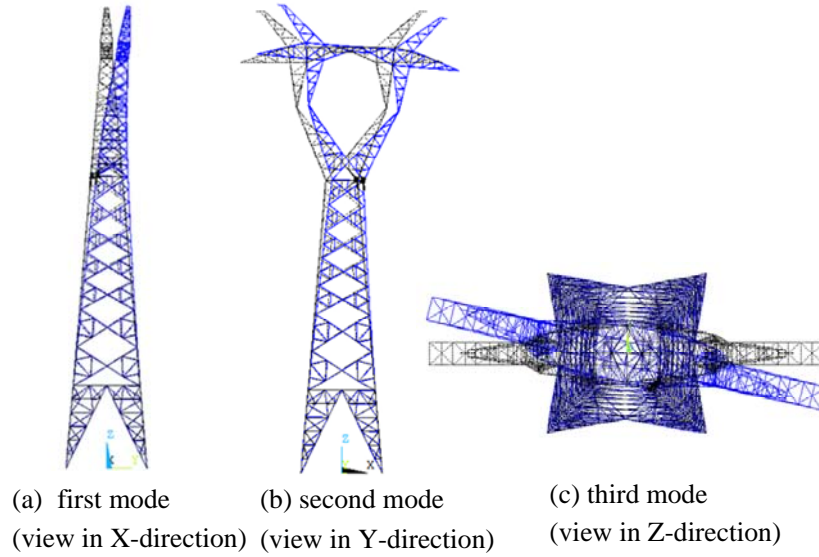


Figure 9. The First Three Mode Shapes of the Tower obtained from the Multi-scale Model

Table 4. Comparison of Natural Frequencies (Hz)

Mode no.	Mode shape description	Measured frequency	Beam model	Error (%)	Multi-scale model	Error (%)
1	Longitudinal bending	16.56	16.39	1.03	16.38	1.09
2	Transverse bending	16.81	16.46	2.08	16.44	2.20
3	Torsion	22.50	23.63	5.02	23.49	4.40
4	Longitudinal bending	44.36	44.40	0.09	44.40	0.09
5	Longitudinal bending	44.50	44.62	0.27	44.63	0.29
6	Longitudinal bending	50.44	53.06	5.19	53.17	5.41
7	Transverse bending	52.30	53.56	2.41	53.62	2.52
8	Transverse bending	59.83	57.54	3.83	57.58	3.76
9	Transverse bending	60.56	57.72	4.69	57.75	4.64

The Modal Assurance Criteria (MAC) is calculated as

$$MAC(\phi_i^{test}, \phi_i^{FE}) = \frac{(\phi_i^{test} \phi_i^{FE})^2}{(\phi_i^{test} \phi_i^{test})(\phi_i^{FE} \phi_i^{FE})} \quad (9)$$

where  $\phi_i^{test}$  and  $\phi_i^{FE}$  are the  $i$ th mode shape from test and finite element analysis, respectively. The MAC values for the beam model and the multi-scale model are listed in Table 5. It can be seen that the multi-scale model and the beam model have almost the same accuracy for mode shapes. The similar natural frequencies and mode shapes from the beam model and the multi-scale model are understandable because the difference between the beam model and the multi-scale model is one local joint model in the multi-scale model, which does not affect the global dynamic characteristics of the tower.

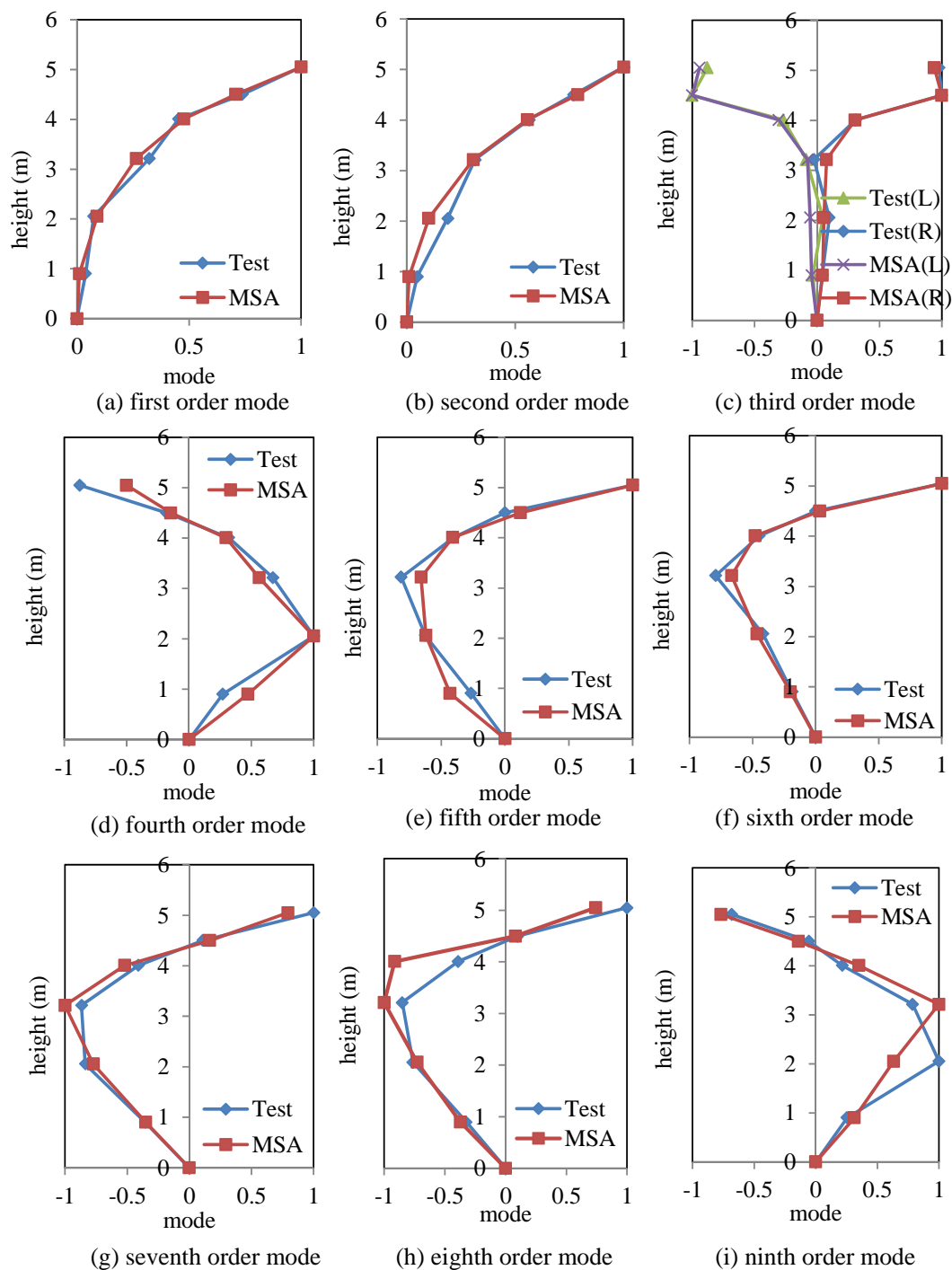


Figure 10. Comparison of the First Nine Mode Shapes from the Multi-scale Analysis and Test

Table 5. MAC of Modal Shapes

Mode number	1	2	3	4	5	6	7	8	9
Beam model	0.9939	0.9958	0.9936	0.9407	0.9653	0.9889	0.9741	0.9089	0.9107
Multi-scale model	0.9940	0.9958	0.9935	0.9377	0.9664	0.9897	0.9719	0.9104	0.9075

## 6. CONCLUSIONS

The multi-scale modeling method has been developed for the simultaneous global and local analysis of a transmission tower structure with bolt connections. The solid elements are used to model the bolted-connection joint that includes angle members, gusset plates and bolts. All other joints are modeled as rigid joints and all other angle members are modeled by the beam elements. A physical model of the transmission tower has been constructed and tested. The calculated results from the multi-scale model and the beam model are compared with those from the tests. The comparative results demonstrate that the calculated displacement responses from the multi-scale model and the beam model are very close to the measured ones if the locations of the concerned displacements are away from the flexible joint modeled by the solid elements. The calculated natural frequencies and mode shapes from the multi-scale model and the beam model are also close to the measured ones. Compared with the beam model, the multi-scale model can obtain more accurate strain and displacement responses of the members connected to the local joint that is modeled by the solid elements. By using the solid elements for modeling the local joint, the multi-scale model effectively simulates the force transmission of bolt connections and provides good accuracy for the strain responses of the main members connected to the local joint modeled by the solid elements. The multi-scale modeling method has great advantages of improving the accuracy of local responses for the large transmission tower.

## ACKNOWLEDGMENTS

The work described in this paper is financially supported by The Hong Kong Research Grants Council through its competitive grant (PolyU 5289/12E) and by the Natural Science Foundation of China through its key research program (NSFC 50830203), to which the authors are grateful.

## REFERENCES

- [1] Albermani, F.G.A. and Kitipornchai, S., "Numerical Simulation of Structural Behaviour of Transmission Towers", *Thin-walled Structures*, 2003, Vol. 41, No. 2–3, pp. 167-177.
- [2] Chan, S.L. and Cho, S.H., "Second-order Analysis and Design of Angle Trusses Part I: Elastic Analysis and Design", *Engineering Structures*, 2008, Vol. 30, No. 3, pp. 616-625.
- [3] Rao, N.P., Knight, G.M.S., Lakshmanan, N. and Iyer, N.R., "Investigation of Transmission Line Tower Failures", *Engineering Failure Analysis*, 2010, Vol. 17, No. 5, pp. 1127-1141.
- [4] Roy, S., Fang, S.J. and Rossow, E.C., "Secondary Stresses on Transmission Tower Structures", *Journal Of Energy Engineering-Asce*, 1984, Vol. 110, No. 2, pp. 157-172.
- [5] Rao, N.P. and Kalyanaraman, V., "Non-linear Behaviour of Lattice Panel of Angle Towers", *Journal of Constructional Steel Research*, 2001, Vol. 57, No. 12, pp. 1337-1357.
- [6] Jiang, W.Q., Wang, Z.Q., McClure, G., Wang, G.L. and Geng, J.D., "Accurate Modeling of Joint Effects in Lattice Transmission Towers", *Engineering Structures*, 2011, Vol. 33, No. 5, pp. 1817-1827.
- [7] Kitipornchai, S., Albermani, F.G.A. and Peyrot, A.H., "Effect Of Bolt Slippage on Ultimate Behavior Of Lattice Structures", *Journal Of Structural Engineering*, 1994, Vol. 120, No. 8, pp. 2281-2287.
- [8] Knight, G.M.S. and Santhakumar, A.R., "Joint Effects on Behavior Of Transmission Towers", *Journal Of Structural Engineering*, 1993, Vol. 119, No. 3, pp. 698-712.
- [9] Xu, Y.L. and Zhang, W.S., "Modal analysis and seismic response of steel frames with connection dampers", *Engineering Structures*, 2001, Vol. 23, No. 4, pp. 385-396.

- [10] Ungkurapinan, N., Chandrakeerthy, S.R.D., Rajapakse, R.K.N.D. and Yue, S.B., "Joint Slip in Steel Electric Transmission Towers", *Engineering Structures*, 2003, Vol. 25, No. 6, pp. 779-788.
- [11] Cheng, J.J.R., Yam, M.C.H. and Hu, S.Z., "Elastic Buckling Strength Of Gusset Plate Connections", *Journal of Structural Engineering*, 1994, Vol. 120, No. 2, pp. 538-559.
- [12] Rosenstrauch, P.L., Sanayei, M. and Brenner, B.R., "Capacity Analysis of Gusset Plate Connections using the Whitmore, Block Shear, Global Section Shear, and Finite Element Methods", *Engineering Structures*, 2013, Vol. 48, No. 1, pp. 543-557.
- [13] Salih, E.L., Gardner, L. and Nethercot, D.A., "Bearing Failure in Stainless Steel Bolted Connections", *Engineering Structures*, 2011, Vol. 33, No. 2, pp. 549-562.
- [14] Salih, E.L., Gardner, L. and Nethercot, D.A., "Numerical Study of Stainless Steel Gusset Plate Connections", *Engineering Structures*, 2013, Vol. 49, No. 1, pp. 448-464.
- [15] Li, Z.X., Chan, T.H.T., Yu, Y. and Sun, Z.H., "Concurrent Multi-scale Modeling of Civil Infrastructures for Analyses on Structural Deterioration—Part I: Modeling Methodology and Strategy", *Finite Elements in Analysis and Design*, 2009, Vol. 45, No. 11, pp. 782-794.
- [16] Dujc, J., Brank, B. and Ibrahimbegovic, A., "Multi-scale Computational Model for Failure Analysis of Metal Frames that Includes Softening and Local Buckling", *Computer Methods in Applied Mechanics and Engineering*, 2010, Vol. 199, No. 21–22, pp. 1371-1385.
- [17] Li, Z.X., Zhou, T.Q., Chan, T.H.T. and Yu, Y., "Multi-scale Numerical Analysis on Dynamic Response and Local Damage in Long-span Bridges", *Engineering Structures*, 2007, Vol. 29, No. 7, pp. 1507-1524.
- [18] Guidault, P.A. and Belytschko, T., "On the L2 and the H1 Couplings for An Overlapping Domain Decomposition Method using Lagrange Multipliers", *International Journal for Numerical Methods in Engineering*, 2007, Vol. 70, No. 3, pp. 322-350.
- [19] Ben Dhia, H. and Rateau, G., "The Arlequin Method as a Flexible Engineering Design Tool", *International Journal for Numerical Methods In Engineering*, 2005, Vol. 62, No. 11, pp. 1442-1462.
- [20] Xu, F., Hu, H., Potier-Ferry, M. and Belouettar, S., "Bridging Techniques in a Multi-scale Modeling of Pattern Formation", *International Journal of Solids and Structures*, 2014, Vol. 51, No. 18, pp. 3119-3134.
- [21] Bauman, P.T., Dhia, H.B., Elkhodja, N., Oden, J.T. and Prudhomme, S., "On the Application of the Arlequin Method to the Coupling of Particle and Continuum Models", *Computational Mechanics*, 2008, Vol. 42, No. 4, pp. 511-530.
- [22] Wellmann, C. and Wriggers, P., "A Two-scale Model of Granular Materials", *Computer Methods in Applied Mechanics and Engineering*, 2012, Vol. 205, No. 1, pp. 46-58.
- [23] Cofer, W.F. and Will, K.M., "A Three-dimensional, Shell-solid Transition Element for General Nonlinear Analysis", *Computers & Structures*, 1991, Vol. 38, No. 4, pp. 449-462.
- [24] Garusi, E. and Tralli, A., "A Hybrid Stress-assumed Transition Element for Solid-to-beam and Plate-to-beam Connections", *Computers & Structures*, 2002, Vol. 80, No. 2, pp. 105-115.
- [25] Gmür, T.C. and Kauten, R.H., "Three-dimensional Solid-to-beam Transition Elements for Structural Dynamics Analysis", *International Journal for Numerical Methods in Engineering*, 1993, Vol. 36, No. 9, pp. 1429-1444.
- [26] Chavan, K.S. and Wriggers, P., "Consistent Coupling of Beam and Shell Models for Thermo-elastic Analysis", *International Journal for Numerical Methods in Engineering*, 2004, Vol. 59, No. 14, pp. 1861-1878.
- [27] Ho, R.J., Meguid, S.A., Zhu, Z.H. and Sauve, R.G., "Consistent Element Coupling in Nonlinear Static and Dynamic Analyses using Explicit Solvers", *International Journal of Mechanics and Materials in Design*, 2010, Vol. 6, No. 4, pp. 319-330.

- [28] McCune, R.W., Armstrong, C.G. and Robinson, D.J., "Mixed-dimensional Coupling in Finite Element Models", *International Journal For Numerical Methods In Engineering*, 2000, Vol. 49, No. 6, pp. 725-750.
- [29] Wang, J.L.W., Lou, Z.W., Min, X. and Zou, J.Z., "A DOF Expanding Method for Connecting Solid and Shell Element", *Communications In Numerical Methods In Engineering*, 1996, Vol. 12, No. 6, pp. 321-330.
- [30] Wang, F.Y., Xu, Y.L. and Qu, W.L., "Mixed-dimensional Finite Element Coupling for Structural Multi-scale Simulation", *Finite Elements in Analysis and Design*, 2014, Vol. 92, No. 1, pp. 12-25.
- [31] ANSYS, "User's Manual", ANSYS. Inc., 2010.





# SEISMIC COLLAPSE ANALYSIS OF CONCENTRICALLY-BRACED FRAMES BY THE IDA METHOD

Gang Li <sup>1,2,3,\*</sup>, Zhi-Qian Dong <sup>1,2,3</sup>, Hong-Nan Li <sup>1,2,3</sup> and Y. B. Yang <sup>4</sup>

<sup>1</sup> School of Civil Engineering, Dalian University of Technology, Dalian, Liaoning Province, 116024, China;

<sup>2</sup> State Key Laboratory of Coastal and Offshore Engineering, Dalian University of Technology, Dalian 116023, China

<sup>3</sup> Institute of Structural Control and Monitoring, Dalian University of Technology, Dalian 116023, China

<sup>4</sup> School of Civil Engineering, Chongqing University, Chongqing, 400045 China

\*(Corresponding author: E-mail gli@dlut.edu.cn)

Received: 18 February 2016; Revised: 27 July 2016; Accepted: 2 September 2016

**ABSTRACT:** Steel concentrically-braced frames (CBFs) as seismic lateral force resisting systems have been widely used in seismic regions. The *incremental dynamic analysis* (IDA) is adopted to construct the *collapse ductility spectrum* for the CBF considering the  $P-\Delta$  effect and sudden loss in strength and stiffness, which is physically more meaningful than existing baseline criteria. The *design performance plot* is constructed by newly combining the *collapse ductility spectrum* with *ductility demand spectrum* on the same figure, from which the threshold period and design ductility region for the frame are determined. A parametric study is conducted for the CBF over the full range of periods and parameters. The results show that the reserve capacity of the CBF contributes appreciably to collapse prevention, and the presented approach is more suitable for assessing the collapse of CBFs with dynamic instability. For moderate seismic regions, the threshold periods of the CBF determined by both the collapse ductility spectrum and existing baseline criteria are quite close. However, for high seismic regions, using the global drift angle limit may yield non-conservative results, since it fails to address the dynamic instability of CBFs with short periods.

**Keywords:** Concentrically-braced frames, collapse limit state, incremental dynamic analysis, ductility demand spectrum, collapse ductility spectrum

**DOI:** 10.18057/IJASC.2017.13.3.5

## 1. INTRODUCTION

The steel concentrically-braced frame (CBF) has been widely used in buildings in seismic regions, since it can provide considerable reserve lateral stiffness and strength after brace fracture. However, the behavior of the CBF is complicated in that each of the brace members may yield in tension and buckle in compression. Previous investigations reveal that buckling of brace members often precedes failure of framed members and causes a great reduction in the overall stiffness and strength, even leading to global collapse [1, 2]. Many CBFs were destroyed and even collapsed in past earthquakes due to their poor performance. Regardless of the fact that numerous experimental and theoretical studies have been carried out for CBFs, the CBF system still suffers from various degrees of damage due to its poor ductility [3-8]. Thus, the CBFs constructed based on poor design guides in earlier days still attract the attention of researchers [9-18]

CBFs in moderate seismic regions (MSRs) are typically designed using a response modification coefficient  $R$  equal to 3, which allows the seismic resistance detailing of a structure to be ignored, e.g., in the United States [19]. Although current codes and rules are obeyed strictly in the CBF design, past numerical simulations showed that the collapse of CBFs is sometimes unavoidable in moderate seismic regions [20]. In fact, the reserve capacity of the CBF after brace fracture has not been duly considered in current design and assessment procedures. Recently, Li and Fahnstock [21] studied the post-brace fracture stability of the CBF considering the reserve strength and reserve stiffness. The *ductility demand spectrum* for the CBF systems of single degree of freedom (SDOF) in moderate and high seismic regions (HSRs) was constructed. Threshold values were

determined for the period of the CBFs as the intersections of the ductility demand spectrum with the specific ductility limit ( $\mu = 3$  in MSRs,  $\mu = 6$  in HSRs) and global drift angle ( $\Theta=0.1$ ), indicative of the ductility capacity and collapse state of the CBFs. However, the specific ductility limit and global drift angle limit used cannot adequately cover all the limit states, as the structural collapse is usually governed by the dynamical instability, in addition to other parameters, of the structure. Thus, there exists a need to develop a reliable method for analyzing the stability of CBFs for the purpose of collapse prevention and understanding of the failure behavior of the system of concern.

The *incremental dynamic analysis* (IDA) is a parametric analysis method for evaluating the limit state and dynamic instability of structures. With this method, the dynamic time history analysis for a structure subjected to earthquake ground motions with increasing peak accelerations is carried out repetitively. Then, we can plot the structural response against the level of input earthquake intensity to obtain the so-called IDA curve, by which the inelastic performance and collapse strength of the structure can be assessed.

The concept of the IDA was put forward firstly by Bertero [22]. Then, it was applied to the seismic hazard analysis of nonlinear structures, particularly, to calculate the seismic drift demand for framed structures [23-26] and selected as the state-of-the-art approach to evaluate the global collapse capacity by Federal Emergency Management Agency [27, 28]. Along these lines, Vamvatsikos and Cornell [29, 30] presented the fundamental concepts, along with unified terminology, for the IDA procedure and verified the effectiveness of the procedure through a 9-story steel moment-resisting frame. Subsequently, they introduced a fast and accurate method to estimate the seismic demand and capacity of multi-degree-of-freedom (MDOF) systems that can be simplified as a SDOF system in regions ranging from near-elastic to global collapse by combining the static pushover with the IDA [31].

Considering that structural states such as the immediate occupancy and collapse limit state can be measured by the IDA curve, Ibarra [32] evaluated the global collapse capacity of SDOF systems using the IDA. Mander *et al.* [33] used the IDA to evaluate the seismic financial risk of reinforced concrete highway bridge piers. In addition, the IDA was used to evaluate the seismic performance sensitivity and uncertainty of structures and lifelines with Monte Carlo simulation [34-36], while Vamvatsikos [37] presented the procedure for performing the IDA in parallel. Recently, a new technique, called the modal incremental dynamic analysis method, was proposed for the dynamic response of structures based on the IDA method [38]. The collapse capacity and dynamic instability of inelastic nondeteriorating SDOF systems were investigated based on the IDA method [39]. Furthermore, seismic fragility and progressive collapse fragility was investigated by performing the IDA for conventional wood-framed houses and low-rise reinforced concrete framed building structures, respectively [40, 41].

In this paper, the IDA method is used to analyze the steel CBF system modeled as a SDOF system, in which the  $P-\Delta$  effect and force-deformation relation were considered for both moderate and high seismic regions. The *median collapse ductility spectrum* (MCDS) of the CBF under both the moderate and high seismic regions is constructed by the IDA method and validated by the seismic fragility and collapse margin ratio (CMR) analyses. Owing to inclusion of various structural properties in the IDA computation, such as period and restoring force versus deformation relation, the *collapse ductility spectrum* appears to be physically more representative than existing baseline criteria, e.g., specific ductility limit and global drift angle limit. The *design performance plot* is constructed by newly combining the MCDS with the *mean ductility demand spectra* (MDDS) used by Li and Fahnstock [21] on the same figure, from which the *threshold period* of the CBF is determined as the intersection of the two curves, and the *design ductility region* as the region embraced by the two curves.

## 2. COLLAPSE DUCTILITY SPECTRA BY THE IDA

### 2.1 Model of Steel Concentrically-braced Frame

Consider a low-ductility steel concentrically braced frame that is modeled as a SDOF system with reserve capacity, for which brace fracture can cause a sudden loss in strength and stiffness. Only a summary will be given of the model herein, as it has been detailed in Li and Fahnestock [21]. The CBF is modeled as a SDOF system with mass  $m$ , vertical load  $P$ , and height  $H$  in Figure 1(a). The frame provides the lateral stiffness and strength as the reserve capacity after brace fracture. As shown in Figure 1(b), after brace fracture, the total strength  $F_y$  of the CBF drops from point A to point B, indicating that the brace fracture cause a sudden loss in strength and stiffness. After passing point B, the strength increases again along line BC until it reaches the frame strength  $F_f$  at point C.

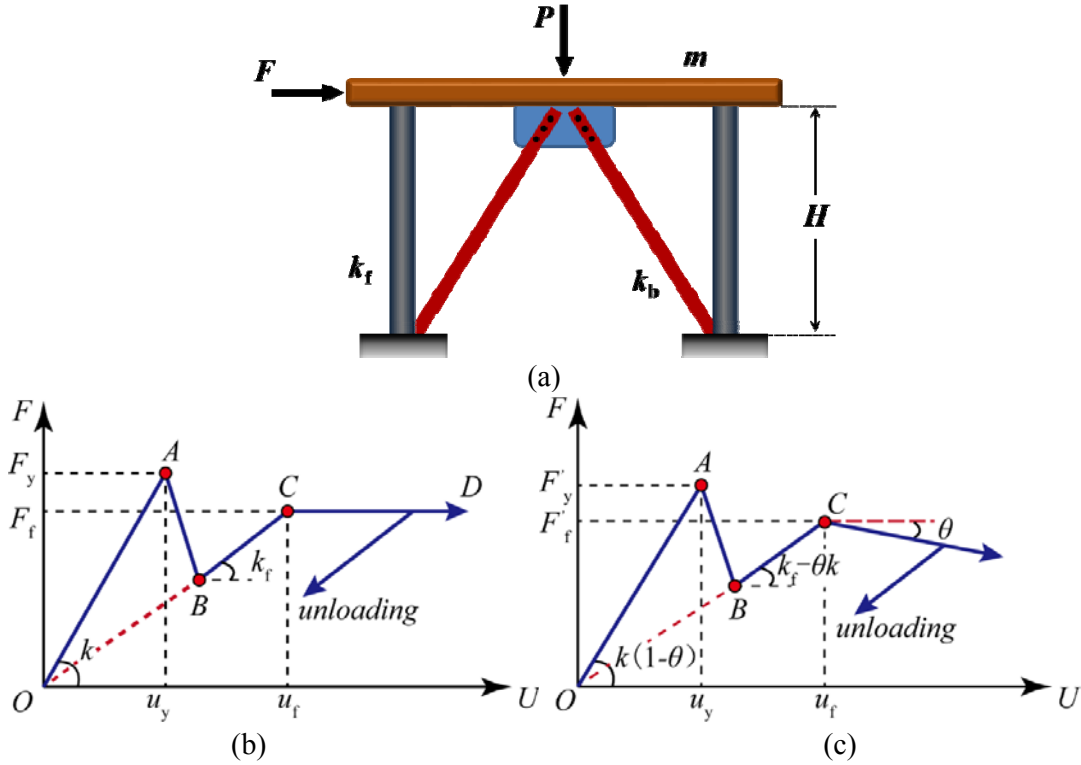


Figure 1. Model of the CBF: (a) Physical Model; (b) Force-deformation response without P-Δ Effect; (c) Force-deformation response with P-Δ effect

The ratio of the frame strength to the total strength,  $\alpha = F_f / F_y$ , is expected to be in the range of 0.1 - 1.5. The total stiffness  $k$  of the CBF system is equal to the sum of the lateral stiffness  $k_b$  provided by the braces and the lateral stiffness  $k_f$  of the moment frame. The ratio of the frame stiffness to the total stiffness,  $\beta = k_f / k$ , is assumed to be less than or equal to  $\alpha$ . In this study,  $\alpha$  is referred to as the *reserve strength*, and  $\beta$  as the *reserve stiffness*.

The stability coefficient  $\theta$  is a variable related to the  $P$ -Δ effect for stiffness reduction, as shown in Figure 1 (c). According to SEI/ASCE 7-10 [19], it can be expressed as

$$\theta = \frac{P}{kH} = \frac{1.45mg}{m\omega_n^2 \left( \frac{T}{C_t} \right)^{\frac{1}{x}}} = \frac{1.45g}{\omega_n^2 \left( \frac{T}{0.0488} \right)^{\frac{1}{0.75}}} \quad (1)$$

where  $g$  is the gravitational acceleration,  $P$  is the vertical load,  $P = 1.45 mg$  [19], with  $m$  indicating the mass of the CBF,  $T$  is the period of vibration,  $\omega_n$  is the circular frequency of the frame, and  $H$  is the height,  $H = (T / C_t)^{(1/x)}$ , with parameters  $C_t = 0.0488$  and  $x = 0.75$  for the CBFs [19].

## 2.2 Governing Equation of Motion for the CBF

The governing equation of motion for the CBF to be used in the IDA is

$$m\ddot{u} + c\dot{u} + F(u, \dot{u}, \theta) = -\lambda m\ddot{u}_g \quad (2)$$

where  $c$  is the viscous damping coefficient;  $u$ ,  $\dot{u}$  and  $\ddot{u}$  are the displacement, velocity, and acceleration of the CBF, respectively;  $F(u, \dot{u}, \theta)$  is the restoring force of the CBF, which is a function of the displacement  $u$ , velocity  $\dot{u}$ , and the stability coefficient  $\theta$ ,  $\lambda$  is the scale factor for adjusting the peak ground acceleration, and  $\ddot{u}_g$  is the input ground acceleration. Here, 14 ground motions developed by Hines *et al.* [42] for Boston in moderate seismic region and 20 ground motions developed as part of the SAC Joint Venture [27, 43, 44] for Los Angeles in high seismic region are adopted as in Li and Fahnestock [21].

After some mathematical operations [45], Eq. 2 can be rewritten as

$$\ddot{u} + 2\zeta\omega_n\dot{u} + \omega_n^2\tilde{F}(u, \dot{u}, \theta) = -\lambda\ddot{u}_g \quad (3)$$

where  $\zeta$  is the viscous damping ratio, and  $\tilde{F}(u, \dot{u}, \theta) = F(u, \dot{u}, \theta) / u_y$  is the normalized restoring force. Defining the ductility or normalized displacement and associated derivatives as  $\mu = u / u_y$ ,  $\dot{\mu} = \dot{u} / u_y$  and  $\ddot{\mu} = \ddot{u} / u_y$ , respectively, one can divide Eq. 3 by the yield displacement  $u_y$ :

$$\ddot{\mu} + 2\zeta\omega_n\dot{\mu} + \omega_n^2\tilde{F}(\mu, \dot{\mu}, \theta) = -\lambda\frac{\ddot{u}_g}{u_y} \quad (4)$$

Here, the yield displacement  $u_y$  is defined as

$$u_y = \frac{F_y}{k} = \frac{F_e / R}{m\omega^2} = \frac{mS_a}{m\omega^2 R} = \frac{S_a}{\omega^2 R} \quad (5)$$

where  $F_e$  and  $F_y$  are the maximum elastic strength and yield strength, respectively. In this study, the response modification coefficient  $R$  is taken as 3, since it represents the case adopted in the design of ordinary steel structures in MSRs where the seismic resistance detailing can be ignored [19]. The spectral acceleration  $S_a = F_e / m$  is related to the elastic response of the CBF system under earthquake ground motions. The system response is then related to the design spectrum by replacing  $S_a$  with the ordinate of the design spectrum at the period considered,  $(S_a)_{DBE}$ . Accordingly, Eq. 4 can be modified as

$$\ddot{\mu} + 2\zeta\omega_n\dot{\mu} + \omega_n^2\tilde{F}(\mu, \dot{\mu}, \theta) = -\lambda\omega_n^2 R \frac{\ddot{u}_g}{(S_a)_{DBE}} \quad (6)$$

In addition, the *frame ductility*  $\mu_f$  is defined as

$$\mu_f = \frac{u}{u_f} = \frac{u}{F_f / k_f} = \frac{u}{\alpha F_y / \beta k} = \frac{\beta u}{\alpha u_y} = \frac{\beta}{\alpha} \mu \quad (7)$$

where  $F_f$  and  $u_f$  are the frame yield strength and displacement. In this study, the frame ductility  $\mu_f$  is employed to evaluate the performance or collapse limit state of the CBF.

### 2.3 IDA Curve and Collapse Ductility Spectrum

The IDA implies repeated dynamic time history analyses for a structure under the same ground motion, but with increasing peak acceleration. Based on this, the relation established for the structural response and intensity level can be used to evaluate the performance or limit state of the structure. Using the IDA approach, the whole deformation process of the structure from elastic to collapse can be captured through the relation of the *maximum engineering demand parameter* (e.g., the peak roof drift or base shear force) and the *intensity measure* (e.g., the peak ground acceleration or the 5%-damped first-mode spectral acceleration  $S_a(T_1, 5\%)$ ) of the structure. The definitions for some relevant parameters of the CBF system are summarized below.

*Engineering demand parameter* (EDP): The frame ductility  $\mu_f$  is taken as the engineering demand parameter, normalized with respect to the frame yield displacement  $u_f$  of the frame.

*Incremental intensity* (IM): The incremental intensity is taken to be 0.05g. Although this relatively small step will make the analysis computationally consuming, it can help identify all states of the CBF when dynamic instability occurs.

*Collapse limit state*: The IDA curve starts with a straight line in the elastic range, of which the slope is marked by  $K_e$ . According to the SAC Joint Venture [27, 28], there are two collapse limit-state rules, i.e., the IM-based rule and EDP-based rule. The IM-based rule is represented by the point with a slope equal to 20% of the elastic slope on the IDA curve, as shown in Figure 2. If the story drift angle  $\theta > 0.1$ , then  $\theta = 0.1$  according to the EDP-based rule, when the collapse limit state is reached. The idea of the IM-based rule is that with the IM increasing, the EDP is increasing at an even higher rate and may approach ‘infinity’, which can be regarded as the occurrence of dynamic instability. Numerical instability similar to dynamic instability is often encountered in analyzing the structure near the collapse state, and divergence in iterations may be adopted as an indicator for judging the collapse limit state. In addition, the effect of yielding and slight ‘softening’ may result in a tangent slope less than the elastic in the initial stage of analysis [30]. However, there still exist IDA curves showing the kind of hardening behavior as in Figure 2. Such a phenomenon was also noted by Ibarra *et al.* [46].

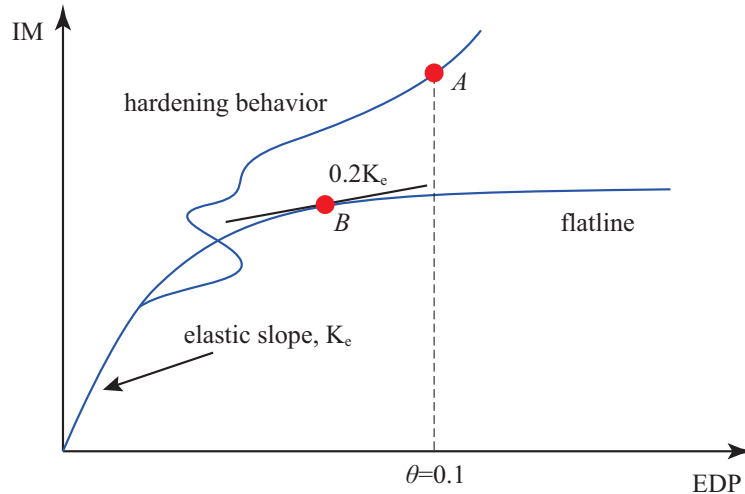


Figure 2. A Schematic IDA Curve

For each IDA curve, the collapse ductility can be determined by the collapse criterion mentioned above. The collapse ductility means that the CBF collapses owing to dynamic instability rather than inadequate ductility. For a specific earthquake, one can conduct the IDA for the CBF for a series of discrete periods, and construct a series of IDA curves similar to the one shown in Figure 3(a). By picking the collapse limit state point from the IDA curve, as in Figure 3(a), and plotting the frame ductility  $\mu_f$  against the structural period  $T$ , one can end up with the *collapse ductility spectrum* shown as in Figure 3(b).

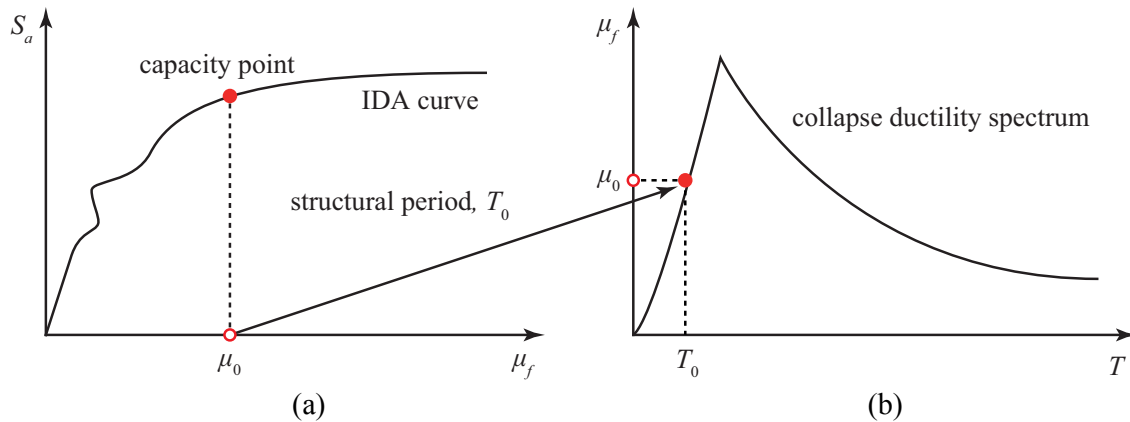


Figure 3. Generation of Collapse Ductility Spectrum for the CBF from the IDA Curve:  
(a) IDA Curve; (b) Collapse Ductility Spectrum

### 3. NUMERICAL SIMULATIONS

Newmark's method of integration with linear acceleration is adopted to solve the governing equation of motion for the CBF in the IDA, Eq. 6. The IDA for various CBFs of SDOF with different periods  $T$ , reserve strengths  $\alpha$ , and reserve stiffnesses  $\beta$  under earthquake ground motions was conducted, along with the collapse ductility spectra. In particular, a wide set of reserve strength  $\alpha$  and reserve stiffness  $\beta$  was investigated for determining the parametric ranges for prevention of the structural collapse, by combining the collapse ductility spectrum with the ductility demand spectrum on the same plot.

### 3.1 P-Δ Effect

The  $P$ -Δ effect on the collapse of structures was previously investigated by researchers [21, 39, 47]. Such an effect on the dynamic instability of CBFs will be investigated as well. Figure 4 shows the IDA curves obtained of the CBF of SDOF with period  $T = 2$  s, reserve strength  $\alpha = 0.7$ , reserve stiffness  $\beta = 0.5$ , stability coefficient  $\theta = 0.0103$  (with  $P$ -Δ effect, calculated by Eq. 1) and  $\theta = 0$  (without  $P$ -Δ effect) subjected to the San Fernando Earthquake Record ES-SJC033 in MSR. As can be seen, the two curves with and without the  $P$ -Δ effect agree well in the elastic range, but deviate from each other in the inelastic range. Particularly, the curve with the  $P$ -Δ effect exhibits obvious ‘yielding’ characteristic compared with the one without the  $P$ -Δ effect, which means that the  $P$ -Δ effect accelerates the emergence of instability or collapse for the CBF. Since the  $P$ -Δ effect has been demonstrated to be significant in the inelastic range, it will be considered in all analyses in the sections to follow.

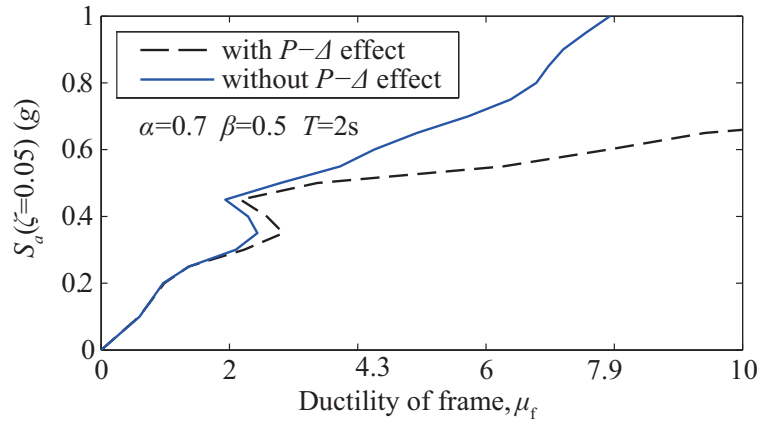
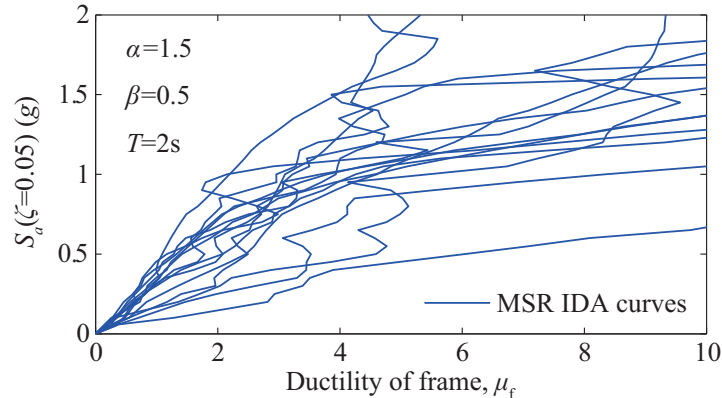


Figure 4. IDA Curves for the CBF System with and without P-Δ Effect

### 3.2 Parametric Study for IDA Curves

In Figures 5(a) and (b), the 5% damped spectral acceleration  $S_a$  is plotted against the frame ductility  $\mu_f$  of the CBF of SDOF with reserve strength  $\alpha = 1.5$ , reserve stiffness  $\beta = 0.5$  and period  $T = 2$  s under the HSR and MSR ground motion suites, respectively. Evidently, the IDA curves depend largely on the ground motion characteristics. The structural responses range from gradual degradation towards collapse to rapid, non-monotonic and back-and-forth oscillating behaviors. For the case of a frame with a smaller reserve strength  $\alpha = 1.3$  subjected to the HSR ground motion suites, the results have been plotted in Figure 5(c). Some of these IDA curves cannot end up with flatlines, which shows that the collapse criterion cannot be reached and dynamic instability can hardly occur under those ground motions.



(a)

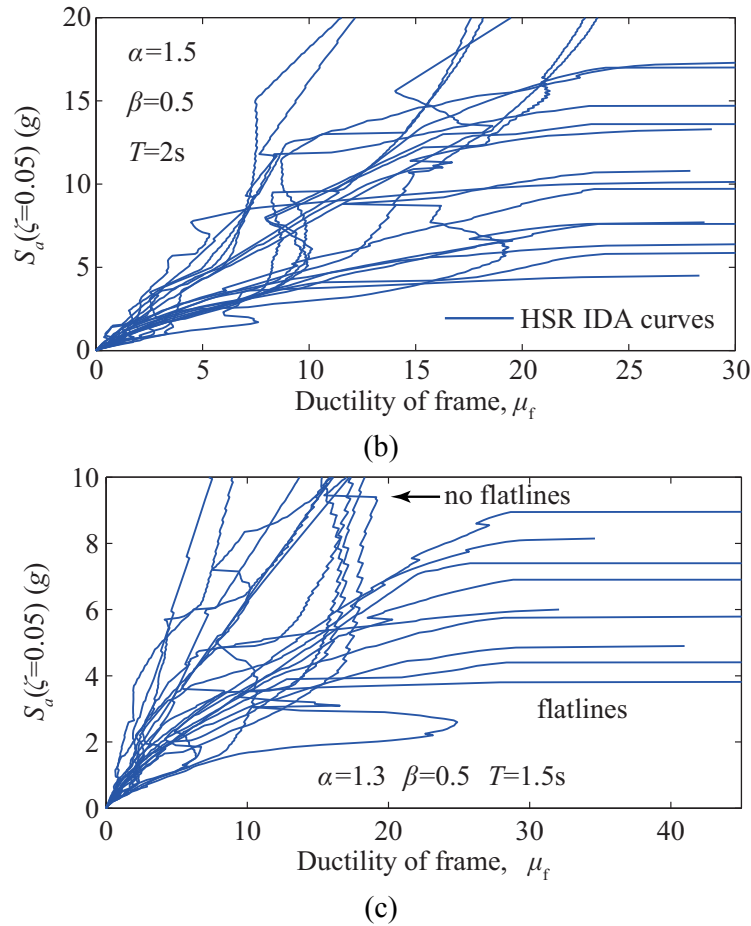


Figure 5. IDA Curves for the CBF System with: (a)  $\alpha=1.5$ ,  $\beta=0.5$  and  $T=2s$  and MSR suite; (b)  $\alpha=1.5$ ,  $\beta=0.5$  and  $T=2s$  and HSR suite; (c)  $\alpha=1.3$ ,  $\beta=0.5$  and  $T=1.5s$  and HSR suite

Although the collapse criterion has been used extensively, care should be taken when using the IDA for some special cases. For example, Figure 6(a) shows the IDA curve of a frame with  $\alpha = 0.8$ ,  $\beta = 0.3$  and  $T = 2.1$  s under the Morgan Hill Earthquake Record ER-CLS310 in MSRs. As can be seen, the point A at which the slope firstly reduces to the value of collapse should not be regarded as the collapse limit state. Rather, it is the second point (point B) that should be regarded as the collapse limit state. Such a phenomenon has been referred to as structural resurrection, which sometimes occurs when the CBF system is pushed to the global collapse under a certain IM, only to reappear as non-collapsing at a higher intensity level, displaying high response but still standing [29]. For a frame with a smaller period, i.e.,  $T = 0.6$  s, and the same values of  $\alpha$  and  $\beta$ , the IDA curve produced for the Morgan Hill Earthquake Record ER-CLS220 in MSRs has been plotted in Figure 6(b). For this case, the point that firstly reaches the collapse limit state is taken as the correct one, because the repeated analysis tends to be nonconvergent.



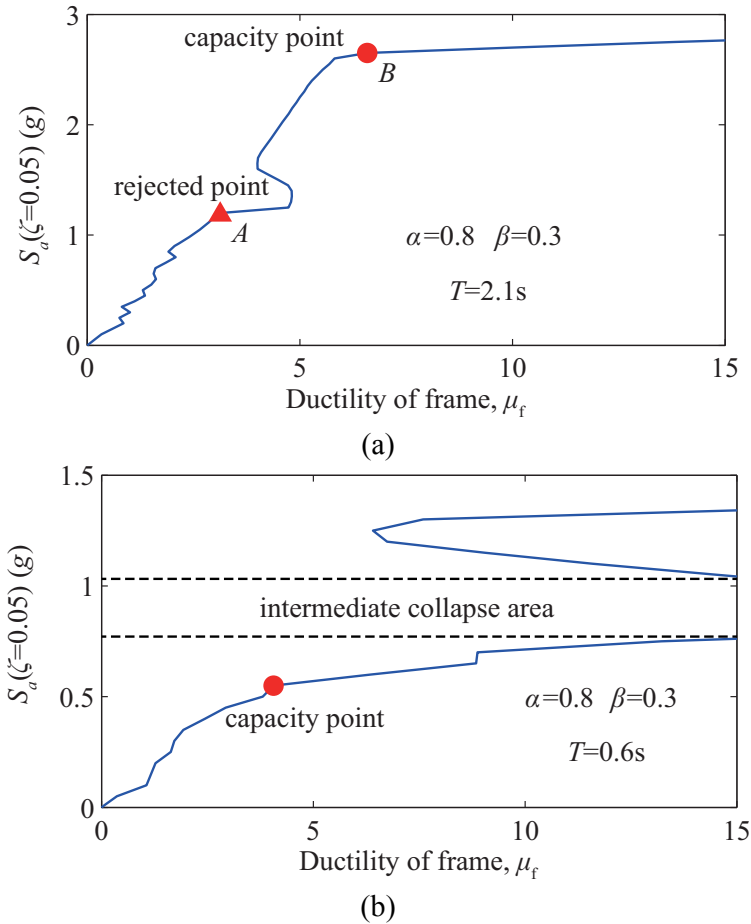


Figure 6. Specific Collapse Limit State:  
(a) resurrection phenomenon; (b) extreme resurrection phenomenon

### 3.3 Median Collapse Ductility Spectrum

The median collapse ductility spectrum (MCDS) is constructed by taking the median values of all the collapse ductility spectra. Figure 7 shows the collapse ductility spectra and the MCDS of the CBFs for the two sets of values:  $\alpha = 0.5, \beta = 0.2$  and  $\alpha = 1, \beta = 0.4$  under both the HSR and MSR ground motion suites. As can be seen, the MCDSs in both the high and moderate seismic regions show similar trends of variation, but they depend mainly on the values of  $\alpha$  and  $\beta$ . When  $\alpha$  and  $\beta$  have large values, the collapse ductility of the CBF with long periods is very large, even unachievable in practice, as shown in Figures 7(c) and (d). For these cases, the MCDS for the frames with long periods are considered infinite, meaning that the frame can never collapse under real earthquakes for these numerical models.

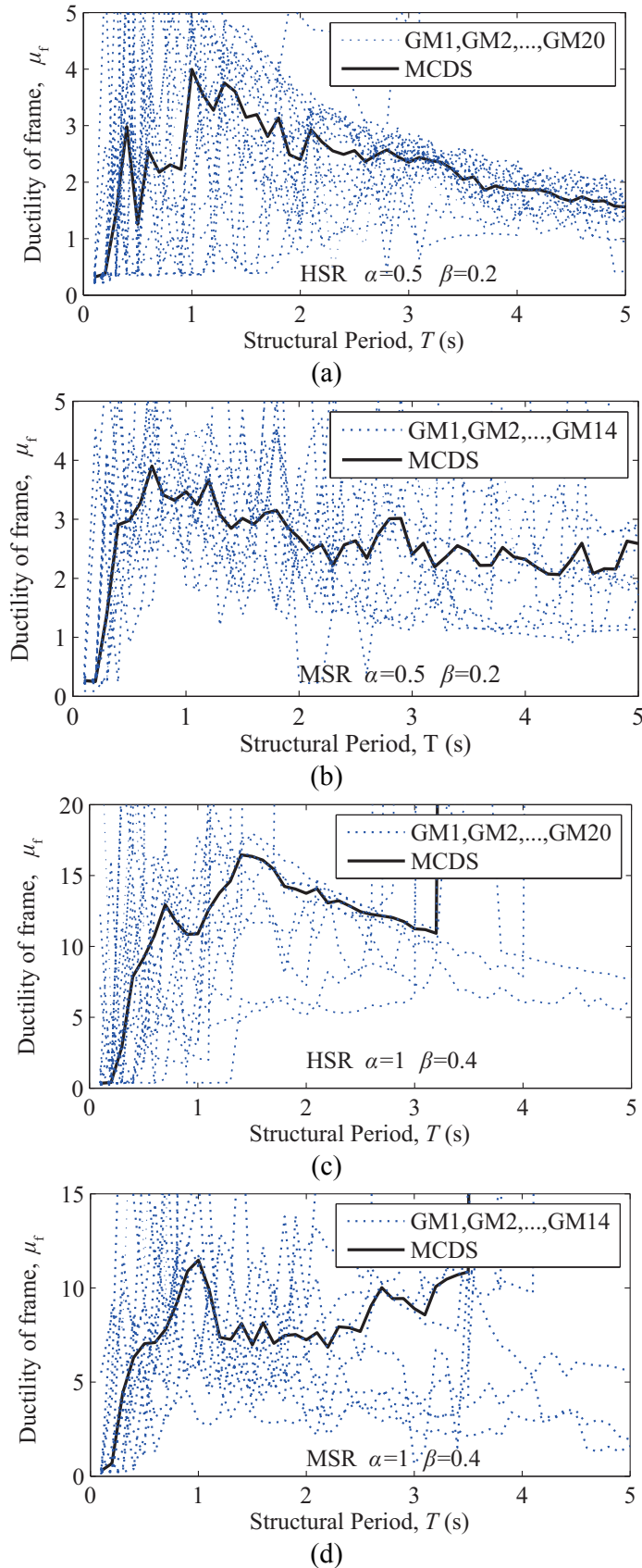


Figure 7. Collapse Ductility Spectra and the MCDS for the CBFs with: (a)  $\alpha=0.5$ ,  $\beta=0.2$  and HSR suite; (b)  $\alpha=0.5$ ,  $\beta=0.2$  and MSR suite; (c)  $\alpha=1$ ,  $\beta=0.4$  and HSR suite; (d)  $\alpha=1$ ,  $\beta=0.4$  and MSR suite

For  $\alpha = 0.8$  but with varying values of  $\beta$ , the frame ductility  $\mu_f$  has been plotted against the structural period  $T$  under the MSR ground motion suite in Figure 8(a). This figure indicates that the reserve stiffness  $\beta$  has significant influence on the response, in that the collapse ductility increases with increasing value of  $\beta$ . On the other hand, for  $\beta = 0.3$ , but with  $\alpha$  increasing from 0.7 to 1.0, the curves for the frame ductility  $\mu_f$  versus the structural period  $T$  in Figure 8(b) shows that the reserve strength  $\alpha$  has relatively little influence on the collapse ductility. Consequently, it is concluded that the collapse ductility spectra is less sensitive to the reserve strength  $\alpha$  rather than the reserve stiffness  $\beta$ .

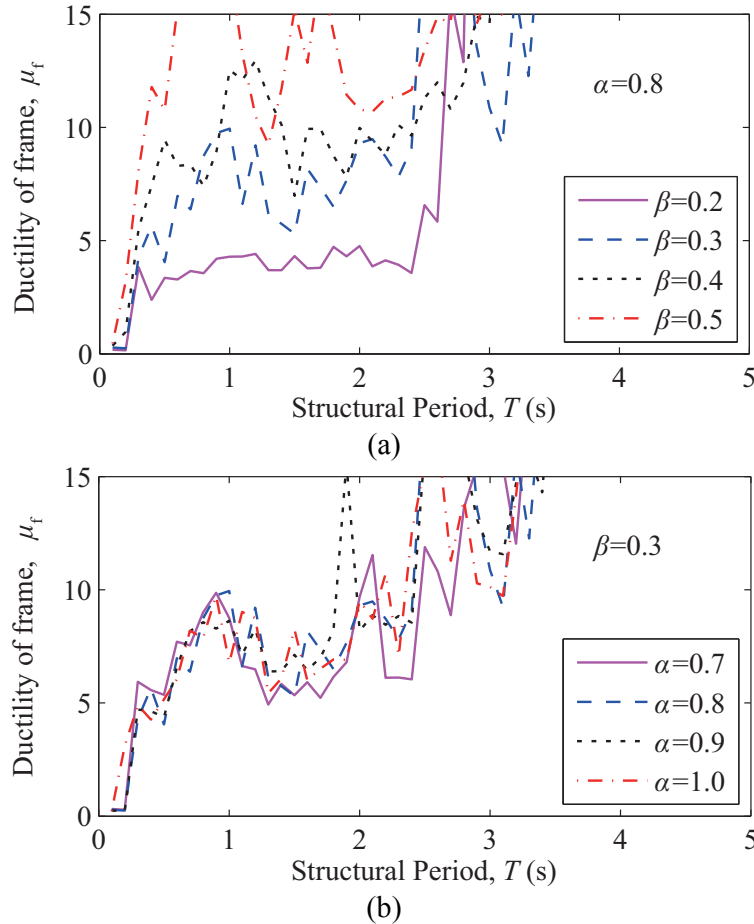
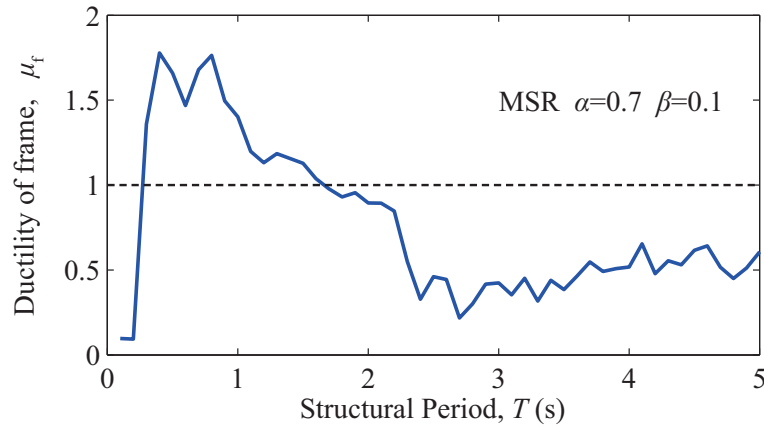


Figure 8 Effects of  $\alpha$  and  $\beta$  for median collapse ductility spectra under the MSR ground motion suite: (a)  $\alpha=0.8$ ,  $\beta=0.2-0.5$ ; (b)  $\beta=0.3$ ,  $\alpha=0.7-1.0$ .

Specifically, for the CBF with  $\beta = 0.1$ , the collapse frame ductility is less than 1 in some period ranges as shown in Figure 9, meaning that brace fracture actually determines the collapse strength of the entire CBF system. It is understood that for such cases, relatively large ductility can hardly be achieved in practice. Thus for CBFs of this type, it is reasonable to ignore unrealistic collapse ductility in practical designs.

Figure 9. MCDS for the CBF system with  $\alpha=0.7$ ,  $\beta=0.1$ 

#### 4. COLLAPSE PREVENTION STATE EVALUATION

##### 4.1 Determination of Threshold Period

The mean ductility demand spectra (MDDS) for steel CBFs were proposed for use together with the specific ductility limit ( $\mu = 3$  in MSRs,  $\mu = 6$  in HSRs) and global drift limit ( $\Theta=0.1$ ) to assess the strength of the CBF by Li and Fahnestock [21]. Rather than using the above two baseline criteria, the *median collapse ductility spectrum* (MCDS) that is physically more representative will be newly adopted herein for assessing the strength of the CBF system. Such an idea was illustrated in the *design performance plot* in Figure 10, in which the curves for both the ductility demand spectrum and collapse ductility spectrum have been plotted, and the threshold period  $T$  of the frame is determined as the intersection of the two curves.

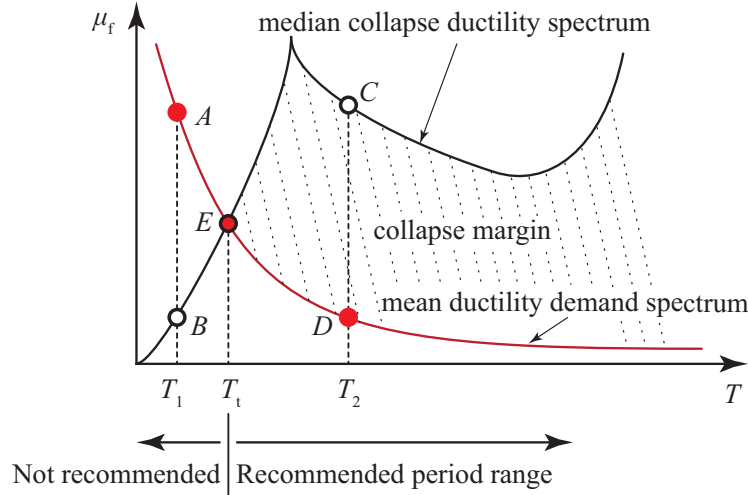


Figure 10. Design Performance Plot based on the Collapse Ductility Spectrum and Ductility Demand Spectrum

In this study, the threshold period  $T$  has been computed for a certain range of  $\alpha$  and  $\beta$  values for the CBF, above which the performance of the frame is considered acceptable. In the performance plot, the ductility demand spectrum represents the minimum ductility that a CBF should possess in a given seismic region. When the CBF undergoes earthquakes with the design intensity, it will be safe. However, if the intensity of input earthquakes exceeds the design level, there is no guarantee for prevention of collapse for the CBF designed solely based on the ductility demand spectra, but excluding the collapse ductility spectrum.

For example, for a CBF with natural period  $T_1$  and a given set of  $\alpha$  and  $\beta$  in Figure 10, it is unsafe, since the collapse ductility at point B is smaller than ductility demand at point A, meaning that the basic ductility demand is not satisfied due to the early collapse of the frame. Meanwhile, for a CBF with natural period  $T_2$ , it is considered safe, due to existence of a large ductility range from point D to point C. Thus, the ductility marked as a shaded region enclosed by the two curves of MCDS and MDDS in Figure 10 can be regarded as the *design ductility region* for the CBF, of which the boundaries are also referred to as the collapse margins.

Figure 11(a) shows the case with  $\alpha = 1$  and  $\beta = 0.3$  under the MSR suite, the MDDS and MCDS curves of the CBF, along with their intersection point. It can be found that the set of  $\alpha$  and  $\beta$  values is suitable to the CBFs with a structural period larger than 0.49 s. For CBFs with a structural period less than 0.49 s, it will collapse when subjected to earthquakes with the design intensity level. A similar case for the HSRs is shown in Figure 11(b).

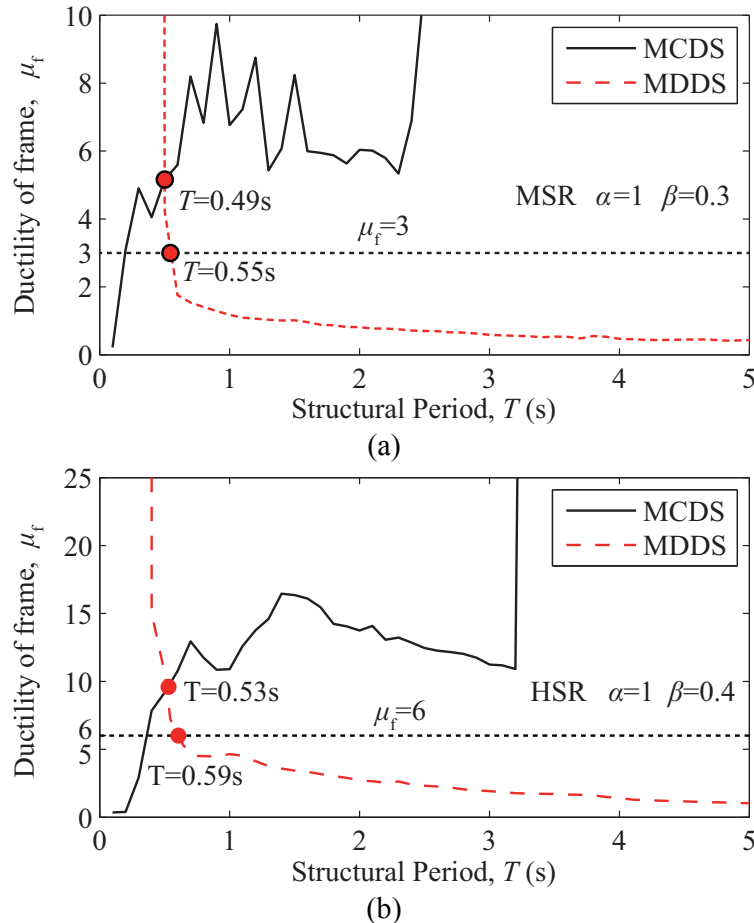


Figure 11. MCDS and MDDS for the CBF with:  
(a)  $\alpha=1$  and  $\beta=0.3$  under the MSR suite; (b)  $\alpha=1$  and  $\beta=0.4$  under the HSR suite

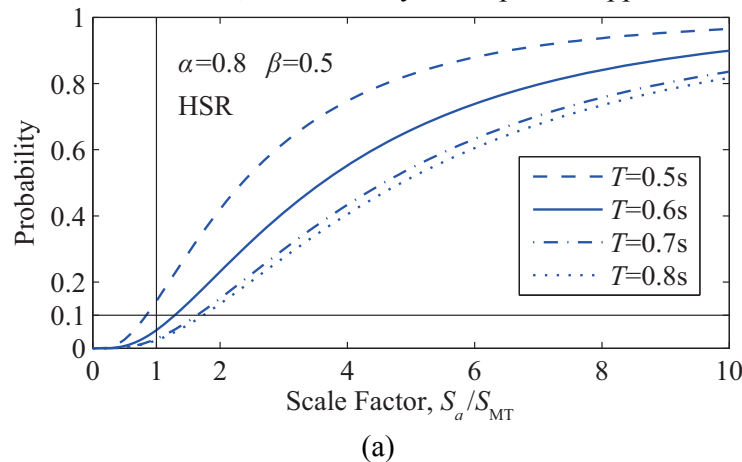
For the two CBF systems shown in Figures 11(a) and (b), the threshold period determined by the local ductility limits of  $\mu = 3$  and 6 [21] are 0.55 and 0.59 s for the MSRs and HSRs, respectively. For comparison, the values obtained by the global drift angle limit are 0.5 and 0.3 s, respectively [21]. The results obtained for other cases with various  $\alpha$  and  $\beta$  also can be found in Tables 1 and 2, as will be explained later in Section 4.3. At this point, it is concluded that for moderate seismic regions, the threshold periods determined by the collapse ductility spectrum, local ductility limit ( $\mu = 3$  in MSRs,  $\mu = 6$  in HSRs) and global drift angle ( $\Theta=0.1$ ) are generally close.

However, for the high seismic regions, using the global drift angle limit to assess the collapse performance of the CBF is generally non-conservative, because the dynamic instability of some CBFs with short periods may occur earlier so that it becomes the dominating factor for collapse. The reason is that the dynamic instability of the CBF systems in the HSRs are more sensitive than that in the MSRs due to the occurrence of larger deformation of the frame in the HSRs. Clearly, the use of single-response, unified limit baseline, whether the specific ductility limit or global drift angle limit, cannot fully represent the limit states of the CBFs over the full range of parameters.

#### 4.2 Verification by Collapse Margin ratio (CMR) Analysis

To further investigate the collapse performance of the CBFs, the collapse performance evaluation method in FEMA P695 [48] will be adopted. The acceptable collapse performance is selected as 10% probability of collapse under the maximum considered earthquake (MCE) level seismic hazard. The seismic fragility curve generated from the cumulative distribution function relates the ground motion intensity to the probability of collapse, by which all the probability of collapse can be computed. The collapse ground motion intensity is assumed to follow the lognormal distribution in plotting the seismic fragility curve [32]. The logarithm of the median collapse capacity is defined as the mean of the natural lognormal distribution, for which the standard deviation can be computed as well. In order to assess the uncertainty in the IDA, the standard deviation should be replaced by the total uncertainty  $\beta_{TOT}$ . According to Stoakes [49], the total uncertainty  $\beta_{TOT}$  for the CBFs is 0.8.

As shown in Figure 12(a), the earthquake intensity is the MCE seismic hazard level when the horizontal coordinate  $S_a / S_{MT}$  equals 1, where  $S_{MT}$  is the MCE intensity. The acceptance criterion of the structural collapse performance under the MCE intensity ground motion is less than 10% of the relative probability. Specifically, the case with  $\alpha = 0.8$ ,  $\beta = 0.5$  and  $T = 0.5$  s shown in Figure 12(a) is not satisfactory with the criterion, while the rest with larger periods are satisfactory, since the probabilities for the latter with the horizontal coordinate equal to 1 all fall below the horizontal line of 10% collapse probability. In comparison, the threshold period identified from Figure 12(b) using the design performance plot based on the MCDS and MDDS curves is  $T = 0.54$  s, which is close to the above value of 0.5 s. Based on this, the reliability of the present approach is confirmed.



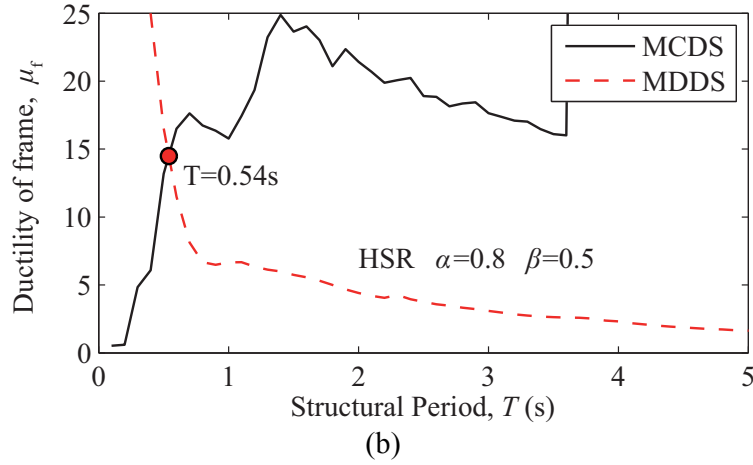


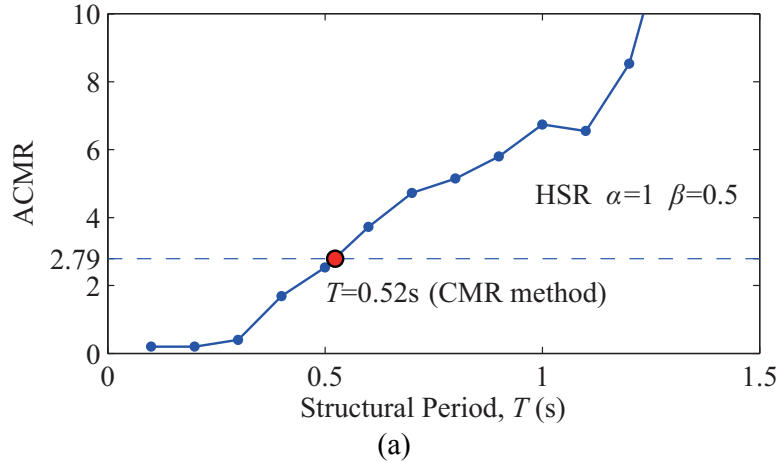
Figure 12. Threshold Period Identified from: (a) fragility curves; (b) the MCDS and the MDDS

One more convenient method is given in FEMA P695 for evaluating the collapse performance [48], in which the collapse margin ratio (CMR) and adjusted collapse margin ratio (ACMR) are calculated for each system. The CMR is used to evaluate the collapse resistance capacity, namely,

$$CMR = \frac{\hat{S}_{CT}}{S_{MT}} \quad (8)$$

where  $\hat{S}_{CT}$  is the median collapse capacity, and  $S_{MT}$  is the MCE intensity. The ACMR can be calculated by multiplying the CMR with the spectral shape factor. The spectral shape factor signifies the effect of collapse capacity by the frequency content of the ground motion record set, which depends on the period  $T$ , period-based ductility, and the applicable seismic design category [48]. The calculated ACMR can be compared with the 10% collapse probability limiting value,  $ACMR_{10\%}$ , which equals 2.79 based on  $\beta_{TOT} = 0.8$  from FEMA P695. Thus, for each CBF with a certain set of  $\alpha$  and  $\beta$ , the CMR method performs well in preventing the collapse of structures as long as the ACMR is greater than 2.79.

In Figure 13(a), the ACMR is plotted of the CBF with  $\alpha=1$  and  $\beta=0.5$  under the HSR ground motion suite. As can be seen, the ACMR exceeds 2.79 when the structural period is greater than 0.52 s, while the period of the intersection of the MCDS and MDDS curves is 0.49 s, as shown in Figure 13(b). That the solutions given by the two methods with different principles are consistent with each other is an indication of the validity of the present approach.



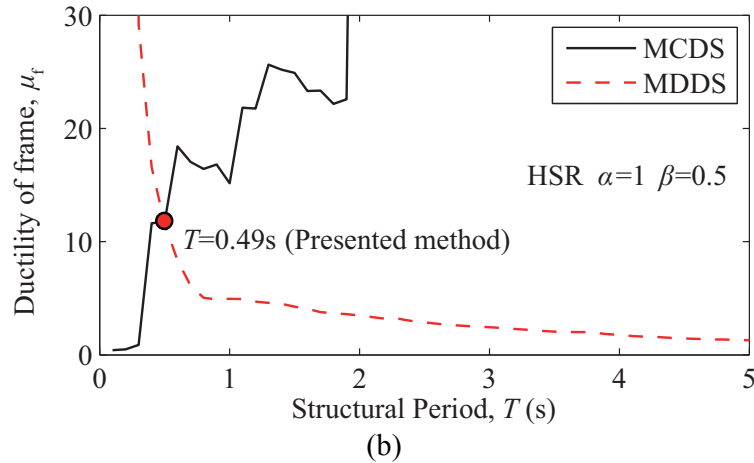


Figure 13. Threshold Period Identified from: (a) the ACMR method; (b) the MCDS and MDDS

### 4.3 Full Range of Parametric Evaluation

Simulation results for the full parametric space of  $\alpha$  and  $\beta$  ( $\alpha=0.1-1.5$ ,  $\beta=0.1-0.5$ ) under the MSR ground motion suite are listed in Table 1. For each permutation, a threshold period is identified, above which the system performance is deemed to be acceptable. It is observed that a significant change in the structural behavior occurs when the reserve stiffness  $\beta$  increases from 0.1 to 0.2, due to the fact that the threshold period is mainly controlled by the ductility demand. The change in behavior indicates that a minimum reserve stiffness as represented by  $\beta = 0.2$  is required for the collapse prevention of the structure. The results in Table 1 reveal that the system will not collapse within the reserve parameters ranges of  $\alpha > 0.7$  and  $\beta = 0.2$  or  $\alpha > 0.7$  and  $\beta \geq 0.3$  for structural periods greater than the threshold of 0.6 s. The CBF with the set of  $\alpha$  and  $\beta$  in the ranges allowed has a credible collapse prevention performance. However, it should be added that the cases with larger periods are not representative of typical low-rise CBF designs.

Table 1. Threshold Periods of the CBFs under the MSR Suite (unit: s)

$\beta \backslash \alpha$	0.1	0.2	0.3	0.4	0.5	0.6	0.7	0.8	0.9	1	1.1	1.2	1.3	1.4	1.5
0.1	>5	>5	>5	>5	>5	>5	4.1	4.2	4.1	3.9	3.9	3.8	3.6	3.6	0.3
0.2	×	>5	>5	>5	1.1	0.7	0.5	0.5	0.4	0.4	0.4	0.4	0.4	0.4	0.4
0.3	×	×	>5	1.5	1.1	0.9	0.7	0.6	0.6	0.5	0.5	0.5	0.4	0.4	0.4
0.4	×	×	×	1.5	1.2	0.9	0.8	0.6	0.5	0.5	0.5	0.4	0.4	0.4	0.4
0.5	×	×	×	×	1.4	1.1	0.7	0.6	0.5	0.5	0.5	0.5	0.5	0.4	0.4

Note: ×= unrealistic combination based on the parameter definitions

Simulation results for the full parametric  $\alpha$  and  $\beta$  space under the HSR ground motion suite are listed in Table 2. With  $\beta$  increasing, the threshold period drops noticeably because of various ductility demands. It is observed that the HSR suite requires larger reserve ductility capacity, and the required reserve strength and stiffness are also larger than those for the MSR. For the case of  $\beta = 0.2$ , only larger reserve strength of the CBF system is available for  $\alpha \geq 1.3$ . The larger the value of  $\beta$  is, the wider the range of  $\alpha$  will be. Cases with smaller values of  $\alpha$  and  $\beta$  are not suggested for the CBF system in the HSRs. If the period is larger, smaller values of reserve strength and stiffness can be chosen according to Table 2. However, as described previously, these larger periods are not representative of typical low-rise CBF designs. In addition, the performance of the CBF system with  $\beta = 0.1$  is not considered acceptable wherever in the MSRs or HSRs. Based on the above



analysis, it is concluded that the reserve parameters  $\alpha$  and  $\beta$  have great influence on the identification of threshold periods, and the performance of the structure can be enhanced by adding reserve capacity.

Table 2. Threshold Periods of the CBFs under the HSR Suite (unit: s)

$\beta \backslash \alpha$	0.1	0.2	0.3	0.4	0.5	0.6	0.7	0.8	0.9	1	1.1	1.2	1.3	1.4	1.5
0.1	>5	>5	>5	>5	>5	>5	>5	>5	>5	>5	>5	>5	>5	>5	>5
0.2	×	>5	>5	>5	>5	>5	4.4	4.1	3.9	2.8	2.8	2.7	0.8	0.7	0.7
0.3	×	×	>5	>5	4.5	4.3	2.8	2.8	2.8	1.3	0.7	0.5	0.5	0.5	0.5
0.4	×	×	×	4.6	4.3	2.8	2.8	0.7	0.6	0.6	0.6	0.5	0.5	0.5	0.5
0.5	×	×	×	×	2.8	2.8	0.6	0.6	0.6	0.5	0.5	0.5	0.5	0.5	0.5

Note: ×= unrealistic combinations based on the parameter definitions

## 5. CONCLUSIONS

In this paper, the incremental dynamic analysis (IDA) was conducted for a low-ductility concentrically braced frame (CBF) with reserve capacity modeled as a single-degree-of-freedom system to generate the collapse ductility spectrum. The ground motion suites typical of the moderate (MSR) and high seismic regions (HSR) were considered as the input excitations. Compared with existing baseline criteria, e.g., specific ductility limit and global drift limit, the collapse ductility spectrum is more representative of the properties of the CBF system involving dynamic instability, and can be reliably used in the collapse evaluation. In the numerical study, the collapse ductility spectrum of the CBF with various reserve strengths  $\alpha$  and reserve stiffnesses  $\beta$  were constructed. The design performance plot is constructed by newly combining the *median collapse ductility spectrum* (MCDS) and *mean ductility demand spectrum* (MDDS) on the same figure, from which the threshold period of the CBF is identified as the intersection of the two curves, and the design ductility region as the region embraced by the two curves. The results obtained were compared with those from the seismic fragility and collapse margin ratio (CMR) analyses. The main conclusions and recommendations are shown as follows:

- The collapse ductility spectrum was adopted to assess the dynamic stability of the CBFs. The reserve stiffness  $\beta$  has much greater influence on the collapse ductility than the reserve strength  $\alpha$ . Compared with existing baseline criteria, e.g., specific ductility limit and global drift angle limit, the collapse ductility spectrum is more representative in that it considers the period, restoring force versus deformation relation, and dynamics instability of the CBF.
- As for the collapse evaluation for the CBFs, numerical results show that for high seismic regions, using the global drift angle limit may result in non-conservative designs, since dynamic instability may occur earlier for some CBFs, and becomes a dominating factor thereafter. For moderate seismic regions, however, the threshold periods predicted by the collapse ductility spectrum are close to those by the specific ductility limit and global drift angle limit.
- The CBF system with long periods shows good dynamic stability on the collapse performance. Generally, a CBF with long periods can sustain earthquakes of large intensities up to the point of collapse, especially for the case with large reserve stiffnesses  $\beta$ .
- The  $P$ - $\Delta$  effect shows large influence on the dynamic instability of the CBFs and should be considered in evaluation of the collapse prevention performance for the CBF system.
- The reserve capacity of the CBF is verified to contribute appreciably to the collapse prevention. The threshold period of the structure is identified as the intersection of the MCDS and MDDS

curves, and the design ductility region as the one embraced by two curves. In addition, the threshold periods in the MSRs are less than those in the HSRs. Numerical results illustrate that the CBF systems will not collapse within the reserve parameter ranges of  $\alpha \geq 0.7$  and  $\beta = 0.2$  or  $\alpha > 0.7$  and  $\beta \geq 0.3$  in the MSRs, and  $\alpha \geq 1.2$  and  $\beta = 0.3$  or  $\alpha \geq 0.9$  and  $\beta = 0.4$  or  $\alpha \geq 0.7$  and  $\beta = 0.5$  in the HSRs. The CBFs with a period greater than 0.6 s and values of  $\alpha$  and  $\beta$  in the above range can exhibit credible collapse prevention performance.

## ACKNOWLEDGEMENTS

Funding for authors was provided by the National Natural Science Foundation of China (Grant No. 51422802, 51421064), the Fundamental Research Funds for the Central Universities (DUT17ZD220).

## REFERENCES

- [1] Tremblay, R., "Inelastic Seismic Response of Steel Bracing Members", *Journal of Constructional Steel Research*, 2002, Vol. 58, No. 5, pp.665-701.
- [2] Tremblay, R., "Achieving a Stable Inelastic Seismic Response for Multi-story Concentrically Braced Steel Frames", *AISC Engineering Journal*, 2003, Vol. 40, No. 2, pp.111-129.
- [3] Scholl, R.E., "Observations of the Performance of Buildings during the 1985 Mexico Earthquake, and Structural Design Implications", *International Journal of Mining and Geological Engineering*, 1989, Vol. 7, No. 1, pp.69-99.
- [4] Tremblay, R., Filiatrault A., Timler P. and Bruneau M., "Performance of Steel Structures during the 1994 Northridge Earthquake", *Canadian Journal of Civil Engineering*, 1995, Vol. 22, No. 2, pp.338-360.
- [5] Tremblay, R., Filiatrault, A., Bruneau, M., Nakashima, M., Prion, H.G. and DeVall, R., "Seismic Design of Steel Buildings: Lessons from the 1995 Hyogo-ken Nanbu Earthquake", *Canadian Journal of Civil Engineering*, 1996, Vol. 23, No. 3, pp.727-756.
- [6] Mahin, S.A., "Lessons from Damage to Steel Buildings during the Northridge Earthquake", *Engineering Structures*, 1998, Vol. 20, No. 4, pp.261-270.
- [7] Moh, Z.C., Hwang, R.N., Ueng, T.S. and Lin, M.L., "1999 Chi Chi Earthquake of Taiwan", *Bulletin of the Seismological Society of America*, 2003, Vol. 93, No. 1, pp.386-396.
- [8] Okazaki, T., Lignos, D.G., Midorikawa, M., Ricles, J.M. and Love, J., "Damage to Steel Buildings Observed after the 2011 Tohoku-Oki Earthquake", *Earthquake Spectra*, 2013, Vol. 29(S1), pp.S219-S243.
- [9] Tremblay, R. and Robert, N., "Seismic Design of Low- and Medium-rise Chevron Braced Steel Frames", *Canadian Journal of Civil Engineering*, 2000, Vol. 27, No. 6, pp.1192-1206.
- [10] Longo, A., Montuori, R. and Piluso, V. "Seismic Reliability of Chevron Braced Frames with Innovative Concept of Bracing Members", *Advanced Steel Construction*, 2009, Vol. 5, No. 4, pp.367-389.
- [11] Hines, E.M. and Fahnestock, L.A., "Design Philosophy for Steel Structures in Moderate Seismic Regions", *Proc. 9th US National and 10th Canadian Conf. on Earthquake Engineering*; Oakland, CA. 2010.
- [12] Okazaki, T., Lignos, D.G., Hikino, T. and Kajiwaru K., "Dynamic Response of a Steel Concentrically Braced Frame", *Structures Congress 2011*, ASCE; 2011.
- [13] Lai, J.W. and Mahin, S.A., "Experimental and Analytical Studies on the Seismic Behavior of Conventional and Hybrid Braced Frames", *PEER Report 2013/20*. Berkeley, CA, Pacific Earthquake Engineering Research Center, 2013.

- [14] Wijesundara, K.K., Nascimbene, R. and Rassati, G.A. "Modeling of Different Bracing Configurations in Multi-storey Concentrically Braced Frames using a Fiber-beam based Approach", *Journal of Constructional Steel Research*, 2014, Vol. 101, pp.426-436.
- [15] Tirca, L. and Chen, L., "Numerical Simulation of Inelastic Cyclic Response of HSS Braces upon Fracture", *Advanced Steel Construction*, 2014, Vol. 10, No. 4, pp.442-462.
- [16] Shen, J., Wen, R. and Akbas, B., "Mechanisms in Two-story X-braced Frames", *Journal of Constructional Steel Research*, 2015, Vol. 106, pp.258-277.
- [17] Kumar, P.C.A., Sahoo, D.R. and Kumar, N., "Limiting Values of Slenderness Ratio for Circular Braces of Concentrically Braced Frames", *Journal of Constructional Steel Research*, 2015, Vol. 115, pp.223-235.
- [18] Longo, A., Montuori, R. and Piluso, V., "Moment Frames – Concentrically Braced Frames Dual Systems: Analysis of Different Design Criteria", *Structure and Infrastructure Engineering*, 2015, Vol. 12, No. 1, pp.122-141.
- [19] ASCE. "Minimum Design Loads for Buildings and Other Structures", ASCE 7-10. New York, NY: American Society of Civil Engineers, 2010.
- [20] Hines, E.M., Appel, M.E. and Cheever, P.J., "Collapse Performance of Low-Ductility Chevron Braced Steel Frames in Moderate Seismic Regions", *AISC Engineering Journal*, 2009, Vol. 46, No. 3, pp.149-180.
- [21] Li, G. and Fahnestock, L.A., "Seismic Response of Single-degree-of-freedom Systems Representing Low-ductility Steel Concentrically-braced Frames with Reserve Capacity", *Journal of Structural Engineering*, 2013, Vol. 139, No. 2, pp.199-211.
- [22] Bertero, V.V., "Strength and Deformation Capacities of Buildings under Extreme Environments", *Structural Engineering and Structural Mechanics*, 1977, Vol. 53, No. 1, pp.29-79.
- [23] Bazzurro, P. and Cornell, C.A., "Seismic Hazard Analysis of Nonlinear Structures, I: Methodology", *Journal of Structural Engineering*, 1994, Vol. 120, No. 11, pp.3320-3344.
- [24] Bazzurro, P. and Cornell, C.A. "Seismic Hazard Analysis of Nonlinear Structures, II: Applications", *Journal of Structural Engineering*, 1994, Vol. 120, No. 11, pp.3345-3365.
- [25] Luco, N. and Cornell, C.A. "Effects of Random Connection Fractures on the Demands and Reliability for a 3-story Pre-Northridge SMRF Structure", *Proceedings of the 6th US National Conference on Earthquake Engineering*, Seattle (Washington), 1998. pp. 1-12.
- [26] Luco, N. and Cornell, C.A., "Effects of Connection Fractures on SMRF Seismic Drift Demands", *Journal of Structural Engineering*, 2000, Vol. 126, No. 1, pp.127-136.
- [27] FEMA, "Recommended Seismic Design Criteria for New Steel Moment-Frame Buildings ": FEMA 350, Washington, DC: SAC Joint Venture, 2000.
- [28] FEMA, "Recommended Seismic Evaluation and Upgrade Criteria for Existing Welded Steel Moment-Frame Buildings", FEMA 351. Washington, DC: SAC Joint Venture 2000.
- [29] Vamvatsikos, D. and Cornell C.A., "Incremental Dynamic Analysis", *Earthquake Engineering & Structural Dynamics*, 2002, Vol. 31, No. 3, pp.491-514.
- [30] Vamvatsikos, D. and Cornell, C.A., "Applied Incremental Dynamic Analysis", *Earthquake Spectra*, 2004, Vol. 20, No. 2, pp.523-553.
- [31] Vamvatsikos, D. and Cornell C.A., "Direct Estimation of Seismic Demand and Capacity of Multidegree-of-freedom Systems through Incremental Dynamic Analysis of Single Degree of Freedom Approximation", *Journal of Structural Engineering*, 2005, Vol. 131, No. 4, pp.589-599.
- [32] Ibarra, L.F., "Global Collapse of Frame Structures under Seismic Excitations", Ph.D. Thesis, Department of Civil and Environmental Engineering, Stanford University, Stanford, CA. 2003.
- [33] Mander, J.B., Dhakal, R.P., Mashiko, N. and Solberg, K.M., "Incremental Dynamic Analysis Applied to Seismic Financial Risk Assessment of Bridges", *Engineering Structures*, 2007, Vol. 29, No. 10, pp.2662-2672.

- [34] Vamvatsikos, D. and Fragiadakis, M., "Incremental Dynamic Analysis for Estimating Seismic Performance Sensitivity and Uncertainty", *Earthquake Engineering & Structural Dynamics*, 2010, Vol. 39, No. 2, pp.141-163.
- [35] Kazantzi, A.K., Vamvatsikos, D. and Lignos, D.G., "Seismic Performance of a Steel Moment-resisting Frame subject to Strength and Ductility Uncertainty", *Engineering Structures*, 2014, Vol. 78, pp.69-77.
- [36] Fragiadakis, M., Vamvatsikos, D., Karlaftis, M.G., Lagaros, N.D. and Papadrakakis, M., "Seismic Assessment of Structures and Lifelines", *Journal of Sound and Vibration*, 2015, Vol. 334, pp.29-56.
- [37] Vamvatsikos, D., "Performing Incremental Dynamic Analysis in Parallel", *Computers & Structures*, 2011, Vol. 89, No. 1, pp.170-180.
- [38] Zarfam, P. and Mofid, M., "On the Modal Incremental Dynamic Analysis of Reinforced Concrete Structures", using a Trilinear Idealization Model", *Engineering Structures*, 2011, Vol. 33, No. 4, pp. 1117-1122.
- [39] Adam, C. and Jäger, C., "Seismic Collapse Capacity of Basic Inelastic Structures Vulnerable to the P-delta Effect", *Earthquake Engineering & Structural Dynamics*, 2012, Vol. 41, No. 4, pp.775-793.
- [40] Goda, K. and Yoshikawa, H., "Incremental Dynamic Analysis of Wood-frame Houses in Canada: Effects of Dominant Earthquake Scenarios on Seismic Fragility", *Soil Dynamics and Earthquake Engineering*, 2013, Vol. 48, pp.1-14.
- [41] Brunesi, E., Nascimbene, R., Parisi, F. and Augenti, N. "Progressive Collapse Fragility of Reinforced Concrete Framed Structures through Incremental Dynamic Analysis", *Engineering Structures*, 2015, Vol. 104, pp.65-79.
- [42] Hines, E., Baise, L. and Swift, S., "Ground-motion Suite Selection for Eastern North America", *Journal of Structural Engineering*, 2010, Vol. 137, No. 3, pp. 358-366.
- [43] FEMA. "State of the Art Report on Systems Performance of Steel Moment Frames Subject to Earthquake Ground Shaking": FEMA 355C. Washington, DC: SAC Joint Venture 2000.
- [44] Somerville, P., Smith, N., Punyamurthula, S. and Sun, J., "Development of Ground Motion Time Histories for Phase 2 of the FEMA/SAC Steel Project", Rep. No. SAC/BD-97/04, Sacramento, CA, SAC Joint Venture, 1997.
- [45] Chopra, A.K., "Dynamics of Structures: Theory and Applications to Earthquake Engineering", Prentice Hall Saddle River, NY, 2001.
- [46] Ibarra, L.F. and Krawinkler, H. "Global Collapse of Frame Structures under Seismic Excitations", Stanford, CA, Pacific Earthquake Engineering Research Center, 2005.
- [47] Bernal, D. "Amplification Factors for Inelastic Dynamic  $p-\Delta$  Effects in Earthquake Analysis", *Earthquake Engineering & Structural Dynamics*, 1987, Vol. 15, No. 5, pp.635-651.
- [48] FEMA. "Quantification of Building Seismic Performance Factors", Rep. No. FEMA P695. Redwood City, CA, Applied Technology Council, 2009.
- [49] Stoakes, C.D., "Beam-column Connection Flexural Behavior and Seismic Collapse Performance of Concentrically Braced Frames", PhD Thesis, Department of Civil and Environmental Engineering, University of Illinois at Urbana-Champaign, Urbana, IL. 2012.

# EXPERIMENT AND STABILITY ANALYSIS ON HEAVY-DUTY SCAFFOLD SYSTEMS WITH TOP SHORES

Jui-Lin Peng<sup>1,\*</sup>, Chung-Sheng Wang<sup>2</sup>, Chung-Wei Wu<sup>3</sup> and Wai-Fah Chen<sup>4</sup>

<sup>1</sup>*Professor, Department of Civil and Construction Engineering,  
National Yunlin University of Science and Technology, Taiwan, ROC*

<sup>2</sup>*Ph.D. Student, Graduate School of Engineering Science and Technology,  
National Yunlin University of Science and Technology, Taiwan, ROC.*

<sup>3</sup>*Ph.D., Graduate School of Engineering Science and Technology,  
National Yunlin University of Science and Technology, Taiwan, ROC*

<sup>4</sup>*Research Professor, Department of Civil Engineering, University of Hawaii, USA*

*\*(Corresponding author: E-mail pengjl@yuntech.edu.tw)*

*Received: 8 February 2017; Revised: 27 March 2017; Accepted: 25 May 2017*

---

**ABSTRACT:** The heavy-duty scaffold system has a higher load capacity than the frame-type steel scaffold system. The independent setup of heavy-duty scaffold system is totally different from a row-style setup of frame-type steel scaffold system in construction. This study explores the load capacity and failure model of full-scale heavy-duty scaffold systems to elucidate their stability behaviors. The results of the study based on lab tests reveal that the load capacity and failure model of an independent three-story heavy-duty scaffold are similar to those of an independent two-story heavy-duty scaffold, with no apparent reduction in the load capacity. For a given height of the structure, the load capacity of a combination of independent two-story heavy-duty scaffolds with steel shores that are made of thin tubes is much lower than that of an independent three-story heavy-duty scaffold. In load tests on outdoor heavy-duty scaffolds with steel shores made of thin tubes, after loading, the entire structural system failed promptly without warning. A second-order inelastic analysis herein demonstrates that the tested and analyzed load capacities of various setups of heavy-duty scaffold systems are very close, revealing that the second-order inelastic analysis is suitable for heavy-duty scaffold systems. On construction sites in Taiwan, heavy-duty scaffolds with shores are often adopted, and the load capacity of the overall combined scaffold system is estimated from the strength of a single member used in the design of a traditional building steel structure. Hence, the load capacity of a heavy-duty scaffold system that is combined with shores of a thin tube tends to be overestimated, leading to a very high risk of collapse the combined scaffold system. Therefore, on a construction site, such a combined setup should be avoided. A heavy-duty scaffold system without any other shores on the top should be used on construction sites.

**Keywords:** Critical load, failure model, heavy-duty scaffold, load capacity, stability

**DOI:** 10.18057/IJASC.2017.13.3.6

---

## 1. INTRODUCTION

The external configuration of heavy-duty scaffolds differs from that of frame-type steel scaffolds. Unlike frame-type steel scaffolds, which are typically set up continuously end-to-end in a single row, heavy-duty scaffolds are often set up independently. Features of heavy-duty scaffolds include their easy and quick setup, the lack of a difference between the strong axis and the weak axis in the scaffold system, and the independence setup from the environmental conditions. Owing to their large load capacity, heavy-duty scaffolds are typically used as falsework for heavy-laden slabs and beams during the construction of a building. They are often used in reinforced concrete structures, such as hi-tech fabrication plants, warehouses and bridges. The use of heavy-duty scaffolds in coordination with modular formwork systems is more convenient than the use of the frame-type steel scaffolds. Therefore, in the construction of heavy-laden reinforced concrete structures, heavy-duty scaffolds are gradually replacing frame-type steel scaffolds.

Currently, no code for the structural design of heavy-duty scaffolds during construction is available in Taiwan. Heavy-duty scaffolds are commonly set up on a construction site based on the experience of construction workers. Since a construction contractor cannot effectively control the load capacity of heavy-duty scaffolds, the risk of collapse of such a scaffold system in service is very high. Figure 1 presents the falsework collapse that occurred during the construction of the access bridge for the 921 Earthquake Museum in Taichung, Taiwan.



Figure 1. Collapse of Falsework in Construction of Access Bridge of 921 Earthquake Museum in Taichung, Taiwan

Numerous studies of the safety of steel scaffolds have been published. Huang *et al.* [4] developed a simplified 2-D model of door-type steel scaffolds, based on which they created a characteristic equation for the structural stability of door-type steel scaffolds with different numbers of stories. Peng *et al.* [9] explored the variation of axial forces of vertical steel tubes in an outdoor full-scale door-type steel scaffold system under different load paths of fresh concrete. Kuo *et al.* [6] and Peng *et al.* [11] investigated the axial forces of vertical steel tubes of door-type steel scaffold systems that are combined with wooden shores under different load paths and load types, and they examined the relationship between the influence-line effect and these loads. Whereas Kuo *et al.* conducted experiments on the rectangular arrangement of the outdoor full-scale steel scaffold system, Peng *et al.* analyzed rectangular, L-shaped and U-shaped arrangements of the door-type steel scaffold system.

Peng *et al.* [8] examined the load capacities of door-type steel scaffolds based on the single-row setup with many bays, which differed from that utilized in other tests, in which only one bay was involved. Previously Peng *et al.* [7] had performed load tests on isolated heavy-duty scaffolds to evaluate the load capacity and determine the failure model of such scaffolds with different arrangements.

With respect to single tube scaffolds, Liu *et al.* [5] carried out load tests on a full-scale large steel scaffolds without X-bracing to determine the load capacity and mechanical behaviors of the overall scaffold system. With respect to system scaffolds, Peng *et al.* [10] performed the second-order analyses and load tests on system scaffolds to determine the load capacity and mechanical behaviors of such scaffolds with different arrangements.

Zhang and Rasmussen (Zhang *et al.* [12]) explored the variability of parameters that affect the strength of steel scaffolds. They studied semi-rigid joint stiffness, load eccentricity, initial geometric imperfection, and system reliability. Zhang and Rasmussen (Zhang *et al.* [13])

subsequently explored the failure model of steel scaffolds, random variables that affect the strength of the scaffold structure, and the reliability of their analysis. Their results revealed that the reliability framework can improve the current working load limit of such a scaffold structure.

As indicated above, most relevant studies concern frame-type steel scaffolds, door-type steel scaffolds, single tube scaffolds and system scaffolds, whereas only a few have addressed heavy-duty scaffolds. Since heavy-duty scaffolds are set up as an independent tower structure, which differs from the aforementioned continuous scaffolding structures, the results of the majority of studies cannot be directly applied to the heavy-duty scaffolds, and especially not to the mechanical behaviors of the large area heavy-duty scaffold systems. Therefore, the load capacities and failure models of full-scale heavy-duty scaffold systems are worthy of further study.

## **2. RESEARCH OBJECTIVES**

This study investigates the stability behavior of the heavy-duty scaffold system regarding the load capacity and the failure model of the system. All tested scaffolds are made of full-scale members and testing installations are based on the setups adopted on real construction sites. The results of this study may provide a reference for the safe design and construction of heavy-duty scaffolds in the construction industry in Taiwan to reduce the risk of collapse. This study makes the following contributions.

- Load tests are performed on the independent heavy-duty scaffolds and the heavy-duty scaffolds that are combined with shores, to determine the load capacities and failure models of various setups of these heavy-duty scaffolds.
- Second-order inelastic analyses of independent heavy-duty scaffolds is performed, and the analytical results are compared with the test results to evaluate the analytical parameters of scaffolds, such as the joint stiffness of each member.
- Load tests on an outdoor full-scale heavy-duty scaffold system that is combined with shores are performed to evaluate the actual load capacity and failure model of such a system.
- The applicability of second-order inelastic analysis is determined by comparing indoor and outdoor test results with the results of the second-order inelastic analysis.

The Geometric and Material Nonlinear Analysis of Frames (GMNAF) that were developed by professor Siu-Lai Chan of The Hong Kong Polytechnic University (Chan [1], Chan et al. [2, 3]) are used in the 3D second-order inelastic analysis herein with semi-rigid joints for various setups of heavy-duty scaffold systems.

## **3. DIMENSIONS AND MATERIAL PROPERTIES**

The heavy-duty scaffolds that are most commonly used on construction sites in Taiwan were adopted in this study. The A heavy-duty scaffolding structure is composed of a triangle-type scaffold unit, lateral braces and horizontal bars. The triangle-type scaffold unit is composed of the main rod, upper rods, middle rods and diagonal braces (as shown in Figure 2).

The cross-sectional dimensions of various members are obtained from measurements of six sets of heavy-duty scaffolds. In Figure 2, the measurements of the cross-sections of various members of the triangle-type scaffold unit were as follows; the average external diameter and thickness of the main rod were 76.35 mm and 3.32 mm, respectively (see cross section A-A); the average external diameter and thickness of the upper rod were 42.26 mm and 2.24 mm, respectively (see cross section B-B); the average external diameter and thickness of the middle rod were 33.62 mm and

2.24 mm, respectively (see cross section C-C); the average external diameter and thickness of the diagonal brace were 33.63 mm and 2.18 mm respectively (see cross section D-D).

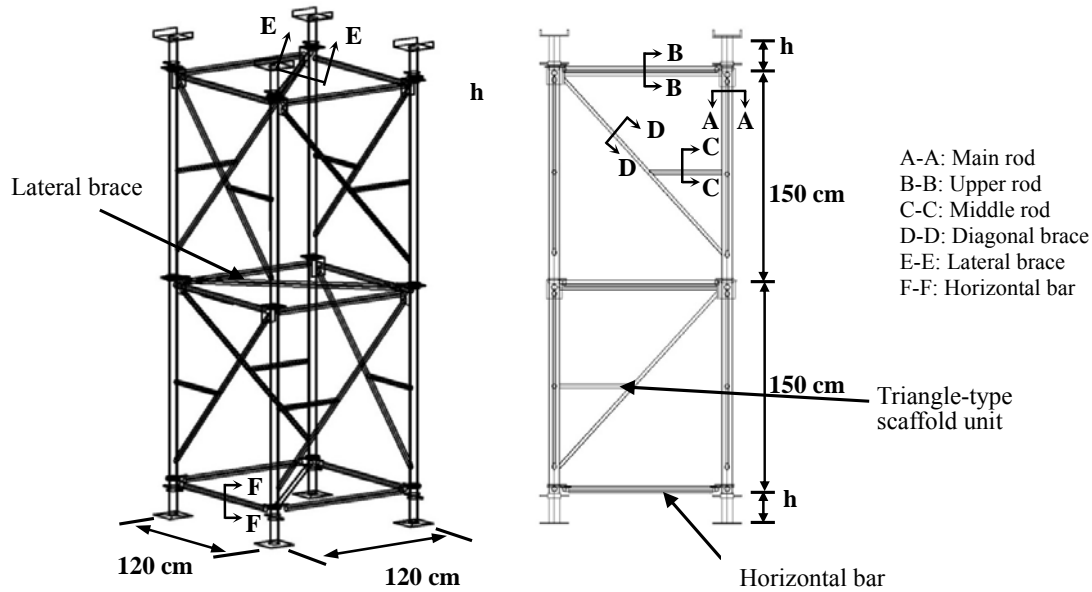


Figure 2. Dimensions and Setup of Internal Members of the Independent Heavy-duty Scaffolds

The measurements of lateral braces and horizontal bars were as follows; the average external diameter and thickness of the lateral braces were 42.27 mm and 1.92 mm respectively (see cross section E-E); the average external diameter and thickness of the horizontal bar were 42.35 mm and 2.40 mm, respectively (see cross section F-F).

In the material tests, since all members of heavy-duty scaffolds are made of the same material, the coupon tests were performed on six randomly selected main rods of the heavy-duty scaffolds to determine the elastic modulus,  $E$ , of the heavy-duty scaffolds. The average elastic modulus,  $E$ , of the 6 main rods was 20,386 kN/cm<sup>2</sup>, which is very close to the nominal  $E$  value 20,012.4 kN/cm<sup>2</sup>. Therefore, when the double modulus theory is used to conduct the second-order inelastic analysis of heavy-duty scaffolds, the reduced modulus,  $E_r$ , equals the elastic modulus,  $E$ , multiplied by a reduction factor,  $\phi$ . (i.e.,  $E_r = \phi E$ ).

#### 4. TEST PLAN

In this study, two groups of tests were carried out: indoor and outdoor load tests. The indoor tests were carried out on both independent heavy-duty scaffolds and heavy-duty scaffolds that were combined with shores, to elucidate the effect of these two setups on load capacities and failure models. The outdoor test of heavy-duty scaffolds that were combined with shores simulated the heavy-duty scaffolding systems that are used on actual construction sites. All scaffolds used in these tests were the full-scale heavy-duty scaffolds.

##### 4.1 Indoor Load Tests on Independent Heavy-duty Scaffolds

###### 4.1.1 Heavy-duty scaffolds

Heavy-duty scaffolds with different numbers of stories have different load capacities. In this study, load tests were conducted on two-story and three-story independent heavy-duty scaffolds to explore



the relation between load capacity of heavy-duty scaffolds and the number of stories. In the setup for testing heavy-duty scaffolds, lateral braces were used for each story; the height of each story was 150 cm; the height of the top jack and the bottom jack bases was 20 cm, and the total heights of the two-story and three-story systems were 340 cm and 490 cm, respectively. Figure 3 displays the relevant arrangements.

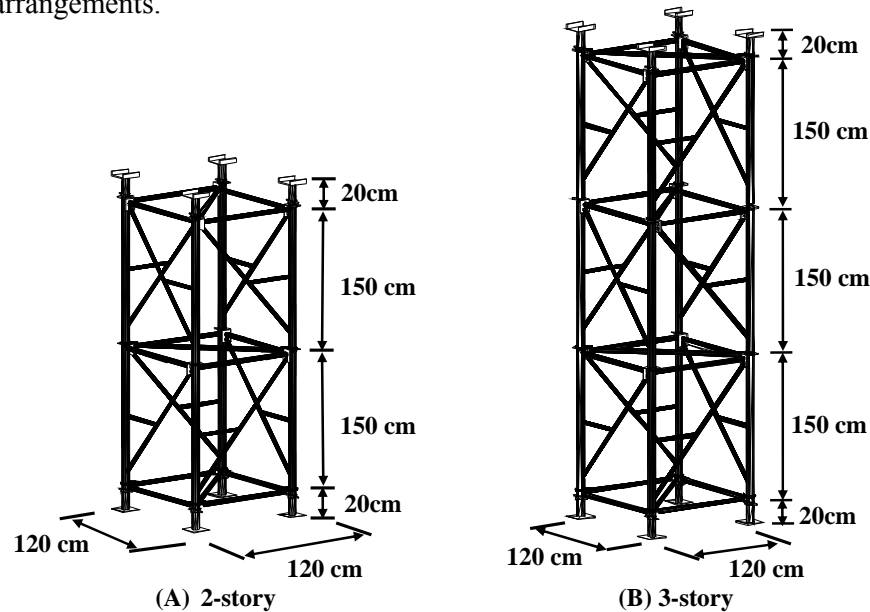


Figure 3. Dimensions and Configurations of Two-story and Three-story Heavy-duty Scaffolds

#### 4.1.2 Heavy-duty scaffolds with shores

The headroom of a building will never be an exact integer multiple of the height of a heavy-duty scaffold. Therefore, when multiple stories of heavy-duty scaffolds are set up, a gap must exist between the top story and the bottom of the slab. To solve this practical problem, workers will often fill the gap with shores, such as steel shores, wooden shores or tubular steel adjustable shores. The difference between the load capacity of heavy-duty scaffolds without and with shores is worth of study.

In the tests on the heavy-duty scaffolds with shores, the steel tubes with different thicknesses and lengths were used on the top of the scaffolds. Figure 4 shows the test configuration. The “thick” steel shores are directly cut from the main rods of heavy-duty scaffolds, with an average external diameter of 76.35 mm and thickness of 3.32 mm. Such thick steel shores are seldom adopted on construction sites, and they are used in this study simply for the purpose of comparison. The “thin” steel shores are made of galvanized steel tubes that are commonly used on construction sites in Taiwan, with an average external diameter of 48.18 mm and thickness of 2.00 mm. On construction sites, the construction contractor uses thin steel shores mainly for convenience and cheapness. The tests herein reveal the upper and lower limits of the load capacity of heavy-duty scaffolds combined with shores.

## 4.2 Outdoor Load Test on Heavy-duty Scaffolds with Shores

### 4.2.1 Resistance

In this study, an outdoor load test on heavy-duty scaffolds with shores were conducted to explore the load capacity of actual heavy-duty scaffolds which is the lower limit strength of the system. Figures 5A and 5B show the setup of a heavy-duty scaffold system with shores in the outdoor load

test. The bottom part of the system was composed of four sets of four-story heavy-duty scaffolds with a total height of 6 m. On top of the heavy-duty scaffolds, 16 thin steel shores, each with a length of 1.5 m were set. Each group of four thin steel shores was reinforced with four horizontal braces.

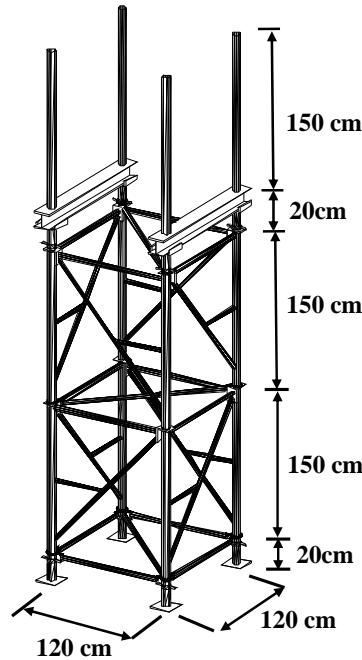


Figure 4. Dimensions and Configuration of Two-story Heavy-duty Scaffolds with 150cm-long Steel Shores on Top

In the outdoor load test, the heavy-duty scaffold system with shores was setup on a 5.4 m×5.4 m square area. As shown in Figures 5A and 5B, a set of heavy-duty scaffold was installed at each corner of this square. The top view area of each set of heavy-duty scaffolds was 1.2 m×1.2 m and the net distance between each set of heavy-duty scaffold was 3 m. A theodolite was arranged on both the north and the west sides of the square area. During the tests, the horizontal displacements and directions of the H-beams between heavy-duty scaffolds and the thin steel shores were measured using the theodolite, as shown in Figures 5A and 5B.

As also shown in Figures 5A and 5B, the eight steel wire ropes above the thin steel shores on the upper-story provided the system with lateral support, to simulate the formwork of beams and slabs, supported by the dried reinforced concrete (RC) columns and walls. Thus, this scaffold framework should not exhibit any lateral displacement. The eight steel wire ropes on top of the heavy-duty scaffolds on the lower stores were used for safety as they stabilized the overall system during installation, reducing the risk of collapse. On the day of the tests, these eight steel wire ropes were detached before loading because such lateral bracing reinforcement is not used on a real construction site.

To prevent uneven settlement due to the heavy load on the base, four large RC blocks were firstly buried in the test field. Four H-beams were then laid on the RC blocks and the heavy-duty scaffolds were then set on these H-beams to spread uniformly the vertical load that was conveyed from the top of the heavy-duty scaffolds.

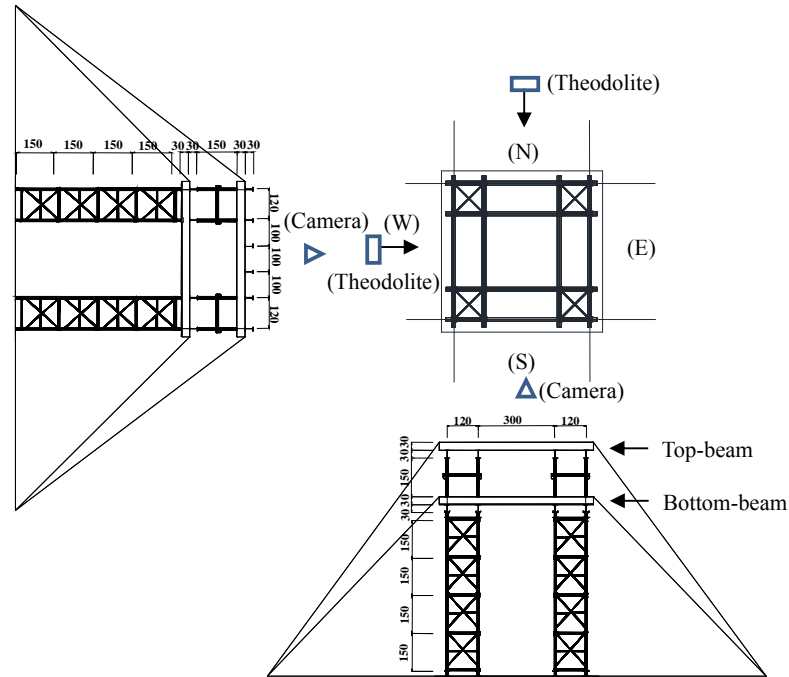


Figure 5A. Three-view Diagram of Setup for Outdoor Load Test of Heavy-duty Scaffolds with Shores

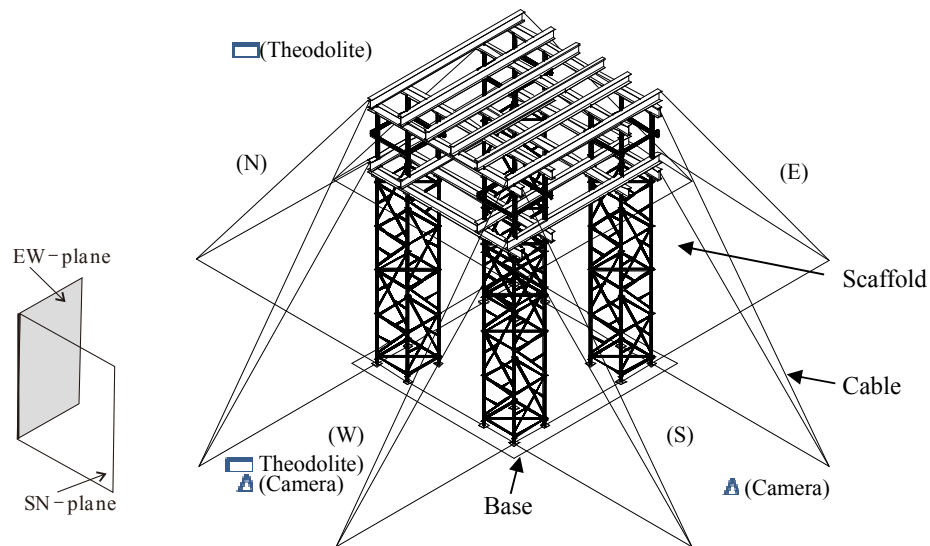


Figure 5B. Setup for Outdoor Load Test of Heavy-duty Scaffolds with Shores

#### 4.2.2 Load

In the tests, RC blocks and sandbags simulated the load of fresh concrete during construction. The RC blocks were placed on two stories. Ten RC blocks were placed on each story, as shown in Figure 6. The same load procedure was used for both stories. For each story, only the first two RC blocks were placed adjacent to each other and the remaining eight RC blocks were placed diagonally. The placement mainly considered the evenness of the load distribution on the overall scaffold system.

Figure 7 displays the order and positions of the placement of the sandbags: the numbers indicate the order of placement. Like the RC blocks, the sandbags were placed diagonally in an order that ensured the evenness of the load distribution on the overall scaffold system.

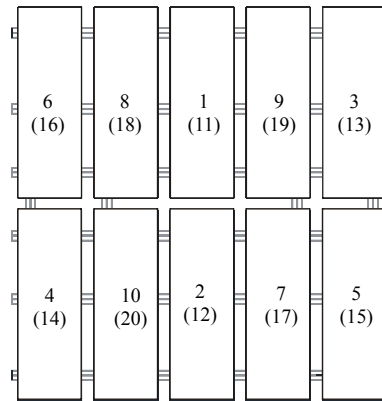


Figure 6. Placement of Two Stories of RC Blocks in Outdoor Load Test on Heavy-duty Scaffolds with Shores

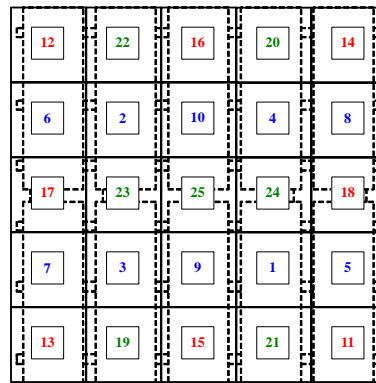


Figure 7. Placement of Sandbags on First Story in Outdoor Load Test on Heavy-duty Scaffolds with Shores

## 5. TEST RESULTS AND ANALYSES

### 5.1 Indoor Load Tests on Independent Heavy-duty Scaffolds






#### 5.1.1 Load capacity of heavy-duty scaffolds

Three sets of load tests were conducted on the two-story heavy-duty scaffolds, yielding an average load capacity of 981.72 kN, as shown in Table 1. The test result on the heavy-duty scaffold system can serve as a basis for comparison with the load capacities of other setups of heavy-duty scaffolds. Figure 8(A) shows the deformations of the two-story heavy-duty scaffolds under loading. Figure 9 plots the load-vertical displacement curve.

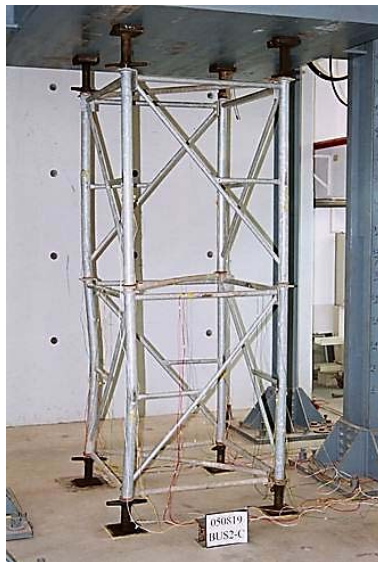
Two sets of load tests were conducted on the three-story heavy-duty scaffolds, and yielded an average load capacity of 921.3 kN, as shown in Table 1. Figure 8(B) shows the deformation of the three-story heavy-duty scaffolds under loading. Figure 10 plots the load-vertical displacement

curve. Comparing the test results of the three-story heavy-duty scaffolds with those of the two-story heavy-duty scaffolds reveals that the average load capacity of the three-story heavy-duty scaffolds is about 93.8%  $(= (921.3/981.72) \times 100\%)$  of that of the two-story heavy-duty scaffolds, so the difference between these two capacities is insignificant.

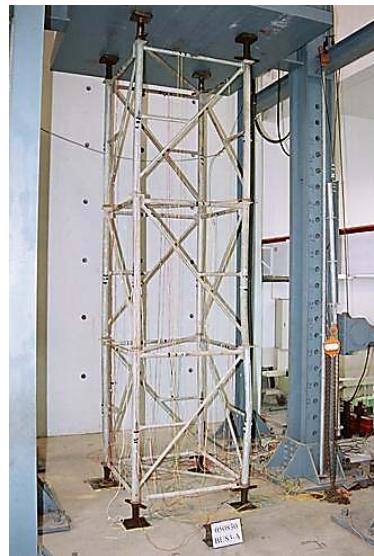
Table 1. Results of Indoor Load Tests on Independent Heavy-duty Scaffolds

Setup type	No. of story	Figure	Numbering	Test values (kN)			
				Test A	Test B	Test C	Average
Setups of various heights	2		BUS2	990.88	1012.99	941.3	981.72
	3		BUS3	951.57	891.04	#	921.31
150cm-long thick steel shores on top	2		TBUS2	773.18	817.1	#	795.14
150cm-long thin steel shores on top	2		TTBUS2	214.86	218.04	#	216.45
80cm-long thin steel shores on top	2		TTBUS2	327.59	330.0	#	328.8

Notes: 1. Each test setup includes top jack, jack base and lateral braces. 2. # refers to no test value.



(A) 2-story



(B) 3-story

Figure 8. Deformations of Two-story and Three-story Heavy-duty Scaffolds under Loading

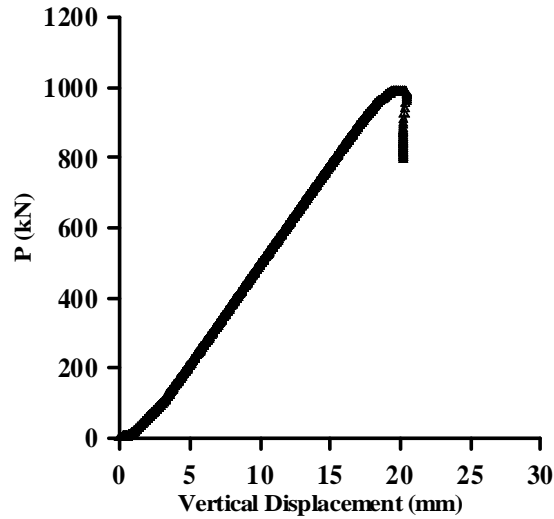


Figure 9. Load-vertical Displacement Curve from Load Test on Two-story Heavy-duty Scaffolds

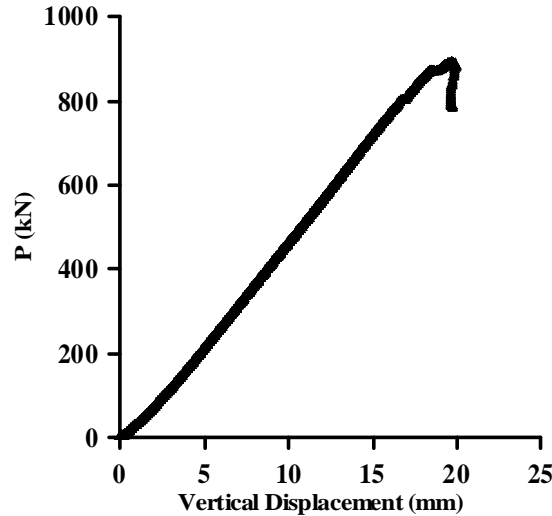


Figure 10. Load-vertical Displacement Curve from Load Test on Three-story Heavy-duty Scaffolds

### 5.1.2 Load capacity of heavy-duty scaffolds with shores

#### 5.1.2.1 150cm-Long thick steel shores on top of scaffold

Two sets of load tests were performed on two-story heavy-duty scaffolds that were augmented with 150cm-long and thick steel shores on the top of scaffolds. The average load capacity was 795.14 kN, as shown in Table 1. Figure 11(A) shows the deformation of this heavy-duty scaffolds with the shores under loading. As shown in the figure, the 150cm-long thick steel shores exhibits no significant deformation. Instead, nearly all of the deformation is in the heavy-duty scaffolds. Figure 12 plots the load-vertical displacement curve, which is similar to those of the two-story and three-story heavy-duty scaffolds. The load capacity of the heavy-duty scaffolds with shores is 86.3%  $(= (795.14/921.31) \times 100\%)$  of that of the three-story heavy-duty scaffolds of the same height.

### 5.1.2.2 150cm-long thin steel shores on top of scaffold

Two sets of load tests were conducted on the two-story heavy-duty scaffolds that were augmented with 150cm-long and thin steel shores on the top of scaffolds. The average load capacity was 216.45 kN, as shown in Table 1. Figure 11(B) presents the deformation of this heavy-duty scaffolds with shores under loading. As shown in the figure, most of the deformation was in the thin steel shores, as the heavy-duty scaffolds exhibited no significant deformation. Figure 13 plots the load-vertical displacement curve, which differs from that of the two-story and three -story heavy-duty scaffolds, and reveals that the stiffness of the heavy-duty scaffolds with shores is less than either.

The load capacity of the heavy-duty scaffolds with shores (216.45 kN) is 23.5%  $(= (216.45/921.31) \times 100\%)$  of that of the three-story heavy-duty scaffolds with the same height (921.31 kN) and 27.2%  $(= (216.45/795.14) \times 100\%)$  of that of the two-story heavy-duty scaffolds that were augmented with the 150cm-long thick steel shores on the top (795.14 kN).

### 5.1.2.3 80cm-long thin steel shores on top of scaffold

Two sets of load tests were conducted on the two-story heavy-duty scaffolds that were augmented with 80cm-long thin steel shores on the top of scaffolds. The average load capacity was 328.8 kN, as shown in Table 1. Figure 11(C) plots the deformation of the heavy-duty scaffolds with shores under loading. As shown in the figure, most of the deformation occurs in the thin steel shores as the deformation of the heavy-duty scaffolds is insignificant. Figure 14 plots the load-vertical displacement curve, which is similar of the two-story heavy-duty scaffolds that were augmented with 150cm-long thin steel shores on the top of scaffolds.

The above test results demonstrate that the load capacity of the heavy-duty scaffolds with shores declines as the length of the augmented thin shores on top of the heavy-duty scaffolds increases. The load capacity of the heavy-duty scaffolds with thin steel shores on top is significantly smaller than that of the same heavy-duty scaffolds with thick steel shores on top. Nevertheless, in Taiwan, heavy-duty scaffolds with thin steel shores on top are commonly used on construction sites.

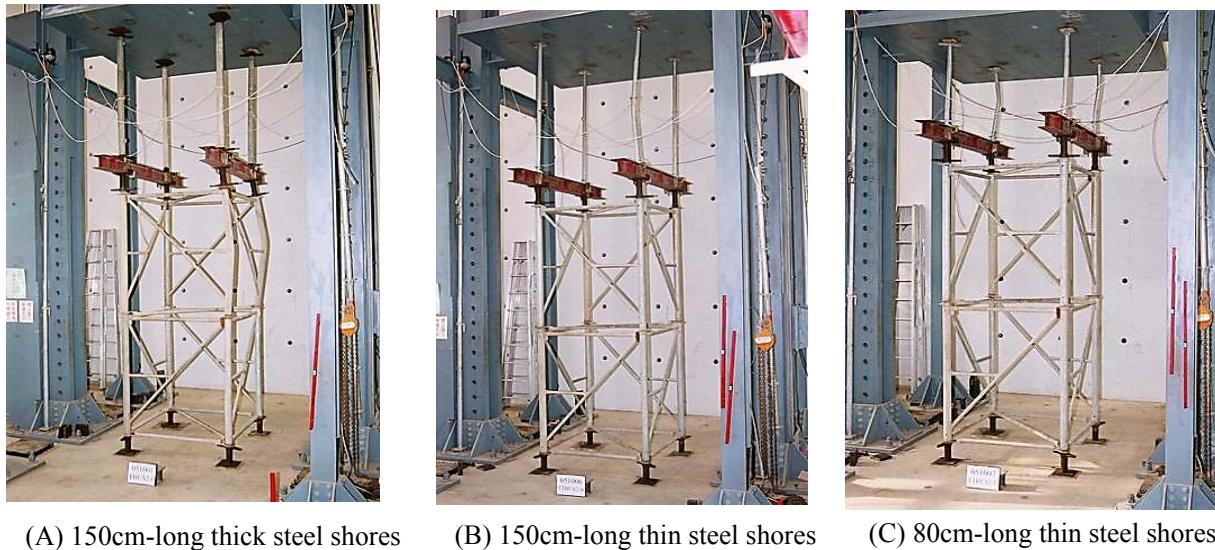


Figure 11. Deformations of Two-story Heavy-duty Scaffolds with Various Shores on Top under Loading

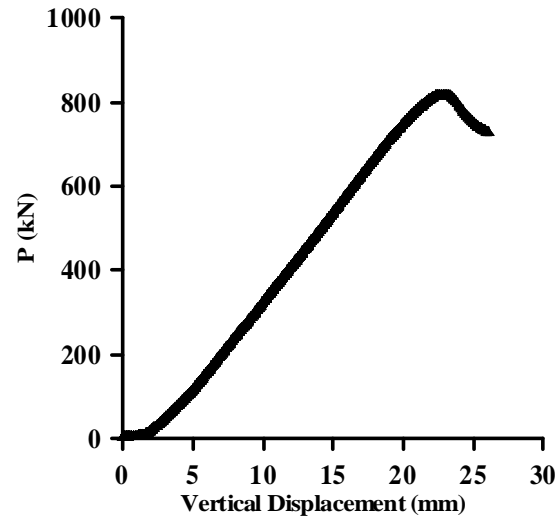


Figure 12. Load-vertical Displacement Curve from Load Test on Two-story Heavy-duty Scaffolds Augmented on Top with 150cm-long Thick Steel Shores

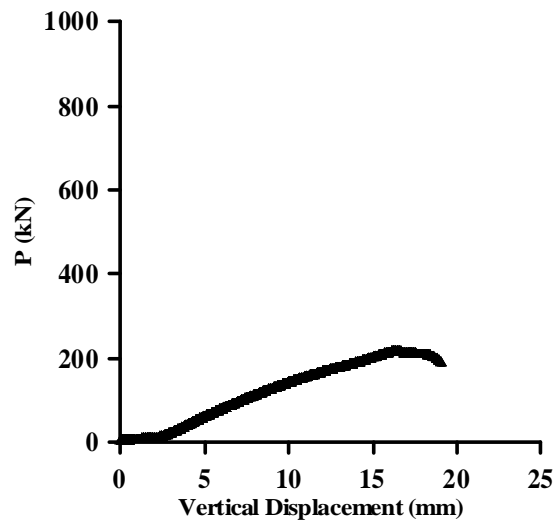


Figure 13. Load-vertical Displacement Curve from Load Test on Two-story Heavy-duty Scaffolds Augmented on Top with 150cm-long Thin Steel Shores



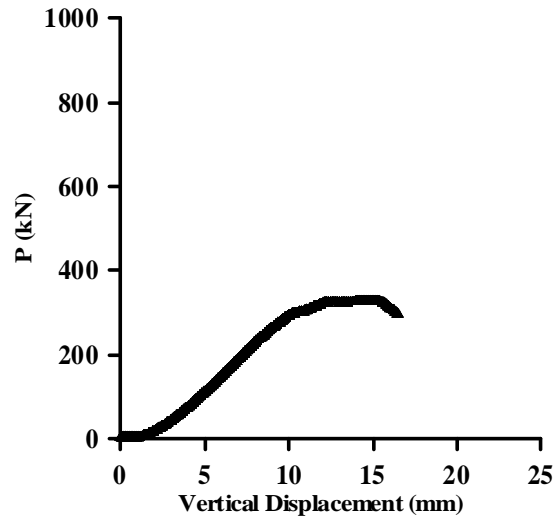


Figure 14. Load-vertical Displacement Curve from Load Test on Two-story Heavy-duty Scaffolds Augmented on Top with 80cm-long Thin Steel Shores

## 5.2 Outdoor Load Test on Heavy-duty Scaffold System with Shores

### 5.2.1 Load

An outdoor full-scale heavy-duty scaffolds with 150cm-long thin steel shores on top were tested because this kind of combined setup is the most commonly used on construction sites in Taiwan. After two stories of RC blocks were laid down on the heavy-duty scaffolds in the specified order, the placement of sandbags began. After the first sandbag (No. 21 load block) was laid down on the system, the theodolite registered a slight but apparent eastward displacement of the top-story H-beams, similar to those observed in tests on indoor independent heavy-duty scaffolds with shores before failure. Figure 15 shows the load conditions of this heavy-duty scaffold system with shores before failure.

### 5.2.2 Resistance

#### 5.2.2.1 System failure

In this test, the scaffold system failed entirely, instead of by a domino effect that was induced by the failure of a single member. When the first sandbag (No. 21 load block) was laid down, the overall system was determined to be liable to failure at any time, so field workers were dispersed rapidly and asked to wait for around 15 minutes while the system was observed. Before the second sandbag (No. 22 load block) was laid down, the overall heavy-duty scaffold system with shores collapsed suddenly without any warning.

During failure, the upper-story RC blocks and sandbags moved eastward, while the H-beams above the heavy-duty scaffolds moved westward under the pushing and jostling of the thin steel shores on the top story. The failure load of the heavy-duty scaffolds with shores was 363.405 kN.

In the tests, cameras were set up to the south and west of the heavy-duty scaffold system with shores to record the collapse process, as shown in Figs. 5A and 5B. Figures 16A and 16B present the collapse process as recorded from the south and west, respectively. As displayed in Figure 16A, the failure of the overall system is dominated by the deformation on the EW-plane (Figure 5B). As displayed in Figure 16B, hardly any lateral deformation on the SN-plane occurred (Figure 5B).

As shown in Figures 16A and 16B, just before the collapse of the scaffold system, all members of the heavy-duty scaffolds and the above thin steel shores were intact, so the collapse of the heavy-duty scaffold system with shores was dominated by the buckling of the overall scaffold system, rather than by a domino effect that originated in the failure of a single member.

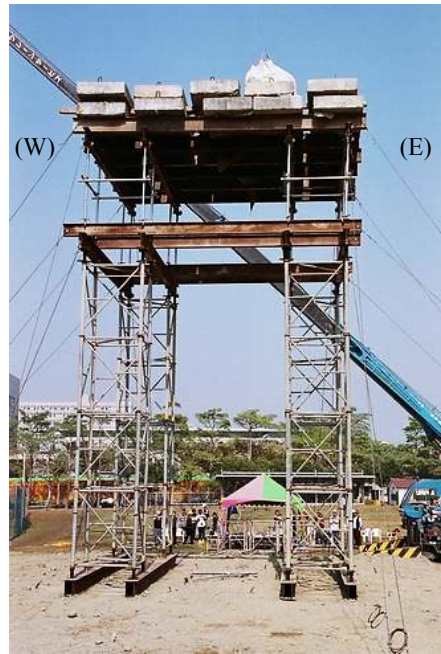


Figure 15. Load Application in Outdoor Test on Heavy-duty Scaffolds with Shores just before Collapse

#### 5.2.2.2 Description of system failure

Table 2 presents the test results, which are converted into the load-displacement curves ( $P-\Delta$  curves) in Figures 17 and 18. Figures 17 and 18 plot the lateral displacements of the upper- and lower-story H-beams, as observed by the theodolites that were set up to the north and the west of the scaffold system, respectively, when the system was loaded.

When the 20<sup>th</sup> record was obtained, the total displacement of the upper-story H-beams was 15 mm. When the 21<sup>st</sup> record was obtained, the applied load was 363.405 kN, and the lateral displacement had increased abruptly to 10 mm, for a total displacement of 25 mm, which is clearly larger than that observed in tests on the indoor independent setup of scaffolds (as shown in Figures 13 and 14). At the 21<sup>st</sup> recording moment, the outdoor scaffold system under loading was judged to have reached the critical load of system instability. Therefore, the test loading stopped for around 15 minutes to enable the system to be quietly observed. Before the 22<sup>nd</sup> sandbag was laid down, the overall heavy-duty scaffold system with shores collapsed suddenly without any warning.

Obviously, this structural system was under only vertical loads – and no lateral loads. Under a fixed vertical load in a static state, the overall structural system collapsed without the failure of any single member. This failure model should be regarded as a typical system buckling that is caused by the structural system instability. When loading reaches the critical load of the structural system, the overall system buckles and collapses by a minor disturbance owing to its unstable equilibrium. Figure 19 schematically depicts the overall buckling and collapse of a heavy-duty scaffold system with shores owing to instability.

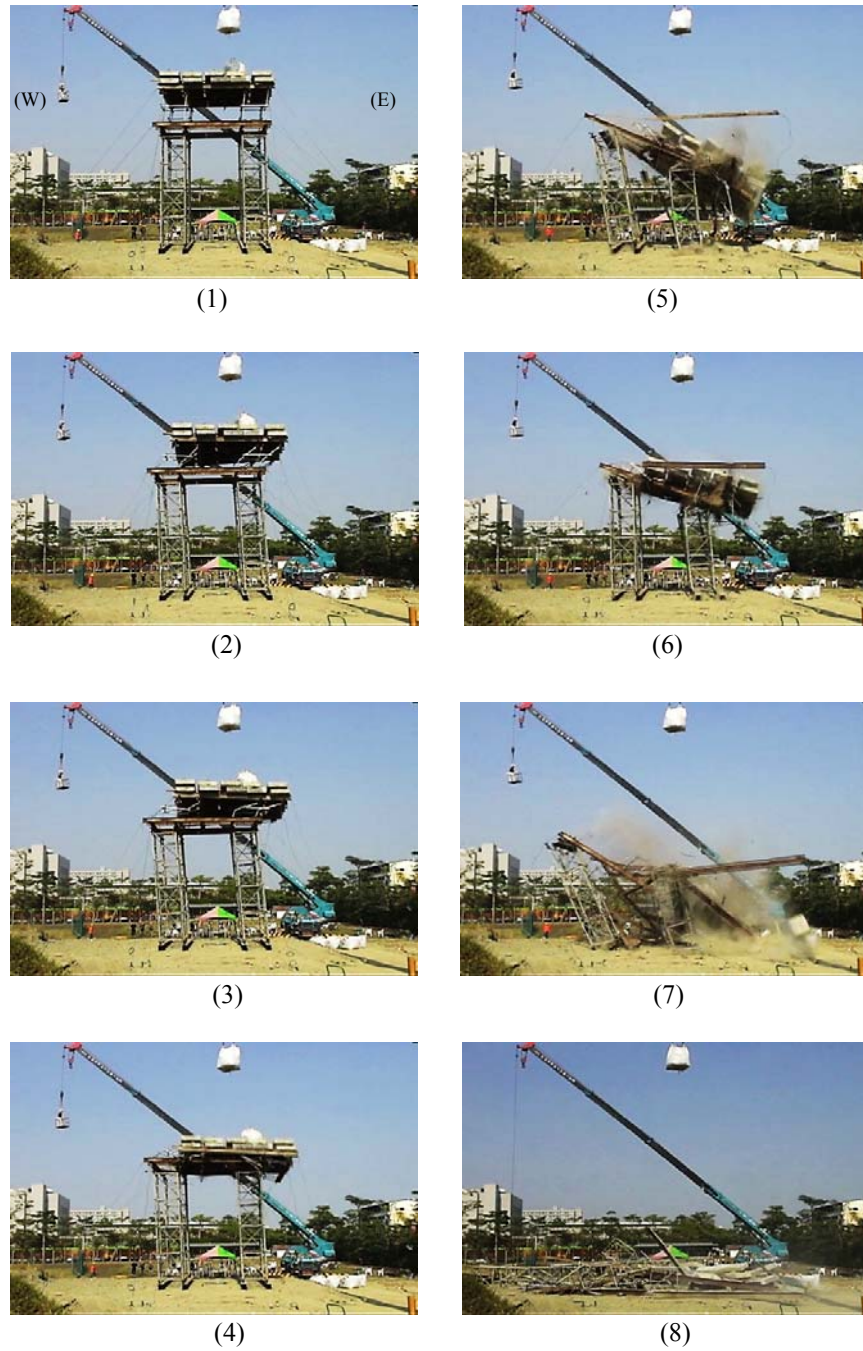


Figure 16A. Collapse of Outdoor Heavy-duty Scaffolds with Shores under Loading, as Recorded by Camera on the South



Figure 16B. Collapse of Outdoor Heavy-duty Scaffolds with Shores under Loading, as recorded by Camera on the West

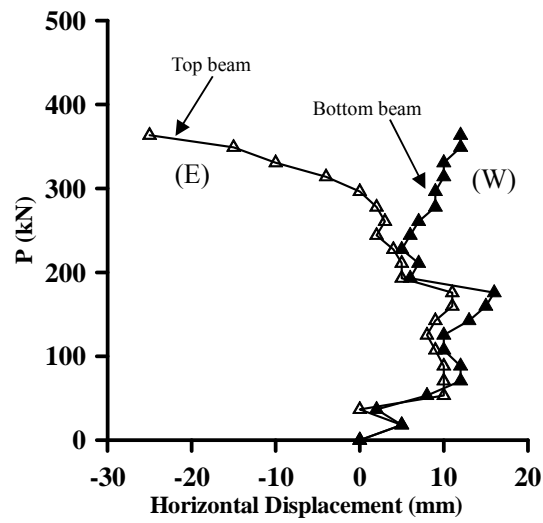


Figure 17. Load-displacement Relation of Upper- and Lower- Story H-beams, obtained by Theodolite on the North

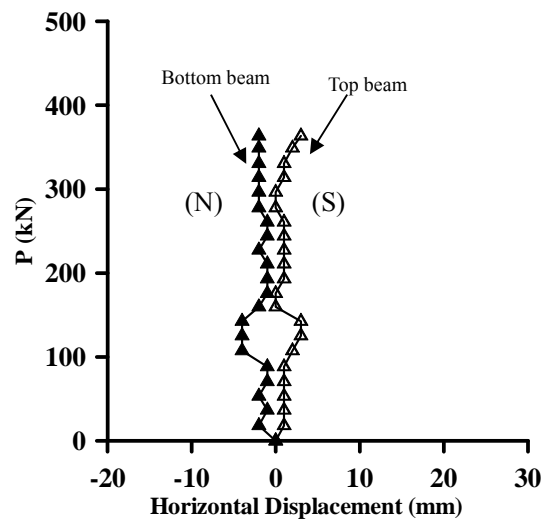


Figure 18. Load-displacement Relation of Upper- and Lower-story H-beams, obtained by Theodolite on the West

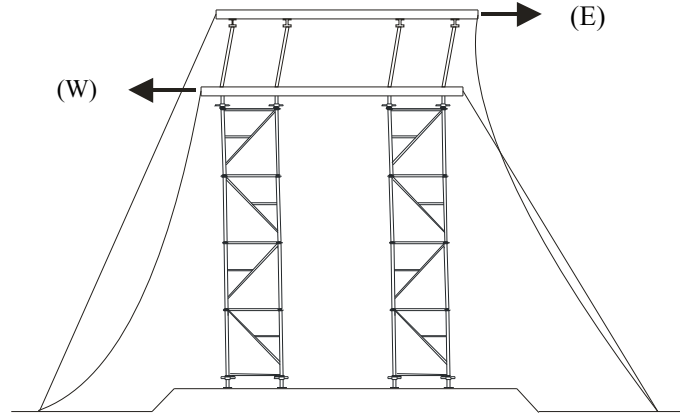


Figure 19. Buckling Failure of Outdoor Heavy-duty Scaffold System with Shores under Loading

Table 2. Weights of RC Blocks and Sandbags and Displacements Recorded on Theodolites during Outdoor Load Test on Full-scale Heavy-duty Scaffolds with Shores

Record No.	Cumulative load (kN)	Theodolite on the north (mm)				Theodolite on the west (mm)			
		D <sub>NT</sub>	Δ <sub>NT</sub>	D <sub>NB</sub>	Δ <sub>NB</sub>	D <sub>WT</sub>	Δ <sub>WT</sub>	D <sub>WB</sub>	Δ <sub>WB</sub>
0	0.000	430	0	340	0	380	0	365	0
1	18.270	435	5	345	5	381	1	363	-2
2	36.677	430	0	342	2	381	1	364	-1
3	53.319	440	10	348	8	381	1	363	-2
4	70.657	440	10	352	12	381	1	364	-1
5	88.378	440	10	352	12	381	1	364	-1
6	107.422	439	9	350	10	382	2	361	-4
7	125.319	438	8	350	10	383	3	361	-4
8	142.540	439	9	353	13	383	3	361	-4
9	159.741	441	11	355	15	380	0	363	-2
10	175.745	441	11	356	16	380	0	364	-1
11	193.113	435	5	346	6	381	1	364	-1
12	210.902	435	5	347	7	381	1	364	-1
13	227.387	434	4	345	5	381	1	363	-2
14	244.097	432	2	346	6	381	1	364	-1
15	260.778	433	3	347	7	381	1	364	-1
16	277.803	432	2	349	9	380	0	363	-2
17	296.377	430	0	349	9	380	0	363	-2
18	313.950	426	-4	350	10	381	1	363	-2
19	330.680	420	-10	350	10	381	1	363	-2
20	349.078	415	-15	352	12	382	2	363	-2
21	363.405	405	-25	352	12	383	3	363	-2

Notes:

1. Δ<sub>ET</sub>、Δ<sub>EB</sub>、Δ<sub>NT</sub>、Δ<sub>NB</sub>:Record number (1~21)–Record number (0)
2. D:original value; Δ:calibration value; w:west; n:north; t:top H-beam; b:bottom H-beam

### 5.2.3 Load Capacity in Outdoor Test, Estimated from Indoor Test

As shown in Table 1, the load capacity of the indoor two-story heavy-duty scaffolds with 150cm-long thin steel shores was 216.45 kN. When this scaffold system failed, the upper-story thin steel shores deformed apparently but the lower story heavy-duty scaffolds deformed much less. Multiplying the load capacity of this independent two-story heavy-duty scaffolds that were test indoors by four yielded a possible load of 865.8 kN (=216.45×4).



Four sets of four-story heavy-duty scaffolds that were augmented on top with 150cm-long thin steel shores were used in the outdoor test. However, the horizontal restraint of the steel wire ropes that was used in the outdoor test was not as good as that of the steel holder on the top of the universal testing machine that was used in the indoor tests.

Comparing the fourfold load capacity of the indoor two-story heavy-duty scaffolds augmented on top with 150cm-long thin steel shores with the load capacities of the outdoor four-story heavy-duty scaffold system augmented on top with 150cm-long thin steel shores (363.418 kN) revealed that the load capacity in the outdoor test was 42% ( $= (363.418/865.8) \times 100\%$ ) of that in the indoor test. Thus, engineers should not calculate the load capacity of an outdoor heavy-duty scaffold system with shores based on an indoor test of an independent heavy-duty scaffold system with shores.

### 5.3 Test results and second-order inelastic analyses of heavy-duty scaffold systems

#### 5.3.1 Indoor heavy-duty scaffolds with shores

##### 5.3.1.1 Restraint Boundary

In this study, a second-order inelastic analysis with semi-rigid joints of the indoor independent two-story heavy-duty scaffolds with 150cm-long thin steel shores on top was conducted. Figure 4 displays the dimensions of the combined system that was used in the analysis. The cross-sections of various members of the heavy-duty scaffolds and thin steel shores are as described in previous sections. An  $E_r$  (reduced modulus) of 14,715 kN/cm<sup>2</sup> (1500 tonne/cm<sup>2</sup>) was utilized in this study.

Based on the method that was used by Peng *et al.* [10], the stiffnesses of the joints in the scaffold systems were estimated by comparing the results of a second-order inelastic analysis with semi-rigid joints with the relevant test results. In this study, the stiffness of the joints in various members of the heavy-duty scaffolds were estimated as follows; the stiffness of the join between the vertical main rods was 5,688 kN-cm/rad; the stiffness of the top jack and the jack base was 9,807 kN-cm/rad, and the stiffness of the joints between horizontal bars and between diagonal braces was the stiffness of typical hinge joints. Based on these joint stiffnesses and the second-order inelastic analysis with semi-rigid joints, the critical load of the independent two-story heavy-duty scaffolds with shores was estimated to be 207.908 kN, which was around 96% of the value obtained in the test ( $= (207.908/216.45) \times 100\%$ ).

Figure 20 displays the deformation of the independent two-story heavy-duty scaffolds with shores under loading based on a second-order inelastic analysis with semi-rigid joints, which is very close to that obtained in the test. Figure 11(B) exhibits the deformation obtained in the test. As displayed in Figure 20, the top of the 150cm-long thin steel shores are restrained in the x-direction and the z-direction but not in the y-direction. Figure 21 plots the P- $\Delta$  curve of the relationship between the lateral displacement and the total vertical load at point A in Figure 20 in the z direction.

##### 5.3.1.2 Unrestrained boundary simulated by linear spring

In the outdoor load test on the heavy-duty scaffold system with shores, eight steel wire ropes were set up on the top of the scaffold system to provide a restrained boundary. However, in the load tests, these eight steel wire ropes relaxed and lateral displacements occurred on the top of the scaffold system. In the second-order inelastic analysis, the linear spring simulated this unrestrained boundary with lateral displacements.

In the second-order inelastic analysis of the independent two-story heavy-duty scaffolds with 150cm-long thin steel shores under spring-like boundary conditions, the boundaries of the top story of the scaffold system were allowed to move in x, y and z directions. However, at the top of the four thin steel shores, the stiffness of 0.4 kN/cm of the linear spring simulated the boundary conditions in the x and z directions. Figure 22 presents the arrangements of the linear springs. The second-order inelastic analysis yields the critical load of this scaffold system as 191.237 kN, which is lower than that of the previous system with the restrained boundary (207.908 kN). Figure 23 displays the deformation of the second-order inelastic analysis of the heavy-duty scaffold system with shores under loading. Figure 24 plots the P- $\Delta$  curve of the vertical load and lateral displacement of point A in Figure 23 in the z direction.

### 5.3.2 Outdoor Heavy-duty Scaffold System with Shores

In the tests on the outdoor heavy-duty scaffold system with shores, steel wire ropes were used to constrain the top story but relaxation occurred during the test. Therefore, in the second-order inelastic analysis of this scaffold system, the linear springs were used to simulate the unrestrained boundary conditions of the top story of the scaffold system. The linear spring with a stiffness of 0.4 kN/cm simulated the boundary condition in the x and z directions at the four corners of the scaffold system. Figure 25 displays the arrangement of the linear springs in the scaffold system.

Based on the joint stiffness that was obtained in the second-order inelastic analysis of the aforementioned indoor two-story heavy-duty scaffold system with shores, a second-order inelastic analysis of the outdoor heavy-duty scaffold system with shores just yielded a critical load of 356.612 kN. This analytical value is very close to the test value (363.418 kN). Figure 26 shows the deformation obtained in the second-order inelastic analysis of the heavy-duty scaffold system with shores under loading. Figure 27 plots the P- $\Delta$  curve of load and lateral displacement of point A in Figure 26 in the x direction.

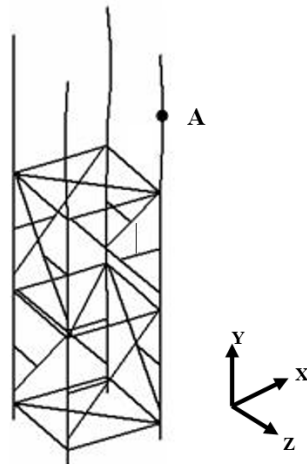


Figure 20. Deformation obtained by Second-order Inelastic Analysis of Independent Heavy-duty Scaffolds with 150cm-long Thin Steel Shores on Top



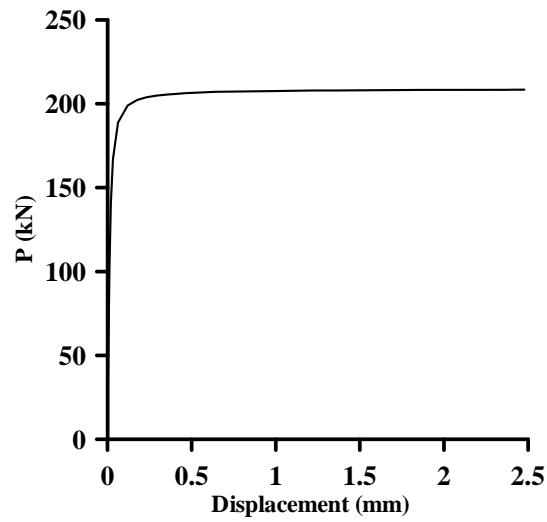


Figure 21. P- $\Delta$  Curve obtained by Second-order Inelastic Analysis of Independent Heavy-duty Scaffolds with 150cm-long Thin Steel Shores on Top (in z direction)

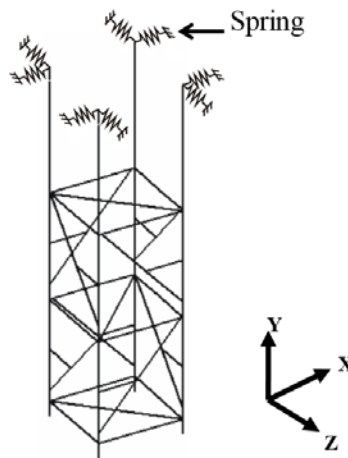


Figure 22. Configuration of Spring Boundary Condition in Second-order Inelastic Analysis of Independent Heavy-duty Scaffolds with 150cm-long Thin Steel Shores on Top

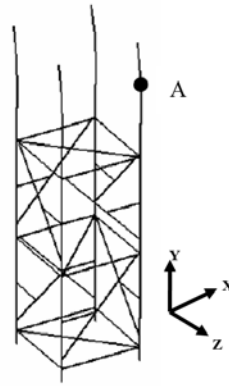


Figure 23. Deformation obtained by Second-order Inelastic Analysis of Independent Heavy-duty Scaffolds with 150cm-long Thin Steel Shores using Linear Spring Boundary Condition

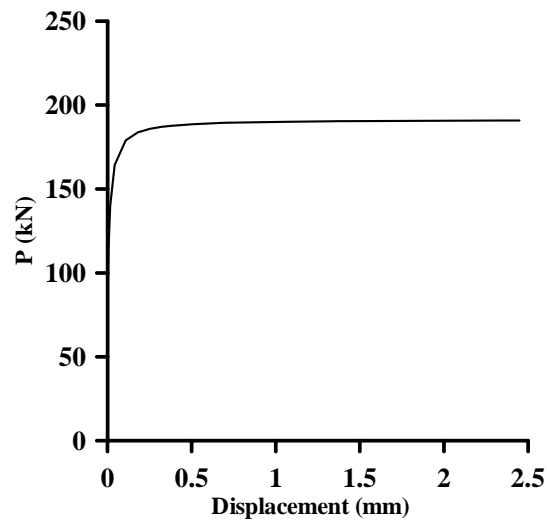


Figure 24. P-Δ Curve obtained by Second-order Inelastic Analysis of Independent Heavy-duty Scaffolds with 150cm-long Thin Steel Shores using Linear Spring Boundary Condition (in z direction)

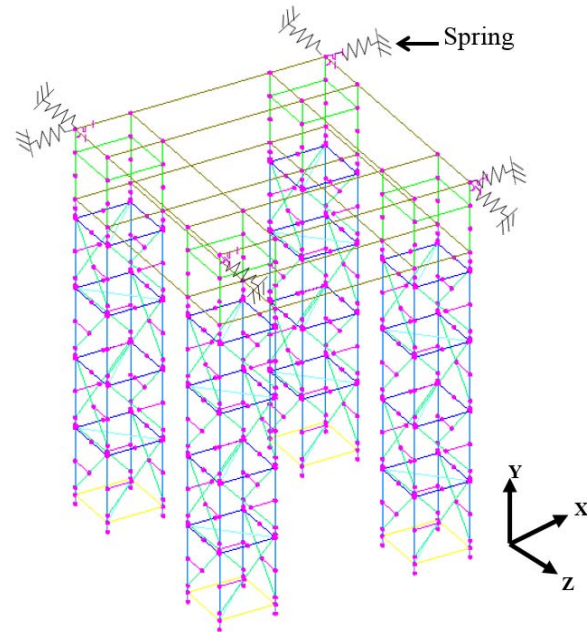


Figure 25. Configuration of Spring Boundary Condition in Second-order Inelastic Analysis of Heavy-duty Scaffold System with 150cm-long Thin Steel Shores on Top

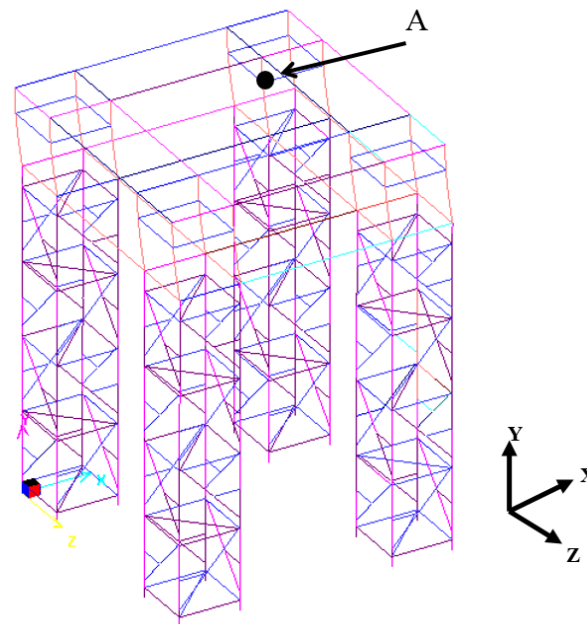


Figure 26. Deformation obtained by Second-order Inelastic Analysis of Heavy-duty Scaffold System with Shores using Linear Spring Boundary Condition

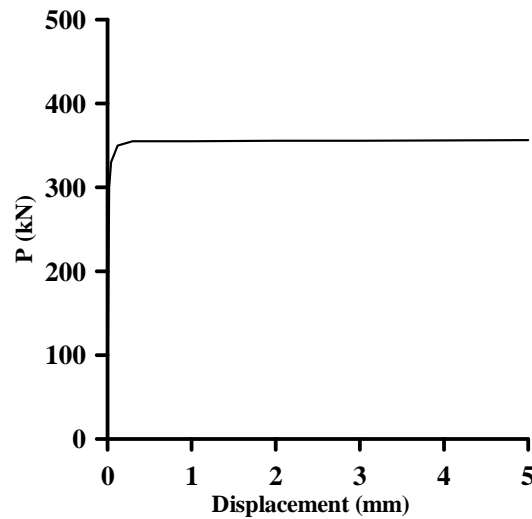


Figure 27. P-Δ curve obtained by Second-order Inelastic Analysis of Heavy-duty Scaffold System with Shores using Linear Spring Boundary Conditions (in x direction)

## 6. CONCLUSIONS

This study involved both practical tests and analyses, and the following findings were obtained.

1. The load capacities of two-story and three-story heavy-duty scaffolds are close to each other and their failure models are similar. Therefore, the load capacity of heavy-duty scaffolds may not significantly decline as the number of stories increases.
2. The load capacity of two-story heavy-duty scaffolds that are augmented on top with 1.5m-long thin steel shores is much lower than that of three-story heavy-duty scaffolds with the same height. Engineers should avoid adopting the heavy-duty scaffolds with thin steel shores on construction sites.
3. The load capacity of two-story heavy-duty scaffolds that are augmented on top with 1.5m-long thick steel shores is very close to that of three-story heavy-duty scaffolds with the same height. This test result herein may serve as a reference for construction contractors in installing safe heavy-duty scaffolds with shores when necessary.
4. Owing to the uneven settlement of the overall heavy-duty scaffold system with shores in the outdoor test, relaxation occurred on the steel wire ropes, causing lateral displacement of the top of the combined scaffold system. Therefore, the critical load of the heavy-duty scaffold system with shores was lower than the expected value. Engineers need to check the uneven settlement of the base of heavy-duty scaffold system with shores on construction sites before the installation.
5. In the second-order inelastic analysis with semi-rigid joints for the outdoor heavy-duty scaffold system with shores, linear springs at the top of the system were used to simulate the lateral displacement of the boundaries due to the relaxation of the steel wire ropes. The analytical values that were generated using this method were very close to the values obtained in the test.
6. In a rough design, the load capacity of a heavy-duty scaffold system with shores is estimated based on that of indoor independent heavy-duty scaffolds without shores. This approximate method tends to misestimate the load capacity of the overall heavy-duty scaffold system with shores, leading to an extremely high risk of collapse, as demonstrated by the outdoor tests in this study.

## ACKNOWLEDGEMENTS

The authors would like to thank the Ministry of Science and Technology for funding this study (MOST 105-2221-E-224-015), Taiwan Hao-Ji Company for providing test materials, and Mr. Ming-zhi Jian for helping to perform the tests. Without their supports, this study would not have been completed.

## REFERENCES

- [1] Chan, S.L., "Geometric and Material Nonlinear Analysis of Beam-columns and Frames using the Minimum Residual Displacement Method", *International Journal for Numerical Method in Engineering*, 1988, Vol. 26, pp. 2657-2669.
- [2] Chan, S.L. and Cho, S.H., "Second-order P- $\Delta$ - $\delta$  Analysis and Design of Angle Trusses Allowing for Imperfections and Semi-rigid Connections", *International Journal of Advanced Steel Construction*, 2005, Vol. 1, No. 1, pp. 157-172.
- [3] Chan S.L. and Zhou Z.H., "A Pointwise Equilibrium Polynomial (PEP) Element for Nonlinear Analysis of Frame", *Journal of Structural Engineering ASCE*, 1994, Vol. 120, No. 6, pp. 1703-1717.
- [4] Huang, Y.L., Kao, Y.G. and Rosowsky, D.V., "Load-carrying Capacities and Failure Modes of Scaffolding Shoring Systems, Part II: Analytical model and its closed-form Solution," *Structural Engineering and Mechanics*, 2000, Vol. 10, No. 1, pp.53-66.
- [5] Liu, H., Zhao, Q., Wang, X., Zhou, T., Wang, D., Liu, J. and Chen, Z., "Experimental and Analytical Studies on the Stability of Structural Steel Tube and Couple Scaffolds without X-bracing," *Engineering Structures*, 2010, Vol. 32, pp.1003-1015.
- [6] Kuo, C.C., Peng, J.L., Yen, T. and Chan, S.L., "Experimental Study of Modular Falsework System with Wooden Shores under Various Path Loads," *Advances in Structural Engineering*, 2008, Vol. 11, No.4, pp.369-382.
- [7] Peng, J.L., Ho, C.M., Chen, C.Y. and Yang, Y.B., "Experimental Study on Load Capacities of Isolated Heavy-Duty Scaffolds Used in Construction," *Journal of Advanced Steel Construction*, 2014, Vol. 10, No. 3, pp.248~273.
- [8] Peng, J.L., Ho, C.M., Lin, C.C. and Chen, W.F., "Load-Carrying Capacity of Single-Row Steel Scaffolds with Various Setups", *Journal of Advanced Steel Construction*, 2015, Vol. 11, No.2, pp.185~210.
- [9] Peng, J.L., Yen, T., Lin, I., Wu, K.L. and Chen, W.F., "Performance of Scaffold Frame Shoring under Pattern Loads and Load Paths," *Journal of Structural Engineering*, 1997, ASCE, Vol. 123, No. 2, pp138-145.
- [10] Peng, J.L., Yen, T., Kuo, C.C. and Chan, S.L., "Analytical and Experimental Bearing Capacities of System Scaffolds," *Journal of Zhejiang University Science A*, 2009, Vol.10, No.1, pp.82-92.
- [11] Peng, J.L., Wu, C.L. and Chan, S.L., "Sequential Pattern Load Modeling and Warning-system Plan in Modular Falsework," *Structural Engineering and Mechanics*, 2003, Vol. 16, No. 4, pp.441-468.
- [12] Zhang, H., Chandrangsu, T. and Rasmussen, K.J.R., "Probabilistic Study of the Strength of Steel Scaffold Systems," *Structural Safety*, 2010, Vol.32, pp.393-401.
- [13] Zhang, H., Rasmussen, K.J.R. and Ellingwood, B.R., "Reliability Assessment of Steel Scaffold Shoring Structures for Concrete Formwork", *Engineering Structures*, 2012, Vol. 36, pp.81-89.



*First Announcement and Call for Papers*

**ICASS '18**  
**9<sup>th</sup> International Conference on**  
**Advances in Steel Structures**  
**Hong Kong, 5-7 December 2018**

Conference web: [www.ascjournal.com/icass2018](http://www.ascjournal.com/icass2018)

Organised by

**Department of Civil and Environmental Engineering**  
**The Hong Kong Polytechnic University**

Sponsored by (to be confirmed)



THE HONG KONG  
INSTITUTION OF ENGINEERS  
香港工程師學會  
Civil, Structural and Fire Divisions



香港  
鋼結構學會  
Hong Kong Institute of  
Steel Construction

**RCATISE**  
**Research Centre for Advanced**  
**Technology in Structural**  
**Engineering**  
The Hong Kong Polytechnic  
University

## Scope and Objectives

This will be the ninth in the international conference series on Advances in Steel Structures, with the first, second, third and sixth of the conferences series held in Hong Kong, fourth in Shanghai, fifth in Singapore, seventh in Nanjing and eighth in Portugal. As with the eight previous successful conferences, this conference is intended to provide a forum for researchers and professionals to discuss and disseminate recent advances in analysis, behaviour, design and construction of steel, aluminium and composite steel-concrete structures.

Papers related to all aspects of analysis, behaviour, design, fabrication and construction of steel and composite steel-concrete structures are invited. The following topics are not exhaustive and papers that fall within the general theme of the conference will be considered for presentations and for publications in the conference proceedings and uploaded to web [www.hkisc.org/icass2018](http://www.hkisc.org/icass2018). Selected papers will also be published in the International Journal of Advances in Steel Construction which carries a mission of technology transfer and is widely circulated among the engineering and building professionals.

Steel Structures, Composite Construction, Mixed Construction, Aluminium and Glass Structures, Cold-Formed Steel, Columns, Beams, Beam-Columns, Frames, Connections, Space Structures, Tall Buildings, Bridges, Cable Structures, Pre-tensioned Structural Systems, Curtain Walling, Scaffolding, Roof Cladding, Silos, Tanks, Pipelines, Offshore Platforms, Chimneys, Transmission Line Towers and Masts, Design Codes, Expert Systems, Structural Stability, Stability Design, Computational Methods, Advanced Analysis, Second-order Direct and Indirect Analysis, Non-linear Analysis, Performance-based Structural Design, Dynamics, Seismic-resistant Structures, Vibration Control, System Identification, Fatigue and Fracture, Corrosion, Fire Engineering, Structural Optimisation, Life-cycle Performance, Code and Standard Development.

## Official Language

English will be the official language of the Conference for both oral and written presentations.

## Key Dates

Submission of Abstracts: 1 March 2018  
Provisional Acceptance: 1 May 2018  
Submission of Final Papers: 1 July 2018  
Final Notice of Acceptance: 31 August 2018  
Conference: 5-7 December 2018

## Proceedings

The proceedings of the conference will be published by the Hong Kong Institute of Steel Construction.

## Registration Fee

The conference registration fee is US\$750 (Early bird registration before 1<sup>st</sup> September 2018)/US\$850, which covers conference proceedings, conference banquet, lunches and refreshments.

## Call for Papers

Authors are invited to submit 200-300 words abstracts of papers to ICASS'18. All enquiries relating to the conference should be addressed to:

Ms Carol Deng  
Conference Secretary  
The Hong Kong Institute of Steel Construction

Email: [carol.deng@hkisc.org](mailto:carol.deng@hkisc.org)  
Conference web: [www.ascjournal.com/icass2018](http://www.ascjournal.com/icass2018)

**Conference chairman** Siu-Lai Chan

**Co-chairmen** Tak-Ming Chan and Songye Zhu



**ORDER  
FORM**

ISSN 1816-112X

**Advanced Steel Construction,  
an international journal**Indexed by the Science Citation Index Expanded,  
Materials Science Citation Index and ISI Alerting Services**From:****To:** Secretariat, Advanced Steel Construction, an international journal  
**Fax:** (852) 2334-6389

I/ We would like to enter a subscription to the *International Journal of Advanced Steel Construction (IJASC)* published by The Hong Kong Institute of Steel Construction.

Please complete the form and send to:

International Journal of Advanced Steel Construction  
c/o Department of Civil and Environmental Engineering  
The Hong Kong Polytechnic University  
Hung Hom, Kowloon, Hong Kong

Fax: (852) 2334-6389 Email: [ceslchan@polyu.edu.hk](mailto:ceslchan@polyu.edu.hk)

Published by : The Hong Kong Institute of Steel Construction  
Website: <http://www.hkisc.org/>

**Please tick the appropriate box**

- ☐ Please enter my hard-copy subscription (**4 issues per year**).  
☐ Please send me a complimentary copy of the *Advanced Steel Construction, an International Journal (IJASC)*.

*Please tick the appropriate box(es)*

	<u>Print</u>	<u>On-line is free</u>
<b>Personal</b>	<input type="checkbox"/> US\$ 125	
<b>Institutional</b>	<input type="checkbox"/> US\$ 280	

**Total Amount** US\$ \_\_\_\_\_

**Methods of payment** ☐ Please invoice me  
(please tick the appropriate box(es)) ☐ Cheque enclosed for US\$ \_\_\_\_\_ payable to  
Hong Kong Institute of Steel Construction Limited  
(No personal cheque accepted)

**Ship to**

Name (Prof./ Dr./ Mr./ Ms.) \_\_\_\_\_  
Address \_\_\_\_\_  
\_\_\_\_\_  
City/ State/ Postal Code \_\_\_\_\_  
Country \_\_\_\_\_  
Email \_\_\_\_\_ Fax \_\_\_\_\_